



**HAL**  
open science

# Modélisation neutronique des réacteurs à lit de boulets dans le code APOLLO2

Maurice Grimod

► **To cite this version:**

Maurice Grimod. Modélisation neutronique des réacteurs à lit de boulets dans le code APOLLO2. Modélisation et simulation. Université Paris Sud - Paris XI, 2010. Français. NNT : . tel-00728695

**HAL Id: tel-00728695**

**<https://theses.hal.science/tel-00728695>**

Submitted on 6 Sep 2012

**HAL** is a multi-disciplinary open access archive for the deposit and dissemination of scientific research documents, whether they are published or not. The documents may come from teaching and research institutions in France or abroad, or from public or private research centers.

L'archive ouverte pluridisciplinaire **HAL**, est destinée au dépôt et à la diffusion de documents scientifiques de niveau recherche, publiés ou non, émanant des établissements d'enseignement et de recherche français ou étrangers, des laboratoires publics ou privés.

# THÈSE DE DOCTORAT DE L'UNIVERSITÉ PARIS-SUD 11

École doctorale: MIPEGE

*Présentée par:*

**MAURICE GRIMOD**

*en vue d'obtenir le grade de*

**Docteur en Sciences de l'Université Paris-Sud 11**

## Modélisation Neutronique des Réacteurs à Lit de Boulets dans le code APOLLO2

-

## Neutronic Modeling of Pebble Bed Reactors in APOLLO2

7 Décembre 2010

Richard SANCHEZ	Directeur de thèse
Piero RAVETTO	Rapporteur
Jan Leen KLOOSTERMAN	Rapporteur
Bernard BERTHIER	Examineur
Abderrafi OUGOUAG	Examineur
Frédéric DAMIAN	Examineur
Frederik REITSMA	Invité



**Laboratoire de rattachement:**

Laboratoire de Protection, d'Études et de Conception  
Service d'Études des Réacteurs et de Mathématiques Appliquées  
Département de Modélisation des Systèmes et Structures  
Délégation aux Activités Nucléaires de Saclay  
Direction de l'Énergie Nucléaire  
Commissariat à l'Énergie Atomique

CEA, centre de Saclay  
DEN / DANS / DM2S / SERMA / LPEC  
91191 Gif-sur-Yvette CEDEX



# Résumé

Dans cette thèse une nouvelle technique itérative d'homogénéisation pour les réacteurs à lit de boulets est développée. Le calcul de flux, dans une géométrie hétérogène multi-boulets, se base sur une approximation "macro-stochastique" du transport dans la méthode des probabilités de collision.

La distribution stochastique des boulets avec différents taux de combustion dans le cœur est traitée par un modèle qui considère les différences spectrales, propres à chaque type de boulet, pour les calculs d'homogénéisation et d'évolution microscopique. Cette méthode est novatrice car, dans les codes de calcul actuellement employés, on considère un seul boulet de composition isotopique moyenne.

Dans le schéma de calcul itératif, le calcul de cœur, par la méthode  $S_N$  en différences finies RZ, permet de récupérer les courants rentrants aux interfaces des régions de spectre qui subdivisent le cœur. Ces courants sont employés comme terme source pour le calcul du flux, sur un maillage énergétique fin, des géométries multi-boulets associées à chaque région de spectre, en imposant le  $k_{eff}$  du cœur.

La méthode développée dans le code de calcul neutronique APOLLO2 a été vérifiée par comparaison avec des simulations Monte Carlo de référence, avec TRIPOLI4. Un modèle simplifié du réacteur PBMR-400 a été construit. Une vérification par étapes successives a été réalisée, dans le but de quantifier les effets sur la réactivité ( $k_{eff}$ ) du cœur, sur la distribution des taux de production, sur le rapport des productions sur les absorptions du cœur et sur les temps de calcul liés aux variations des paramètres de calcul tels que: le nombre de groupes, le maillage spatial, l'ordre de quadrature angulaire  $S_N$  et le nombre de régions de spectre dans le calcul RZ du cœur.

Une vérification plus complète est faite avec un modèle où les boulets sont positionnés un par un dans la cavité du cœur et ils possèdent six différents niveaux de taux de combustion, aléatoirement distribués. Le mélange stochastique microparticules/matrice en graphite, contenu à l'intérieur des boulets, est décrit par un milieu homogène équivalent. Les résultats obtenus par le modèle APOLLO2 sont peu différents de la référence (moins de 100 pcm sur le  $k_{eff}$ , de  $\pm 4\%$  sur la distribution des taux de production, avec une différence de 3% au point chaud).

Ensuite, une première validation a été réalisée par rapport à la première divergence du prototype HTR-10. Les résultats ont été comparés à ceux d'un benchmark international où l'on devait évaluer le nombre total de boulets, pour un mélange de boulets combustibles et modérateurs, à charger dans le cœur pour le rendre critique. Le nombre obtenu avec le nouveau modèle est seulement de 77 boulets en dessous de la valeur expérimentale de 16890 boulets. Ce résultat est très bon comparé aux résultats obtenus par les participants au benchmark.

Une méthode a ensuite été développée pour évaluer la composition du cœur à l'équilibre et elle a été appliquée pour analyser le modèle simplifié du PBMR-400 chargé avec différents types de combustible ( $UO_2$ , Pu, Pu + actinides mineurs). La nouvelle méthode a été appliquée pour évaluer le biais associé à l'utilisation d'un seul boulet de composition isotopique moyenne. Il a été montré que, grâce à une "compensation de l'erreur", ce biais est faible quand le cœur est chargé en  $UO_2$ , avec des écarts sur les facteurs de puissance et sur les concentrations des principaux nuclides à la décharge compris dans un intervalle de  $\pm 1\%$ . Les différences spectrales entre les différents types de boulets étant en grande partie dues aux résonances du  $Pu^{240}$ , le biais est plus important quand le cœur est chargé avec un combustible de Pu. Dans cette configuration, les écarts sur les distributions de puissances et les concentrations atteignent  $\pm 10\%$ .

Pour conclure, en se basant sur l'expérience accumulée au CEA sur la modélisation des réacteurs à haute température à blocs prismatiques et avec la méthode développée dans ce travail de thèse, on pourrait monter un schéma complet itératif de calcul couplé neutronique – thermo-hydraulique, en calculant le cœur 3D en diffusion (ou en transport si nécessaire) et en associant à chaque région de spectre une géométrie multi-boulets.

*Mots Clé: Réacteur à lit de boulets, homogénéisation itérative, géométrie multi-boulets, cœur à l'équilibre, APOLLO2*



# *Abstract*

In this thesis we develop a new iterative homogenization technique for pebble bed reactors, based on a "macro-stochastic" transport approximation in the collision probability method.

A model has been developed to deal with the stochastic distribution of pebbles with different burnup in the core, considering spectral differences in homogenization and depletion calculations. This is generally not done in the codes presently used for pebble bed analyses, where a pebble with average isotopic composition is considered to perform the cell calculation. Also an iterative core calculation scheme has been set up, where the low-order RZ  $S_N$  full-core calculation computes the entering currents in the spectrum zones subdividing the core. These currents, together with the core  $k_{eff}$ , are then used as surface source in the fine-group heterogeneous calculation of the multi-pebble geometries.

The developed method has been verified using reference Monte Carlo simulations of a simplified PBMR-400 model. The pebbles in this model are individually positioned and have different randomly assigned burnup values. The APOLLO2 developed method matches the reference core  $k_{eff}$  within  $\pm 100$  pcm, with relative differences on the production shape factors within  $\pm 4\%$ , and maximum discrepancy of 3% at the hot spot.

Moreover, the first criticality experiment of the HTR-10 reactor was used to perform a first validation of the developed model. The computed critical number of pebbles to be loaded in the core is very close to the experimental value of 16890, only 77 pebbles less.

A method to calculate the equilibrium reactor state was also developed and applied to analyze the simplified PBMR-400 model loaded with different fuel types ( $UO_2$ , Pu, Pu + MA). The potential of the APOLLO2 method to compute different fluxes for the different pebble types of a multi-pebble geometry was used to evaluate the bias committed by the average composition pebble approximation. Thanks to a "compensation of error", this bias is small when the core is loaded with  $UO_2$  fuel, with discrepancies on the power shape factors and main nuclide densities in discharged pebbles within  $\pm 1\%$ , except for plutonium isotopes, with an underestimation of 3% for  $Pu^{240}$  at discard. The spectral differences between the pebbles being mostly linked to the resonance of  $Pu^{240}$ , this bias is important for the Pu loaded core, where differences up to  $\pm 10\%$  on the power shape factors and on the main nuclide densities are observed.

Based on the accumulated experience at CEA on prismatic HTGRs modeling, a coupled neutronic-thermal hydraulic 3D core model of a PBR could be built, associating a multi-pebble geometry to each three-dimensional spectrum zone of the core.

*Key Words: Pebble Bed Reactor, iterative homogenization, multi-pebble geometry, equilibrium core, APOLLO2*





# Nomenclature of PBR Modeling

**PBR;** Pebble Bed Reactor

**Fuel Pebble;** it is a ball constituted by a heterogeneous inner fuel region and a homogeneous outer graphite region. The inner fuel region is composed by a stochastic distribution of coated fuel microparticles dispersed in a graphite matrix.

In our calculations, both the microparticles and the pebbles are numerically subdivided into several radial volumes called *computational shells*.

**Core cavity;** the bed of pebbles is contained in a cavity (cylindrical or annular) delimited by graphite reflectors. The pebbles flow downward through the reactor cavity.

**Flow-line;** it is the statistical average of the vertical trajectories of the pebbles starting from a top point of the bed. Each flow line is associated to an average flow velocity.

**Packing fraction ( $pkf$ );** it is defined over a core sub-region as the ratio of the volume of the pebbles and the total (pebble + coolant) volume.

**Discharged Pebbles;** in several fuel management schemes, the pebbles are continuously discharged from the bottom of the reactor through defueling cones.

The discharge burnup value of a pebble is indirectly on-line estimated by measuring its  $\gamma$ -activity.

**Discarded Pebble;** it is a discharged pebble with a discharge burnup value exceeding the burnup limit for recirculation. It is thus sent to a spent fuel tank.

**Recycled (or re-circulated) Pebble;** if a pebble is not discarded then it is re-charged in the cavity from the top. It then performs an ulterior pass through the core.

**Pebble Family;** the pebbles having performed the same number of passes and having the same fresh pebble nuclide composition belong to the same pebble family.

Due to the axial flow, the pebbles are more depleted at the bottom part of the core. Furthermore, the pebbles with the same number of passes can have different depletion histories (depending on the location of the pebble axial flow-lines at each pass in the core). Hence, pebbles of the same family comprised in a core sub-region may have different nuclide compositions.

**Flow Channels;** they subdivide the computational core model in vertical channels having the horizontal top and bottom surfaces perpendicular to a flow-line. All the pebbles flowing in the channel have the same flow velocity. The channel radial

boundaries are determined both by the pebbles flow profile and by common spectral characteristics of the comprised pebbles.

**Spectrum Zone (SZ);** it is an axial subdivision of a channel for computing reasons, it is associated to a multi-pebble geometry and has homogeneous microscopic cross sections.

**Multi-pebble Geometry;** it is associated to a SZ and to the whole set of pebbles, possibly of different families, comprised in the corresponding core sub-region. It is composed by a set of one-dimensional spheres, each belonging to a different pebble type, with a multiplicity equal to the number of pebbles of that type.

**Pebble type;** the nuclide composition assigned to a pebble type is an *average over all the pebbles of the same family* comprised in the sub-region.

**Average Composition Pebble Approximation;** all the presently existing codes treating PBRs neutronics use this approximation. For the fine-group heterogeneous flux calculations, the multi-pebble geometry is replaced with a single pebble having the *volume-weighted average nuclide composition of the different pebble types*.

**Surface-to-Surface Geometrical Probabilities;** in our modeling, *pebble-to-pebble*, *pebble-to-boundary*, *boundary-to-pebble* and *boundary-to-boundary* ( $p_{k'k}^{b,b}$ ) geometrical probabilities are assigned to each SZ. They quantify the probability for a neutron leaving isotropically a surface (of a pebble type or of a contact boundary) to reach the other surface in a straight-line without crossing any other surfaces.

**Clustering;** the core containing several pebble families, a clustering can originate. It is a bunch of pebbles of the same family localized in a spectrum zone. Compared to the stochastic uniform mix the clustered pebbles are closer together and thus they have a greater self pebble-to-pebble probability.

**Reaction Shape factor;** it is the ratio between the average reaction rate per unit volume in the spectrum zone and the average reaction rate density in the core.

**Equilibrium Core;** it is a core state where, due to the continuous recirculation, the nuclide compositions of all the pebble types are statistically time-stable.

In this configuration, all the stochastically averaged neutronic quantities do not vary with time. A pebble bed reactor is mainly operated at the equilibrium state. Only after the start-up phase or following a full core discharge (i.e. for maintenance needs), the equilibrium state is preceded by a running-in period.

# Contents

<b>Introduction .....</b>	<b>1</b>
<b>1 High Temperature Gas-Cooled Reactors .....</b>	<b>3</b>
1.1 Inherent Safety Features of HTGRs .....	8
1.2 Coated Fuel Particles .....	11
1.3 The South-African PBMR-400.....	15
1.3.1 Start-up and Reloading of the Core .....	20
1.4 Pebble Flow and Packing in Pebble Bed Reactors .....	20
<b>2 APOLLO2 Transport Methods.....</b>	<b>23</b>
2.1 The Transport Equation .....	24
2.2 Development of the Scattering Operator .....	26
2.3 Multigroup Discretization .....	27
2.4 Self-Shielding of Multigroup Cross Sections.....	28
2.5 Power Iterations .....	31
2.6 Flux Solvers.....	33
2.6.1 Discrete Differences $S_N$ Method.....	33
2.6.2 Collision Probability Method .....	34
2.6.2.1 Double-Heterogeneity Treatment.....	36
2.7 Cross Sections Homogenization.....	36
2.8 Depletion Calculation .....	37
<b>3 Model for PBRs Neutronic Calculations .....</b>	<b>39</b>
3.1 Survey of Existing Codes Methodologies .....	40
3.1.1 Homogenized Cross Sections Generation .....	42
3.1.2 Full-Core Calculation .....	48
3.2 Description of the Model Developed in APOLLO2.....	50
3.2.1 Iterative Core Calculation Scheme .....	50
3.2.2 Model for "Macro Stochasticity" .....	52
3.2.3 CP Treatment of the Multi-Pebble Geometries .....	54
3.2.4 Surface-to-Surface Geometrical Probabilities Modeling .....	55
3.2.5 Clustering .....	56
3.3 Implementation in APOLLO2 .....	57
3.4 Analysis of Boundary-to-Boundary Geometrical Probabilities.....	58
3.5 Convergence Analysis of Steady-State Reactor .....	62
3.5.1 Cylindrical Core Containing a Single Pebble Type.....	63
3.5.2 Annular Core Containing Six Pebble Types .....	65
3.5.2.1 Analysis of Pebbles Spatial Discretization.....	69
3.5.2.2 Clustering Simulations .....	72

3.6	Conclusions to the Chapter.....	74
<b>4</b>	<b>Verification and Validation .....</b>	<b>79</b>
4.1	Verification of APOLLO2 Double-Heterogeneity Treatment.....	81
4.2	Verification of the Developed Method by Monte Carlo Simulations .....	82
4.2.1	TRIPOLI4 Reactor Model.....	83
4.2.2	APOLLO2 Reactor Model.....	89
4.2.3	Comparison of the Results for Different TRIPOLI4 Cores.....	91
4.2.3.1	Homogeneous Core .....	94
4.2.3.2	Heterogeneous Core with Homogeneous Spectrum Zones .....	95
4.2.3.3	Single Type Individually Positioned Pebbles.....	99
4.2.3.3.1	Analysis of the Entering Currents from Reflectors ...	104
4.2.3.3.2	Evaluation of 281-group P1 XS in T4.....	108
4.2.3.4	Multiple Types Individually Positioned Pebbles.....	111
4.2.3.4.1	Reaction Rates per Pebble Type.....	113
4.2.3.4.2	Analysis of the Computing time.....	115
4.2.3.4.3	Sensitivity Analysis to $pkf$ and $p_{k'k}^{b,b}$ Variations.....	117
4.3	Validation on the HTR-10 First Criticality .....	120
4.3.1	APOLLO2 Reactor Model and Results .....	124
4.4	Conclusions to the Chapter.....	127
<b>5</b>	<b>Search of the Equilibrium Core .....</b>	<b>129</b>
5.1	Survey of Existing Codes Methodologies .....	132
5.2	Developed Method in APOLLO2.....	137
5.2.1	Depletion Algorithm.....	138
5.2.2	Mixing Algorithm.....	142
5.3	HTGRs Fuel Cycles.....	144
5.4	Equilibrium Core Calculations for Different Fuel Cycles.....	146
5.4.1	Low Enriched Uranium Fuel Cycle.....	149
5.4.1.1	Average Composition Pebble Approximation.....	153
5.4.1.2	Limitations of the Implemented Mixing Algorithm.....	158
5.4.2	Plutonium Based Fuel Cycle .....	161
5.4.2.1	Average Composition Pebble Approximation.....	166
5.4.3	Mixed Plutonium – Minor Actinides Based Fuel Cycle .....	171
5.4.3.1	Average Composition Pebble Approximation.....	175
5.5	Conclusions to the Chapter.....	179
<b>6</b>	<b>Conclusions and Perspectives .....</b>	<b>181</b>
	<b>References .....</b>	<b>185</b>
	<b>Acknowledgments .....</b>	<b>191</b>

<b>APPENDIX A: Notation .....</b>	<b>193</b>
<b>APPENDIX B: Model for Macro Stochasticity .....</b>	<b>197</b>
<b>APPENDIX C: CP Treatment of the Multi-Pebble Geometries .....</b>	<b>201</b>
<b>APPENDIX D: Surface-to-Surface Geometrical Probabilities .....</b>	<b>205</b>
<b>APPENDIX E: Clustering .....</b>	<b>209</b>
<b>APPENDIX F: Mixed Type Individual Pebbles Simulation Results .....</b>	<b>213</b>



# Introduction

*"The Generation IV International Forum (GIF) is a cooperative international endeavor organized to carry out the research and development needed to establish the feasibility and performance capabilities of the next generation nuclear energy systems".<sup>1</sup>*

The main objective of GIF is to establish revolutionary designs of nuclear reactors, which should become critical around the '30s. Compared to the Generation III+ evolutionary designs presently at the mature phase and ready for the construction (EPR, AP1000, ABWR, ACR1000, APWR, ESBWR, etc.), to the Generation IV reactors is asked to be safer, sustainable, still economically competitive with the most cost-effective technologies expected to be available in the future and more proliferation resistant and physically secure.

The GIF selected six families of nuclear systems as candidate for Generation IV: the Sodium-Cooled Fast Reactor (SFR), the Gas-Cooled Fast Reactor (GFR), the Lead-Cooled Fast Reactor (LFR), the Molten Salt Reactor (MSR), the Super-Critical Water-Cooled Reactor (SCWR) and the Very-High Temperature Reactor (VHTR).

Particularly, the VHTR is akin to the already existing High-Temperature Gas Cooled Reactors (HTGR), described in Chapter 1, except for the coolant outlet temperature which has to reach 1000 °C. At such high temperatures, the system can be operated with a very high efficiency supplying both electricity and process heat to a broad spectrum of applications, such as for hydrogen production from only heat and water by using thermo-chemical processes or, most unlikely, for the petrochemical industry, helping the high nature-destructive extraction of oil from tar sands.

The heart of the HTGR concept relies on the multiple-coated fuel microparticles, developed at the beginning of last century '60s.<sup>2</sup> They are constituted by a fuel kernel enrobed by successive ceramic layers which act as the first barrier for fission product retention up to a very high threshold temperature (e.g. 1600 °C). The microparticles are embedded in a graphite matrix formed either into a fuel compact inserted in hexagonal graphite blocks for the prismatic block-type core reactors, either into a graphite coated pebble for PBRs.

The unique properties of the coated microparticles allow designing a nuclear reactor which is inherently safe. This coveted objective can be achieved when the decay heat removal from the core relies only on the conduction, convection and radiation heat transfer physical phenomena to keep the temperature of the microparticles under the threshold in all the possible accidental conditions.

It turns out that this mechanism is achievable only with small power density cores, thus leading to the design of relatively low power (few hundreds MW<sub>th</sub>) modular reactors.

On behalf of the Generation IV objectives, the outstanding safety features of modular HTGRs position this family of reactors to the highest place for public acceptance of nuclear energy. Nevertheless, the necessary low power density of the core reduces their economical



competitiveness, which could nevertheless be reached easier if the process heat applications would be coupled to the energy production ones.

From the point of view of sustainability, the very flexible neutronic properties of HTGR allow charging the core with a wide variety of fuel types, ranging from Low Enriched Uranium, pure reactor and weapon grade plutonium, minor actinides and thorium without degrading the safety features.

The core of a PBR is a cavity filled with a large number of pebbles, each of which embedding thousands of coated fuel microparticles. During operation the pebbles slowly flow through the cavity by gravity; they are discharged at the bottom of the reactor and then reinserted on the top of the bed multiple times before being discarded. At equilibrium, each region of the core is composed by a mix of pebbles having different isotopic compositions, which are representative of the burnup cumulated during the multiple passes through the core.

From the neutronic modeling point of view, the pebble bed reactors pose unique challenges associated to the double level of stochasticity of the problem, due to:

- 1) the stochastic dispersion of the microparticles inside each pebble,
- 2) the stochastic distribution of different burnup pebbles inside the core.

Moreover, due to the long neutron migration length in the graphite moderator, the flux inside a pebble is strongly dependent on the surroundings so the « classical » two-step approach for the core calculation (decoupling of assembly and core calculations using multi-parameterized cross sections libraries) is no longer adapted.

In this thesis, an innovative neutronic modeling for PBRs has been developed in the CEA transport code APOLLO2, presented in Chapter 2.

In the developed method, presented in Chapter 3, a fix eigenvalue source problem is solved, with the core  $k_{eff}$  and the entering currents from the neighboring zones, to homogenize the multi-pebble geometries. The neutron exchange between the different pebble types comprised in a spectrum zone and with the zone's boundary surfaces is accounted for by an innovative "macro-stochastic" transport model.

The results of the developed method verification, with reference Monte Carlo simulations, and validation, with the HTR-10 first criticality experiment, are presented in Chapter 4.

In Chapter 5, the potentiality of the developed method have been applied to search the equilibrium core of a simplified PBR model charged with different fuel types and to analyze the limitations of the average composition pebble approximation.

Finally, the conclusions and the perspectives on the realized work are summarized in Chapter 6.

<b>1</b>	<b>High Temperature Gas-Cooled Reactors .....</b>	<b>3</b>
1.1	Inherent Safety Features of HTGRs .....	8
1.2	Coated Fuel Particles .....	11
1.3	The South-African PBMR-400.....	15
1.3.1	Start-up and Reloading of the Core .....	20
1.4	Pebble Flow and Packing in Pebble Bed Reactors .....	20

# 1 High Temperature Gas-Cooled Reactors

Gas cooled nuclear reactors were considered in the United States as material reactors and also for early power reactors.<sup>3</sup> Both graphite-moderated experimental reactors at Brookhaven National Laboratory and at Oak Ridge National Laboratory were air cooled. In 1943, water cooling of the Hanford piles was chosen rather than helium cooling, mainly because of the difficulties anticipated in providing blowers and in preventing helium leakage from large pressure vessels. As early as 1945, Farrington Daniels proposed a helium-cooled, BeO (or graphite) moderated, high-temperature power reactor that was not pursued since it required too much development and because of the priority given to high power density, water-cooled submarine reactors, which led to the development of pressurized water reactors (PWRs). But interest in gas cooling was revived in the United States in the mid-1950s and a number of gas cooled reactor projects were started. Several of these reactors were built, among which the more well-known are the UNGG (Uranium Naturel Graphite Gaz) in France and the Magnox and AGR in the UK. These graphite-moderated gas cooled reactors used CO<sub>2</sub> as coolant and metallic uranium or UO<sub>2</sub> pellets in a metallic cladding as fuel element.

To improve the fuel performance and the limitations on the surface temperature of the metallic cladding, a core with all ceramic material was studied. The fuel, carbide or oxide, is dispersed through the ceramic material on the form of coated microparticles.

Moreover, with the possibility of reaching higher temperatures in the core due to the absence of metallic materials, helium was preferred as coolant since it is inert, has a very small total cross section for neutron interactions and has satisfactory heat transfer and transport properties at modest pressures, from 2 to 50 bar, with acceptable pumping power. These features are common to all high temperature gas-cooled reactors (HTGRs, called also HTRs), with fuel in the form of coated particles (where coatings serves as pressure vessel for fission gas) within a graphite matrix. Graphite was chosen as moderator, fuel containment material and core structure because of:

- its good neutronic properties (very low capture cross-section),
- its good thermal and mechanical properties under irradiation and high-temperature,
- its low cost.

The HTGR was first conceived as a nuclear heat source capable of providing the high temperature necessary to obtain modern steam condition for electricity generation and, at the same time, capable of extending the application of nuclear power to high-temperature industrial processes.

The use of thorium as a fertile material, rather than  $U^{238}$ , has also been proposed since the beginning, in order to match the extended fuel element lifetime inherent to the moderator-diluted design with the excellent neutronic properties of the bred  $U^{233}$  fuel. The basic HTGR concept has a number of variants for its fuel cycle, fuel design, thermodynamic cycle, and industrial applications. The reactor can utilize highly enriched  $U^{235}$  with thorium as the fertile material, or it can operate in a low-enriched uranium cycle.  $U^{235}$ ,  $Pu^{239}$  can be used as fissile materials for the thorium cycle to avoid recycling  $U^{233}$  or using  $U^{233}$  coming from other HTGRs or from fast breeders. The fuel element could be cylindrical, as in the Dragon or Peach Bottom reactors, spherical, like the pebbles in the AVR or THTR reactors, or prismatic, as in the Fort St. Vrain power plant. The detailed design of the fuel elements and coated particles can be readily modified in order to reach specific goals, such as the increase of the outlet temperature or the conversion ratio.

Historically, initial design efforts on HTGR were started at the Atomic Energy Research Establishment in the United Kingdom in 1956.<sup>4</sup> Simultaneously, another independent study was initiated in Germany to design a pebble bed version of the system. The work in the UK resulted in the construction of the DRAGON reactor, a 20 MW<sub>th</sub> test reactor, at Winfith, England. This facility was extensively utilized to demonstrate capabilities of high temperature gas-cooled reactor and coated particle fuel. It has been operated from 1964 to 1976. The helium coolant had an inlet temperature of 350°C and a mixed outlet temperature of 750°C with heat rejection to the atmosphere by air-blast coolers in a tertiary circuit. The reactor was fuelled with a mixture of 93% enriched uranium and thorium carbides in sintered compacts contained in graphite, which acts both as cladding and moderator. The active portion of the core consisted of 37 hexagonal fuel-moderator assemblies surrounded by movable and fixed reflector blocks.

The development of the prismatic block-type HTGRs has been carried on by the construction and the operation of other reactors, such as Peach Bottom (first power operation in 1967) and Fort St. Vrain in the United States, and the HTTR currently

operating in Japan. Fort St. Vrain delivered its first electricity in 1976. Due to many first-of-a-kind engineering equipment used in the plant, there were many unexpected problems that led to a low reactor average availability over its lifetime. Although disappointing as an electricity producer, it provided valuable experience for the development of the HTGR technology. It demonstrated the exceptional fission product retention of the Triple-coated Isotropic (TRISO) particle fuel by having very small release rates compared to other reactor types. It also provided ground for changes in the regulatory structure, so that the regulations for HTGR are different from those of a LWR or BWR. Fort St. Vrain also provided valuable operational data on performance of helical once-through steam generators as well as information on the helium purification system and its component. The high temperature reactor concept with prismatic fuel is currently utilized in the design of the High Temperature Test Reactor (HTTR) in Japan Atomic Energy Research Institute. It is a small  $30\text{MW}_{\text{th}}$  test reactor which uses pin-in-block type fuel with  $\text{UO}_2$  TRISO coated fuel particles.<sup>5</sup> The coated fuel particles are dispersed in the graphite matrix and sintered to form a fuel compact as shown in Figure 1.1. Fuel compacts are contained in a graphite sleeve to form a fuel rod, which is then inserted into vertical holes bored in a hexagonal graphite block.

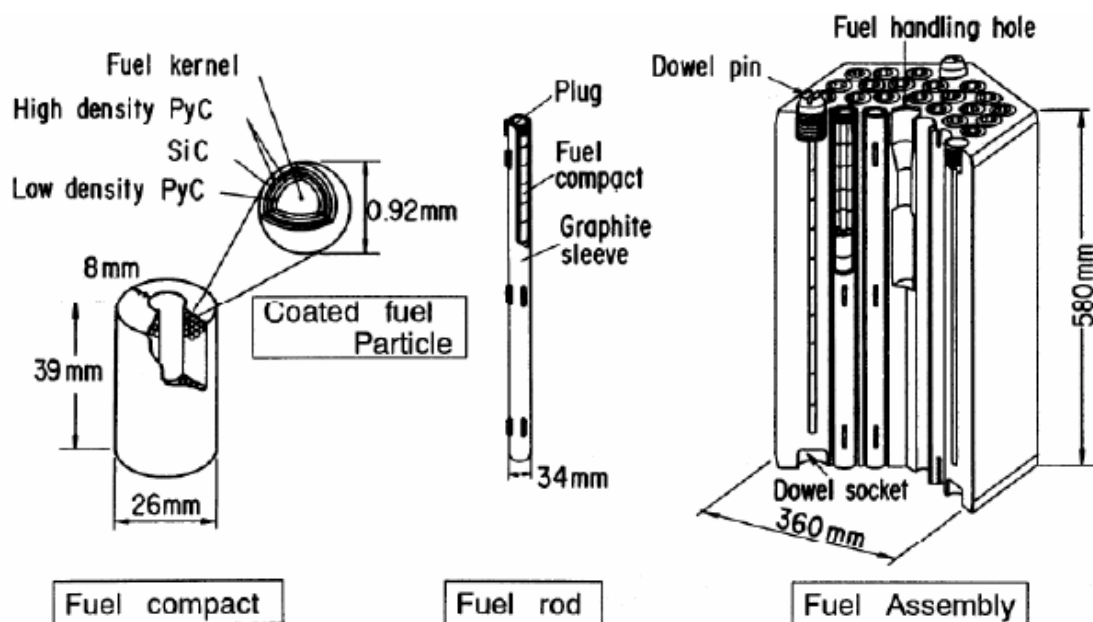
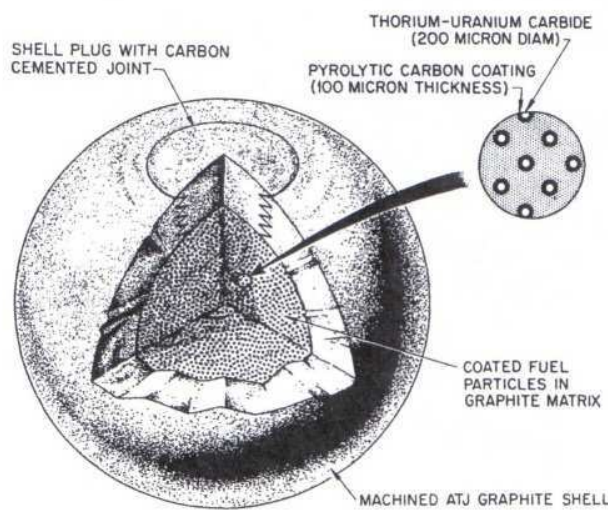


Figure 1.1: HTTR fuel assembly<sup>5</sup>

Parallel to the block-type HTGRs, the pebble bed reactors were also developed, starting with the AVR (Arbeitsgemeinschaft Versuchs Reaktor),<sup>6</sup> built at Jülich in Germany during the 1960's and operated since 1966. This reactor operated exceptionally well for more than 20 years, accumulating 122000 hours of operation, and was decommissioned in the 1980's. It had a steel pressure vessel that housed helium circulators and steam generators, driving a traditional Rankine power generation cycle, above the pebble bed

core. The pebble bed was made up of 100000 pebbles of 6cm diameter, initially loaded with only 30000 spheres, showed in Figure 1.2, that each contained 6.8g of  $U^{235}$  in the form of  $(ThU)C_2$  coated particles filling the inner 4cm internal diameter, with a fuel free layer of 1cm thickness. By 1976, more than 2 millions fuel pebbles had been circulated in the reactor during operation without mechanical difficulties, and six different types of fuel pebbles had been tested. The number of damaged spheres was about 8 per 100000 spheres circulated. One group of fuel pebbles attained a burnup of 160MWd/kg at a maximum temperature of 1250°C without significant damage (some AVR pebbles have even reached a burnup of 200MWd/kg). No serious problems have occurred in the core due to corrosion or mechanical damage of the pebbles.



**Figure 1.2: Pebble of the AVR<sup>3</sup>**

The two most important contributions of the AVR are demonstration of the safety features inherent to the HTGR concept, as well as acting as a fuel development platform. Numerous fuel particle designs were tested, from the early BISO particles up to the current state-of-the-art Low Enriched Uranium (LEU) TRISO particles. Detailed description of the fuel kernels will be given afterwards. Various fuels were tested, such as uranium carbide, thorium/uranium combinations as well as several degrees of uranium enrichment.

The next HTGR was also built in Germany, the 750MW<sub>th</sub> Thorium High Temperature Reactor (THTR) at Schmehausen. The THTR delivered its first electricity in 1985. It was however shut down and dismantled after 1988, due to the political climate changing strongly against nuclear energy after the Chernobyl disaster. Except for the control rods that were designed to be forced into the pebble bed, the THTR operate flawlessly during its short operational lifetime. It was fuelled with a mixture of Highly Enriched Uranium (HEU) and thorium, housed in TRISO particles that were dispersed in 60mm graphite spheres. The core, steam generators and helium coolant circulators were all housed in a pre-stressed concrete vessel. As with AVR, the primary helium loop provided heat for a secondary water based Rankine power cycle.

The most recent pebble bed HTR to be operated is the Chinese HTR-10. It is a 10MW<sub>th</sub> reactor intended for research on the general operation of pebble bed HTRs and went critical for the first time in 2000. It is fuelled with LEU TRISO particles in a 60mm graphite sphere, following the fuel design standardized in Germany. Since the start of its operation, results from the HTR-10 research program have been widely publicized and provides valuable experimental data for computer code validation.

Due to the fact that gas cooled reactor are generally graphite moderated, they have large volumes and therefore relatively low power densities compared to the typical 100MW/m<sup>3</sup> of the PWRs and the 50MW/m<sup>3</sup> of the BWRs. Among HTR, the core power density also varies according to the design. Table 1.I presents some values of interest for the reactors described above.

**Table 1.I : Characteristics of some previous and existing HTGRs**

Parameter	DRAGON	Peach Bottom	Fort. St. Vrain	HTTR	AVR	THTR	HTR-10
Thermal Power [MW]	20	115.5	842	30	46	750	10
Electrical Power [MW]	-	40	330	-	15	300	3
Net efficiency [%]	-	34	39.2	-	33	40	30
Average core power density [MW/m <sup>3</sup> ]	14	8.3	6.3	2.5	2.2	6	2
Primary coolant pressure [bar]	20	20	49.2	40	11	30	30
Core height [m]	2.54	2.3	4.7	2.9	3	4.32	2
Core diameter [m]	1.07	2.8	5.9	2.3	3	2	1.8
Type of fuel element	Rods in clusters	Rods	Blocks	Blocks	Pebbles	Pebbles	Pebbles
Fuel and fertile material	UO <sub>2</sub> , ThO <sub>2</sub>	UO <sub>2</sub> , ThO <sub>2</sub>	UC <sub>2</sub> , ThC <sub>2</sub>	UO <sub>2</sub>	UO <sub>2</sub> , ThO <sub>2</sub>	UO <sub>2</sub> , ThO <sub>2</sub>	UO <sub>2</sub>
ΔT coolant through the core [°C]	350 →750	344 →770	387 →767	395 →850	270 →950	250 →750	250 →700

Up to now, electricity generation with nuclear energy has been provided by steam cycle systems. Increased cycle efficiency and modern steam conditions may be obtained from advanced nuclear systems, breeders, AGRs and of course HTGRs. The high helium outlet temperature in the HTGR has allowed a considerable reduction in the required boiler surface, even for modern steam conditions of 520 to 540°C. But a different type of power cycle deriving real benefits from the high-temperature source, namely, the gas turbine, could be an ideal match for the HTGR core. Instead of exchanging its heat with water and steam in a steam generator, helium leaving the reactor may be expanded in a closed-cycle gas turbine that drives both a helium compressor and a generator for electricity production. Potential advantages of this advanced system are its compactness, since the steam plant is eliminated, its potential high thermal efficiency, with the higher top gas temperature obtained from HTGR cores, and also the fact that its high reject heat temperature greatly facilitates the use of dry cooling towers.

Besides electricity generation, with either a steam cycle or a direct gas turbine cycle, the HTGR could be utilized to broaden the application of nuclear energy to a number of industrial processes. Because of the low temperature of light water reactors, their industrial applications are limited to the production of low quality steam, or the use of rejected heat for district heating, impacting the plant efficiency. High-temperature and high-pressure steam available from HTGRs with proven operating conditions could be utilized in a number of industries: chemical plants, pulp and paper plants, oil refineries, tar sand mining or in situ recovery of tar sands, cogeneration, electricity and steam.

The higher helium temperature obtainable from HTGR cores, for example 950°C in the AVR system, would make achievable the production of synthetic gaseous and liquid fuels from coal, and even direct production of hydrogen by thermo-chemical decomposition of water. These really attractive processes, nevertheless, would still require several R&D efforts before being deployed at industrial scale.

### 1.1 Inherent Safety Features of HTGRs

There are four principles of stability which must be fulfilled in order to avoid core melting or overheating to unacceptable values of temperature in severe accidents. These principles, illustrated in Figure 1.3, are nuclear, thermal, chemical and mechanical stability.<sup>7</sup>

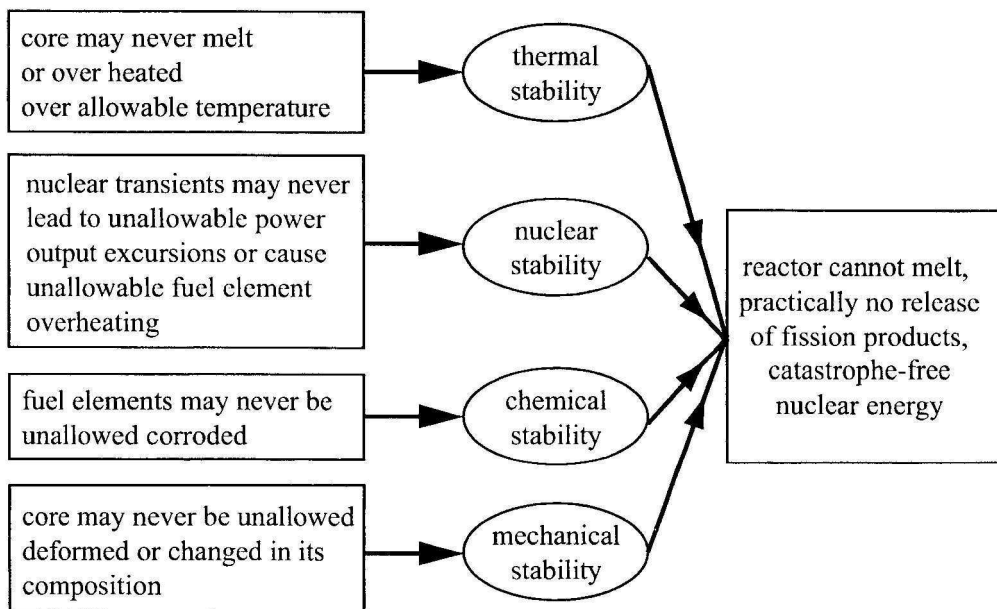


**Figure 1.3: Principles of stability to avoid fission products release from the fuel<sup>7</sup>**

If the fuel temperature stays below allowed values, the fission products and the fissile material are contained inside the fuel elements and reactor integrity is guaranteed without any active measures. A necessary condition to reach safety features is the fuel

capability to retain radioactivity nearly completely till specified temperatures. All the principle enumerated here can be fulfilled by a suitably designed and dimensioned HTR.

In all existing power reactors,<sup>4</sup> safety objectives are achieved by means of custom-engineered, active safety systems. In contrast, a modular HTR can be inherently safe as a result of the design, the material used, the fuel, and the physics involved. This means that, should a worst-case accident scenario occur, no human intervention is required in the short or medium term. Transient accidents are principally driven by the residual power generated by the fuel after the chain reaction is stopped. This power is generated by radioactive decay of fission products (decay heat). If the decay heat is not removed, it will heat up the nuclear fuel until its fission products retention capability is degraded and its radioactive nuclides are released.

In "conventional" reactors, the heat removal is achieved by active cooling systems (such as pumps), which rely on the presence of the heat transfer fluid (i.e. water). Because of the potential for failure in these systems, they are duplicated to provide redundancy. Other systems, such as the containment building, are provided to mitigate the consequences of failure and to act as a further barrier to radioactive release. In a modular HTR, the removal of the decay heat is independent of the reactor coolant conditions. The combination of the very low power density of the core, as discussed above, combined with specific geometrical arrangement of the core (annular core configuration) and resistance to high temperature of fuel in billions of independent particles, underpins the superior safety characteristic of this type of reactor. The helium used as coolant is chemically inert, it cannot combine with other chemicals and it is non-combustible. Even if there is a failure of the active systems that are designed to shut down the nuclear reaction and remove the decay heat from the core, the reactor itself will inherently shut down, due to the strong negative reactivity temperature coefficient. Eventually, it will cool down naturally by heat transport to the environment, which is based on physical phenomena, as the irradiation of heat from the non-isolated metallic surfaces of the vessel to the passive-cooling system (which is a natural circulation water circuit) situated around the reactor or to the concrete wall around it.<sup>8</sup>

The self-acting decay heat removal is a very important characteristic of a modular HTR, which allows it to respect the four principles of stability in each accident scenario, and it is linked to the follow essential features of these types of reactors:

- low power density in the core,
- specific geometrical shape of the core (small cylinder or annular),
- high heat conductivity in the core,
- high heat storage capability of the core,
- high temperature stability of the core materials,
- high heat transfer coefficients through the core structures,
- high ratio of surface to volume for the core,
- permanent outer heat sink outside the reactor pressure vessel.



The difference between the inherent safe principles of decay heat removal and a system with active decay heat removal is that active systems can be carried out with a very high degree of redundancy and diversity, but still there remains a very small probability that they can fail. Inherent processes of transport of decay heat out of the reactor can never fail, because the only involved processes are conduction, radiation and natural convection. If the plant has been designed and constructed following the principle mentioned above, the concept of self-acting decay heat removal works.

One very important result of the development of HTGR, with the use of TRISO particles fuel kernels imbedded in graphite matrix, is that these elements nearly retain the fission products in all accidents till a temperature of 1600°C, keeping their integrity, as shown in Figure 1.4(b). A limitation of release of  $10^{-5}$  of the inventory can be realized, if the temperature is limited to values less than 1600°C. Higher temperatures than 1600°C would cause higher release rates; for instance for the isotope  $Kr^{85}$  the release rate would rise by a factor  $10^3$  above 2200°C, as shown in Figure 1.4(a).

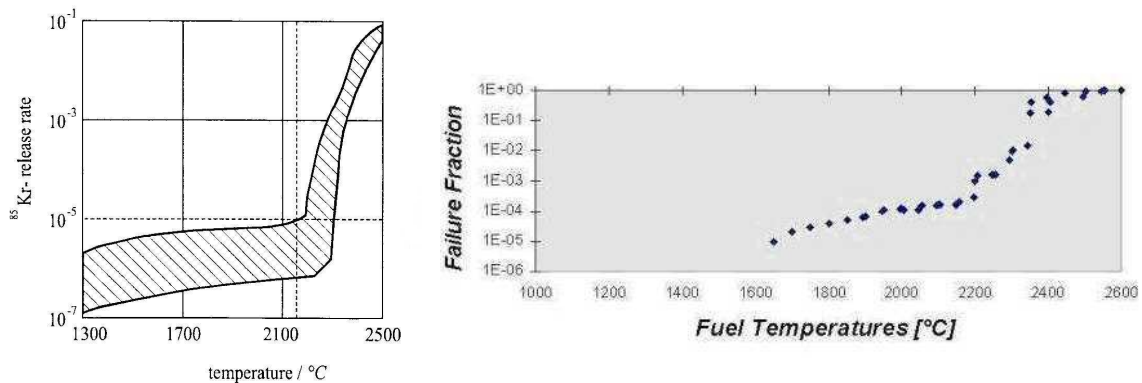


**Figure 1.4: (a) Release Rate of  $Kr^{85}$  Depending on Temperature<sup>7</sup> (b) Failure Fraction of TRISO particles with Temperature<sup>9</sup>**

The main requirement therefore for a modular HTR is that the maximal fuel temperatures will remain at values below 1600°C in all accident conditions or to limit the amount of fuel and the time that this fuel will experience these high temperatures so that the fission products release would stay below the regulatory limit.

Several safety tests have already been performed with operating HTGR. For instance,<sup>3</sup> in the AVR a simulation of the simultaneous failure of the cooling system and the shutdown rods has been performed. The helium flow was interrupted and the control rods were kept un-moved. The reactor became subcritical after about 5s, and after 90s the average moderator temperature reached a maximum only 25°C above its operating value. After about 20 hours, the reactor became critical again. The decay heat was conducted to the reactor vessel by natural convection and from there to the containment.

An accident that could still happen in a reactor of this type is linked to air ingress into the primary circuit, and then into the core, which will lead to the corrosion of the graphite, accelerated by the high temperature. The consequence of this accident would

be corrosion of the graphite and dangerous formation of gases (CO). There are several measures that can be adopted to avoid high corrosion damages of graphite by air ingress:

- inert gas filling of the reactor building (but this would mean to have an hermetic containment);
- limitation of the volume of the air content of the inner concrete structure (citadel) around the primary system by suited design;
- use of a burst protected primary enclosure with small penetrations;
- use of a thin SiC-layer (100 mm thick) on the surface of the fuel element;
- apply intervention measures after leaks in the primary system (inert gas, sand, foam, granulate to cover openings and to reduce amount of air).

The possibility to use a SiC-layer of protection is very promising. Measurements show that at 1200 °C during 50 hours air attack would result in a corrosion rate in the order of 1%. Another possibility would be to cover the pebble surface with a vaporized diamond thin film, which is a very resistant carbon structure with a very good thermal conductivity.<sup>10</sup>

## 1.2 Coated Fuel Particles

All HTGR fuel are based on the coated fuel particle concept, in which a small kernel, consisting of oxides, carbides or oxycarbides of heavy metals (Th<sup>232</sup> or U<sup>238</sup> as fertile material; U<sup>233</sup>, U<sup>235</sup> or Pu<sup>239</sup> as fissile material), is coated with a number of layers, typically two to four, or ceramic materials, i.e. pyrolytic carbon (PyC) or silicon carbide (SiC). The coated particles are the fundamental safety element of the HTR reactors, they act as the first barrier for retention of the fission products and they are the basis for the inherent safety features of the modular HTRs. As the core of a modular HTR contains billions of coated fuel particles, if a small fraction of them fails the total radioactivity release would stay under acceptable values. Moreover the micro-particles resist very well irradiation and so they make possible to reach a very high fuel burnup. Due to their central role in all the key HTGRs concepts, it is important to describe their structure and their actual limitations.

Two main types of coating particles have been developed during the history of the high temperature reactors: the BISO and the TRISO particles. Typically, TRISO particles are used in HTGRs for fissile fuel kernels while BISO coatings may be used for fertile particles (e.g. ThO<sub>2</sub>).

In the BISO particles the heavy metal kernel is first coated with an inner buffer layer of a low density PyC to attenuate the recoils of the fission products and to provide enough void to accommodate fission gasses and the swelling of the fuel kernel. An outer layer of dense isotropic PyC provides high-temperature containment for fission gasses and mechanical strength for the particles. However, the more volatile fission products metals such as cesium and strontium will gradually diffuse through the PyC layers over a long period of time. In operating HTGRs, such as the Peach Bottom reactor, it has

been found that a fraction of the cesium and strontium diffusing out of the fuel rods is usually held in the graphite structure of the fuel element.

In the most recent projects of HTGRs, TRISO coated fuel particles with Low Enriched Uranium  $\text{UO}_2$  kernels are the basis for the fuel elements, whether block-type or spherical ones. The state-of-the-art of these coated particles has been established by the German experience, with the German Proof Test fuel for the HTR-Module which was extensively tested and evaluated in Germany.<sup>8</sup> TRISO particles consist of a spherical uranium dioxide kernel surrounded by four concentric coating layers. The first layer surrounding the kernel is a porous pyrocarbon layer, known as the buffer layer. An inner high-density pyrocarbon layer, a silicon carbide layer, and an outer high density pyrocarbon layer follow this layer. The layers are deposited sequentially by dissociation of gaseous chemical compounds in a continuous process in a fluidized bed. The total diameter of the TRISO particle, shown in Figure 1.5, is  $920\mu\text{m}$ .

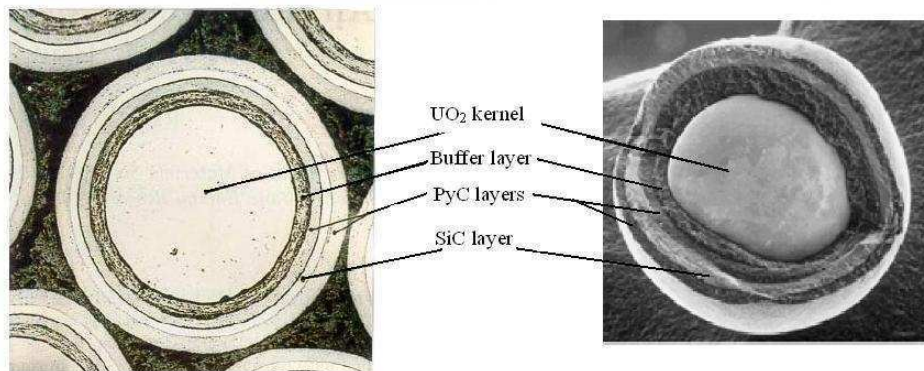


**Figure 1.5: TRISO Fuel Particles Showing Detailed Features<sup>11</sup>**

Let summarize the main features of each component of a TRISO particle:<sup>12</sup>

- **Kernel:** nuclear fission reactions in the kernel produce a mixture of radioactive fission products. Among these there are some gaseous as well as some volatile (mainly metallic) chemical elements which cause stress in the coatings surrounding the kernel, because of the pressure they exert. Therefore wet chemical processes that produce highly spherical kernels are used during the initial stages of kernel manufacture. This ensures that stress concentrations leading to cracks formation in coating layers during irradiation in the reactor are prevented. The spherical fuel kernel consists in stoichiometric uranium dioxide ( $\text{UO}_2$ ).
- **Buffer layer:** the first layer in contact with the kernels is known as buffer layer. The purpose of the buffer layer is to provide void volume for gaseous fission products in order to limit pressure build-up within the coated particle. It also serves to decouple the kernel from the inner pyrocarbon layer to accommodate kernel swelling, thereby reducing the build-up of stress in the outer coating layers during irradiation.

- **Inner pyrocarbon layer:** the inner high-density, isotropic layer of pyrolytic carbon is also referred to as the Inner Low Temperature Isotropic (ILTI) pyrocarbon layer. The ILTI layer forms the first load-bearing barrier against the pressure exerted by fission products within the fuel kernel and the buffer layer, thereby reducing the pressure on the next layer, which consists of silicon carbide (SiC). During irradiation, the ILTI and Outer Low Temperature Isotropic (OLTI) layers shrink at first, expanding again as higher neutron dose levels are reached. The interaction between the ILTI and the OLT high-density pyrocarbon layers and the SiC layer sandwiched between them plays an important part in keeping the SiC layer under compressive stress as long as possible during irradiation. Although an intact ILTI layer forms a practically impenetrable barrier for fission gases and iodine, it becomes increasingly pervious to cesium, silver and strontium at higher temperatures.
  
- **Silicon carbide layer:** when SiC is vapor-deposited at approximately 1500°C under the correct conditions a layer of nearly 100% theoretical density is obtained. At high temperatures, the ILTI and OLT layers partially lose their ability to contain cesium, silver and strontium. The purpose of the SiC layer is to prevent the release of these fission products into the graphite matrix, and hence into the reactor coolant stream. The SiC thus acts as the principal pressure and fission product retention barrier in the coated particle. The coated particle structure results in the SiC layer being kept under compression as long as possible by interaction with the ILTI and the OLT pyrocarbon layers as described above. The production of fuel elements having coated particles with intact SiC layers, and the guarantee that these layers will remain intact under the foreseeable reactor core conditions, form the most fundamental basis for the safe operation of a modular HTGR.
  
- **Outer pyrocarbon layer:** the function of this layer is to protect the SiC layer against damage in the fuel manufacturing processes following on the coating process. It also provides pre-stress on the outside of the SiC layer, due to its interaction with the ILTI layer under fast neutron irradiation under the full lifetime in the reactor core.
  
- **Overcoating:** before the final pressing of the graphite matrix, with spherical or cylindrical shape, in which the coated particles are inserted, a coating of finely ground graphite is applied to the outer surface of each coated particle in a rotating drum. This coating is known as the 'overcoat' and its purpose is to prevent coated particles from coming into contact with each other, thereby damaging their coatings during pressing of the fuel elements.

A large number of in- and out-of-pile tests have shown that performance of coated particles is generally limited by four mechanisms.<sup>13</sup>

- **Kernel migration or “amoeba effect”**: kernel migration is defined as movement of the kernel in the coated particle toward the coating. If the migration is excessive, the kernel will penetrate the TRISO coating leading to failure of the particle. Kernel migration is associated with carbon transport in the particle in the presence of a temperature gradient. This movement of carbon appears in photomicrographs of fuel as a movement of the kernel down the temperature gradient and hence the name kernel migration, as shown in Figure 1.6. This phenomenon is strongly dependent on the temperature gradient in the fuel with secondary dependence on temperature and burnup.

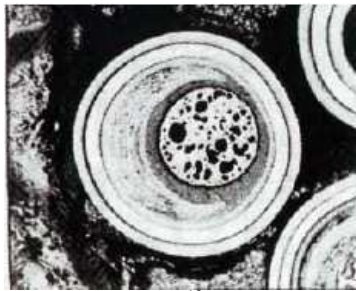


**Figure 1.6: Photomicrograph of Kernel Migration**<sup>13</sup>

In prismatic cores with  $\text{UO}_2$  fuel, where particle loadings and power densities are greater, the potential for kernel migration is greater. In pebble bed cores, the power densities and hence the thermal gradients are much smaller. Moreover, the block fuel stays in the temperature conditions for the length of the cycle, while the pebbles stay in a specific orientation and temperature conditions only for short periods, due to their vertical flow through the core. Therefore, even if the temperature gradient should be the same as for the block fuel, this fact virtually makes the pebble fuel immune to damage of the coatings layers by the amoeba effect.<sup>14</sup>

- **Fission product attack**: past irradiation experiment indicate that fission products can be transported from the kernel to the inner surface of the SiC where they interact and can damage and potentially fail the SiC layer. In  $\text{UO}_2$  kernels, palladium is very important, as are some of the rare earth and noble fission products. In addition, the migration of silver in these particles has been observed. Silver release has been observed on apparently intact fuel, suggesting that silver is transported through intact silicon carbide layers.<sup>15</sup> It can so be released into the reactor coolant system where it will deposit on cold surfaces. For direct cycle gas reactors, this cold deposition may take place in the turbine, which has important maintenance and worker dose implication. The migration of the fission products is thought to be functions of time at a certain temperature and burnup, as well as temperature gradient. Thus, these fission products attack mechanisms are expected to play a more important role in prismatic reactors where fuel particles experience higher temperatures and longer times at a given temperature than particles in a pebble bed reactor. Some advanced fuel particle coating options actually studied are considering the use of ZrC as a substitute for, or in addition to SiC.<sup>16</sup> The major advantage of a ZrC coating compared to SiC is its higher temperature capability, but a stable protective oxide layer is not formed to the same

degree as for SiC in an oxidizing environment of air and water. The retention of certain fission products by ZrC is better than in SiC, with a complete retention of the silver and no attack from palladium, but others have a higher diffusion rate, as Ru<sup>106</sup>.

- **Overpressure:** under irradiation coated particle fuel is subjected to a number of forces that put stress on the TRISO coating. One of the earliest recognized mechanisms is overpressure resulting from gas generation under irradiation. During irradiation, fission gases are released from the kernel into the porous buffer layer. The pressure that is generated exerts tensile forces on the ILTI pyrocarbon and SiC layer. In addition to fission gas, in coated particle fuel with UO<sub>2</sub> kernels, there is excess oxygen released during fission which reacts to the buffer to form CO gas. Both the fission gas and CO production are function primarily of burnup and temperature.

- **Manufacturing defects:** a small number of particles in some coating batches receive incomplete or defecting coatings. Particles with defective coatings are expected to fail progressively with increasing burnup, and therefore the fraction of defective particles is strictly regulated by fuel specifications and quality control procedures.

### 1.3 The South-African PBMR-400

The PBMR-400 is a helium-cooled, graphite moderated high temperature pebble bed reactor, designed for a rated thermal power of 400 MW<sub>th</sub> and a maximum rating of the turbine-generator of 175 MW<sub>e</sub>.<sup>17</sup>

The reactor is based on the design developed as part of the extensive High Temperature Reactor program carried on in Germany, which leads to the construction and the operation of the AVR and the less successful THTR. It is presently the unique pebble bed reactor design under development, together with the Chinese designed HTR-PM,<sup>19</sup> which is not described in this thesis.

The reactor unit of the PBMR-400 consists of the reactor pressure vessel, the core structures, composed by the graphite reflectors and the core barrel supporting them, the control elements, which are located in borings in the outer and central reflectors, and the core which is the pebble bed.

The core consists of an annular region around a central fixed graphite reflector. The central reflector has a radius of 1 m and the core region extends from 1 m to 1.85 m, with an effective core height of 11 m. An external graphite reflector is then present from 1.85 m up to a radius of 2.75 m.

A vertical cross sectional view of the reactor is shown in Figure 1.7, since a horizontal one in Figure 1.8.

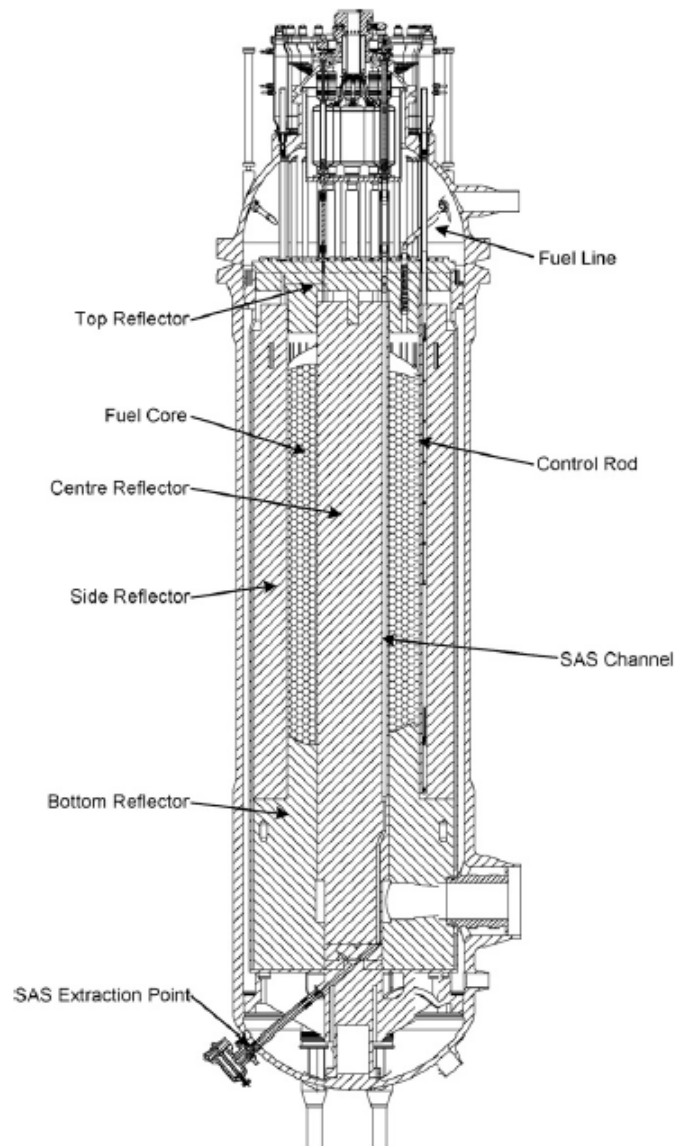


**Figure 1.7: Vertical cross sectional view of the PBMR-400 unit<sup>18</sup>**

The core ceramic assembly consists of the reflector, the reflector restraints and the expansion compensator. The reflector consists of graphite bricks arranged to accommodate thermal and radial induced deformations throughout the life of the reactor, while maintaining its functions. Graphite keys and dowels connect the bricks together to prevent excessive movement during abnormal events, e.g. seismic, while allowing relative movement due to thermal expansion. This also reduces leak flows.

The annular core contains the pebble bed. Pebbles are continuously inserted at the top of the core, from three fuel loading positions, and discharged at the bottom, from three defueling tubes. They are then passed through a  $\gamma$ -detector which measures the  $Cs^{137}$  concentration in the fuel, thus deriving the pebble burnup, as it is explained in Chapter 5. If the burnup does not exceed a target limit value for recirculation the pebble is re-

circulated, until the target burnup is reached, otherwise it is discarded to a spent fuel tank. On average,<sup>20</sup> 2936 pebbles are re-circulated per day, with 489 fresh pebbles loaded daily, passing through the core, which contains roughly 452000 pebbles, six times before being discharged to the spent fuel tanks. The residence time in the core is about 923 days with an average discharge burnup of 90800 MWd/t. That means that at equilibrium, the core will be composed of a nearly homogeneous mix of pebbles with different nuclide compositions, corresponding to the different burnup reached in each pass.

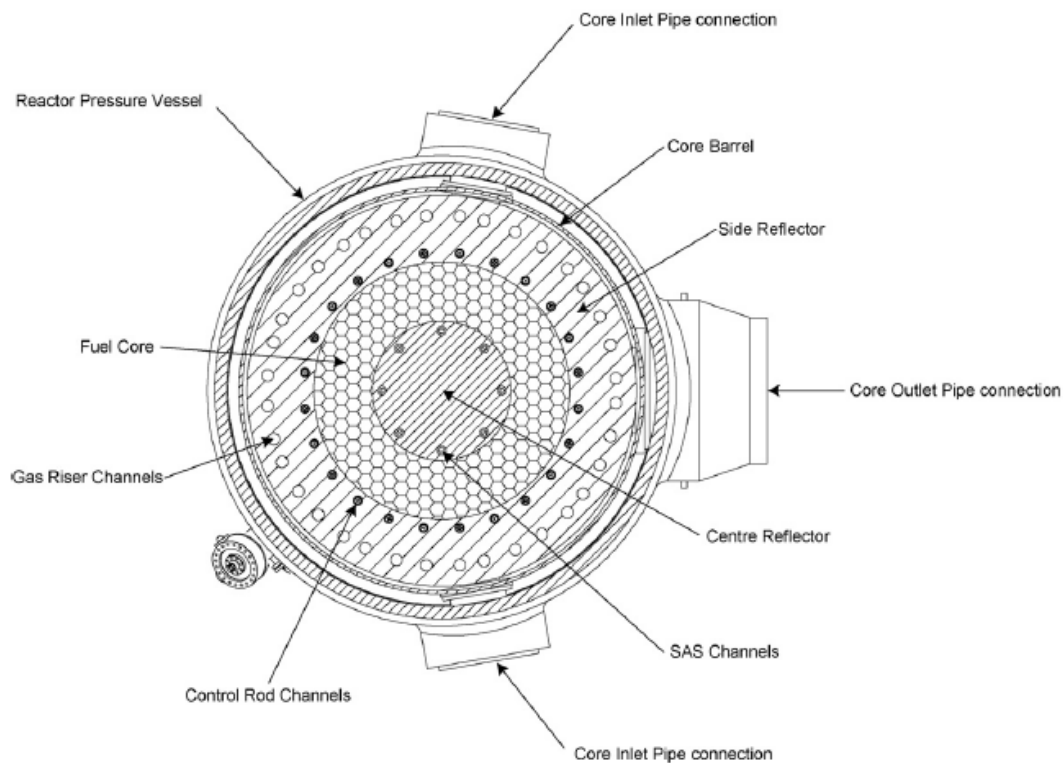


**Figure 1.8: Horizontal cross sectional view of the PBMR-400 unit<sup>18</sup>**

The pebbles used in the PBMR-400 are based on the German reference fuel design. The pebbles have a diameter of 6 cm, with an external 0.5 cm thick layer of pure graphite. Each pebble contains about 15000 kernels of low enriched uranium (9.6% wt) TRISO fuel particles, as the one described in Section 1.2, in a graphite matrix. The main features of the pebble are shown in Figure 1.9.



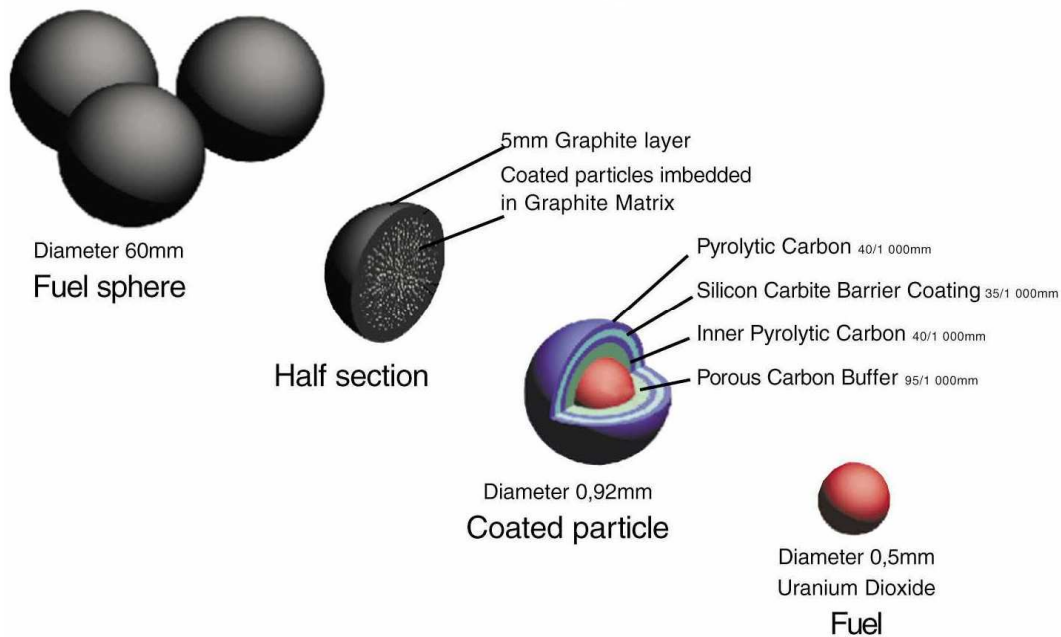


**Figure 1.9: The PBMR-400 pebble<sup>20</sup>**

The main properties of the pebbles and of the coating particles used in the PBMR-400 are summarized in Table 1.II.

**Table 1.II: PBMR-400 pebbles parameters**

	Units	Values
Pebble radius	cm	3.0
Thickness of fuel free zone	cm	0.5
Density of graphite in matrix/fuel free zone	g/cm <sup>3</sup>	1.74
<sup>235</sup> U enrichment	wt%	9.6
Kernel diameter	μm	500
Kernel density	g/cm <sup>3</sup>	10.4
Coating materials		PyC/PyC/SiC/PyC
Layer thickness	μm	95/40/35/40
Layer densities	g/cm <sup>3</sup>	1.05/1.90/3.18/1.90
Sublimation temperature of SiC	°C	> 1800
UO <sub>2</sub> melting point	°C	~ 2880
Maximum design allowable power production per pebble	kW	4.5

Two reactivity control systems are provided to compensate for excess reactivity,<sup>21</sup> to ensure an adequate shutdown margin, and to control changes in reactivity that occur during operation.

The first system, called the RCS, consists of 24 partial length active control elements divided into two groups of 12 (with every other control rod belonging to a group), one upper and one lower. The RCS are positioned in borings in the side reflector, 13 cm in diameter (11 cm with a sleeve in place) and with the boring centre points positioned at a distance of 197 cm from the core centre. The RCS control rods consist of a 0.8 cm thick B<sub>4</sub>C annulus with an outer diameter of 10.0 cm and a density of 2.2 g/cm<sup>3</sup>, and with an inner and outer incoloy structure.

The second system is the Reserve Shutdown System (RSS) consisting of eight reserve shutdown units making use of Small Absorber Spheres (SAS). The RSS are positioned in borings in the central reflector that are, as the case of the RCS, 13 cm in diameter (11 cm with a sleeve in place) and with the boring centre points positioned at a distance of 86 cm from the core centre. The RSS borings can be filled with SAS with a diameter of 1 cm, containing 10% B<sub>4</sub>C, and with an overall density of 1.7 g/cm<sup>3</sup>. The RSS must be capable of shutting the core down and keeping it subcritical at the cold shutdown average temperature of 100 °C. The RSS is designed to be able to keep the reactor subcritical under all normal operating conditions and for Anticipated Operational Occurrences and Design Based Accidents that require no rapid changes in reactivity, and to keep it subcritical in the long term.

The two systems are totally different in design with no common mode failure. This contributes to the defense in depth of the design. Moreover, the on-line fuelling allows a small excess reactivity in the core.

The PBMR-400 design provides two diverse methods to control the core reactivity.<sup>22</sup> Firstly, the reactor has a strong negative temperature coefficient of reactivity over the entire operating range. Therefore, by opening the by-pass valve, the helium inlet temperature increases, with a slight rise in the mean core temperature, and causes the reactor to become subcritical. Secondly, the core reactivity is controlled by insertion and extraction of the RCS rods.

During normal operation the RCS rods are partially inserted, to a depth of 2 m from the bottom of the top reflector (taking into account a void gap of 78.5 cm between the pebble bed and the bottom of the top reflector) which provides for a small excessive reactivity that is just enough to overcome the xenon build-up for the power load follow requirement. The reactivity requirement for the core to perform 100-40-100% power load follow was calculated to be 1.4%  $\Delta k/k$  (or 1400 pcm), thereby bounding the reactivity addition even in the case of a full control rods withdrawal. If the load follow requirement does not need to be fulfilled, the RCS can further withdrawn, leading to a lower excess reactivity and thus also a larger shutdown margin for the RCS.

Detail analyses give strong indications that the annular PBMR-400 core will present xenon stability.<sup>23</sup> The axial and the radial xenon and power oscillations are strongly damped for several load follow scenarios as well as for possible operator induced initiating conditions. The damped oscillations only cause relatively small temporary

changes in the fuel temperatures and power densities without exceeding any design limits.

### **1.3.1 Start-up and Reloading of the Core**

Before the initial approach to criticality, the core cavity is filled with graphite pebbles.<sup>20</sup> The first loading of start-up core and any other reloading of the core will be done on top of this graphite bed. The start-up fuel will have an enrichment lower than the equilibrium fuel (present best estimate is 5.7%). In addition, the start-up core will contain a mixture of fuel and graphite pebbles in a ratio of 1:1. While loading this fuel and graphite mixture, graphite pebbles will be unloaded from the core and routed to the graphite storage tank. The present estimate is that at cold criticality the active core volume will be filled to about 80% of its active volume. The core cavity should be full at hot conditions, with some fission products in the core. As more fission products are generated, the fuel and graphite mixture will be enriched by a net removal of graphite pebbles. This will be continued until all the graphite pebbles have been removed. Afterwards, equilibrium fuel will be loaded when a start-up pebble is removed.

Each of the de-fueling chutes leads into a Core Unloading device (CUD) where the pebbles are singularized and the pebbles that are broken, damaged or have a too small diameter are removed from the lines. Following discharge from the CUD, the pebble passes through a gross gamma activity measurement machine which identifies whether it is graphite or a fuel pebble. This measurement is made only during the start-up phase. After the pebble type is identified, the fuel pebbles are transported pneumatically to the top of the reactor, where each of them is assayed for burnup. After the burnup is determined, through the Cs<sup>137</sup>  $\gamma$ -measure, the fuel pebble is either routed to the reactor or discarded to the spent fuel tanks. When necessary, as during reflectors maintenance operations, it is also possible to unload all the fuel to a used fuel tank capable of containing an entire core inventory of bunt pebbles.

### **1.4 Pebble Flow and Packing in Pebble Bed Reactors**

In a pebble bed reactor the pebbles are continuously extracted from the bottom of the core and loaded on the top. This determines a flow of pebbles through the core cavity. A lot of studies have been done, both by experiments and by simulations, in order to determine the flow characteristics and the average packing properties in the bed of pebbles. A complete overview of the different simulation techniques can be found in Ref. 24, since the results obtained applying a modern simulation technique in Ref. 25. In this last, the pebble flow in a typical pebble bed reactor has been simulated by a powerful Discrete Element Method (DEM) technique,<sup>26</sup> which models accurately each pebble as a sphere undergoing realistic frictional interactions with other pebbles.

The main points to be retained on the flow and packing characteristics are depicted here.

- The pebbles flow through the core is very slow, in the order of some cm per day.
- The flow profile is a nearly uniform plug flow in the larger height of the reactor, corresponding to the upper cylindrical region, and smoothly transits to a converging flow in the lower funnel region, where the defueling cones are situated. This means that the pebbles flowing close to the reflector walls have a higher residence time in the reactor. This aspect has to be considered properly as it has important implications for the non-uniformity of the fuel pebbles burnup.
- In the upper cylindrical region, the pebble flow is practically vertical with a very low degree of mixing. Although there is some horizontal diffusion in the funnel region, pebbles depart from the streamlines of the mean flow by less than one pebble diameter prior to exiting the core.
- In the plug-flow region, the bulk of the core has a packing fraction near the jamming point (~63%), but there is an oscillating transition towards lower fractions (55% - 60%) against the reflector walls. This phenomenon is illustrated in Figure 3.3 of Chapter 3.
- The wall friction affects the mean flow deep into the bulk. Reduces the wall friction increases radial ordering near the walls and makes the flow profile more uniform.
- Critical values for the defueling cone angle and for the discharge tubes diameter exist. These values have to be properly designed in order to avoid the possibility of pebbles bridge formation which could obstruct the passage.



<b>2</b>	<b>APOLLO2 Transport Methods</b> .....	<b>23</b>
2.1	The Transport Equation .....	24
2.2	Development of the Scattering Operator .....	26
2.3	Multigroup Discretization .....	27
2.4	Self-Shielding of Multigroup Cross Sections.....	28
2.5	Power Iterations.....	31
2.6	Flux Solvers.....	33
2.6.1	Discrete Differences $S_N$ Method.....	33
2.6.2	Collision Probability Method .....	34
2.6.2.1	Double-Heterogeneity Treatment.....	36
2.7	Cross Sections Homogenization.....	36
2.8	Depletion Calculation.....	37

## 2 APOLLO2 Transport Methods

APOLLO2<sup>27,28,29</sup> is a spectral transport modular code, developed at the Commissariat à l'Energie Atomique et aux Energies Alternatives (CEA), with financial support from AREVA and EDF. APOLLO2 solves the neutron transport equation over a discretized 1D or 2D geometrical domain. A 3D capability is envisaged for its successor APOLLO3.<sup>30</sup>

Besides solving the transport equation by obtaining the multigroup fluxes, APOLLO2 performs several other actions needed in reactor physics, such as microscopic cross sections self-shielding for resonant nuclides, homogenization over energy and spatial meshes, depletion calculations and perturbation calculations, among others.

In the following, we will introduce the basic quantities and the equation of neutron transport, describing some methods implemented in APOLLO2 which have been used in this thesis.

Further mathematical details are given in several reactor physics books. In this short survey we refer to Ref. 31 and Ref. 32.

## 2.1 The Transport Equation

The main purpose of a neutronic calculation of a nuclear reactor is to determine the neutron population density  $n(\vec{r}, \vec{v}, t)$  (neutrons/cm<sup>3</sup>) at each (discretized) point  $(\vec{r}, \vec{v})$  in phase space at time  $t$ .

The neutron transport equation describes the statistical interaction of a neutron population with a background medium. This equation is written in terms of the angular flux  $\psi(\vec{r}, \vec{v}, t)$ , which is the product of the neutron speed  $v$  times the averaged neutron density  $n(\vec{r}, \vec{v}, t)$ . The neutron transport equation express a local neutron balance in an elementary volume  $d\vec{r}$  around  $\vec{r}$  and  $d\vec{v}$  around  $\vec{v}$ :

$$\left( \frac{1}{v} \partial_t + \vec{\Omega} \cdot \vec{\nabla} + \Sigma_t \right) \psi = H\psi + P\psi + S_0. \quad (2.1)$$

The equation is completed by the initial flux at time equal zero and the boundary values of the flux.

In practice, the velocity  $\vec{v}$  is replaced by the direction  $\vec{\Omega}$  and by the speed  $v$  as  $\vec{v} = v\vec{\Omega}$ .

Moreover, the speed is generally expressed in terms of the neutron energy  $E$ , since  $E = (1/2)mv^2$ .

The different contributions to the neutron balance of Eq. (2.1) are listed her.

- The term  $\frac{1}{v} \partial_t \psi$  is the time variation of the flux, which is null for a steady-state problem.
- The streaming term  $\vec{\Omega} \cdot \vec{\nabla} \psi$  accounts for the surface leakage out of the volume  $d\vec{r}$ .
- The removal term  $\Sigma_t \psi$  expresses all the reactions of neutrons with matter. The total macroscopic cross section  $\Sigma_t(\vec{r}, E, t)$  is the total probability per unit track length for a neutron to interact with matter. It is computed as  $\Sigma_t(\vec{r}, E, t) = \sum_i N_i(\vec{r}, t) \sigma_{t,i}(E)$ , where the sum in  $i$  is for all the isotopes contained in the matter,  $N_i(\vec{r}, t)$  is the nuclide density and  $\sigma_{t,i}(E)$  is the total microscopic cross section of isotope  $i$ . This last is expressed as  $\sigma_{t,i}(E) = \sum_x \sigma_{x,i}(E)$ , where  $x$  are all the possible reactions that neutrons can have with the isotope. The microscopic cross section represents an equivalent area of interaction and it is generally expressed in barns (b), with  $1 \text{ b} = 10^{-24} \text{ cm}^2$ .

- The transfer term accounts for all the neutrons locally appearing from reactions other than fission and it is expressed as

$$H\psi(\vec{r}, E, \vec{\Omega}, t) = \int d\vec{\Omega}' \int dE' \Sigma_s(\vec{r}, E' \rightarrow E, \vec{\Omega}' \cdot \vec{\Omega}, t) \psi(\vec{r}, E', \vec{\Omega}', t), \quad (2.2)$$

where  $\Sigma_s(\vec{r}, E' \rightarrow E, \vec{\Omega}' \cdot \vec{\Omega}, t)$  is the density of probability per unit track length for a neutron travelling with an energy  $E'$  in the direction  $\vec{\Omega}'$  to be transferred to an energy  $E$  in the direction  $\vec{\Omega}$ .

- The production term  $P\psi$  accounts for the neutrons produced by fissions.
- The term  $S_0$  accounts for the external sources.

One has to notice that the streaming term couples locally the flux in space, while the transfer and production terms couple the energies and the directions.

In the above expressions, we wrote the different terms for an isotropic medium. This is generally the case for the materials used in nuclear reactors, in the sense that their properties are independent of the direction of the incident neutron. Thus, the cross sections are independent from the direction  $\vec{\Omega}$  and depend only on the incident neutron energy. Moreover, the transfer cross section depends angularly only on the cosine of the deviation angle,  $\vec{\Omega}' \cdot \vec{\Omega}$ .

With the isotropic medium assumption, the reaction rate, for reaction of type  $x$ , in a volume  $V$  is

$$\tau_x(V, t) = \sum_i \int_V d\vec{r} \int (\Sigma_{x,i} \phi)(\vec{r}, E, t) dE, \quad (2.3)$$

where

$$\phi(\vec{r}, E, t) = \int_{4\pi} d\vec{\Omega} \psi(\vec{r}, E, \vec{\Omega}, t) \quad (2.4)$$

is the scalar flux. In the neutronic analysis of a nuclear reactor, the reaction rates in the different regions of the core are the main quantities of interest. Hence, the scalar flux is the most important quantity to compute.

The angular flux is used to compute the neutron current as



$$\vec{J}(\vec{r}, E, t) = \int_{4\pi} \vec{\Omega} \psi(\vec{r}, E, \vec{\Omega}, t) d\vec{\Omega}. \quad (2.5)$$

If the neutron crosses the surface  $dS$ , with  $\vec{N}$  being the normal to the surface, we can define the exiting current  $J^+$  and the entering current  $J^-$  by integrating the angular flux over outgoing and incoming directions, respectively. We thus write

$$J^\pm(\vec{r}, E, t) = \int_{\pm\vec{\Omega} \cdot \vec{N} > 0} |\vec{\Omega} \cdot \vec{N}| d\vec{\Omega} \psi(\vec{r}, E, \vec{\Omega}, t), \quad (2.6)$$

so that the net current is

$$\vec{J}(\vec{r}, E, t) \cdot \vec{N} = J^+(\vec{r}, E, t) - J^-(\vec{r}, E, t). \quad (2.7)$$

To describe the "normal" operation of a nuclear reactor, one must consider a steady-state problem with no sources. Because the flux of such a problem vanishes except if 1 is an eigenvalue, one is brought to consider a general critical eigenvalue problem:

$$\left(\vec{\Omega} \cdot \vec{\nabla} + \Sigma_t\right) \psi = H\psi + \frac{P}{\lambda} \psi, \quad (2.8)$$

completed with the boundary conditions for the flux. Here  $\lambda$  is a complex number. More than one value of  $\lambda$  can give a non-null solution of the equation, but it turns out that the  $\lambda$  with the largest absolute value is real and positive and gives a positive solution. This  $\lambda$  is called the multiplication factor of the system and it is noted  $k_{eff}$ .

## 2.2 Development of the Scattering Operator

Thanks to the rotational invariance of the scattering operator in an isotropic medium, the  $H\psi$  term can be developed in terms of real spherical harmonics  $A_{m,l}(\vec{\Omega})$ .<sup>33</sup> The spherical harmonics are the eigenfunctions of the laplacian operator, which is also invariant by rotations.

Firstly, the differential scattering cross section is developed in Legendre polynomial up to the order  $L$ :

$$\Sigma_s(\vec{r}, E' \rightarrow E, \vec{\Omega}' \cdot \vec{\Omega}) = \frac{1}{4\pi} \sum_{l=0}^L (2l+1) \Sigma_{s,l}(\vec{r}, E' \rightarrow E) P_l(\vec{\Omega}' \cdot \vec{\Omega}), \quad (2.9)$$

where

$$\Sigma_{s,l}(\vec{r}, E' \rightarrow E) = 2\pi \int_{-1}^1 \Sigma_s(\vec{r}, E' \rightarrow E, \vec{\Omega}' \cdot \vec{\Omega}) P_l(\vec{\Omega}' \cdot \vec{\Omega}) d(\vec{\Omega}' \cdot \vec{\Omega}) \quad (2.10)$$

is the scattering kernel of order  $L$ .

Then, since  $P_l(\vec{\Omega} \cdot \vec{\Omega}') = \sum_{m=-l}^l A_{m,l}(\vec{\Omega}) A_{m,l}(\vec{\Omega}')$ , we obtain

$$H\psi(\vec{r}, E, \vec{\Omega}) = \sum_{l=0}^L \sum_{m=-l}^l A_{m,l}(\vec{\Omega}) \int dE' \Sigma_{s,l}(\vec{r}, E' \rightarrow E) \phi_{m,l}(\vec{r}, E'), \quad (2.11)$$

where

$$\phi_{m,l}(\vec{r}, E') = \frac{2l+1}{4\pi} \int d\vec{\Omega}' A_{m,l}(\vec{\Omega}') \psi(\vec{r}, E, \vec{\Omega}') \quad (2.12)$$

are called the angular flux moments.

### 2.3 Multigroup Discretization

The numerical solution of the transport equation is done by introducing approximations in energy, direction and space. The universally used approximation in energy is the multigroup discretization. This approach consists in dividing the energy domain in a set of  $g$  energy groups inside which the neutrons are assumed to behave as mono-energetic particles and to write a transport equation for the multigroup flux  $\psi^g(\vec{r}, \vec{\Omega}) = \int dE \psi(\vec{r}, E, \vec{\Omega})$ .

The multigroup form of Eq. (2.8) has to preserve the reaction rates of the continuous in energy equation. For instance, the reaction rate  $(\Sigma\psi)(\vec{r}, E)$  requires adopting the definition

$$\sigma^g = \frac{\int_{E \in g} \sigma(E) \psi(\vec{r}, E, \vec{\Omega}) dE}{\int_{E \in g} \psi(\vec{r}, E, \vec{\Omega}) dE} \rightarrow \sigma^g(\vec{r}, \vec{\Omega}). \quad (2.13)$$

However, this expression results in a cross section that depends on  $\vec{\Omega}$ , which would result in a complicated multigroup equation for a non-isotropic medium. In order to avoid this dependence, one has to define groups fine enough so that  $\sigma(E)$  does not

change much within the group. In which case one can replace  $\psi(\vec{r}, E, \vec{\Omega})$  with a weighting flux  $\phi_W(E)$  representative of the reactor. The result is

$$\sigma^g = \frac{\int_{E \in g} \sigma(E) \phi_W(E)}{\int_{E \in g} \phi_W(E)}. \quad (2.14)$$

The spectrum  $\phi_W(E)$  can be adapted to the type of nuclear reactor, but, for thermal reactors, it is generally adopted with a  $\chi(E)$  value for fast groups, a  $1/E$  trend for epithermal groups and a Maxwellian shape for thermal groups.

The approach adopted in Eq. (2.14) is good for non-resonant isotopes, for which the cross sections vary slowly with energy, but it is not adapted for resonant ones, since this will require to use a huge number of groups (tens of thousands). Thus, resonant data require a special treatment in which a flux accounting for spatial heterogeneity and very fast variations in energy is computed. This formalism is called self-shielding. Considering Eq. (2.13), it is clear that self-shielded multigroup cross sections are space dependent, contrarily to the cross sections obtained via Eq. (2.14) for non-resonant isotopes.

In APOLLO2, the point-wise cross section data may come from any evaluated data file in the ENDF format such as JEF, JEFF, ENDF/B and JENDL. The three standard multigroup libraries have 99, 172 and 281 groups respectively. The first corresponds to the energy mesh of the predecessor APOLLO code,<sup>34</sup> the second is the standard XMAS structure<sup>35</sup> and the third is the recently optimized SHEM energy mesh.<sup>36</sup>

## 2.4 Self-Shielding of Multigroup Cross Sections

A brief description of the self-shielding technique used in APOLLO2 is given here.<sup>37,38</sup>

As it has been explained in the previous section, the self-shielded cross sections should preserve the reaction rates, but since the flux is unknown these reaction rates are not known a priori for a given geometry.

The APOLLO2 method for computing self-shielded cross sections is based on a simplified problem where only the slowing-down energy range comprising the resonances is considered. The spatial detail can be the entire domain to be calculated, but most often only a restrained domain with reflected boundary conditions is used. Furthermore, a further approximation is introduced to simplify the equation, leading to the Livolant – Jeanpierre (L-J) equation for the fine-structure flux  $\varphi$ .<sup>39</sup> This approximation can be written both for a heterogeneous geometry and for an infinite

homogeneous medium. For simplicity, we consider an infinite medium and write the slowing-down equation as

$$\left(N_0\sigma_0 + N_1\sigma_1\right)\phi = R_0(\phi) + R_1(\phi), \quad (2.15)$$

where  $R_0$  is the slowing-down operator for the single resonant heavy isotope,  $R_1$  the slowing-down operator the non-resonant isotopes,  $N$  the atomic densities and  $\sigma$  the total cross sections.

Following L-J we write  $R_1(\phi) = \Sigma_{s,1}\chi$ , where  $\Sigma_{s,1}$  is the macroscopic scattering cross section for the non-resonant (moderator) isotopes. Note that the non-resonant operator,  $R_1$  has a large energy range and therefore acts as a smoothing operator on the actual flux  $\phi$ . As a result, the macroscopic flux  $\chi$  varies slowly with energy within a group. We can then define the fine-structure flux  $\varphi$  by writing

$$\phi = \varphi \chi, \quad (2.16)$$

a formula that express the flux as the product of a function  $\varphi$  that changes fast over energy (driven by the resonances) times a function  $\chi$  that does not change much with the energy within a group.

Eq. (2.16) led L-J to introduce the approximation

$$R_0\phi = R_0(\varphi \chi) = \chi R_0(\varphi), \quad (2.17)$$

which is physically plausible because  $\chi$  is practically constant within the range of  $R_0$ , which is an operator with a small energy range (heavy resonant isotope).

Thus, the L-J form for Eq. (2.15) reads

$$\left(\sigma_0 + \sigma_b\right)\varphi = r_0(\varphi) + \gamma\sigma_b, \quad (2.18)$$

where  $\sigma_b = (N_1\sigma_1)/N_0$  is the background microscopic cross section,  $\gamma = \sigma_{s,1}/\sigma_1 \approx 1$  the gamma factor and  $r_0 = R_0/N_0$ .

Eq. (2.18) can be solved with a very fine multigroup approximation with NJOY<sup>41</sup> and the result can be used to compute the APOLLO2 broad-group reference, infinite medium reaction rates. Since (2.18) is a linear equation with source  $\gamma\sigma_b$  the reaction rates are tabulated in terms of the background cross section  $\sigma_b$  and the temperature:  $\tau_\infty(\sigma_b, T)$ .

A schematics of a self-shielding calculation is shown in Figure 2.1, where also an iteration over the isotopes is shown since APOLLO2 can treat resonant mixtures, by taking into account the resonance overlapping between the various resonant components.<sup>39</sup>

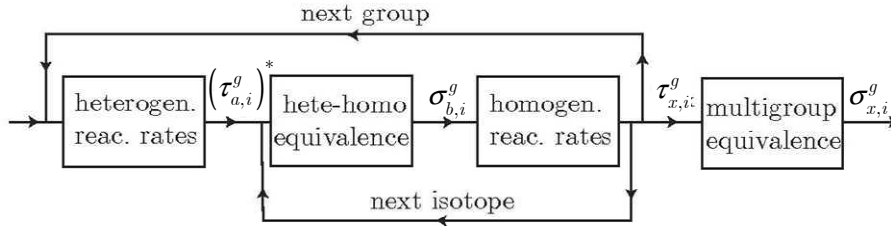


Figure 2.1: Schematics of a self-shielding calculation in APOLLO2

The APOLLO2 method for computing self-shielded cross sections is based on a scheme comprising four steps:

- 1) The heterogeneous problem is computed solving the heterogeneous form of Eq. (2.18) with the collision probability method (described in section 2.6.2) over the detailed reflected geometry, computing a single average flux for each self-shielding region. Notice that in this way space-dependent interference effects are directly incorporated via the use of a full collision probability description with no need for geometrically dependent Dancoff factors. The resulting  $P_{ij}$  equations are coupled both in space via the collision probabilities and in energy via the heavy slowing-down operator. The first coupling is treated exactly, but for the second one an approximate slowing-down model for the resonant isotope must be adopted in order to reduce the computing time. The models available in APOLLO2 are the Narrow Resonance (NR), the Wide Resonance (WR), the Statistical (ST) and the TR one. In this work we have used the TR model, a generalization of the ST one which can treat all resonance shapes. The TR model leads to a quasi-analytical expression for the flux  $\varphi$  and the group reaction rates  $(\tau_{a,i}^g)_{het}^*$  are computed with the helps of quadrature formulas based on probability tables tabulated and kept in the external library.<sup>42</sup>
- 2) A homogeneous problem with the TR slowing down approximation is now considered, and an equivalent background cross section  $\sigma_{b,i}^g$  is determined by requesting that the homogeneous problem give the same absorption reaction rates as the heterogeneous problem  $(\tau_{a,i}^g)_{\infty}^* (\sigma_{b,i}^g, T) = (\tau_{a,i}^g)_{het}^*$ .

- 3) With the  $\sigma_{b,i}^g$  determined at the previous step, the "exact" reaction rates  $\tau_{x,i}^g$  are obtained by interpolating from the tables  $(\tau_{x,i})_{\infty}(\sigma_b, T)$ . This step is meant to correct the approximation introduced by the TR model. The reactions considered are absorption, production and scattering.
- 4) Since the total reaction rates are now known for all resonant groups for the heterogeneous problem, the final multigroup self-shielded cross sections can be determined by iteratively solving a multigroup problem which reproduces these reaction rates. This is a typical equivalence non linear problem.<sup>43</sup>

## 2.5 Power Iterations

The different numerical methods applied to solve the differential transport equation in (2.8) are based on an iterative scheme to converge the fission source distribution over the domain and to compute the problem eigenvalue  $\lambda$ .

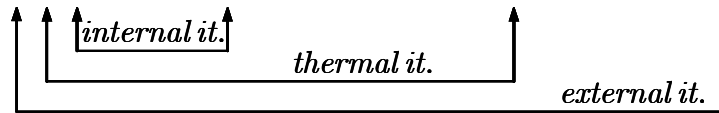
Thanks to the multigroup approximation the neutron balance is solved independently over the energy groups, starting from the highest energy group until the last thermal group. Notice that groups are numbered in the decreasing energy order.

Let us take Eq. (2.8) expressing the sum of the leakage and the removal operators as  $L$  and splitting the scattering operator in 3 parts as

- the self-scattering contribution:  $(H\psi)_{in}^g = (H\psi)^{gg}$  ;
- the slowing-down contribution:  $(H\psi)_{s-d}^g = \sum_{g' < g} (H\psi)^{gg'}$
- the up-scattering contribution:  $(H\psi)_{u-s}^g = \sum_{g' > g} (H\psi)^{gg'}$

where the index  $^{gg'}$  indicates a scattering from group  $g'$  to  $g$ . The iterative solution of the system of equations over the energy groups is then written as

$$[(L\psi)^g]^{(e+1)} = [(H\psi)_{in}^g + (H\psi)_{s-d}^g + (H\psi)_{u-s}^g]^{(e+1)} + \left[ \frac{(P\psi)^g}{\lambda} \right]^{(e)}. \quad (2.19)$$



The external iterations serve to converge on the  $k_{eff}$  and the fission source distribution,  $F_i(\vec{r}) = \sum_g \left( \nu \Sigma_f \right)_i^g(\vec{r}) \phi_i^g(\vec{r})$ , where  $\left( \nu \Sigma_f \right)_i^g$  is the number of emitted neutrons per fission times the macroscopic fission cross section for fissile isotope  $i$  in group  $g$ . Every external iteration updates the values of  $k_{eff}$  and  $F_i(\vec{r})$  by using the previous values of these quantities to compute the fission source

$$\left( S_{fission} \right)^g(\vec{r}) = \frac{1}{k_{eff}} (P\psi)^g(\vec{r}) = \frac{1}{4\pi k_{eff}} \sum_i \chi_i^g F_i(\vec{r}), \quad (2.20)$$

where  $\chi_i^g$  is the probability for a neutron emitted by fission of fissile isotope  $i$  to have an energy within group  $g$ , and get a new multigroup flux by solving the equations

$$(L\psi)^g = (H\psi)^g + \left( S_{fission} \right)^g. \quad (2.21)$$

The new flux  $\psi^g$  is then used to compute the updated values for  $F_i(\vec{r})$  and  $k_{eff}$ . The latter is usually obtained by multiplying Eq. (2.2) by a weight and integrating over the phase space:

$$\lambda^{(e+1)} = \lambda^{(e)} \frac{\langle W, P\psi^{(e+1)} \rangle}{\langle W, P\psi^{(e)} \rangle}. \quad (2.22)$$

where  $\langle W, P\psi \rangle$  is an integration over the entire phase space and  $W$  is a weighting function. The choice in APOLLO2 is  $W = P\psi^{(e)}$ .

In order to compute the multigroup flux solution of Eq. (2.8) one solves iteratively the multigroup equations for each group  $g = (1, \dots, N_g)$  using the last value of the multigroup fluxes for the sources external to the group. This solution involves iterations on the thermal group range because the upscattering source is not known.

Thus, the angular and the spatial dependences of the flux are solved by the numerical flux solver method over the domain  $D$  for a one-group source problem (internal iterations). Only the within-group scattering source depends on the group flux, whereas all the other contributions are treated as external known sources. Depending on the adopted flux solver method, the flux  $\psi^g$  is then computed in an internal iteration loop (as for the  $S_N$  method) or directly (as for the  $P_{ij}$  method).

## 2.6 Flux Solvers

In order to compute the one-group angular flux  $\psi^g$ , in the power iteration loop, several numerical methods are available in APOLLO2.

The methods used in this thesis for PBR modeling are briefly described in the following: the discrete differences  $S_N$ , in section 2.6.1, and the  $P_{ij}$ , in section 2.6.2.

Moreover, the double-heterogeneity treatment of the  $P_{ij}$  method is described in section 2.6.2.1. This treatment is used to compute the flux in the average microparticle and in the surrounding matrix contained in each shell in which the inner fuel region of a pebble is subdivided.

### 2.6.1 Discrete Differences $S_N$ Method

In the  $S_N$  method the one-group form of the differential transport equation is solved for a set of discretized angular directions associated to weights,  $\{\bar{\Omega}_n, w_n\}_{n=1, N}$ , where  $N$  is an even integer. The discretization of the angular variable  $\bar{\Omega}$  as a set of discrete directions  $\bar{\Omega}_n$  is defined in terms of specific direction cosines. Different quadrature sets are available in APOLLO2. For the RZ calculation we have used the appropriated level-symmetric formula.<sup>44</sup>

The one-group discretized angular flux  $\psi_n = \psi(\vec{r}, \bar{\Omega}_n)$  at internal iteration  $(i + 1)$  is computed as

$$\left[ (\bar{\Omega}_n \cdot \nabla + \Sigma_t) \psi_n \right]^{(i+1)} = \sum_{l=0}^L \Sigma_{s,l} \sum_{m=-l}^l A_{m,l}(\bar{\Omega}_n) \left[ \phi_{m,l}(\vec{r}) \right]^{(i)} + S_{ext}(\bar{\Omega}_n), \quad (2.23)$$

where  $L$  is the scattering order,  $\phi_{m,l}(\vec{r})$  are the flux moments defined in (2.12) and  $S_{ext}$  contains all the extra-group contributions (slowing-down, up-scattering, fission).

The spatial discretization of Eq. (2.23) depends on the geometry. For example, in the RZ geometry cartesian finite differences are used. For a given direction  $\bar{\Omega}_n$ , the flux is computed successively in each cell by propagating upstream along  $\bar{\Omega}_n$  the solution of the angular flux, starting from the inward boundary (which depends on  $\bar{\Omega}_n$ ) of the geometry. Thus, the averaged flux for cell  $i$ ,  $\psi_{n,i}$ , is derived from the value of the surface-averaged entering flux,  $\psi_{n,i}^-$ , at the inward cell's surfaces. To propagate the



solution to the next neighboring cells, the surface-averaged exiting flux,  $\psi_{n,i}^+$ , is obtained by a linear interpolation of  $\psi_{n,i}$  and  $\psi_{n,i}^-$  as

$$\psi_{n,i}^+ = \frac{\psi_{n,i} - \alpha \psi_{n,i}^-}{1 - \alpha}. \quad (2.24)$$

If the factor  $\alpha$  of this last equation is equal to  $1/2$  the differencing scheme is called diamond, otherwise is called weighted and it is introduced to obtain positive values of the exiting fluxes.

A swap of the geometry is computed for each angular direction yielding the cell-averaged fluxes  $\psi_{n,i}$  for all cells and directions.

Next, the updated angular flux moments are computed as

$$[\phi_{m,l}]^{(i+1)} = \frac{2l+1}{4\pi} \sum_n w_n [\psi_n]^{(i+1)} A_{m,l}(\bar{\Omega}_n), \quad (2.25)$$

and a next internal iteration can be performed.

## 2.6.2 Collision Probability Method

The collision probability (CP) method solves the integral form of the (2.2) transport equation, in the one-group form, with isotropic scattering and sources over a heterogeneous domain  $D$  with an angular flux entering isotropically through the boundary  $\partial D$ . The interest of this method is that it directly computes the scalar fluxes. However, the assumption of isotropic scattering is not realistic in reactor physics and it is necessary to improve it by introducing transport corrected cross sections. The transport correction consists of using a modified P0 scattering law which includes a singular contribution in the direction  $\bar{\Omega}' = \bar{\Omega}$  and preserves the moment of the P1 scattering law.<sup>32</sup>

The domain is partitioned into a set of homogeneous regions  $D_i$  that defines on the boundary  $\partial D$  a set of surfaces  $\partial D_\alpha$ .

Two approximations are made in the collision probability method:

- 1) A region-wise constant flat-flux approximation is used for the scalar flux:  $\phi(\vec{r}) = \phi_i(\vec{r})$ ,  $\vec{r} \in \text{region } i$ ;

- 2) the angular flux entering through  $\partial D$  is approximated by a surface-wise constant expansion  $\psi^-(\vec{r}, \bar{\Omega}) = \frac{J_\alpha^-}{\pi A_\alpha}$ ,  $\vec{r} \in$  surface  $\alpha$ , where  $J_\alpha^-$  is the current entering via surface  $\alpha$  of area  $A_\alpha$ .

The formulation of the flat-flux collision probability method for a general geometry can be written as:

$$\begin{aligned} V_i \Phi_i &= \sum_j C_{ij} F_j + \sum_\alpha I_{i\alpha} J_\alpha^-, \\ J_{\alpha'}^+ &= \sum_j E_{\alpha'j} F_j + \sum_\alpha T_{\alpha'\alpha} J_\alpha^-, \end{aligned} \quad (2.26)$$

where the sums in  $j$  and  $\alpha$  are, respectively, over all the regions in the domain and over all the surfaces on its boundary and

- $V_i$  = volume of homogeneous region  $i$ ,
- $\phi_i$  = average scalar flux in region  $i$ ,
- $F_i = \Sigma_{si} \phi_i + Q_i$  = average angle-integrated emission density in region  $i$ ,
- $\Sigma_{si}$  = region scattering cross section,
- $Q_i$  = average angle-integrated sources in region  $i$ ,
- $\Sigma_i C_{ij} / V_j$  = collision probability from region  $j$  into region  $i$ ,
- $\Sigma_i I_{i\alpha}$  = incoming probability from surface  $\alpha$  into region  $i$ ,
- $\Sigma_i$  = region total macroscopic cross section,
- $E_{\alpha'j} / V_j$  = escape probability from region  $j$  to surface  $\alpha'$ ,
- $T_{\alpha'\alpha}$  = transmission probability from surface  $\alpha$  to surface  $\alpha'$ .

The matrix CP coefficients  $C$ ,  $I$ ,  $E$  and  $T$  are computed via a numerical integration over the area transverse to the neutron trajectory.<sup>29</sup>

One can notice that knowing the values of the entering angular flux and the external sources, the values of the scalar flux in each region  $i$  is straightforward obtained by a matrix inversion. Thus, with the  $P_{ij}$  method no internal iterations are needed in the power iteration loop (the matrix is generally inverted by an iterative method, but these are other type of iterations).

### 2.6.2.1 Double-Heterogeneity Treatment

By adopting Askew's approximation APOLLO2 can treat a geometry with regions  $D_i$  containing a stochastic dispersion of microparticles in a homogeneous matrix.<sup>45,46</sup> This approximation considers that the current exiting the particles, due to the sources inside the particles, is equivalent to an uniform and isotropic source in the matrix. This hypothesis is more adapted when the number of grains dispersed in the fuel matrix is large.

Thanks to Askew's approximation it is possible to compute equivalent homogeneous cross sections for the regions  $i$  containing the grain, thus reducing the problem to the piece-wise homogeneous one described in the previous section.

This homogenization is performed defining the  $p_{mm}$ ,  $p_{pm}$ ,  $p_{mp}$  and the  $p_{pp}$  probabilities, where  $m$  and  $p$  stay for matrix and particle respectively. All these probabilities can be obtained from the elementary CP coefficients of the microparticles and between the matrices in different regions. The latter probabilities are obtained via a homogenization procedure.<sup>46</sup>

Finally, the CP equations are solved for the fluxes in all grain and matrix regions.

## 2.7 Cross Sections Homogenization

In this work, 'homogenize' is used to denote either space homogenization or energy collapsing of the cross sections or both.

Two methods are available for creating few-group homogenized cross sections from a fine-group (self-shielded) library. In the flux weighting method, the multigroup scalar flux result of the fine-group transport calculation over the heterogeneous geometry is used to define homogenized cross sections in a set of broad groups by invoking reaction rate preservation:

$$\sigma_I^G = \frac{\sum_{g \in G} \sum_{i \in I} \sigma_i^g \phi_i^g}{\sum_{g \in G} \sum_{i \in I} \phi_i^g}, \quad \sigma_I^{G \rightarrow G'} = \frac{\sum_{g \in G} \sum_{i \in I} \left( \sum_{g' \in G'} \sigma_i^{g \rightarrow g'} \right) \phi_i^g}{\sum_{g \in G} \sum_{i \in I} \phi_i^g}, \quad (2.27)$$

where  $\phi_i^g$  is the volume-integrated scalar flux in region  $i$ ,  $G$  and  $G'$  denote broad groups and  $I$  is a macroregion.

However, this approach does not really preserve reaction rates and it fails to generate accurate cross sections for lattices that are far from uniform or periodic. That is, the reaction rates obtained from a calculation with the homogenized cross sections do not reproduce the reaction rates obtained from homogenization of the reference values. In order to obtain the same reaction rates one has to use an equivalence procedure that effectively preserves reaction rates. The equations are as before, but in the denominator

one has to use the actual fluxes generated by the broad-group calculation over the homogenized regions:

$$\sum_{g \in G} \sum_{i \in I} \phi_i^g \rightarrow \phi_I^G. \quad (2.28)$$

In this way we make sure that the new calculation will reproduce all the reactions rates predicted by the fine-group reference calculation. However, since the  $\phi_I^G$  depend on the unknown cross sections  $\sigma_I^G$ , one has to deal with a non-linear problem that must be solved by iterations.

We point out here that the flux weighting method has always been used for homogenization in the present work.

## 2.8 Depletion Calculation

The exposure of an isotope to the neutron flux results in nuclear reactions that modify its nuclear characteristics. Moreover, some isotopes are subjected to radioactive decay. Both events lead to the modification of the number of neutrons and/or protons of the original nuclide. These isotopic depletion effects may occur for all isotopes in a nuclear reactor but are more important for the heavy isotopes present in the fuel. The state of the fuel is a function of its burnup, a parameter describing its time-integrated produced energy per initial unit mass. The burnup is generally expressed in MWd/t.

The depletion of the reactor materials produces modifications in their macroscopic cross sections which, in turn, produce a modification of the neutron flux in the reactor.

The system of differential depletion equations for the various isotopes, called Bateman equations,<sup>47</sup> is solved using the depletion chains available in the cross section library. In APOLLO2, different library versions allow for highly accurate description of the isotopic chains for the depletion calculations with energy-dependent fission yields.<sup>27</sup>

Fuel depletion calculations are treated in a quasi-static approximation, where the flux is considered stationary but the concentrations are allowed to change with time. The depletion variables may be time, burnup or fluence. A predictor-corrector algorithm or a step-halving method is applied to control concentration errors at each depletion step. The flux is re-calculated at the end of each step with the new concentrations.



<b>3</b>	<b>Model for PBRs Neutronic Calculations .....</b>	<b>39</b>
3.1	Survey of Existing Codes Methodologies .....	40
3.1.1	Homogenized Cross Sections Generation .....	42
3.1.2	Full-Core Calculation .....	48
3.2	Description of the Model Developed in APOLLO2.....	50
3.2.1	Iterative Core Calculation Scheme .....	50
3.2.2	Model for "Macro Stochasticity" .....	52
3.2.3	CP Treatment of the Multi-Pebble Geometries .....	54
3.2.4	Surface-to-Surface Geometrical Probabilities Modeling .....	55
3.2.5	Clustering .....	56
3.3	Implementation in APOLLO2 .....	57
3.4	Analysis of Boundary-to-Boundary Geometrical Probabilities.....	58
3.5	Convergence Analysis of Steady-State Reactor .....	62
3.5.1	Cylindrical Core Containing a Single Pebble Type.....	63
3.5.2	Annular Core Containing Six Pebble Types .....	65
3.5.2.1	Analysis of Pebbles Spatial Discretization.....	69
3.5.2.2	Clustering Simulations .....	72
3.6	Conclusions to the Chapter.....	74

### 3 Model for PBRs Neutronic Calculations

Due to the physical and technological differences of pebble bed reactors compared to the classical light water reactors, the neutronic modeling adopted for such nuclear systems has to account for their specific features and need to implement specific models.

From the neutronic point of view, the recirculation of the pebbles in the reactor leads to a double level of stochasticity of the problem, due to:

- a) the stochastic dispersion of TRISO particles within each pebble and
- b) the stochastic distribution in the core of pebbles with different burnups.

Moreover, for the homogenization problem, since the neutron mean free path in a PBR core is several times larger than the pebble diameter,<sup>36</sup> the flux inside a pebble is strongly dependent on its surrounding. As a consequence, the approach classically adopted for light water reactors neutronic calculations, based on the two-step core calculation scheme, is not adequate. This scheme consists in the decoupling of the detailed assemblies calculations (computed with reflecting boundaries conditions and critical buckling) and the core calculation, through the constitution of multi-parameterized cross sections libraries. Furthermore, due to the thin and tall core cavity geometry, the thermalized neutrons scattered back from the graphite reflectors highly influence the flux in the larger part of the core. Therefore, the homogenization of the

core sub-regions (spectrum zones) has to account for surface leakage, which must be evaluated from the core calculation, resulting thus in an iterative homogenization technique. This technique is akin to the iterative advanced techniques which are being investigated for LWRs.<sup>49</sup>

In this thesis, a new homogenization model for the spectrum zones, based on a macro-stochastic approach has been developed, which accounts for inter-pebble neutron transport in the calculation of the flux and includes spectral effects in the homogenization. Thus, an iterative scheme has been implemented to couple the calculation of the spectrum zones with the actual core calculation, which is carried out with a low-order transport operator. In this scheme, the broad-group current entering each boundary surface of each SZ, expanded in the fine-group structure by a current shape factor, and the core  $k_{eff}$  are recovered from the core calculation.

In this Chapter, a survey of the methodologies presently implemented in the codes treating the neutronic simulation of pebble bed reactors is presented in section 3.1. The method developed in the APOLLO2 code will be exposed in section 3.2. Section 3.3 presents an analysis performed to evaluate input data needed for the model, namely the boundary-to-boundary geometrical probabilities. This has been realized by a Monte Carlo simulation of the individually positioned pebbles in the PBMR-400. The implementations carried out in APOLLO2 will be briefly summarized in section 3.4. The convergence analysis of the developed iterative computational scheme performed on some simplified reactor models is presented in section 3.5, together with the analysis of the pebbles spatial discretization and of the clustering phenomenon.

### 3.1 Survey of Existing Codes Methodologies

The neutronic simulation of a reactor is constituted by two main phases: the generation of homogenized cross sections and the full-core calculation. Furthermore, thermal-hydraulic calculations have to be coupled with the neutronic code to provide the thermal-hydraulic feedbacks.

To generate the homogenized cross sections, detailed flux calculations are performed using a high number of energy groups on heterogeneous core sub-regions. The homogenized cross sections have to preserve the reference reaction rates computed in the detailed heterogeneous model while assigned to a sub-region of the homogenous model. For example, PWR fine-group calculations are performed at the fuel pin level or, more often, at the fuel assembly one. Previously, the fine-group cross sections have been self-shielded in order to account for geometrical effects and for the flux depression in the resonances domain. The energy range where resonances are located can be divided in two parts: the resolved part, where single resonances are distinguishable, and the unresolved one, where individual resonances are indistinguishable. The calculations are generally made assuming reflecting boundary conditions and representing the core-conditions leakage by calculating a critical buckling. Then few-group cross sections are obtained homogenizing the heterogeneous geometry. Together with the cross sections (total, absorption, nu-fission, scattering, transport, "excess") also other quantities are

homogenized, as fission spectra and yields, diffusion and equivalence parameters. These few-group quantities are rather stored in a multi-parameterized library (depending on, for example, the fuel temperature, the burnup level, the moderator density and temperature) which is, in the second step, used for the full-core calculation or iteratively generated on-the-fly in the iterative homogenization schemes.

The full-core calculation is generally performed by a 2D or a 3D diffusion solver which assigns to the materials of the geometry the proper few-group cross sections.

Several codes have been developed to account for the neutronic simulation of pebble bed reactors. Each of them has its proper methodology to perform the self-shielding of the multi-group cross sections and the homogenization of the pebble geometry, accounting for the double heterogeneity. Moreover, the larger leakage in the bed of pebbles close to the reflectors and the stochastic distribution of pebbles with different burnup levels in the same spectrum zone have also to be accounted for.

A brief survey of the different methodologies used in the most commonly used codes for pebble bed reactors simulation will be given here. The most widely used and mature tool is the Very Superior Old Programs (VSOP) suite of codes,<sup>50</sup> developed at the Jülich Research Centre for the German HTR program. The code system has been updated and improved for the design and licensing of the South African PBMR.<sup>51</sup> Moreover, VSOP is the neutronic code used also for the design of the Chinese HTR-PM reactor. In the last decade, several other codes have been developed or adapted for PBRs modelling. The Nuclear Research and Consultancy Group (NRG) of Petten, The Netherlands, developed the PANTHERMIX code,<sup>52</sup> based on a coupling between the lattice code WIMS,<sup>53</sup> the three-dimensional steady-state and transient core physics code PANTHER<sup>54</sup> and the two-dimensional RZ HTR thermal-hydraulics code THERMIX-DIRECT.<sup>55</sup> Still in the Netherlands, the Delft university of Technology developed the DALTON – THERMIX code system,<sup>56</sup> using some routines of the SCALE code system<sup>57</sup> instead of WIMS. Moreover, they developed a new three-dimensional (xyz or rθz coordinates) diffusion solver, DALTON. The application of the SCALE code system to the simulation of PBRs has also been done at Oak Ridge National Laboratory, using a slightly different algorithm for the cross sections self-shielding and homogenization with respect to the Delft methodology. The full-core calculations were performed using the Monte Carlo KENO modules of SCALE. In the U.S, in the frame of the U.S. Department of Energy's (DOE's) Next Generation Nuclear Plant (NGNP) project,<sup>58</sup> the PEBBED code systems is under development, since 2002, at the Idaho National Laboratory.<sup>59</sup> It couples the PEBBED diffusion code with the thermal-hydraulic THERMIX – KONVEK module used in VSOP 1994. The cross sections generation is performed by different codes and methodologies, using the MICROX-2 code<sup>60</sup> or the INL developed COMBINE code<sup>61</sup>. Recently, the methodology employed by Oak Ridge National Laboratory, using SCALE 6, has also been coupled with PEBBED.<sup>62</sup>



Finally, others codes have been applied to the analysis of PBRs, such as the HELIOS/CAPP code system developed at the Korea Atomic Energy research Institute,<sup>63</sup> but they will not be illustrated in this thesis.

Let us only mention a work at the beginning of the '80s using an interface-current transport method,<sup>64</sup> implemented in the ROLAIDS code,<sup>65</sup> to treat a double-heterogeneous multi-system geometry composed by multiple 1D spheres exchanging neutrons between themselves. ROLAIDS is an interface-currents integral transport program which performs an energy point-wise slowing-down calculation in one-dimensional multi-region geometries. The one-dimensional spheres are coupled at their external boundaries through a current balance. The incoming current, which is considered to be the same at the outer boundary of all the spheres, is computed as the weighted sum of the outgoing currents from all the spheres. The weights correspond to the relative external surface area of each type of spheres. This method is similar to the stochastic multi-cell method developed in the past in the APOLLO code.<sup>34</sup> It shares with the method developed in this thesis the idea of coupling several 1D spherical geometries by a current balance. Nevertheless, the method developed in APOLLO2 treats the neutron transport in the spheres by the collision probability method, which is a much better transport approximation compared to the interface-current one. Furthermore, the neutron exchange between the pebbles comprised in a spectrum zone and the zone's boundary surfaces is also accounted for, which is necessary to properly consider, in the heterogeneous fine-flux calculation, the leakage in the corresponding core sub-region. At last, the presence of the helium coolant in between the pebbles is also accounted for via a stochastic approximation.

In the following, we will briefly describe the methodology adopted by the mentioned codes to self-shield and generate the homogenized cross sections and to perform the full-core calculation. A summary of the main features of each code, compared to the ones of the method developed in APOLLO2, is given in the conclusions for this Chapter in Table 3.VII.

### 3.1.1 Homogenized Cross Sections Generation

#### - VSOP

Spectrum calculations are based on the GAM-I and THERMOS codes.<sup>66</sup> Correspondingly, the codes need the two respective libraries. The epithermal GAM library is given with a 68-group structure, ranging from 10 MeV to 0.414 eV, and the thermal THERMOS one with a 30-group structure ranging from 2.05 eV to 0. GAM iteratively provides a slowing-down source to THERMOS, which computes the flux in the thermal region and supplies the fission source to GAM. Thus, upscattering is treated no over than 2.05 eV.

The self-shielding in the resolved and unresolved resonance ranges is performed by the ZUT code.<sup>67</sup> Effective or averaged parameters are given for the unresolved resonances

of  $\text{Th}^{232}$  and  $\text{U}^{238}$ . In the resolved resonance range the Nordheim Integral Treatment is applied,<sup>68</sup> which involves a numerical integration of an integral form of the collision density equation as a function of energy, derived from the collision probability method in a two-region unit-cell containing a resonant absorber isotope and a maximum of two moderating materials. In this slowing-down problem, flat sources are assumed in both the fuel and moderator region, with a  $1/E$ -flux and no absorption taking place in the moderator. The integral equation depends, among others, on the first-flight escape probability, which is the probability that a neutron originating in the fuel region (homogeneously and isotropically) will reach the surface of this region without any collisions in the fuel. The presence of more than one fuel region in the moderator, such as the micro-particles dispersed in the graphite matrix of the inner pebble region, is accounted for using a Dancoff(-Ginsburg) factor.<sup>69</sup> This factor corrects the first-flight escape probability for a single fuel kernel to consider that a neutron which escapes a fuel region can have its next collision in another fuel region. The Nordheim's Dancoff corrected escape probability thus relies on the calculation of a Dancoff factor, which depends only on the geometry of the system and on the total macroscopic cross section of the moderator. Since the latter varies hardly in the resonance range, the Dancoff factor is calculated, analytically or by numerical integrations, only once for a given geometry.

GAM-I performs a P1 slowing-down calculation in an infinite homogeneous medium with a fixed source, generally with a  $\text{U}^{235}$  fission energy spectrum. Leakages are accounted by a geometrical buckling, computed for each spectrum zone from the diffusion core calculation. It is then necessary to iterate between the spectrum calculation and the diffusion core calculation in order to obtain the leakage factors. The leakage factors are provided in the broad-group structure of the core calculation.

THERMOS performs a collision probability calculation in a 1D spherical geometry, where the fuel region of the pebble is represented as a homogeneous material. Once again, a fixed source problem is solved, where the uniformly distributed slowing-down source is given by the previous GAM calculation. Leakages are represented by an albedo on the surface of the pebble, which is also computed from the diffusion core calculation for each spectrum zone.

Both GAM and THERMOS deal with the second level of stochasticity of the problem in the same way. The stochastic distribution of the pebbles with different burnup is not really treated, but a single pebble with an average material, obtained by volume averaging the isotopic atomic densities of the different pebble types contained in a zone, is used for the calculation. As a consequence, a single neutron flux spectrum is used to homogenize and deplete all the pebble types contained in a spectrum zone. This approximation is also made by all the other codes presently developed and described here.

## - PANTHERMIX

In this code a multi-parameterized cross section library, depending on the fuel burnup, the fuel temperature and the xenon density is created to provide two-group cross sections to the PANTHER diffusion code.<sup>70</sup>

The unit cell calculations, preceded by the generation of shielded fine-group cross sections in the resonance energy range, are performed rather with WIMS or with SCALE.<sup>71</sup> The method adopted in SCALE is presented hereafter while describing the DALTON – THERMIX code system.

In WIMS a 172-group flux calculation is performed employing the WIMS-module WPROCOL. Since it is impossible to model a spherical geometry containing grains in the WIMS code, neutron transport is computed in an equivalent infinite cylinder containing coated particle fuel. The cylindrical transformation is applied by the conservation of the mean chord length of the fuel zone. The double heterogeneity is accounted for by Askew's approximation.

Self-shielding is performed by the subgroup method only for a few main isotopes (as this method is time-consuming), and an approximated resonance treatment is applied for all the other resonant isotopes. The infinite dilution nuclide resonant integrals are tabulated in function of the background scattering cross section  $\sigma_b$  and temperature. The WPROCOL module computes collision probabilities in the equivalent cylinder, of which the inner zone contains the coated particles. This CP matrix is used for both the resonance calculation and the flux calculation. The collision probabilities are used to calculate the subgroup fluxes and appropriately weighted broad-group resonance cross sections for the main isotopes. Resonance shielding for all the other resonant absorbers is carried out in an approximate way based on equivalence theory and applied to a slab geometry. A  $\sigma_b$  is calculated in the slab geometry and it is used to interpolate in the table of resonance integrals. The slab geometry is constructed in such a way that the effective mean chord length of the inner layer of the slab is equal to the effective mean chord length of a fuel kernel dispersed in the graphite matrix. This effective mean chord length is computed with the radius of the fuel kernel corrected by a Bell factor, which has a fixed value and originates from a modification of Wigner's rational approximation for the first-flight escape probability, and by a Dancoff factor.

The Dancoff factor is analytically derived by the method developed by Bende et al. specifically for pebble bed reactors.<sup>72</sup> In this derivation, the Dancoff factor is calculated as the sum of two probabilities. The first one is the probability that a neutron leaving the fuel kernel will enter another kernel without any collision in the moderator within the same pebble, called the intra-pebble Dancoff factor. The other one is the probability that a neutron leaving a particular kernel will enter a fuel kernel in another pebble without collisions in the moderator, which has been designated as the inter-pebble Dancoff factor. This formulation is based on a two-region (fuel and moderator) model, with the value of the total Dancoff factor as a function of the geometry and the one-group macroscopic total cross section of the moderator material. For the grain geometry the moderator material is computed smearing the fuel kernels coatings and for the pebble geometry the moderator is the fuel free graphite shell. It is then necessary to evaluate

these total cross sections before performing the Dancoff factor calculation using a pre-determined flux spectrum (as thermal Maxwellian + 1/E + fission spectrum).

After the cell calculation, the pebble materials are smeared to a homogeneous material and the nuclear data are homogenized to 16 energy groups. One-dimensional  $S_N$  radial and axial calculations are then performed, representing cuts of the reactor model, to embrace the spectral differences over the core. The 16-group cross sections are then collapsed to two groups. Two group data are generated for several burnup steps (*i.e.* 27), fuel temperatures and xenon concentrations. One has to observe that these 1D calculations are performed with a unique homogeneous material for the core, corresponding to a single burnup value of the pebbles in the cavity. This is far from a more realistic situation where, even considering only the average composition pebble, the burnup distribution varies slightly radially and greatly axially in the core cavity.

Finally, each mesh volume in the PANTHER model contains a certain material that corresponds to a set of nuclear constants, obtained interpolating the two group data. The data for the axial bottom and top layers of the pebble bed is taken from the library associated to the axial 1D calculations, while the data for the remaining part is taken from the radial ones.

This multi-scale approach based on successive 1D  $S_N$  calculations is similar to a methodology proposed in 1986 to simulate the critical KHATER facility with the RSYST<sup>73</sup> code system.<sup>74</sup> In this approach, the double heterogeneity of the TRISO particles was accounted for by computing flux disadvantage factors for the particle – graphite matrix unit cell. These factors express the ratio of the heterogeneous to the homogeneous spectra.

#### - DALTON – THERMIX

The methodology used in this code is also based on a multi-scale approach.<sup>75</sup> Here a 9-group two-dimensional cross sections library ( $\Sigma(r, z)$ ) is created to associate the broad-group cross sections to each spectrum zone of the diffusion core calculation. The transport code used is SCALE-5.

The resonance shielding calculation, which uses the Bende's Dancoff factor derivation, is performed by the Bondarenko method for the unresolved resonances and by the Nordheim Treatment for the resolved ones. The Bondarenko method<sup>76</sup> uses a simple expression for the flux computed in a homogeneous medium, as the inverse of the total cross section in function of lethargy. It then considers one resonant nuclide and it expresses the sum of the total cross sections of all the other nuclides as an effective background scattering cross section  $\sigma_b$ , constant within an energy group. The collapsed cross section of the considered nuclide is then expressed as an infinite dilution average value times a Bondarenko factor, function of the  $\sigma_b$  and of the temperature. This factor is calculated in the specific problem by interpolating in tables of pre-calculated data for different  $\sigma_b$  's and temperatures.

Firstly, a 1D  $S_N$  calculation of the TRISO particle surrounded by an equivalent graphite layer is performed in 172 groups. The geometry is then homogenized in a single

material, but without energy collapsing, which is used to describe the fuel region of a pebble surrounded by an equivalent helium layer. Secondly, another 1D  $S_N$  calculation is performed with this pebble geometry and again cross sections are homogenized without energy collapsing. Finally, additional 1D  $S_N$  calculations are performed on radial cuts of the reactor model, corresponding to different cross-sections of the core. In order to model the transverse neutron leakage in these 1D calculations, the reactor height is used to provide an axial buckling value. The computed flux is used to collapse the cross-sections to the 9-group structure. The zone-weighted cross sections are allocated to the corresponding spectrum zones materials, creating a 2D cross section map.<sup>77</sup>

A limiting factor in this methodology is that the different burnup levels of the pebbles contained in neighboring SZ for a 1D radial cut calculation have to be evaluated previously. In DALTON-THERMIX, the nuclide densities in the core are calculated by the code system prior to the above procedure using the PEBBED method that converges directly to the equilibrium core.<sup>59</sup>

#### - SCALE

The SCALE code has also been used in a stand alone approach for the analyses of PBRs.<sup>78,79</sup> In this case, the homogeneous cross sections representing the pebble geometry are generated for a Monte Carlo core simulation. A 238-group cross section library is used.

The self-shielding of the unresolved resonances is performed with the Bondarenko method. In the resolved resonances energy range, the CENTRM code<sup>80</sup> performs a 1D  $S_N$  point-wise spectrum calculation of the fuel kernel surrounded by the equivalent moderator (coatings and graphite) layer, using a point-wise cross sections library. In the lower and upper energy ranges, a classical multigroup approximation is used. CENTRM solves the fixed source form of the transport equation, with a user-specified fixed source term. A slowing-down problem is solved, with no eigenvalue calculation and with  $s$ -wave scattering approximation in the point-wise range. Point-wise flux disadvantage factors are then computed and used to create the point-wise particle/matrix mixture cross sections. In this way the double heterogeneity is accounted for.

Another module called PMC then creates the 238-group cross sections to perform a 1D  $S_N$  calculation of the cell with the source iterations. The cell is then homogenized in a single material without energy collapsing. The homogenized point-wise cross sections are then used in a successive CENTRM calculation of the pebble geometry surrounded by the helium layer and a final 1D  $S_N$  calculation is performed to create the resonance-shielded multigroup cross sections that represent the fuel pebble.

This methodology does not rely on the calculation of Dancoff factors to represent the double heterogeneity of the fuel. Neither does it account for the leakage effect in the self-shielding and in the cross sections homogenization.

## - PEBBED

The cross section generation for the PEBBED diffusion code used to be performed with the MICROX-2 code for an infinite lattice of pebbles.<sup>81</sup> MICROX-2 solves the integral transport equation for a one-dimensional two-region cell, the two regions being coupled through collision probabilities. The cross sections in the unresolved resonances range are self-shielded by the Bondarenko method and in the resolved resonance range by a slowing-down  $B_1$  calculation using point-wise cross section data. The double heterogeneity of the geometry is accounted for through a Dancoff factor computed with Bende's formalism. A 193-group structure is used. A two-step calculation is performed. As a first step, the flux is computed on the unit cell composed by the fuel kernel surrounded by a homogenized shell of smeared TRISO coatings and graphite matrix nuclides. Next, another two-region problem is solved where the internal zone is associated with the fine-group cross sections obtained for the fuel region in the previous step and the external zone is a mixture of the external graphite layer and helium. No energy collapsing is performed in this study since the results obtained by computing a reflected pebble are compared to a reference Monte Carlo.

In a following development, this methodology has been completed applying a Spectral History Correction (SHC) method to account for the leakages in the associated core spectrum zone.<sup>82</sup> The objective of the SHC method is to reduce the number of calls to the lattice spectrum code to iteratively homogenize the cross sections for the diffusion code during the convergence to an equilibrium fuel cycle. The description of the equilibrium fuel cycle and of the PEBBED methodology to compute it is given in Chapter 5. Briefly, in the SHC method, fine-group data are pre-computed for a range of isotopic states, in function of the  $U^{235}$  atomic density, in the pebble geometry with reflected boundary conditions. These tabulated microscopic cross sections are used together with the actual nuclide number densities in the spectrum zone, obtained iteratively from the core calculation, to construct fine group macroscopic cross sections. These last, together with fission spectra, flux disadvantage factors and zone buckling, are used in the solution of the slowing-down balance in a homogeneous medium to generate an updated spectrum. The zone buckling values for all the spectrum zones are computed by the diffusion core calculation in the broad-group energy structure. Thus, a constant buckling term is used for all the fine-groups contained in the corresponding broad group. The microscopic cross sections are then re-collapsed with the new spectrum in a 6-group energy structure for the corresponding spectrum zone in the core calculation. This is the same approach to account for leakage which is used in GAM-I. The difference here is that the flux is recomputed on the detailed pebble geometry by MICROX-2 only at some iterations interval. Thus, this is a sort of synthetic acceleration method with the low order operator computed by the SHC method.

Recently, alternatively to MICROX-2, also the COMBINE code has been used to generate the homogenized cross sections for PEBBED.<sup>83</sup> COMBINE computes the flux with the  $B_1$  or  $B_3$  approximation in a unit cell with group-wise buckling terms to

account for leakage. Nevertheless, presently only a one-group buckling value is supplied for each spectrum zone by the core diffusion calculation in an iterative sequence.<sup>84</sup>

The Bondarenko method is used for the treatment of the unresolved resonances region and either the Bondarenko or Nordheim Treatment for the resolved resonances. Spatially varying Dancoff factors, computed with the Monte Carlo code PEBDAN<sup>85</sup> for the different spectrum zones and depending on the zone's packing fraction, are used to account for the double heterogeneity. In PEBDAN the intra-pebble and the inter-pebble Dancoff factors are computed by a Monte Carlo ray tracing method applied to the geometry simulating the pebble positions in the core cavity. The positions of the pebbles are computed by a rain model, where a pebble is randomly dropped in the cavity until it reaches another pebble. With respect to the Bende's formulation, the enhanced neutron streaming close to the reflectors, due to the pebbles packing rearrangement, is accounted for by a variation of the inter-pebble Dancoff factor. This last factor drops several tens of percents close to the side reflectors as neutrons originating in pebbles in the side regions of the core experience a larger escape probability.

A multi-scale calculation, similar to the one employed in PANTHERMIX, is performed making a 167-group spectrum calculation firstly for the unit cell composed by the kernel and the surrounding moderator layers. Then with the same group structure the flux is computed on a second unit cell composed by the pebble fuel region surrounded by the external graphite layer and by a mixture of graphite and helium layer, representing the surrounding moderator pebbles and coolant. The unit cell calculations are performed with white boundary conditions. With the flux computed in the pebble cell, the 167-group structure is homogenized in a 99-group structure which is used for the homogeneous material in 1D  $S_N$  radial calculations of reactor transverses. Finally, the cross sections are collapsed in a 16-group structure for all the zones in the reactor and are passed to the PEBBED diffusion code.

Apart from the number of groups employed at each level of the calculation, this methodology differs from the one of PANTHERMIX for the use of an improved Dancoff factor and because an iterative homogenization technique is employed, rather than building a cross sections library. This is done to capture the effect of transverse leakage in a zone by the buckling term computed in the core calculation, since the 1D flux calculation in the transverse capture the radial leakage.

### **3.1.2 Full-Core Calculation**

VSOP, PANTHERMIX, DALTON-THERMIX and PEBBED generate the broad-group cross sections for the 2D or 3D diffusion calculation of the core with a different number of broad energy groups.

VSOP and PEBBED iteratively homogenize the cross sections recovering the zones' buckling terms from the core calculation. CITATION, which is the diffusion solver in VSOP, uses a 4-group energy structure, and PEBBED uses a variable number of broad

groups: 6, 16 or even 28 in the analysis where the cross sections are generated by the SCALE-6 methodology.

PANTHERMIX and DALTON- THERMIX build a multi-parameterized cross sections library (depending on fuel burnup, fuel temperature and xenon density) in, respectively, 2 and 9 energy groups.

The diffusion codes which simulate the PBRs have to deal with the difficulty of treating the gas plenum between the top of the core and the top reflector, since the diffusion approximation is not valid in this void region. Generally, this is done using the Gerwin and Sherer's method that treats the cavity as a diffusion region with effective anisotropic diffusion constants ( $D_r$  and  $D_z$ ) and zero reaction cross sections.<sup>86</sup>

Because the cell homogenization algorithms described in the previous section do not preserve the inter-pebble leakage rate, the correction developed by Lieberoth and Stojadinović is applied to adjust the diffusion coefficients.<sup>87</sup>

If the reactor geometry is described by a 2D RZ model, the streaming effect of control rod holes, coolant channels and boron absorber ball channels can not be considered. A three-dimensional core calculation is necessary to evaluate the effect on reactivity of neutron streaming through these void channels drilled in the internal and external reflectors.

Finally, we mention an analysis<sup>88</sup> which has been performed simulating a pebble bed reactor by a RZ  $S_N$  transport method with the DORT code.<sup>89</sup> The cross sections were generated with the MICROX-2 code. A parametric study was carried out to analyze the sensitivity of the  $S_N$  calculation to the spatial discretization, the angular quadrature order, the scattering order and the energy group structure. From the results it was observed that the core eigenvalue, the axial power and flux distribution were not significantly affected varying angular quadrature after  $S_4$  and using a P3 scattering order rather than a P1. Thus, with a P1- $S_4$  scattering and quadrature orders, it was observed that the results were not much impacted by refining or broadening the spatial mesh. Moreover, using a 4, 7 or 13 groups structure, it was observed that the eigenvalue was significantly impacted by the number of groups utilized, since for the power distribution the differences were quite small. The results were then compared to the ones obtained by a diffusion calculation performed with the NEM-THERMIX code system.<sup>90</sup> It was observed that when the top gas plenum is eliminated from the geometry, there is an excellent agreement between diffusion and transport theory results. On the contrary, when the gas plenum is considered, the axial power profile computed with diffusion is shifted downwards compared to the respective transport results.



## 3.2 Description of the Model Developed in APOLLO2

This work is an extension of an infinite-lattice homogenization technique, earlier implemented in the CEA transport code APOLLO2, to treat a finite spectrum zone by explicitly accounting for interactions between pebbles with different burnup histories.<sup>91</sup>

A stochastic model to account for the random distribution of different burnup pebbles within a given spectrum zone, which represents the second level of stochasticity of the problem, is introduced. Each SZ is associated to a multi-pebble geometry in which pebbles are grouped into a finite number of pebble types, characterized by average burnup and multiplicity. The pebble-to-pebble interactions are described by a collision probability (CP) formulation for one-dimensional spheres which exchange neutrons among themselves and with a set of external surfaces (interfaces with neighboring spectrum zones or reflectors). The contribution of the coolant is also included. A set of pebble-to-pebble, pebble-to-boundary and boundary-to-boundary geometric probabilities are introduced to write the closure relations between the average neutron currents entering and exiting each pebble type and each surface. For example, the pebble-to-pebble geometric probability  $p_{\beta,\alpha}^{p,p}$  is the probability for neutrons exiting uniformly and isotropically pebbles of type  $\alpha$  to enter a pebble of type  $\beta$  without crossing any other pebble. All these probabilities obey reciprocity and conservation relations and can be derived from a basic set of surface-surface probabilities and from a statistical description of the pebbles distribution in the zone.<sup>91</sup> A *uniform* model is invoked, according to which the probability to find a pebble of a given type in a given location within the spectrum zone is proportional to the multiplicity of the type. In the present work a more physical *renormalized* model is also introduced. These two models are described in Section 3.2.4. Moreover, for safety analysis applications, a *clustering* model, presented in Section 3.2.5, has been derived from the *uniform* and *renormalized* models by artificially increasing the geometric self-probability for pebbles of a given type.

The final spectrum zone model is characterized by a set of equations giving the fluxes for each pebble type in terms of currents entering the surfaces, providing the possibility to independently compute each zone from the currents entering it. The notation is given in Appendix A.

### 3.2.1 Iterative Core Calculation Scheme

Let  $D$  be the geometric domain of a spectrum zone which comprises pebbles of different types and the helium coolant. The flux in  $D$  obeys the exact transport source equation:

$$\begin{aligned}
(\vec{\Omega} \cdot \vec{\nabla} + \Sigma)\psi &= H\psi + \frac{1}{\lambda_{core}} P\psi, & x \in X, \\
\psi_- &= \psi_{-,core}, & x \in \Gamma_-,
\end{aligned} \tag{3.1}$$

where  $H$  and  $P$  are, respectively, the scattering and fission operators,  $\lambda_{core}$  is the core  $k_{eff}$ ,  $\psi_{-,core}$  is the angular flux entering the domain via its surface  $\partial D$ ,  $X$  is the phase space associated to domain  $D$  and  $\Gamma_-$  the incoming boundary of  $X$ .

For each spectrum zone, the cross sections to be utilized in the full transport or diffusion broad-group core computation are flux-weighted homogenized from a fine-group solution of Equation (3.1) over a corresponding multi-pebble geometry.

For the spectrum zone calculation we assume that the core entering angular flux is isotropic and piecewise uniform over a set of external surfaces, as defined by the contacts with the neighboring zones or reflectors. Therefore, the angular flux entering each surface  $k$  is represented by the value of the entering current  $J_{-,k}^g$ .

It has to be noted that, because both the  $k_{eff}$  and the entering currents must be obtained from the broad-group core computation, the calculation scheme is necessarily iterative. Finally, the value of  $J_{-,k}^g$  is obtained by preserving the corresponding  $(J_{-,k}^G)_{core}$  core value:

$$(J_{-,k}^g)^{(n)} = \left[ \frac{(J_{+,k}^g)_{neighbor}}{\sum_{g \in G} (J_{+,k}^g)_{neighbor}} (J_{-,k}^G)_{core} \right]^{(n-1)}, \tag{3.2}$$

where the quantities on the right hand side are obtained from the previous iteration,  $g$  is the fine group index and  $G$  is the coarse group index.

This iterative core homogenization scheme is illustrated in Figure 3.1. The iterations are initialized from a critical-buckling infinite-lattice calculation for each spectrum zone, which is solved by using the CP equations with reflected boundaries, as described in section 3.3.

Note that the spectral shape factor for the entering current,

$$\chi_k^{gG} = \frac{(J_{+,k}^g)_{neighbor}}{\sum_{g \in G} (J_{+,k}^g)_{neighbor}}, \tag{3.3}$$

is obtained from the fine-group transport current  $(J_{+,k}^g)_{neighbor}$  exiting the corresponding neighboring spectrum zone or reflector wall.

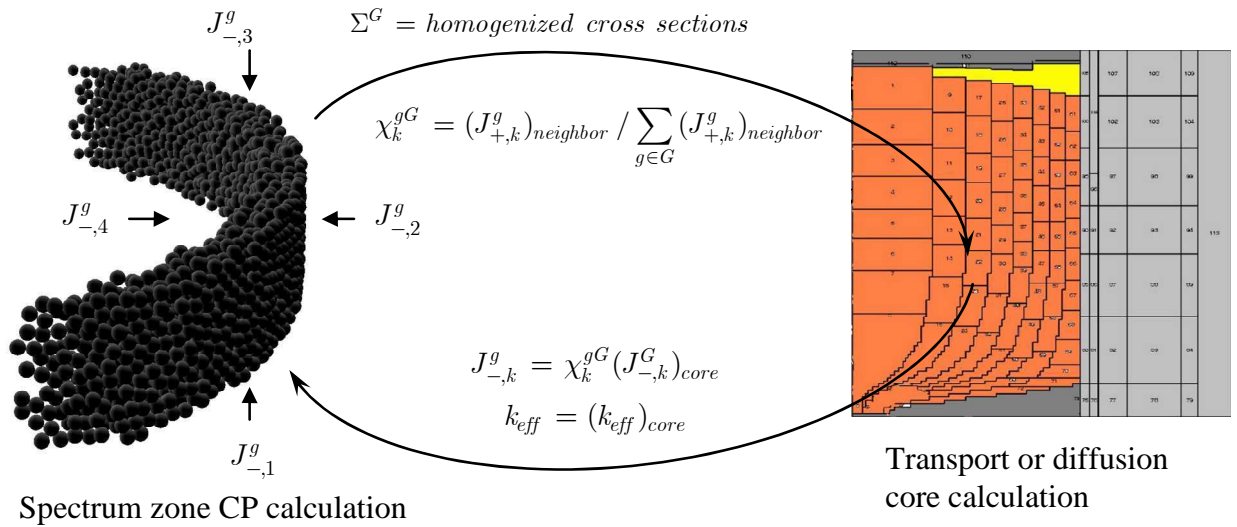


**Figure 3.1: Iterative Spectrum Zones – core calculation scheme**

All the iterations begin with the fine-group transport calculations for the spectrum zones and end with a full coarse-group core calculation. The latter is converged as usual on the fission integral shape and the  $k_{eff}$ . The convergence criteria for the iterative core calculation is achieved when the maximum relative difference between two consecutive iterations on the fission integrals, the core currents entering the spectrum zones and the homogenized total cross sections, as well as the absolute difference in the  $k_{eff}$ , are below user's prescribed values. One can notice that when these parameters are converged also the core fluxes and the core power distribution have to be converged. Finally, a transport calculation of the graphite reflectors is needed to obtain the homogenized coarse-group cross sections and to determine the current spectral shape factor for the spectrum zones having surfaces in contact with the reflectors. In the developed calculation scheme, this was done by performing axial and radial 1D fine-group transport calculations of the reactor, using for the core the cross sections obtained by homogenizing the spectrum zones with the initial infinite-lattice calculations.

### 3.2.2 Model for "Macro Stochasticity"

In a spectrum zone containing different pebbles in interaction among themselves and with the zone surfaces, one would expect that each pebble will reach a unique equilibrium flux that will depend on the pebble composition (burnup) and on the current entering the pebble. If a homogenization process is invoked for the core calculation, then these are the fluxes that should be used to collapse and homogenize cross sections within the domain.

As it has been described in section 3.1.1, this is not what is presently done by the codes used to model the neutronics of PBRs. In fact, this level of stochasticity is treated assuming a single pebble composition, volume-averaged over the spectrum zone, from

all the different compositions representing the various passages of the pebbles through the core. This approximation does not allow accounting for the flux differences in the different composition pebbles for cross sections homogenization.

The model described in this section, on the contrary, predicts this type of solution by making a stochastic approximation on the way in which pebbles and surfaces interact. The mathematical details of the model are given in Appendix B.

The neutron exchange between the different pebble types contained in a zone and the zone's boundary surfaces is described by introducing pebble-to-pebble, boundary-to-pebble, pebble-to-boundary and boundary-to-boundary geometrical probabilities. These probabilities are indicated, respectively, as  $p^{p,p}$ ,  $p^{p,b}$ ,  $p^{b,p}$  and  $p^{b,b}$  in Equations (3.4) and (3.5) and they are the probabilities for a neutron to leave a surface (of a pebble or of a zone's boundary) and reach another surface without crossing any other surface.

Neglecting the helium contribution, the currents entering the different pebble types  $\vec{J}_-(E)$  originate from the currents exiting the pebbles  $\vec{J}_+(E)$  and from the currents entering the zone surfaces  $\vec{J}_-^{bd}(E)$ :

$$\vec{J}_-(E) = p^{p,b} \vec{J}_-^{bd}(E) + p^{p,p} \vec{J}_+(E), \quad (3.4)$$

where  $\vec{J}_\pm = \{J_{\pm,i}\}$  and  $J_{\pm,i}$  is the total current exiting (+) or entering (-) the overall surface of the pebbles of type  $i$ ,  $\vec{J}_\pm^{bd} = \{J_{\pm,k}^{bd}\}$  and  $J_{\pm,k}^{bd}$  is the total current exchanged through the zone surface  $k$ .

The total current leaving the domain via its surfaces is:

$$\vec{J}_+^{bd}(E) = p^{b,b} \vec{J}_-^{bd}(E) + p^{b,p} \vec{J}_+(E), \quad (3.5)$$

From these equations one can notice that the different pebble types are coupled through a current balance, which accounts for the exchanges with the zone boundary surfaces.

The validity of this modeling relies on the assumptions of isotropicity and piece-wise uniformity of the entering angular fluxes.

The appropriateness of the current piece-wise uniformity hypothesis can be easily verified by subdividing the boundary surface of the spectrum zone in multiple pieces. This has been done in section 4.2.3.3 to analyze the spectral variations of the current entering from the lateral reflectors the upper and lower spectrum zones of a simplified PBMR-400 model.

The assumption of isotropic entering angular flux is a strong approximation and it is known that the angular flux leaving a pebble is not isotropic but forward peaked.<sup>85</sup> Nevertheless, considering the time-varying stochastic positions of the pebbles in the geometry, it has no sense to consider the angular dependence of the pebble's entering flux. In fact, as a stochastic system is described, a given pebble distribution would

represent only one of the possible physical realizations, while in this case only the statistically averaged quantities are physically meaningful. In this sense, the isotropic approximation of the angular fluxes entering the pebbles is valid.

The isotropic approximation could be weak for the entering angular fluxes from the zone's boundary surfaces corresponding with reflector walls. The reflector walls, in fact, are the only fixed surfaces in the problem and the angular dependence of the flux entering the cavity from the graphite reflectors is determined.

Next, the helium contribution is taken into account by considering a volume-averaged flux value over the spectrum zone. The source in the helium is a volume-averaged value and it is supposed isotropic. Since the neutronic effects of the presence of helium are small this should not insert a significant error in the model.

The exponential flux decrease in helium, due to neutron absorption, is modeled through the density of probability for a chord length  $l$  between pebbles, which is approximated by a Markovian distribution.

Finally, the volume-averaged flux value in helium is associated to the currents through the boundaries and pebbles surfaces by solving a neutron balance equation over the spectrum zone volume.

### 3.2.3 CP Treatment of the Multi-Pebble Geometries

In this section, a model is developed to solve a system of equations for the flux in the spherical geometries of the different pebble types plus the helium region. The details are given in Appendix C.

Each pebble type is represented by a 1D spherical geometry. The flux in the single sphere is computed through the collision probability (CP) approximation which leads to the system of equation (3.6). The double heterogeneity of the TRISO particles dispersed in the inner graphite matrix is explicitly accounted for by the APOLLO2 method based on the Askew's approximation and described in Chapter 2.

$$\begin{aligned} V_i \vec{\Phi}_i &= C_i \vec{F}_i + \vec{I}_i J_{-,i}, \\ J_{+,i} &= \vec{E}_i \vec{F}_i + T_i J_{-,i}, \end{aligned} \tag{3.6}$$

where the group index is omitted,  $i$  denotes the pebble type,  $C_i$ ,  $\vec{I}_i$ ,  $\vec{E}_i$  and  $T_i$  are the coefficients of, respectively, the collision, the incoming, the escape and the transmission probabilities,  $V_i$  contains the pebble region volumes,  $\vec{\Phi}_i$  is the vector of region-averaged fluxes,  $\vec{F}_i = \sum_{s_i} \vec{\Phi}_i + \vec{Q}_i$  and  $\vec{Q}_i$  accounts for fission and external transfers.

Thus, knowing the problem eigenvalue and the fine-group uniform and isotropic entering flux in a pebble, the fluxes in all its regions are determined by solving the first equation in (3.6). The exiting current is also determined by the second equation. It is

then possible to couple the equations referred to each pebble type with the current balance expressed in Equations (3.4) and (3.5), considering also the neutron balance in helium and introducing the average flux in helium,  $\Phi_{He}$ , to have a  $\vec{\Phi}' = \begin{bmatrix} \vec{\Phi} & \Phi_{He} \end{bmatrix}$ , where  $\vec{\Phi} = \{\vec{\Phi}_i\}$ . Coupling the systems in such a way one obtain

$$\begin{aligned} V' \vec{\Phi}' &= \tilde{C} \vec{F}' + \tilde{I} \vec{J}_-^{bd} \\ \vec{J}_+^{bd} &= \tilde{E} \vec{F}' + \tilde{T} \vec{J}_-^{bd} \end{aligned} \quad (3.7)$$

where  $V'$  contains all the region volumes in the multi-pebble geometry, including the inter-pebble helium, and  $\tilde{C}$ ,  $\tilde{I}$ ,  $\tilde{E}$  and  $\tilde{T}$  are the modified CP matrices.

We thus obtain a response system which allows computing the fluxes in all the regions of the multi-pebble geometry and the response exiting currents from the entering currents through the zone boundaries and the core  $k_{eff}$ .

### 3.2.4 Surface-to-Surface Geometrical Probabilities Modeling

All the set of surface-to-surface geometrical probabilities can be derived from the values of the  $p_{k'k}^{b,b}$  boundary-to-boundary probabilities. For details see Appendix D.

The notation introduced in section 3.2.2 is used for the surface-to-surface probabilities. For a spectrum zone,  $p_{k'k}^{b,b}$  is the probability for a neutron entering uniformly and isotropically surface  $k$  to leave the zone via surface  $k'$  without crossing any pebble. The surface-to-surface geometrical probabilities depend on the zone packing fraction and on the shape of the domain, but, because of purely geometrical reasons, they obey the reciprocity and conservation relations. Note that the reciprocity relations are valid only if the angular fluxes leaving the pebbles and entering the boundary surfaces can be considered isotropic.

Thanks to the conservation relation, the probability for a neutron entering surface  $k$  to enter the pebbles,  $p_k^b$ , can be computed as the complement to the probability for this neutron to exit the zone directly through one of its boundaries, obtaining

$$p_k^b = \sum_i p_{ik}^{p,b} = 1 - \sum_{k'} p_{k'k} \quad (3.8)$$

Then, a redistribution model has to be adopted describing the probability for this neutron to enter a given pebble type  $i$ , so that

$$p_{ik}^{p,b} = a_i p_k^b, \quad \sum_i a_i = 1. \quad (3.9)$$

In the work in Ref. 91 a *uniform* model was proposed, where this probability is proportional to the ratio of the surface of the pebbles of that type over the total surface of the pebbles contained in the zone, resulting in

$$a_i = \frac{N_i A_i}{\sum_i N_i A_i}. \quad (3.10)$$

In this thesis, a *renormalized* model is introduced to take into account that the available entering surface for the pebbles of the same type has to be reduced by the surface of the emitting pebble, whereas respecting the conservation relations of the surface-to-surface probabilities.

Knowing the boundary-to-pebble probability  $p_{ik}^{p,b}$ , one can compute the pebble-to-boundary one,  $p_{ki}^{b,p}$ , thanks to the reciprocity relation, as

$$p_{ki}^{b,p} = \frac{p_k^b A_k}{\sum_i N_i A_i}. \quad (3.11)$$

Once again, thanks to the conservation relations, one can compute the probability for a neutron exiting pebble  $i$  to enter another pebble  $j$  as the complement to the probability to exit the zone directly through its boundaries,  $\sum_k p_{k,i}^{b,p}$ .

Finally, applying the same redistribution model used previously, one obtains the pebble-to-pebble probabilities:

$$p_{ji}^{p,p} = a_j \left( 1 - \sum_k p_{k,i}^{b,p} \right). \quad (3.12)$$

### 3.2.5 Clustering

For safety analysis in pebble bed reactors, it would be interesting to study the effect of the formation of a cluster of pebbles belonging to the same family. The *uniform* and the *renormalized* models can be easily modified to represent clustering and the mathematical description of this derivation is given in Appendix E.

Assume that pebbles of type  $m$  create a cluster in a spectrum zone. This ought to result in an increase of the self pebble-to-pebble probability  $p_{m,m}^{p,p}$  and, eventually, a change of

the probabilities  $p_{k,m}^{b,p}$ . This two phenomena can be modeled introducing two clustering parameters,  $\alpha$  and  $\alpha^p$ , which, respectively, multiply  $p_{m,m}^{p,p}$  and  $\sum_k p_{k,m}^{b,p}$ .

All the other probabilities then have to be renormalized.

### 3.3 Implementation in APOLLO2

To implement the model described in section 3.2, several modules have been developed or modified in the APOLLO2 code. A short description of the functions performed by each of them is described here.

- A module was modified to create a multi-pebble geometry. This geometry is an incomplete geometry and it will be completed, with contact and volume data, when associated to a spectrum zone in the RZ geometry of the reactor.
- The module computing the collision probability matrices has been modified to treat the multi-pebble geometry, both for the  $P_{ij}$  flux solver and for the self-shielding calculations.
- A module has been created to compute the exiting currents  $\vec{J}_+^{bd}$  from the multi-pebble geometries. This is used to compute the current spectral shape factors  $\chi_k^{gG}$ .
- The  $S_N$  flux solver module has been modified in order to compute the values of the exchanged currents at the mesh interfaces in the RZ geometry.
- The module which accelerates the external iterations of the  $S_N$  flux solver has been modified to allow the calculation of the flux with an imposed  $k_{eff}$ . This is made by renormalizing, at the end of each iteration, the fission integrals by this constant eigenvalue.
- A module has been created to assign the entering currents  $\vec{J}_-^{bd}$  to all the multi-pebble geometries, once computed the flux in the RZ geometry. The total current, computed in broad groups  $G$  over every zone boundary surface, is expanded it in the fine groups  $g$  by the means of the  $\chi_k^{gG}$  associated to the neighboring spectrum zone or to the graphite reflectors (computed with radial and axial 1D  $S_N$  calculations). The module, finally, verify the convergence of the spectrum zones – RZ core iterations.



### 3.4 Analysis of Boundary-to-Boundary Geometrical Probabilities

As it is shown in Section 3.2.4, once the set of boundary-to-boundary probabilities,  $\{p_{k'k}^{b,b}\}$ , is known and a distribution model for the pebbles is assumed (the *uniform* one or the *renormalized* one), all the other geometrical probabilities needed to compute the CP coefficients for a zone are deduced.

However, in the scheme implemented in APOLLO2 the  $p_{k'k}^{b,b}$  have to be provided, for all the spectrum zones in the core, as external data, so it is necessary to evaluate them independently. The  $p_{k'k}^{b,b}$  depend on the core (cylindrical or annular) and the size, shape and position of the spectrum zone in the core. The oscillations of the packing fraction near the reflector, described in Chapter 1, increase the neutron streaming. In our model, radial and axial streaming effects, which occur in the zones in contact with the reflector, can be easily accounted for by adopting appropriate surface-surface probabilities. Indeed, the presence of a wall forces the pebbles to rearrange close to it, resulting in a locally less dense packed bed and an increase of the  $p_{k'k}^{b,b}$ .

A study for a pebble bed randomly packed in an annular core was carried out with the Monte Carlo code TRIPOLI4<sup>92</sup> to evaluate the values of the  $p_{k'k}^{b,b}$  in a typical bed and to observe the influence of the external and internal reflectors on the surface-surface probabilities.

The random pebble distribution has been taken from a data set representing the central positions of the pebbles packed in an annulus of 100 cm internal radius, 186 cm external radius and 10 m height. The pebbles have a diameter of 6 cm and the bed is characterized by an average packing fraction of 0.61, a typical value for PBRs. These data have been computed with the code PFC<sup>3D</sup><sup>93</sup> by Pebble Bed Modular Reactor Pty which kindly furnished them.<sup>94</sup> They have been obtained simulating the pebbles flow through the PBMR-400 and they represent a snapshot of the pebble positions at a given time. PFC<sup>3D</sup> is a particle flow computer program that uses the Distinct Element Method (DEM) to simulate the non-linear interaction of a large number of particles and which simulates directly the physics driving the movement of the particles. The PFC<sup>3D</sup> geometry is constructed from CAD models and captures the pebble flow paths. An illustration of such a model showing the defueling cones of the PBMR-400 is shown in Figure 3.2, where also the natural irregular packing of the pebbles is visible.<sup>95</sup> The oscillations of the packing fraction near the reflector are illustrated in Figure 3.3.

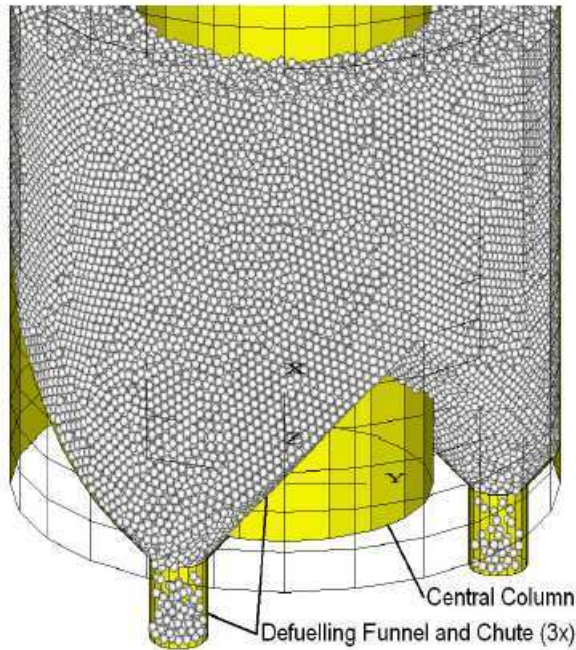


Figure 3.2: PFC<sup>3D</sup> model of the PBMR-400 showing defueling cones and chutes<sup>95</sup>

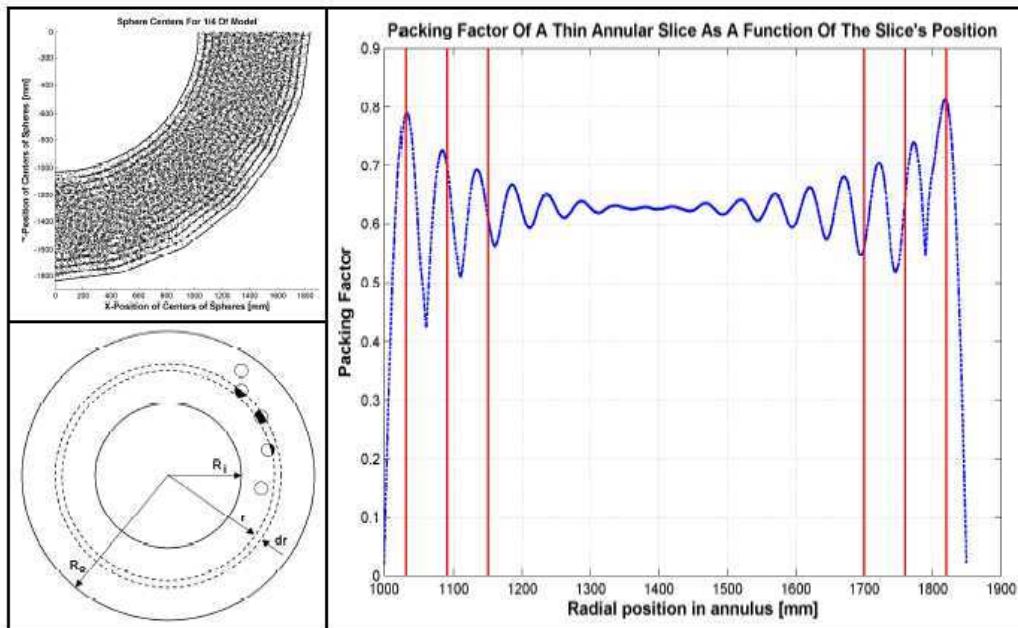


Figure 3.3: Radial oscillations of the packing fraction in the PFC<sup>3D</sup> model<sup>95</sup>

In the TRIPOLI4 geometry, zones of various sizes are positioned in different parts of the core and the surface-surface probabilities are obtained by applying a uniform and isotropic neutron source on a boundary surface and scoring only the neutrons crossing the zone without entering any pebble. To score and generate the particles, four very thin volumes are built on the external side of the boundary surfaces of the zone. In one of

them neutrons are generated uniformly and isotropically (so statistically one half of the generated weight enter the zone) and the other three are used to tally the current passing through the surfaces separating the zone volume with each of the thin volumes. To tally the neutrons which cross the bed without having any collision with the pebbles, a quasi-infinite absorber simulated by B<sub>10</sub> (which has a very high thermal absorption cross section) at very high density is used as pebble material. A mono-energetic neutron source is used and the current tallies are divided in two energy bins, one very small around the energy of the source and one for the inferior energies. So even in the unlikely event that a neutron colliding with a pebble would not be absorbed and then exits straight the zone through one of its surfaces, it would not be tallied in the higher energy bin.

The schematic of the simulated geometry is shown in Figure 3.4.

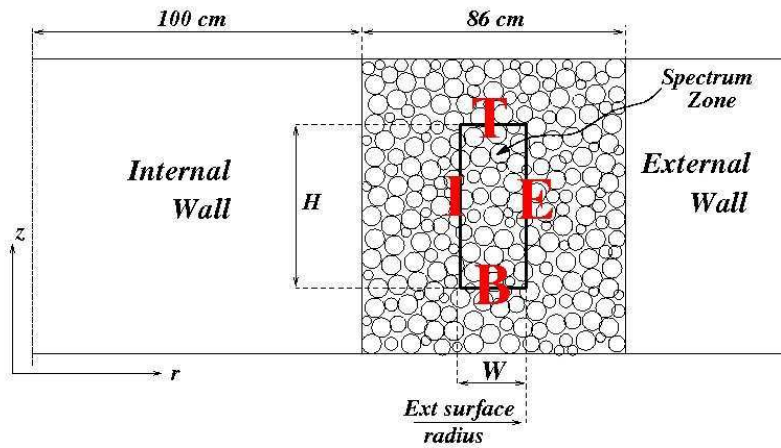


Figure 3.4: Schematic of the geometry used to analyze the  $p_{k'k}^{b,b}$  of a spectrum zone

The various zones defined for the analysis have the shape of an annulus with rectangular cross-section. It is thus possible to distinguish an External, an Internal, a Top and a Bottom surface. For example,  $p^{BT}$  is the top to bottom probability.

One can notice that each zone requires a set of 16  $p_{k'k}^{b,b}$ , but these probabilities must satisfy the reciprocity relation  $p_{k'k}^{b,b} A_k = p_{kk'}^{b,b} A_{k'}$ , so that the corresponding matrix is symmetric and the elements to be determined are reduced to 10. Moreover, the form and symmetries of the zone require that  $p^{TT} = p^{BB} = p^{II} = 0$ , and that statistically  $p^{TE} = p^{BE}$  and  $p^{TI} = p^{BI}$ , which leaves only five probabilities to be determined.

The results are shown in figures 3.5 to 3.9. In these figures  $p_{k'k}^{b,b}$  is indicated as  $k \rightarrow k'$  (e.g.  $p^{BT}$  as T  $\rightarrow$  B) and H, W and  $R_E$  denote the zone's height, width and the External surface radius, respectively (see Figure 3.4).

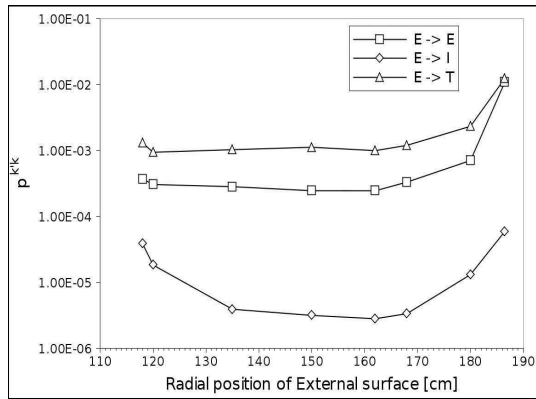


Figure 3.5:  $p_{k^l k}^{b,b}$  for  $H = 50$  cm and  $W = 18$  cm versus external radius  $R_E$  position

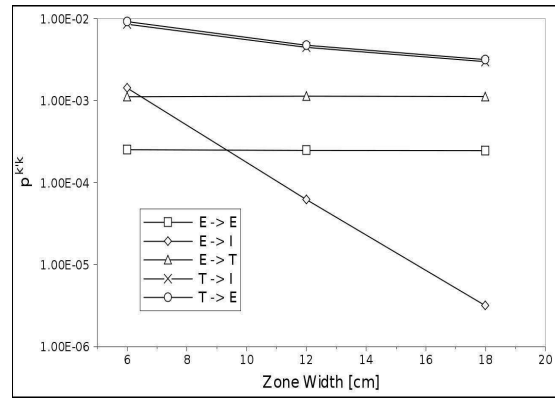


Figure 3.6:  $p_{k^l k}^{b,b}$  for  $H = 50$  cm and  $R_E = 150$  cm versus zone width  $W$

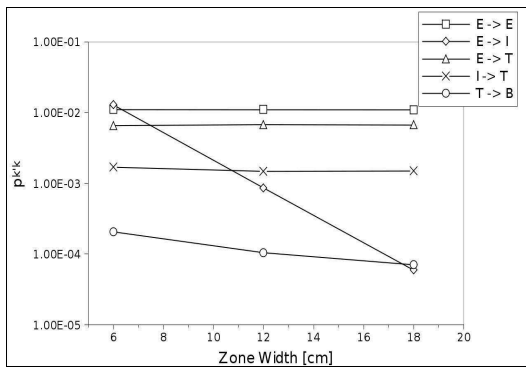


Figure 3.7:  $p_{k^l k}^{b,b}$  for  $H = 50$  cm and  $R_E = 186$  cm (external surface on the reflector wall) versus zone width  $W$

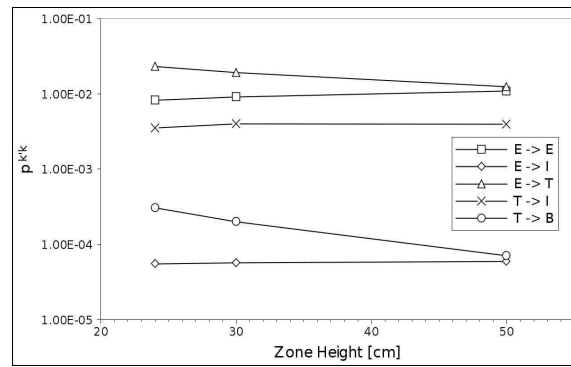


Figure 3.8:  $p_{k^l k}^{b,b}$  for  $W = 18$  cm and  $R_E = 186$  cm (external surface on the reflector wall) versus zone height  $H$

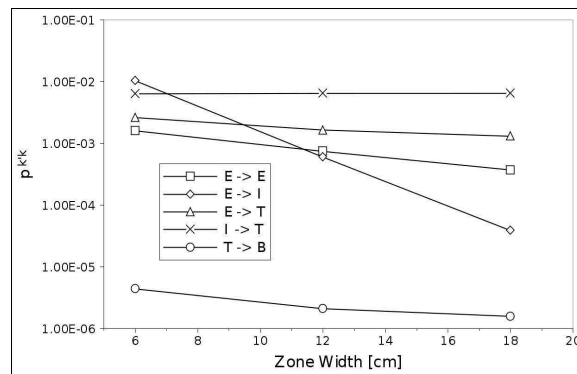


Figure 3.9:  $p_{k^l k}^{b,b}$  for  $H = 50$  cm and  $R_I = 100$  cm (internal surface on the reflector wall) versus zone width  $W$

From Figure 3.5 it is possible to evaluate the increase of the  $p_{k^l k}^{b,b}$  when the zone is close to the reflectors, starting at about 3 pebble diameters from the wall. In the internal part

of the core, these values are almost constant. In Figure 3.6, the zone has a fixed height and a variable width, with the external surface in a fixed position at a radius  $r = 150$  cm. The  $p^{BT}$  is not represented, because it is very small, when the zone is not close to a reflector (also when the height is smaller than 50 cm; tests were made decreasing the height until 20 cm). Moreover, notice that  $p^{IT} \approx p^{ET}$  even if the internal surface has a smaller area than the external one, and that  $p^{TE}$  does not increase when the width of the zone, and so the top area, increases. This means that the larger contribution to  $p_{k'k}^{b,b}$  between two perpendicular surfaces mainly occur in the corner region. From Figure 3.7 and Figure 3.9 it is noticeable that, when the zone is in contact with the reflector,  $p^{IE}$  is one order of magnitude greater than in Figure 3.6 and that  $p^{BT}$  is not negligible, showing the locally enhanced radial and axial neutron streaming close to the wall. From Figure 3.8 one can notice that  $p^{BT}$  varies slightly with the zone height and that  $p^{TE}$  increases when the height decreases, due to the fact that a larger fraction of the external surface is in the corner region with the top surface.

This analysis evaluates the  $p_{k'k}^{b,b}$ , depending on the size and position in the core of the spectrum zones, which can be used to establish a core model. However, this analysis is made in a particular core configuration, so not all the aspects needed to generalize the modeling to all possible reactor designs are included. The sensitivity of the core calculation to the values of the boundary-to-boundary probabilities have been partially investigated in section 4.2.3.4.

### 3.5 Convergence Analysis of Steady-State Reactor

A set of preliminary calculations have been made on two simplified reactor models, one cylindrical and one annular, in order to test the convergence of the developed iterative scheme. Furthermore, some quantities have been checked to ensure that they had a physical sense. The model and the results are presented in section 3.5.1 for the cylindrical model and in 3.5.2 for the annular one.

The pebbles contained in the reactors have the characteristics of the typical pebbles used in the PBMR-400, presented in Table 1.II. To have different pebble types, the flux in a single pebble surrounded by an external helium layer, with an equivalent radius of 3.54 cm corresponding to a packing fraction of 0.61, has been computed with a reflecting boundary condition. The pebble was depleted up to several burnup levels and the corresponding isotopic densities have been associated to the fuel kernels of the pebbles contained in the reactor models. The micro-particle is subdivided in 3 computational equivolumetric shells for the fuel kernel and one shell for each of the 4 coating layers, for a total of 7 shells. The fuel region of the pebble is subdivided in 3 equivolumetric computational shells and the 0.5 cm thick external graphite region in 2 shells.

It has to be noted that each different shell of the fuel region contains a proper representative micro-particle. Thus, each additional fuel region shell adds 7 (the micro-particle) + 1 (the graphite matrix) computational regions to the geometry.

An analysis of the sensitivity to the pebble spatial discretization on the power distribution in the pebble, on the core  $k_{eff}$  and on the computing time has been performed, in the case of the annular core, in section 3.5.2.1.

For both reactors, the *uniform* and the *renormalized* model for the surface-to-surface geometrical probabilities computation have been tested. They gave practically the same results (within  $\pm 1$  pcm on the core  $k_{eff}$ ) with the same computing time. So it has been decided to always use the *renormalized* model.

### 3.5.1 Cylindrical Core Containing a Single Pebble Type

In this case the core cavity is cylindrical, with 50 cm radius and 300 cm height, surrounded by upper, lower and external reflectors of 1 m thick. The core contains only pebbles with a burnup of 30000 MWd/t. The core is subdivided using 6 spectrum zones of 25 cm width and 100 cm height, each of them containing a different number of pebble types, having all the same isotopic compositions, with a packing fraction of 0.61. Even if all the pebbles have the same composition, more than one pebble type is assigned to the spectrum zones to check if the CP matrices and the surface-to-surface geometrical probabilities are well constructed. This is done by checking on the results if the symmetry of the problem is respected. The number and proportion of the pebble types in the spectrum zones are given in Table 3.I and a schematic of the reactor is shown in Figure 3.10.

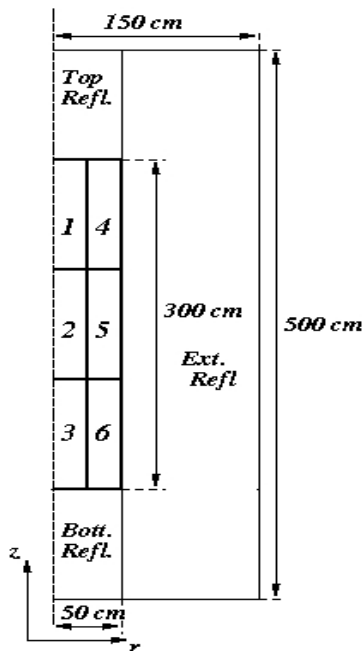


Figure 3.10: Schematics of the simulated annular reactor

Table 3.I: Fractions of pebble types in the spectrum zones

SZ 1 Nber pebble types: 2 Proportion: 10%-90%	SZ 4 Nber pebble types: 2 Proportion: 20%-80%
SZ 2 Nber pebble types: 2 Proportion: 50%-50%	SZ 5 Nber pebble types: 2 Proportion: 50%-50%
SZ 3 Nber pebble types: 3 Proportion: 10%-30%-60%	SZ 6 Nber pebble types: 1 Proportion: 100%

In this Chapter for a sake of simplicity the  $P_{ij}$  calculations of the multi-pebble geometries were done with the 172-group JEFF2.2 library, whereas the RZ core was computed with a discrete ordinates diamond differencing scheme and 8 broad-energy groups. AlThus, radial and axial 1D  $S_N$  calculations were carried out to homogenize the reflectors and to compute the spectra  $\chi_k^{gG}$  of the currents exiting them. One axial calculation is performed, to homogenize the graphite cross sections of the top and bottom reflectors, and one radial for the external reflector.

The RZ geometry is numerically subdivided radially in 20 – 20 – 40 cells, and axially in 40 – 50 – 50 – 50 – 40 cells, for a total of 18400 regions.

Spectrum zones 1, 2 and 3 contain 1058 pebbles each, while spectrum zones 4, 5 and 6 contain 3176; for a total of 12702 pebbles in the reactor. All the materials are at a temperature of 20 °C. The final value of the computed core  $k_{eff}$  was 0.97097.

Thirty spectrum zones – core iterations were performed checking how the fission integrals, the entering currents per group and per boundary surface, the homogenized total cross sections and the  $k_{eff}$  converged. Figure 3.11 shows the maximum relative differences between iterations for these core quantities. This figure illustrates the convergence of the scheme, which depends also on the convergence precisions adopted for the collision probability calculations of the spectrum zones and for the  $S_N$  calculation of the core. One can observe that the checked values asymptotically converge to a sufficiently high precision, thus showing the good convergence trend of the scheme.

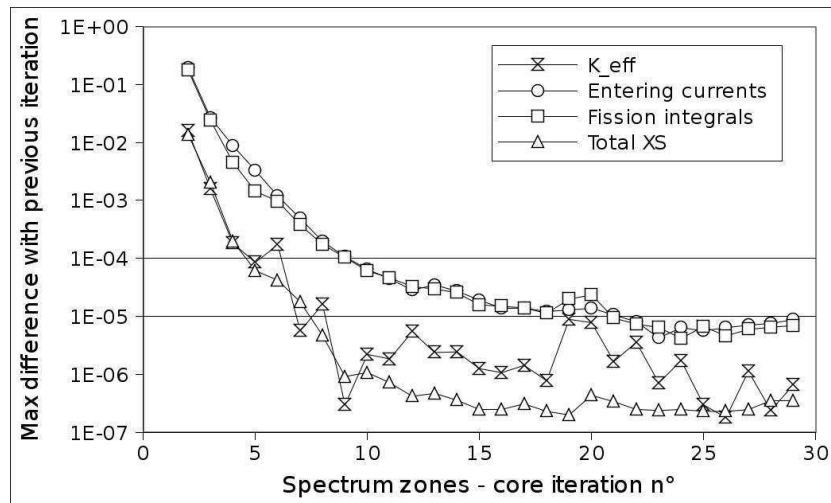


Figure 3.11: Convergence trend of the cylindrical core calculation

An analysis of the current exchanged at the zone boundaries was performed. The broad-group currents exiting the spectrum zones per boundary surface, computed in the RZ  $S_N$  core calculation, were compared with the fine-group currents  $\vec{J}_+^{bd}$  computed, with the second equation in (3.7), in the corresponding multi-pebble geometries. For this comparison, the total currents (over the energy groups) were checked. The smaller is the discrepancy between the zone's exiting currents computed in the heterogeneous and in the homogeneous problem, the better is the homogenization. Comparing the total exiting currents per contact of the spectrum zones, the maximum relative difference, between the ones computed in the multi-pebble geometry with the CP equations and the ones computed by the  $S_N$  RZ calculation of the core, is 0.4%, which is a good agreement.

Due to the symmetry of the geometry, the currents entering in the spectrum zones 1 and 3 and in the 4 and 6, respectively, have to be equal for the corresponding contacts. This means, for example, that the entering current from SZ 5 has to be the same for SZ 1 and SZ 3. Comparing the entering currents per contact surface, in the 8 broad energy groups, between the corresponding zones and contacts, the maximum relative difference is of 0.07%. This small difference indicates that the symmetry of the problem is respected. The same order of the maximum relative difference is found also when the entering currents are compared in 172 energy groups, which means that also the current spectral shape factors  $\chi_k^{gG}$ , defined in Eq. (3.3), are well defined.

### 3.5.2 Annular Core Containing Six Pebble Types

The annular core, with 1 m internal radius, 1.54 m external radius and 1.50 m height, surrounded by upper and lower reflectors of 1 m thick and by an external reflector of 0.70 m thick, contains 6 different pebble types with different burnup levels, as described in Table 3.II.

The core is subdivided in 9 spectrum zones of width 18 cm and height 50 cm each of them containing the 6 different pebble types with a packing fraction of 0.61. The proportions of the different pebble types in the spectrum zones are also given in Table 3.II and a schematic of the reactor is shown in Figure 3.12. Spectrum zones 1, 2 and 3 contain 3324 pebbles each, while spectrum zones 4, 5 and 6 contain 3870, and spectrum zones 7, 8 and 9 contain 4422; for a total of 34857 pebbles in the reactor. The RZ geometry is subdivided radially in 40 – 20 – 20 – 20 – 30 cells, and axially in 40 – 40 – 40 – 40 – 40 cells, for a total of 26000 regions. All the materials are at a temperature of 20 °C.

The details regarding the calculation scheme are the same as for the cylindrical model.



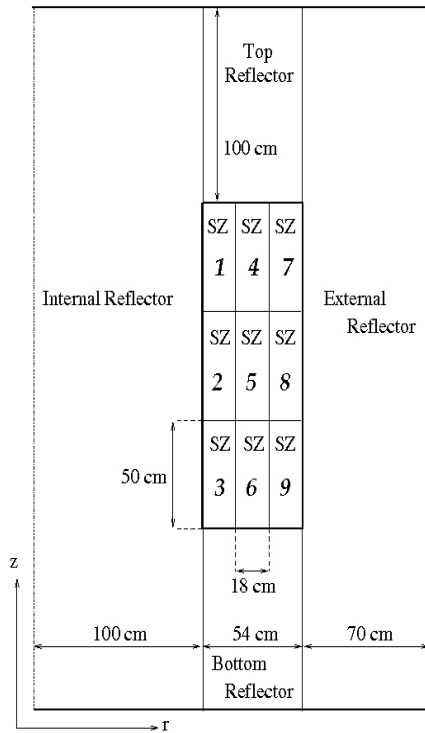


**Table 3.II: Burnup of pebble types in the core and fractions in the spectrum zones**

Pebble type	Burnup [MWd/t]	Fraction in spectrum zones		
		1, 4, 7	2, 5, 8	3, 6, 9
A	0	0.25	1/6	0.10
B	15000	0.20	1/6	0.11
C	30000	0.18	1/6	0.16
D	50000	0.16	1/6	0.18
E	75000	0.11	1/6	0.20
F	95000	0.10	1/6	0.25

**Figure 3.12: Schematics of the simulated annular reactor**

The convergence precision for the maximum relative differences from the previous iteration, were fixed at  $10^{-4}$  for the fission integrals and for the entering currents per group and per boundary surface, and at  $10^{-5}$  for the homogenized total cross sections and for the  $k_{eff}$  (for this last parameter the precision is checked on the absolute difference).

The core calculation scheme converged after 14 spectrum zones – core iterations with  $k_{eff} = 0.99944$ , with a computing time of 509s on an Intel® Xeon® 2.66 GHz processor.

The convergence trend, which is similar to the one observed for the cylindrical case of the previous section, is gathered in Figure 3.13.

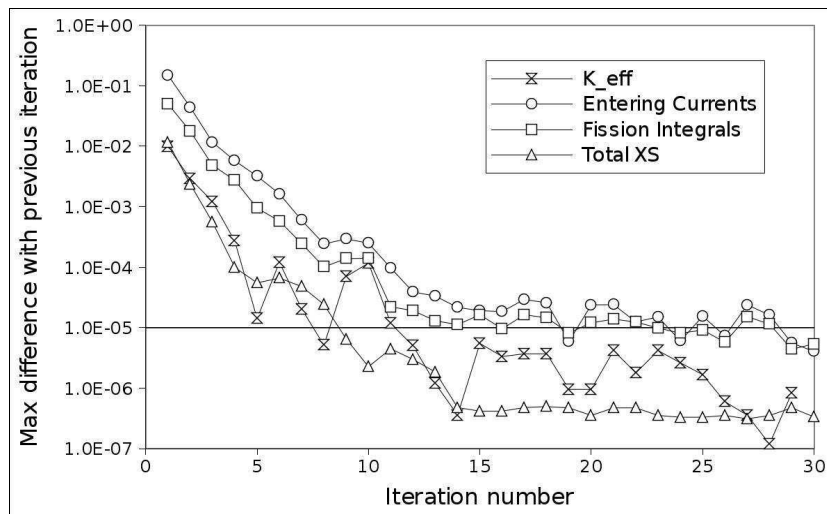


**Figure 3.13: Convergence trend of the annular core calculation**

To illustrate the spectral effects, Figure 3.14 shows the normalized currents entering spectrum zone (SZ) 8, expanded in 172 groups by the corresponding  $\chi_k^{gG}$  shape factors. The presence of the external reflector is clearly highlighted by the highly thermalized current entering the corresponding boundary. One can observe that the spectrum of the current entering from SZ5, which is located in the centre of the core, is harder than the ones from SZ7 and SZ9, which are close to the reflector.

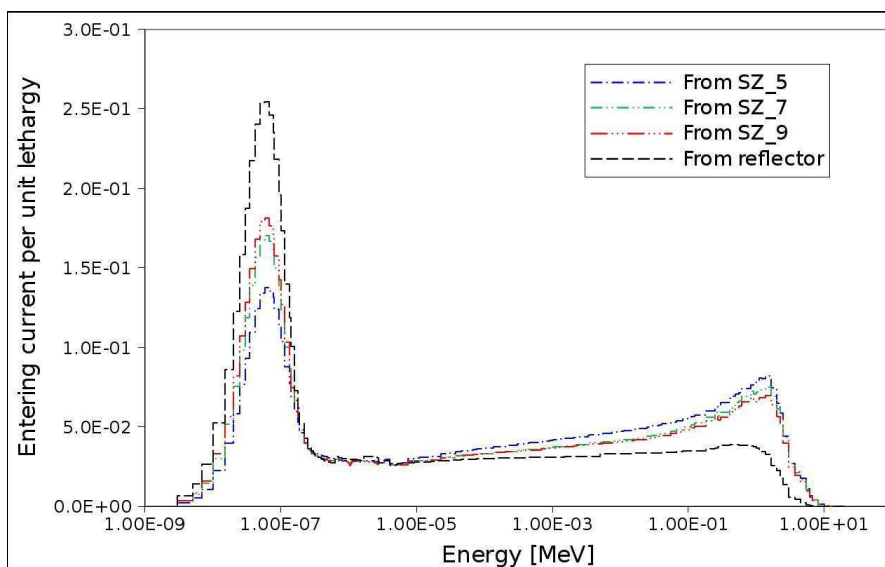


**Figure 3.14: Spectra of currents entering SZ 8**

Next, the methodology adopted by the actual codes to treat the stochastic distribution of the different pebble types in the core by using a single average composition type per spectrum zone, as explained in section 3.1, was compared to the developed method.

To do that, the same reactor was computed with the spectrum zones containing a single pebble type. This single pebble type owns the average isotopic composition of the different types contained in the zone, weighted on the number of pebbles reported in Table 3.II. The fluxes in the spectrum zone regions are still computed through the first equation in (3.1). The geometric probabilities, used to construct the CP coefficients for a spectrum zone, are deduced starting from the same set of boundary-to-boundary probabilities  $p_{k'k}^{b,b}$  as for the previous calculation. The self-shielding is also performed using the multi-pebble geometries CP matrices, so still taking into account both the intra-pebble and the extra-pebble contributions to the first-flight collision probability for a neutron generated inside a fuel kernel to collide in another kernel, of the same pebble or of a neighboring one.

The normalized fluxes in the fuel kernels of the different pebble types in SZ 5 have been compared with the one computed in the kernels of the corresponding average composition pebble. The relative differences between the spectra are shown in Figure 3.15.

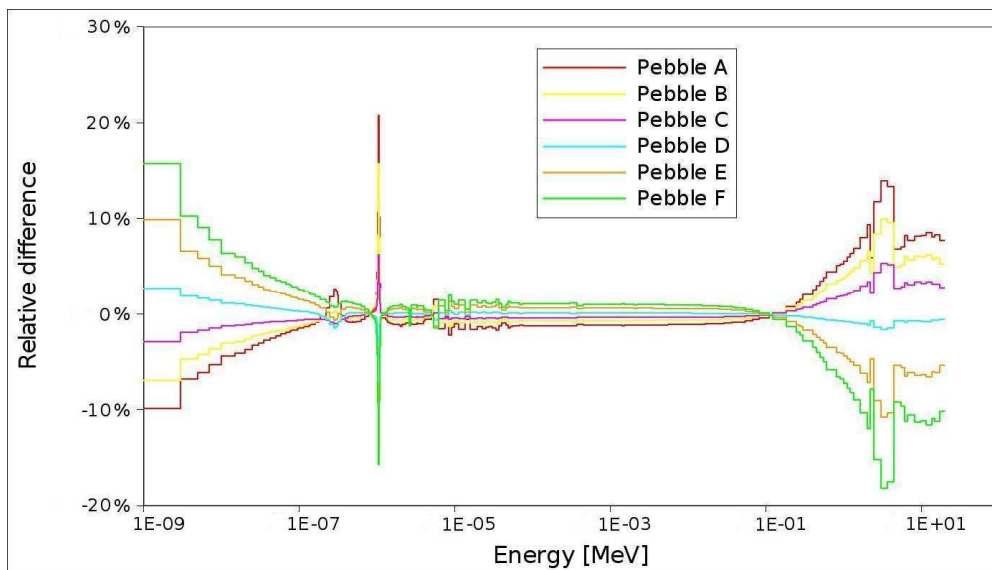


**Figure 3.15: Differences in the kernels spectra relative to the average pebble in SZ 5**

The strong effect on the spectra of the Pu240 resonance peak, at 1.06 eV, is highlighted. For pebble A, a smaller influence of Pu239 and Pu241 resonances at about 0.3 eV can be noticed. The magnitude of the differences is similar to those observed in others independent previous analyses.<sup>96,97</sup> In one of them, the spectral differences between the fluxes in the fuel kernels of different burnup pebbles and of an average composition one were analyzed by a Monte Carlo simulation.

When an average pebble is used for the flux calculation, the computed core  $k_{eff}$  is 1.00013, only 86 pcm higher than the one obtained in the first calculation. The maximum relative difference between the two cases in the total 8-group homogenized cross sections of the spectrum zones is 0.12%, in the group ranging from 0.625 to 1.67 eV, where the Pu240 resonance peak is located. The difference is rather small, and this is due to an error compensation which occurs when the 6 pebbles are averaged in a single composition pebble, as the differences in the spectra are symmetrically distributed. Also the maximum relative difference in the broad-group entering currents per boundary surface in the spectrum zones is small and does not exceed 0.57%. The effects of using the proper spectra in the different pebble types, comprehending for the calculation of the equilibrium core, are deeper investigated in session 5.4.

### 3.5.2.1 Analysis of Pebbles Spatial Discretization

In order to analyze the influence of the pebbles spatial discretization on the main physical quantities, firstly a fresh pebble surrounded by an equivalent helium layer has been computed with reflected boundary conditions. This has been done varying the number of equivolumetric shells in which the fuel kernel (*FK*) and the pebble fuel region (*FR*) have been subdivided. Two shells are for the outer graphite layer and one region for the helium.

Each fuel region shell contains a corresponding micro-particle in which is computed the average flux for all the particles contained in the shell.

A different fuel material (but with the same isotopic composition) has been assigned to each different fuel kernel shell per fuel region shell. The cross-sections of the fuel kernels are self-shielded using the flux computed in the corresponding fuel region shell. Therefore, a different set of microscopic self-shielded cross sections is assigned to each fuel material.

In the reference calculation both the fuel kernel and the fuel region are subdivided in 6 equivolumetric shells, for a total of 69 computational regions in the geometry. The computed pebble + helium  $k_{\infty}$  is of 1.52867. In Table 3.II the differences in reactivity from the reference, obtained by changing the subdivision, are shown.

**Table 3.III: Reflected pebble reactivity differences from 6 *FR* and 6 *FK* discretization**

<i>FR</i> shells	<i>FK</i> shells	Total n° regions	$\Delta\rho$ [pcm]
3	3	24 + 3	-1
3	1	18 + 3	-8
1	6	11 + 3	-2
1	3	8 + 3	-3
1	2	7 + 3	-5
1	1	6 + 3	-9

One can observe that the variations on the  $k_{\infty}$  are in any case very small and that decreasing the number of computational shells in the fuel region has a larger impact than in the fuel kernels.

For the second analysis, the same effect was evaluated on the core  $k_{eff}$ . The pebbles of the 6 different types composing the multi-pebble geometries of the cylindrical reactor were subdivided in different numbers of computational shells, as for the single fresh pebble. Here, a unique fuel material is assigned to the corresponding kernel shells of the micro-particles contained in the different fuel region shells. This means that the average of the fluxes computed over the different shells is used to self-shield each kernel shell. Thus, the fuel kernels in the different fuel region shells have all the same set of microscopic self-shielded cross sections.

The reference calculation is the one presented in section 3.5.2 with 3 shells for the kernels and 3 for the fuel regions, for a total of 157 computational regions in each multi-pebble geometry. The computed core  $k_{eff}$  was 0.99944 and the computing time 509s. The reactivity difference from the reference for the core  $k_{eff}$  and the corresponding computing times are shown in Table 3.IV for different spatial discretizations.

**Table 3.IV: Computing time and reactivity difference from the reference for the cylindrical core computed with different pebbles discretizations**

<i>FR</i> shells	<i>FK</i> shells	Total n° regions in a multi-pebble geo.	$\Delta\rho[pcm]$	Calc. time [s]
1	1	49	20	322
1	2	55	15	367
5	4	283	-24	871

One can observe that the reactivity differences have an opposite trend than the one observed for the reflected pebbles, where decreasing the number of shells induces an decrease of the  $k_{\infty}$ . Moreover on the core  $k_{eff}$  the reactivity differences are larger, but remain small. Thus, considering also the gain in computing time, it seems acceptable to use a single shell for the fuel region and one or two shells for the fuel kernel.

Next, the variation of the power density in the fuel kernels belonging to different fuel region shells, of the fresh pebble in SZ 5, have been plotted in Figure 3.16 for the 5 *FR* – 4 *FK* subdivision. The fuel regions are numbered from the internal one FR1 to the external one FR5. The power densities have been normalized to the value obtained using a single shell in the fuel region and in the fuel kernel. This last value is 0.07% smaller than the one which is obtained averaging the different power densities in the 5 *FR* – 4 *FK* case, showing that it rightly represents the average power density in the fuel kernels of the pebble.

Moreover, it can be noticed that the variation of the power densities in the different fuel kernel shells are comprised within  $\pm 2\%$  from the average value.

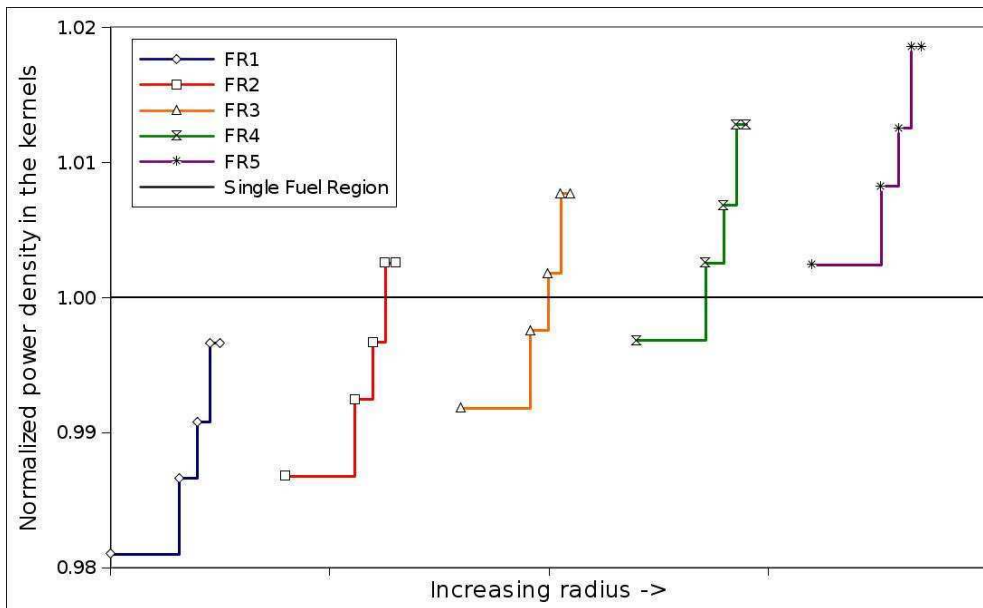


**Figure 3.16: Normalized power densities in the fresh pebble kernels in SZ5**

As to conclude, a study was performed depleting a reflected pebble up to 150000 MWd/t and varying the number of shells in which the fuel kernels and the pebble fuel region were subdivided. Each shell corresponded to a different depleting material, so that the flux variation over the kernel and the fuel region radii was correlated to the differences on the nuclide concentrations computed in the various shells. Moreover, the impact on the  $k_{\infty}$  at various burnup steps was also checked.

A first set of calculations was realized depleting the reflected micro-particle geometry. In the reference calculation the  $UO_2$  kernel was subdivided in 8 shells. When using a single material for the kernel, the differences in reactivity did not exceed 46 pcm up to 150000 MWd/t, since the relative differences on the main nuclides concentrations stayed below 0.5%.

A second set of calculations was realized depleting the reflected pebble geometry, with the  $UO_2$  kernels subdivided in 2 shells and decreasing the number of fuel region shells starting from 10 as a reference. When using a single depleting material for the fuel region, the differences in reactivity did not exceed 13 pcm up to 150000 MWd/t, since the relative differences on the main nuclides concentrations stayed below 0.1%.

These calculations showed that considering a single depleting material for the  $UO_2$  kernels has a larger impact, on the  $k_{\infty}$  and on the computed nuclide concentrations, than for the pebble fuel region. Nevertheless, the discrepancies with the reference calculations resulted quite small. Thus, in the calculations performed in Chapter 5 to compute the equilibrium core a single depleting material will be used both for the fuel kernel and for the pebble fuel region.

### 3.5.2.2 Clustering Simulations

A cluster of a pebble type in a zone is intended as a variation of the uniform stochastic distribution such as the total number of pebbles of that type remains constant but a fraction of them are clumped around a given point of the core.

Using the clustering model described in section 2.3.5, a cluster of 50 pebbles of type A and F have been simulated in SZ 5. The spectrum zone contains 645 pebbles of each type.

Thus, the pebble type which cluster has been divided in two separated groups: a first one composed by 595 pebbles and a second one composed by 50 pebbles. The self pebble-to-pebble probability,  $p_{mm}$ , of this last 50-pebble group has been increased by a factor  $\alpha$  of 10 or 100. It is difficult to evaluate what is the physical equivalent to be associated to these factors, but the main objective is to determine the trend of the power density in the fuel kernels while the clustering factor  $\alpha$  increases.

The parameter  $\alpha^p$  is assumed equal to 1.

Considering the packing fraction of 0.61, a cluster of 50 pebbles around a point in the core is contained inside an equivalent sphere of about 13 cm radius. Of course, outside this imaginary sphere, the fraction of this pebble type over the total number of pebbles will be reduced, compared to the not-clustered case.

The total reactor power has been normalized at 0.1 KW/g of initial heavy atoms in the fuel. This value has been computed roughly considering that in the PBMR-400 the core power is 400 MW whereas the core is filled with about 400000 pebbles and each fresh pebble contains 9 g of uranium.

The average power densities in the fuel kernels of the different pebble types in SZ 5 are shown in Table 3.V for a cluster of 50 type A pebbles and in Table 3.VI for 50 type F pebbles. The presence of these clusters has not impacted the core  $k_{eff}$ .

**Table 3.V: Power densities in the fuel kernels in SZ5 and rel. diff. with a cluster of 50 fresh pebbles**

Pebble Type	Average power density [KW /cm <sup>3</sup> ]	Rel. diff. from uniform mix	
	$\alpha = 1$	$\alpha = 10$	$\alpha = 100$
Clust. A (50)	1.165	-0.067%	-1.918%
A (595)	1.165	0.001%	0.026%
B	1.061	0.000%	0.024%
C	0.948	0.000%	0.022%
D	0.792	0.000%	0.022%
E	0.596	0.000%	0.019%
F	0.445	0.000%	0.018%

**Table 3.VI: Power densities in the fuel kernels in SZ5 and rel. diff. with a cluster of 50 most burnt pebbles**

Pebble Type	Average power density [KW /cm <sup>3</sup> ]	Rel. diff. from uniform mix	
	$\alpha = 1$	$\alpha = 10$	$\alpha = 100$
A	1.165	0.000%	-0.032%
B	1.061	-0.002%	-0.032%
C	0.948	-0.002%	-0.030%
D	0.792	0.000%	-0.028%
E	0.596	0.000%	-0.030%
F (595)	0.445	0.000%	-0.029%
Clust. F (50)	0.445	0.079%	2.582%

The results show that when the cluster is composed of fresh type pebbles, the average power density in the clustered pebbles decreases while the clustering factor  $\alpha$  increases. The opposite trend is observed when the cluster is composed by the most depleted pebbles. This seems apparently opposite to the first intuitive idea.

In previous works,<sup>96,98</sup> a fresh pebble clustering in the core has always been thought as been able to create a power peaking in the fuel kernels of the clustered pebbles. Nevertheless, in these studies the clustering in a spectrum zone has always been simulated increasing the fraction of fresh pebbles over the total number of pebbles contained in the zone (for example considering a zone containing only fresh pebbles). In this case, it is obvious that the power density in the whole zone increases, as the average U<sup>235</sup> atomic density in the zone increases.

However in our approach to clustering, the average U<sup>235</sup> atomic density in the zone remains constant and the total number of pebbles of each type does not vary. But the positions of the pebbles inside the spectrum zone vary from the uniform mix, increasing  $\alpha$ , toward a configuration where 50 pebbles of the same type are all grouped together. 50 grouped pebbles, with a packing fraction of 0.61, are contained inside a virtual 13 cm radius sphere.

The trend observed in the calculation could be reasonable while considering that the neutron mean migration length, which is the root-mean-square distance travelled by a neutron between his birth with a fission and its absorption in the thermal range,<sup>99</sup> in a typical pebble bed is on the order of 80 cm.<sup>100</sup>

As a consequence, the 50 fresh pebbles, grouped inside the 13 cm radius sphere, will mostly probably never experience a fission from a neutron which is born inside this



sphere. They would rather act as a higher density neutron source, compared to the uniform mix, concentrated in this sphere and sending more neutrons to the neighboring pebbles. This would justify the increase of the average power density in the fuel kernels of the pebble types which are not clustered.

In the same way, when the most depleted pebbles group, the surrounding pebbles will be in average fresher than in the uniform mix. Thus, the clustered pebbles will act as a concentrated neutron sink, resulting in an increase of the power density in their kernels with a decrease in the neighboring pebbles' kernels.

These observations are only hypotheses and should be confirmed by a verification process with some reference Monte Carlo simulations. Unfortunately, in the time period of this thesis it was not possible to perform this verification. Thus, no other clustering simulations will be performed in the next Chapters, as the results of the developed model have still to be verified.

### **3.6 Conclusions to the Chapter**

In this Chapter the new iterative homogenization technique, developed in APOLLO2, for neutronic computation of pebble bed reactors has been presented.

As opposed to previous methods, where a single volume-averaged composition pebble per spectrum zone is used for homogenization purposes, our technique includes the effects of local spectral differences in the self-shielding and homogenization processes.

In the majority of the existing codes the pebble double-heterogeneity is accounted for by the Nordheim's Dancoff corrected escape probability. By using a Dancoff factor, it has to be considered that the extra-pebble contribution comes from pebbles which are of the same type as the one in which self-shielding is performed. On the contrary, in the APOLLO2 developed method, self-shielding is performed over the heterogeneous reflected multi-pebble geometry, thus considering explicitly the different pebble types.

The core is decomposed into several spectrum zones, each one of which comprises a stochastic distribution of pebbles with different burnups. Each zone is associated to a multi-pebble geometry where the pebbles are grouped into different burnup types and a collision probability description is derived by introducing a "macro-stochastic" model. This model describes the neutron exchanges between pebbles of different types and between pebbles and zone surfaces. These exchanges are accounted for by introducing a set of surface-to-surface geometrical probabilities. By modifying these probabilities, it is possible to model clustering phenomena.

The core is computed with a low-order transport operator and, at each iteration, every spectrum zone is independently homogenized by solving a fixed  $k_{eff}$  source problem, where the  $k_{eff}$  and the entering currents are obtained from the previous core calculation. The convergence of the scheme has been verified and the results obtained for various configurations are satisfactory.

The boundary-to-boundary probabilities have been evaluated by Monte Carlo simulations of the bed of pebbles in the PBMR-400 core, with the pebbles individually positioned by a Discrete Element Method code. The enhanced neutron streaming close to the reflector walls is considered, by the probabilities variation, both in the self-shielding and in the homogenization processes.

The results of the test calculations show that the use of an average composition pebble results in rather small bias in  $k_{eff}$  but discernible flux differences.

An analysis of the pebbles spatial discretization showed that the average power density value computed with a single shell both in the fuel kernels and in the pebble fuel region is sufficiently precise and representative of the whole pebble's micro-particles. Moreover, while depleting a reflected pebble with a single material both for the  $UO_2$  kernels and for the pebble fuel region, the discrepancies on the resulting  $k_{\infty}$  and nuclide concentrations with a finer subdivided model are small.

Finally, clustering simulations shown that the power density in the fuel kernels of 50 fresh clustered pebbles should be smaller than in the not-clustered case. Nevertheless, this trend still needs to be verified by a comparison with reference Monte Carlo simulations.

To conclude the Chapter, the methodologies used by the presently existing codes to solve the main computational steps of the neutronic modeling are summarized in and they are compared to the APOLLO2 method.

It is to note that a part from APOLLO2, all the existing codes use diffusion as full-core flux solver and the average composition pebble approximation to describe with a single cell the different pebble types comprised in the zone.

**Table 3.VII: Main features of presently used codes for PBRs neutronic and developed APOLLO2 model**

	<i>Homogenization technique</i>	<i>Geometry for homog. XS generation</i>	<i>Self-shielding (s.-s.)</i>	<i>Double – heterogeneity of microparticles</i>	<i>Flux solver for homog. XS generation</i>	<i>Core leakage</i>
<b>VSOP</b>	Iterative. Recovering buckling and albedo terms from the full-core calc. 68g in GAM, 30g in THERMOS, 4G in CITATION	Infinite medium in GAM. Single reflected pebble with homogeneous fuel region in THERMOS	Effective parameters for the unresolved resonances of $Th^{232}$ and $U^{238}$ . Nordheim integral treatment for other resonances	Dancoff factors	$U^{235}$ fission source 68g P1 slowing down in GAM. 30g $P_{ij}$ in THERMOS	Broad-group buckling terms in GAM (3 G). 1G albedo term in THERMOS

	<i>Homogenization technique</i>	<i>Geometry for homog. XS generation</i>	<i>Self-shielding (s.-s.)</i>	<i>Double – heterogeneity of microparticles</i>	<i>Flux solver for homog. XS generation</i>	<i>Core leakage</i>
<b>PANTHERMIX</b>	Multi-parameterized XS library. By multi-scale approach: 172g then 16g then 2G in PANTHER	equivalent infinite cylinder containing microparticles + 1D radial and axial cuts	P <sub>ij</sub> subgroup fluxes for main nuclides. $\sigma_b$ in equivalent slab for other nuclides	Askew's approximation for P <sub>ij</sub> calculations (flux and main nuclides s.-s.). Bende's Dancoff factor for other nuclides s.-s.	172g P <sub>ij</sub> for equivalent cylinder + 16g S <sub>N</sub> for 1D reactor-cuts	16g 1D axial and radial reactor-cuts S <sub>N</sub> calculations
<b>DALTON-THERMIX</b>	Multi-parameterized XS library. By multi-scale approach. 172g, no collapsing till the end, then 9G in DALTON	Successive 1D S <sub>N</sub> calculations TRISO + Pebble + radial cuts	Bondarenko method for unresolved resonances. Nordheim integral treatment for resolved ones	Bende's Dancoff factor	172g S <sub>N</sub>	172g 1D axial and radial reactor-cuts S <sub>N</sub> calculations + axial buckling from reactor height
<b>SCALE</b>	238g XS library. Energy collapsing from point-wise to 238g Monte Carlo full-core calc.	Successive 1D S <sub>N</sub> calculations TRISO + Pebble	Bondarenko method for unresolved resonances. 1D SN point-wise calc. for resolved resonance	Point-wise flux disadvantage factors	238g S <sub>N</sub>	Not accounted for
<b>PEBBED + MICROX</b>	Iterative, with SHC method. Fine-group data pre-computed, function of U <sup>235</sup> density. 193g then collapsed in 6G in PEBBED	1D two-region cells TRISO + Pebble	Bondarenko method for unresolved resonances. Slowing-down B <sub>1</sub> calculation using point-wise cross section in resolved res.	Bende's Dancoff factor in s.-s. + Point-wise flux disadvantage factors	193g slowing-down B <sub>1</sub> or B <sub>3</sub>	Broad-group buckling terms (6G) from core calc.
<b>PEBBED + COMBINE</b>	Iterative. By multi-scale approach. 167g then 99g then 16G in PEBBED	167 B <sub>1</sub> or B <sub>3</sub> 1D two-region cells TRISO + Pebble + 99g 1D S <sub>N</sub> radial cuts	Bondarenko method for unresolved resonances. Nordheim integral treatment for resolved ones	Spatially varying Dancoff factor computed by ray-tracing code PEBDAN.	167g slowing-down (B <sub>1</sub> or B <sub>3</sub> ) + 99g S <sub>N</sub> for 1D reactor-cuts	1D radial cuts + 16G (presently only 1G) buckling terms from core calc.

	<i>Homogenization technique</i>	<i>Geometry for homog. XS generation</i>	<i>Self-shielding (s.-s.)</i>	<i>Double – heterogeneity of microparticles</i>	<i>Flux solver for homog. XS generation</i>	<i>Core leakage</i>
<b>APOLLO2</b>	Iterative. Recovering entering currents and core $k_{eff}$ from core calc. 281g for multi-pebble geom. then 13G or 26G in APOLLO2 RZ $S_N$	Multi-pebble geom.: 1D spheres containing microparticles. Different pebble types coupled through exchanged currents	$P_{ij}$ flux calculation on the multi-pebble geom. TR resonance treatment with heterogeneous-homogeneous equivalence.	Askew's approximation. Spatial variation of leakage accounted by $p_{k'k}^{b,b}$ computed by ray-tracing	281g $P_{ij}$	281g reconstructed currents per contact entering the SZ boundary surfaces and imposed $k_{eff}$



<b>4</b>	<b>Verification and Validation .....</b>	<b>79</b>
4.1	Verification of APOLLO2 Double-Heterogeneity Treatment.....	81
4.2	Verification of the Developed Method by Monte Carlo Simulations .....	82
4.2.1	TRIPOLI4 Reactor Model .....	83
4.2.2	APOLLO2 Reactor Model.....	89
4.2.3	Comparison of the Results for Different TRIPOLI4 Cores.....	91
4.2.3.1	Homogeneous Core .....	94
4.2.3.2	Heterogeneous Core with Homogeneous Spectrum Zones .....	95
4.2.3.3	Single Type Individually Positioned Pebbles.....	99
4.2.3.3.1	Analysis of the Entering Currents from Reflectors ...	104
4.2.3.3.2	Evaluation of 281-group P1 XS in T4.....	108
4.2.3.4	Multiple Types Individually Positioned Pebbles.....	111
4.2.3.4.1	Reaction Rates per Pebble Type.....	113
4.2.3.4.2	Analysis of the Computing time.....	115
4.2.3.4.3	Sensitivity Analysis to $pkf$ and $p_{k'k}^{b,b}$ Variations.....	117
4.3	Validation on the HTR-10 First Criticality .....	120
4.3.1	APOLLO2 Reactor Model and Results.....	124
4.4	Conclusions to the Chapter.....	127

## 4 Verification and Validation

Verification (code to code comparisons including comparisons to reference modeling) and validation (comparison to experimental data) are indispensable processes to assess the confidence in the results provided by a calculation scheme.

The codes used for neutronic simulations of nuclear reactors are based on both deterministic methods and stochastic Monte Carlo method. The Monte Carlo codes are generally regarded as the reference tools to reproduce the physics of a neutron transport problem and so they are taken as a reference for the deterministic codes. The verification process of a deterministic transport code consists in evaluating the methodological biases on some important core parameters (effective multiplication factor, neutron flux and reaction rate distribution, control rod worth, temperature coefficients, etc.)<sup>101</sup> with the reference results (taking into account their uncertainties) obtained with a continuous energy Monte Carlo simulation. In a deterministic code several quantities are discretized (energy groups, angular directions, spatial mesh) and several precisions are imposed to check the convergence of the iterative methods used. It is intended that finer the discretization is and lower the convergence precisions are, better the deterministic results will fit the reference ones (as long as the multigroup cross sections used in the deterministic simulation are physically representative of the problem). Nevertheless, the computing time necessary for the calculation will increase.

As the industrial interest in a code is also strongly connected with the requested time for a calculation, with clearly a preference for faster codes at equivalent precision, the other interest of the numerical verification is to find the best approximations that can be adopted keeping the degradation of the results to an acceptable level.

It has to be noticed here that the Monte Carlo simulation provides the best physical description of the problem when the geometry and the composition of the core are well known. But this is not always the case. For example Monte Carlo can not be used, up to now, as a reference for the depletion problems. Also in the case of pebble bed reactors its validity as the best method to represent the physical problem is questionable, as both fuel particles and fuel pebbles are stochastically distributed inside the core.

In the validation process, the calculation results have to be compared with the data obtained in an experimental facility. The errors which can then be observed in a neutron transport code results are mainly due to two contributions: the physical model adopted and the cross-sections libraries used for the calculations. To evaluate the reliability of cross sections libraries, a Monte Carlo simulation of the experimental facility is performed with a great number of histories, in order to reduce the variance, so that the residual error can be attributed to the errors on the cross sections. International benchmarks are generally organized to compare the results of different codes with the experimental data obtained by some facility, where the cross sections sets are provided by the organizer.

For the verification process carried on in this Chapter, the Monte Carlo simulations have been performed with the CEA code TRIPOLI4<sup>92</sup> which simulates the 3D transport of neutrons, photons, electrons and positrons. TRIPOLI4 uses both pointwise cross-sections produced with the NJOY processing code system or self-shielded homogenized multigroup cross-sections produced by lattice calculations as APOLLO2. It addresses radiation shielding and neutronic (subcritical and critical) problems.

A common realistic reactor model is set up for TRIPOLI4 and APOLLO2 and the details of both of them are given in sections 4.2.1 and 4.2.2 respectively.

The progressive verification of the developed iterative core calculation method, exposed in section 3.2, is performed comparing the results of the APOLLO2 calculations to the corresponding TRIPOLI4 simulations of four different types of core. This is done to progressively analyze the discrepancies in the results, starting from a simplified homogeneous core up to a core containing a random mixture of different type pebbles individually positioned in the Monte Carlo geometry. These different verification steps are presented in section 4.2.3.

Before presenting the verification on the full reactor calculations, the results of several studies aiming at verifying the double-heterogeneity treatment of APOLLO2 with Monte Carlo references are presented in section 4.1.

For the validation of the developed method in APOLLO2, the calculation of the critical bed height in the Chinese experimental reactor HTR-10 was performed and will be

presented in section 4.3. Clearly, it does not represent an extensive and exhaustive validation process for the developed method as should be done if a nuclear industry would use it to design a commercial reactor. Nevertheless, it can provide a preliminary demonstration on the reliability of the method.

#### 4.1 Verification of APOLLO2 Double-Heterogeneity Treatment

The first part of the analysis is devoted to the verification of the double-heterogeneity modeling in APOLLO2 in the case of a typical pebble used in PBRs. Using this treatment it is possible to compute the flux, and so the reaction rates, inside the kernels of the TRISO particles stochastically dispersed in the graphite matrix of the inner fuel region, derived from the entering current through the pebble.

To verify this treatment we will refer in this thesis to an internship work conducted in our lab and we will report its main conclusions. The pebble modeled is of the type used in an irradiation experiment conducted in the Dutch HFR reactor with an external diameter of 6 cm and the diameter of the internal fuel region of 4.4 cm. The pebble contains 9560 TRISO particles with  $\text{UO}_2$  fuel kernels of 500  $\mu\text{m}$  in diameter enriched at 16.75%.

A white boundary condition is adopted on the external surface of the pebble and the infinite multiplication factor is computed. The fuel pebble collision probabilities calculation in APOLLO2, including the double heterogeneity model, is performed using the 281-group SHEM energy mesh<sup>36</sup> and JEFF-3.1.1 library<sup>102</sup>. In the TRIPOLI4 model continuous energy cross sections are used and the geometry is modeled using both a random distribution for the microparticles (being the most realistic one) and a cubic lattice. For the cubic lattice the pitch is adapted in order to keep the same number of particles but also to avoid cutting particles on the border of the inner fuel region zone (by removing the particles in those positions). This is done to improve the comparison with the random distribution, which could not be satisfactory otherwise.<sup>103</sup>

Calculations are performed for different uniform temperatures, of 27 °C and 1250 °C, and at different burnups of 0, 60000 and 120000 MWd/t (computed with the reflected pebble).

The reference results are the one obtained in TRIPOLI4 with the random grain distribution, where the relative  $k_{inf}$  are computed with a variance  $\sigma$  on the order of 40 pcm in the different calculations.

The comparison shows that the  $k_{inf}$  obtained with the lattice distribution in TRIPOLI4 are within  $3\sigma$ . In the same way, the results obtained by the APOLLO2 calculations are always within  $3\sigma$ .

The double heterogeneity treatment of the TRISO particles in APOLLO2 fits well with the reference results for pebble configuration (fuel content and enrichment) that will be encountered in the core model.

A supplementary verification with a TRIPOLI4 comparison of the APOLLO2 double heterogeneity treatment in a prismatic HTR fuel was made in Ref. 104. In this study the



influence of the grain size was analyzed and a slightly worsening of the relative differences with reference was observed for particles diameter greater than 400  $\mu\text{m}$ . Finally, the homogenization with APOLLO2 of the pebble fuel region was used to model the first criticality of the HTR-10.<sup>105</sup> In this work the authors use TRIPOLI4 to model the geometry of the reactor with a lattice description of the pebbles inside the core. The fuel region of the pebbles is represented both via a lattice of microparticles both by a set of multigroup cross sections (172 energy groups) obtained from the APOLLO2 calculations. For this last configuration, a 1D calculation of a pebble containing the microparticles in the fuel region is performed with white boundary condition and critical buckling. The core  $k_{eff}$  computed in TRIPOLI4, using the APOLLO2 libraries, is very close to the one calculated using the detailed description of the microparticles in a regular lattice and with continuous energy cross sections. The relative small effect on the  $k_{eff}$  confirmed on the one hand the appropriate treatment of the double heterogeneity in APOLLO2 and on the other hand that the calculation scheme using multigroup cross sections in the fuel region appears as a reliable approach.

#### 4.2 Verification of the Developed Method by Monte Carlo Simulations

A common reactor model was set up in order to compare the results issued from the iterative core calculation scheme developed in APOLLO2, and exposed in section 3.2, with the ones obtained with TRIPOLI4 simulations. The details of the TRIPOLI4 model are given in section 4.2.1, and the ones of the APOLLO2 model in section 4.2.2.

**Table 4.I List of test cases computed for the verification**

<p>SZs containing a homogeneous material both in T4 and in AP2. Standard RZ <math>S_N</math> core calculation in AP2. Full cylindrical geometry in T4.</p>	<p>SZs containing individual pebbles in T4 or associated multi-pebble geometries in AP2. 281-group homogenized pebble fuel region. <math>\frac{1}{4}</math> cylindrical geometry in T4</p>
<p><b>1)</b> Homogeneous core: from a single 50000 MWd/t pebble homogenized. 8-group XS in T4 and in AP2. Fine and broad RZ spatial meshes. Cold core conditions.</p> <p><b>2)</b> Heterogeneous core: diverse SZ materials from homogenizing reflected AP2 multi-pebble geometries. 281-group P1 T4 XS. 8, 13, 26 and 281 group XS in AP2 RZ <math>S_N</math>. Diffusion tested with CRONOS2. Cold core conditions.</p>	<p><b>3)</b> One pebble type of 50000 MWd/t in the whole core. Continuous or 281-group P1 and P0* T4 graphite XS. 8, 13, 26 and 281 group XS in AP2 RZ <math>S_N</math>. Cold and hot core conditions.</p> <p><b>4)</b> 3 random mixtures of 6 pebble types. Diverse pebble types fractions and reaction rates per type in each SZ. 281-group P1 T4 XS. 13 and 26 group XS in AP2 RZ <math>S_N</math>. <math>S_8</math> and <math>S_4</math> angular quadrature. Cold and hot core conditions</p>

In order to progressively verify the results of the APOLLO2 (AP2) calculations against the ones obtained with the corresponding TRIPOLI4 (T4) simulations, four different types of core are considered and analyzed in both codes.

The characteristics of each of them are resumed in Table 4.I and are deeper explained in section 4.2.3.

An important limitation for the Monte Carlo geometry build-up is that the number of volumes to be described is huge due to the amount of pebbles in the core, in the order of  $10^5$ , and it is not possible to describe all the volumes if the microparticles are explicitly defined inside each pebble. This is due both to memory requirements and computing time. It is consequently not possible to model the core geometry taking into account the double heterogeneity of the fuel pebbles.

Nevertheless, as the capability of the double-heterogeneity treatment of APOLLO2 to properly describe the presence of the TRISO particles inside the pebbles was verified in section 4.1, it will be possible to assume an equivalent homogenized fuel region material in the inner fuel zone. Thus, the pebble geometrical description will consist, both in TRIPOLI4 and in APOLLO2 models, in two homogenous regions, the outer graphite shell and the inner fuel region.

This will verify the whole interactive core calculation scheme, allowing to compare both local quantities such as the power distribution between the pebbles of different types in a given spectrum zone, and the integral ones, as the core  $k_{eff}$  and neutron leakage.

In order to assign a homogeneous material to the pebbles inner fuel region, a single pebble, with the properties specified in table 1.II, was computed with APOLLO2 using an external layer of helium, up to the diameter of 3.537 cm to account for an average packing fraction of 0.61, with white boundary conditions and using the 281-group SHEM JEFF-3.1.1 library. A depletion calculation was carried on up to the value of 95000 MWd/t and a set of fine groups P1 anisotropy cross sections were stored at the burnups of 0, 15000, 30000, 50000, 75000 and 95000 MWd/t. These cross sections were used to describe the inner fuel region of the pebbles both in APOLLO2 and in TRIPOLI4. The self-shielding was performed on the full geometry (pebble + extra-region including helium) thus accounting for the interpebble leakage. The pebble flux is computed with the collision probabilities method, accounting for the double heterogeneity of the micro-particles, and self-shielding is repeated at each depletion substep.

#### **4.2.1 TRIPOLI4 Reactor Model**

In order to describe the geometry of the problem the ROOT program<sup>106</sup> was used. The ROOT system is developed by CERN and provides a set of object oriented frameworks with all the functionalities to handle and analyze large amounts of data in an efficient

way. Using ROOT it is possible to easily describe a complex geometry which can be read afterwards from TRIPOLI4.

The advantage of using the ROOT geometry constructor is that it is possible to create and place geometrical objects using logical operators, loops, subroutines and to read data from external files. These functionalities were very useful for constructing the pebble bed itself, as it was possible to place each pebble individually and to assign them a specific material for the fuel region to represent different burnups.

The individual positions of the pebbles are deduced from the data set provided by PBMR Pty Ltd<sup>94</sup> which has already been used for the calculation of the  $p_{k/k}^{b,b}$  boundary-to-boundary probabilities, as explained in section 3.4. This guarantees consistency between the data that are used to describe the multi-pebble geometry in APOLLO2 and the effective pebble distribution in the core of the TRIPOLI4 model.

Besides the motivation of the coherence of the  $p_{k/k}^{b,b}$ , modeling the core with the pebble positions individually described allows taking properly into account the effects of packing redistribution close to the wall, which has been described in section 1.4. This effect, which enhances neutron streaming close to the reflectors, would not be accounted if a lattice was used to model the bed. The lattice approach is the mostly used one when PBRs are modeled with a Monte Carlo code.<sup>107-110</sup> In this case, the pebbles are positioned as the elements of a lattice, which varies from body-centered cubic, face-centered-cubic, hexagonal close-packed, etc., and the core cavity is filled with this lattice. Obviously, this approach has several limitations: the packing fraction remains constant in the whole core and does not decrease close to the reflectors, the streaming effect close to reflectors is no longer represented, several pebbles of the lattice which are intersected by the reflectors surfaces are un-physically cut. The advantage of the lattice description compared to the pebbles individually positioned is the great gain in computational effort needed. While in a random positioned geometry all the intersections with all the surfaces of the geometry have to be computed before transporting a neutron along a straight line, in a lattice is already known that the closest volumes are the ones in the adjacent element of the lattice. This elementary observation is the one which makes simulations in a lattice structure much faster than in an unstructured geometry. As a consequence, the use of ROOT to build the geometry gives another advantage compared with the standard TRIPOLI4 geometry. When building the geometry, ROOT creates other additional structures, called voxels, which are a sort of bounding boxes filling the geometry space and subdividing it in sub-spaces. This structure fast up the research algorithm of the nearest intersected surfaces, as they will be searched only in the voxels adjacent to the one (and of course in itself) containing the point from where the particle is transported. The process of voxels creation is called voxelization and, as it will be explained in section 4.2.1, it gave a limitation for the size of the geometry. Conscious of the larger computational effort, but of the better physical description of the individually positioned pebble, it was considered possible to execute the simulation with this geometry thanks to the large parallel processors capacity of the CEA clusters.

The main interest of this verification process is to verify the iterative homogenization scheme based on the "macro-stochastic" transport approximation in the multi-pebble geometry. For this reason, the reactor model was simplified, in order to focus on the representation of the core itself and to reduce the possible gaps between the results of TRIPOLI4 and APOLLO2 models to the treatment of the bed of pebbles. In order to avoid geometrical complex shapes, from the data of pebbles positions distribution in the PBMR-400, the top part of the bed, in which the pebble are still not packed like in the lower heights, and the bottom one, which is influenced by the presence of the three discharge cones, have been cut out. From the 11 m height of the PBMR-400 core, only 9 m, starting 1 m under the bed top, have been retained. The 50 cm helium gap between the top reflector and the top of the core has also been neglected. Nevertheless, if the presence of this void cavity is of difficult treatment when performing the core calculation in diffusion, it should not create particular problems when the core is computed with a transport method.<sup>88</sup>

Finally, the geometry of the reactor model consists in a 9 m height annular cavity, with radius ranging from 100 cm to 187 cm and a central graphite column of 1 m radius, an external graphite reflector of 1 m thickness and a top and bottom graphite reflectors of 1 m height. The cavity was subdivided in annular regions to represents the spectrum zones subdivision used in the deterministic code. In this thesis specific studies concerning the optimization of spectrum zones subdivision were not carried out. This can be done both by testing different subdivisions in the deterministic code and comparing the result to the reference Monte Carlo calculation and also like in a recently proposed methodology, but where the core calculation is performed in diffusion, by analyzing some predefined spectral indices.<sup>111</sup> Thus, the VSOP spectrum zone subdivision of the PBMR400, which is based on engineering evaluation,<sup>21</sup> was adopted: the core is divided in 5 axial channels (A to E) to represent the flow channels, the internal and the external one, which are close to the reflector region, are axially subdivided in 15 equivolometric zones, since the three central ones are subdivided in 11 equivolometric axial zones, for a total of 63 spectrum zones. The spectrum zones are numbered from the top to the bottom and from the internal to the external channels. The boundaries of the channels and the volumes of the respective spectrum zones are given in Table 4.II.

**Table 4.II: Flow channels radial positions and SZ volumes**

	Chan. A	Chan. B	Chan. C	Chan. D	Chan. E
Ext. rad. [cm]	110.0	135.0	152.0	177.0	187.0
SZ Vol. [cm <sup>3</sup> ]	3.958E+05	1.574E+06	1.254E+06	2.114E+06	6.861E+05

A different axial subdivision is employed in VSOP to simulate the relative velocity of the pebbles, which is lower in the regions close to the reflectors. In this way, if a fixed time  $T$  is assumed for the pebbles to flow through the height of a zone, the ones flowing

close to reflectors will spend  $15T$  to get out of the core from the top, and the central ones will spend  $11T$ .

The pebbles have been individually positioned inside each spectrum zone. For the ones which are overlapping between two or three zones, the proper portions of the volume are accounted in the corresponding spectrum zones in which they are comprised.

The burnup of each pebble is assigned in two different manners: in the first analyzed case all the pebbles of the core have the same burnup level, while in a second set of cases six different burnup levels were used. The burnup was assigned randomly to each pebble, with a uniform probability. Three different random distributions were simulated in order to evaluate the impact on the core characteristics and the capability of the APOLLO2 calculations to reproduce different situations. When using pebbles of different burnup types, some sources of uncertainty were introduced for the comparison with the deterministic calculation. This is due to the fact that in the APOLLO2 model it is necessary to furnish the fraction of the different burnup pebbles over the total number of pebbles contained in the zone. Thus, during the construction of the ROOT geometry, in order to count the number of pebbles of different type comprised in a zone, when a positioned pebble overlaps between several zones the relative portion of the volume belonging to each zone should be evaluated. Nevertheless, also neglecting the curvilinear internal and external surfaces of the zone and approximating them with two planes, to compute the fractions of the volume in which a sphere is divided when intersected by two perpendicular planes is a complex problem. Thus, for the purposes of this verification, it has been considered that, due to the large number of pebbles contained in a spectrum zone (at least 650 in the smaller zones, the ones of the internal channel), each time that a pebble was overlapping with a zone surface it was accounted only by half of its volume, and when it was intersected by a corner of the zone only by a fourth. This approach has been considered a statistically good approximation to evaluate the portion of different burnup type pebbles in each zone, but it can introduce an error when comparing the reaction rate per pebble type between TRIPOLI4 and APOLLO2, as explained in section 4.2.3.4.1.

At this point, having defined all the dimensions and materials, the ROOT geometry of the full core, which contains 366561 pebbles, was built, but a problem was encountered during the voxelization phase due to a limitation on the number of allowed volumes in the geometry.

It was necessary to restrain the geometry to one fourth of the core, using reflecting boundary conditions on the lateral sides, which gave the final geometry used for the simulations and illustrated by Figure 4.1 (where the pebbles are placed only in the bottom of the core in order to show the spectrum zone subdivision). Of course, it is possible to use such a restrained geometry due to the axisymmetric nature of the problem. This also allows to have a better statistic and a faster simulation (as the total number of surfaces is smaller) with the same number of random particles. Nevertheless, this introduces a supplementary approximation, which effects are difficult to evaluate, of un-physical cut pebbles at the lateral sides of the geometry. Still, the fraction of

lateral cut pebbles over the total number present in the 1/4 geometry (94198) is only 5.24%, so this approximation should not have a significant influence on the results.

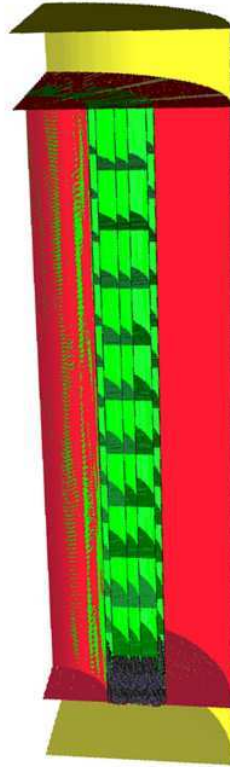


**Figure 4.1: TRIPOLI4 Reactor Model**

In order to furnish all the necessary data to the APOLLO2 model, it was also necessary to evaluate the packing fraction of the pebbles in each zone. This has been done computing the helium volume in each zone in two separate ways: first using the volume evaluation option of TRIPOLI4 and secondly developing a script in ROOT which allows to generate random points in the geometry and to evaluate the volume of a given material and the associate uncertainty. For both, the relative error on the helium volume was set at  $10^{-4}$  of the zone volume. Knowing the helium volume in a zone, the packing fraction  $pkf$  is straightforward derived as  $pkf = 1 - V_{He} / V_{Zone}$ , where  $V_{He}$  is the helium volume and  $V_{Zone}$  is the spectrum zone volume. The results obtained with the two codes are slightly different. The  $pkf$  computed with ROOT has been retained to be used for the verification calculations. They are shown in Table 4.III, together with the relative difference of the TRIPOLI4 ones from them in Table 4.IV. The relative differences between the two set of  $pkf$  show a systematic deviation, but the reasons of this have not been investigated. These two different sets of packing fraction will be used to evaluate the sensitivity of the results ( $k_{eff}$  and core power distribution) to the  $pkf$  in section 4.2.3.4.3. As it can be noticed, the packing fractions of the zones in channel A

(the internal one) and channel E (the external one) are lower than in the central channels, showing that the redistribution of the pebbles close to the walls effectively result in a locally less densely packed bed. Moreover, in a given channel the  $pkf$  are lower at top and bottom and they are not symmetrically distributed respect to the middle height. This is due to the fact that, since the pebble distribution data are computed for the PBMR-400, on the top of the core the bed is still not compacted as on the lower parts, whereas at the bottom the pebbles start to re-arrange approaching the discharge cones.

**Table 4.III: ROOT computed packing fractions**

CHAN A	CHAN B	CHAN C	CHAN D	CHAN E
0.518	0.585	0.590	0.586	0.457
0.526				0.458
0.528	0.592	0.606	0.594	0.467
0.525	0.596	0.613	0.596	0.471
0.524	0.597	0.614	0.597	0.463
0.530				0.469
0.525	0.595	0.616	0.599	0.476
0.533	0.599	0.615	0.599	0.476
0.540	0.601	0.617	0.601	0.483
0.535				0.482
0.540	0.602	0.617	0.602	0.478
0.537	0.600	0.619	0.604	0.496
0.535	0.602	0.618	0.604	0.502
0.539				0.500
0.549	0.591	0.601	0.596	0.491

**Table 4.IV: Rel. diff. of T4 computed packing fractions from ROOT ones**

CHAN A	CHAN B	CHAN C	CHAN D	CHAN E
0.45%	0.11%	0.00%	-0.09%	-0.48%
0.49%				-0.43%
0.45%	0.18%	0.01%	-0.05%	-0.46%
0.41%	0.20%	0.02%	-0.07%	-0.45%
0.46%	0.20%	0.00%	-0.11%	-0.43%
0.43%				-0.46%
0.45%	0.25%	0.00%	-0.07%	-0.47%
0.47%	0.20%	0.02%	-0.07%	-0.43%
0.47%	0.17%	0.00%	-0.08%	-0.48%
0.40%				-0.45%
0.46%	0.16%	0.03%	-0.07%	-0.46%
0.43%	0.18%	0.00%	-0.09%	-0.45%
0.45%	0.15%	0.00%	-0.06%	-0.49%
0.48%				-0.46%
0.43%	0.14%	0.02%	-0.01%	-0.48%

Finally, two different temperature distributions are used to simulate the cold conditions and the hot power ones. For the cold reactor all the materials are at the room temperature of 27 °C, and for the hot one the graphite of the pebbles and of the reflectors are at 701 °C, and the kernels and the coating layers are at 900 °C.

#### 4.2.2 APOLLO2 Reactor Model

The same reactor dimensions of the one used in the TRIPOLI4 model are used to describe the core RZ geometry in APOLLO2, illustrated in Figure 4.2.

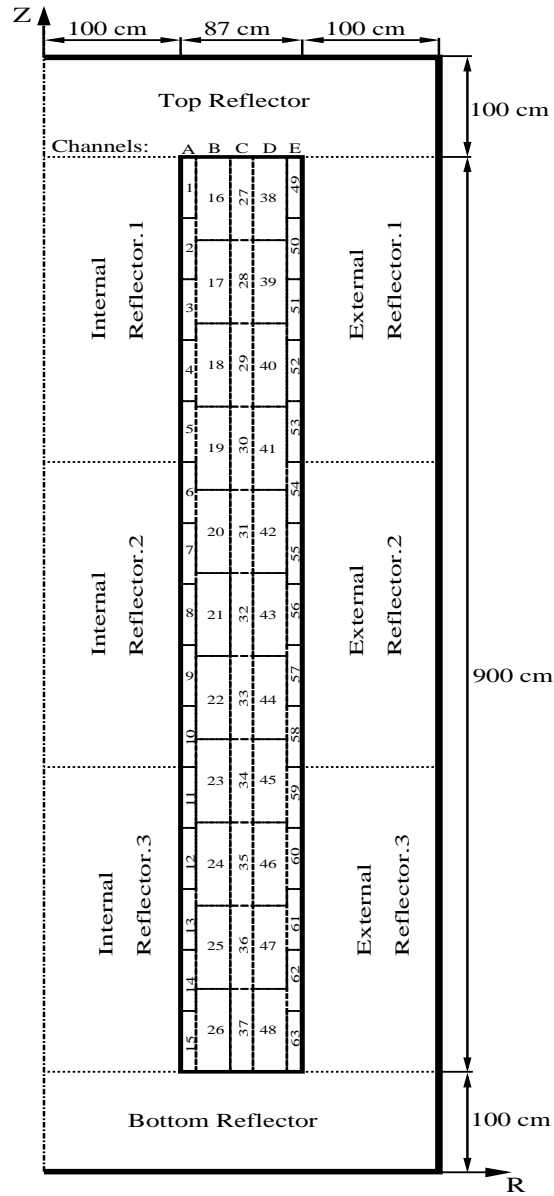


Figure 4.2: APOLLO2 RZ reactor model

The lateral reflectors were divided in three different materials, whose homogenized cross sections are obtained by three 1D  $S_N$  calculations representing the radial structure. One more 1D  $S_N$  calculation of an axial structure is performed to compute the broad group cross sections (together with the spectral shape factor for the entering current,



$\chi_k^{gG}$ ) of the top and bottom reflectors. These calculations were performed assigning to the core region of the 1D geometry a set of homogenized fine group cross sections corresponding to the different spectrum zones. This set was obtained computing with reflected boundary conditions the related multi-pebble geometries. For example, for the 1D geometry representing a radial cut at the central height of the core (used to homogenize Internal Reflector.2 and External Reflector.2 and compute their  $\chi_k^{gG}$ ), the homogenized cross sections of the SZ 8, 21, 32, 43 and 56 were assigned to the relative radial regions.

The pebbles which compose the multi-pebble geometry comprise two homogeneous regions, the outer graphite shell of 0.5 cm thick, which was divided in 3 equivolumetric computational layers, and the internal fuel region, divided in 10 computational layers, which is associated with the 281 groups P1 cross sections also used in TRIPOLI4. All the fine-group cross sections are taken from the JEFF-3.1.1 CEA library. In the collision probabilities calculations of the multi-pebble geometries, the P0 transport corrected (P0\*) cross sections are used. For the  $S_N$  RZ core calculation different broad-group structures were tested: a 8 groups structure<sup>112</sup> which was developed for the transport calculations of PWRs, a 13 groups structure<sup>113</sup> developed specially for HTRs, a 26 groups structure<sup>114</sup> developed by CEA for transport calculations in PWRs and also the 281 SHEM structure without energy collapsing. The calculations performed with no energy collapsing will allow determining the appropriateness of the methodology utilized to homogenize the graphite reflectors.

The spatial mesh of the RZ geometry has been determined by performing some preliminary calculations with different meshes as presented in section 4.2.3.1.

The  $S_N$  calculations of both the 1D equivalent structure and of the RZ core are performed using the diamond differencing scheme and a  $S_8$  angular discretization. In a previous published work on the  $S_N$  calculation of a RZ pebble bed reactor model,<sup>88</sup> it was observed that the core eigenvalue, the axial power and flux distribution changed very little when increasing the angular quadrature over  $S_4$ . At the end of the verification process in section 4.2.3.4, an evaluation is made on the saved computing time passing from  $S_8$  to  $S_4$ , together with the relative differences on the results.

To complete the input data needed to define the multi-pebble geometries, the respective packing fractions of Table 4.III have been assigned to each of them. Moreover, for the three cases where six different burnup types were assigned to the pebbles, the fractions of each type present in each spectrum zone was assigned as they were computed while building the ROOT geometry.

Finally, the boundary-to-boundary  $p_{k'/k}^{b,b}$  probabilities were deduced from the data presented in section 3.4, particularly distinguishing between the zones adjacent to the

internal (channel A) or to the external (channel E) reflectors and the ones belonging to the central channels (B-C-D).

### 4.2.3 Comparison of the Results for Different TRIPOLI4 Cores

In order to progressively verify the results of the AP2 calculations against the ones obtained with the corresponding T4 simulations, four different types of cores, whose characteristics are depicted in Table 4.I, are considered and analyzed in both codes.

In the first two simulations the spectrum zones of both T4 and AP2 models contain a homogenized material and a full cylindrical reactor model is used in T4 (instead of  $\frac{1}{4}$ ). The main objective of this set of calculations is to assess the capability of the AP2 RZ  $S_N$  solver to properly compute a large size geometry, optimizing the computational parameters and analyzing the effects of changing group structure. All the simulations are carried out at a uniform temperature of 27 °C.

- Core 1): a homogeneous core is simulated where all the spectrum zones contain the same material, both in T4 and in AP2.  
The core material is obtained homogenizing in 8 groups with AP2 a single reflected pebble.  
The coherence of the AP2 RZ core spatial mesh, used all along the next calculations, is checked toward a refined one. The convergence parameters of the  $S_N$  solver are optimized. The results are presented in section 4.2.3.1.
- Core 2): the simulation (results gathered in section 4.2.3.2) is carried out with the cross sections of the spectrum zones obtained by homogenizing in AP2 the respective multi-pebble geometries with reflected boundary conditions. The multi-pebble geometries contain a single pebble type of 50000 MWd/t, but they differ in the  $pkf$  and the  $p_{k'k}^{b,b}$ . Thus, the spectrum zones of the T4 model contain a homogeneous material, but with a different set of 281-group cross section per zone.  
For the AP2 calculations different broad-group energy structures are tested. This allows checking the precision of the RZ  $S_N$  solver of AP2 on a heterogeneous core and evaluating the computing time associated to the different group structures. Moreover, the core is computed also with a diffusion solver, in order to evaluate the associated precisions and gain in computing time.

In the second set of simulations, the core cavity of the T4 model is filled with individually positioned pebbles. The  $\frac{1}{4}$  cylindrical geometry is simulated in T4. In the corresponding AP2 model each spectrum zone of the RZ core is associated to a multi-pebble geometry and the core is computed with the iterative calculation scheme developed in this thesis.

Both a low-temperature (*LT*) and a high-temperature (*HT*) model are simulated. This is the proper verification of the developed APOLLO2 model.

- Core 3) the core cavity contains a single type of pebbles with a burnup of 50000 MWd/t. The results are presented in section 4.2.3.3.  
 In T4 the graphite material is associated to a set of 281-group P1 cross sections, but an analysis is performed using also P0 transport corrected (P0\*) and continuous energy cross sections. This last analysis, presented in section 4.2.3.3.2, allows quantifying the effects of using multigroup P1 cross sections for graphite in TRIPOLI4.  
 For the AP2 full-core calculation several group structures are used and the discrepancies with the T4 results are checked.  
 Two different ways of computing the production rates are compared: one using the RZ flux computed over the homogenized zone's material and the other using the heterogeneous flux computed over the associated multi-pebble geometry.  
 The spectra of the entering currents from the reflectors are analyzed, in section 4.2.3.3.1, and compared between T4 and AP2.
- Core 4): the core cavity contains six different types of pebbles randomly distributed. Three different random distributions are simulated.  
 In T4 the graphite material is associated to a set of 281-group P1 cross sections.  
 In AP2 the 26-group and the 13-group structures are used for the full-core calculations.  
 For the reaction rate comparison, both the distribution of the average values over the spectrum zones and the repartition over the six pebble types in each zone are verified. This last verification is made in section 4.2.3.4.1.  
 To conclude the verification process, an analysis of the computing time is performed, in section 4.2.3.4.2, verifying also the  $S_4$  angular quadrature in the AP2 RZ calculation. Finally, a sensitivity analysis on the results for  $pkf$  and  $p_{k'k}^{b,b}$  variations is presented in section 4.2.3.4.3.  
 This is the most complex core used in the verification process and it helps verify the capability of the developed AP2 iterative core calculation scheme to properly compute a PBR core containing a stochastic mixture of different pebble types.

For all these simulations, when comparing the results of a given calculation with a reference one, the difference with the reference  $k_{eff}$  will be expressed in terms of reactivity as

$$\Delta\rho = \frac{1}{k_{eff,Ref}} - \frac{1}{k_{eff}}. \quad (4.1)$$

To compare the total reaction rate densities  $\tau$  of each spectrum zone in the core, we express the maximum relative difference with the reference result. This is done for the rates of reaction  $r$  over the  $SZ$  which have a shape factor,  $sf$ , larger than 1:

$$\Delta_{sf>1}^{\%} \tau_r = \max \left( \frac{|\tau_{r,SZ} - \tau_{r,SZ,Ref}|}{\tau_{r,SZ,Ref}} \right), SZ = 1, N_{SZ}, \text{ for } SZ \text{ with } sf > 1, \quad (4.2)$$

where  $N_{SZ}$  is the total number of spectrum zones in the core.

The shape factor is the ratio between the average reaction rate per unit volume in the spectrum zone and the average reaction rate density in the core. The zone with the highest power shape factor is called hot spot and it is of particular interest in analyses of nuclear reactors as its conditions generally determine the thermal-hydraulic and mechanical safety factors.

In AP2, the average total reaction rate density over a  $SZ$  is computed as

$$\tau_r = \frac{\sum_{x \in V} \int dE \int d\mathbf{r} \Sigma_{r,x}(E, \mathbf{r}) \phi(E, \mathbf{r})}{V_{SZ}}, \quad (4.3)$$

where  $x$  denotes a fissionable isotope,  $V_{SZ}$  is the zone volume and  $\Sigma_{r,x}$  is the macroscopic cross section for reaction  $r$  and isotope  $x$ . In this study production rates, with  $\Sigma_{r,x} = \nu \Sigma_{f,x}$ , and absorption rates, with  $\Sigma_{r,x} = \Sigma_{a,x}$ , were computed. In the presentation of the results the production rates will be indicated as  $\tau_{PROD}$ , and the absorption ones as  $\tau_{ABS}$ . The distribution of the production rate in the core is very similar to the power rate, but it has been preferred as comparison parameter for a question of coherence between T4 and AP2.

The reaction rates integrated over the different spectrum zones of the AP2 RZ model can be computed in two different ways.

They can be computed directly with the fluxes of the RZ core. A spectrum zone is composed by a homogeneous material associated to a single set of homogenized broad-group cross sections. The reaction rates, thus, are computed summing the product of these cross sections by the values of the broad-group flux over the computational cells belonging to the spectrum zone in the RZ geometry.

A second possible way is to compute the reaction rates over the multi-pebble geometries with the fine-group heterogeneous fluxes. In this case, the reaction rates are computed with the proper fluxes of each pebble types over the heterogeneous multi-pebble geometry. The spatial variation of the flux over the zone region in the RZ geometry is not accounted for, rather an averaged value coming from the current balance is used.

Because the multi-pebble geometries are coupled through the interface currents, it is only necessary to normalize the sum of their total rates to the total core value.

In the presentation of the results, the rates computed with the RZ broad-group fluxes are indicated as  $\tau^{HOM}$  and the ones computed with the fine-group multi-pebble geometries fluxes are indicated as  $\tau^{HET}$ . Obviously, this distinction can not be made for the cores 1) and 2) where the spectrum zones of the AP2 model are not associated to any multi-pebble geometry.

Finally, the T4 simulations were performed generating 10000 batches of 50000 particles, for a total of  $5 \cdot 10^8$  ran particles. Each simulation is parallel computed on a cluster of 64 Itanium2 1.6 GHz processors, taking ~48 h. This high number of histories was necessary to reach an uncertainty on the core eigenvalue in the order of 10 pcm and on the reaction rates lower than 1%.

The AP2 calculations were executed on a AMD/Opteron 64 bit 2,8 GHz CPU.

#### 4.2.3.1 Homogeneous Core

The homogeneous core was created assigning to all spectrum zones the same cross sections in the 8-group structure, both to the T4 and to the AP2 models. These cross sections are obtained, as described in section 4.2, by computing a single reflected pebble with a burnup of 50000 MWd/t with a critical buckling search. This burnup value has been chosen as it is close to the average burnup of 53000 MWd/t calculated for the pebbles contained in the PBMR-400 in equilibrium state.<sup>115</sup> All the materials are at a temperature of 27 °C.

For the graphite reflectors the 8-group cross sections are issued from the homogenization of the external graphite fuel free zone of the pebble. The cross sections have been furnished to the T4 model and to the RZ  $S_N$  core model of AP2 with the P1 scattering approximation.

To define the spatial mesh of the AP2 RZ core model, a coarse mesh has been compared to a finer one. It has to be noticed that, due to the different number (15 or 11) of spectrum zones per channel, using a constant step mesh only a common multiple of these numbers can be used to axially subdivide the core. Thus, the broad mesh had 25 cells for radial and axial subdivision of the reflectors, 25 cells for the radial and 165 for the axial subdivision of the cavity. While the finer mesh had 50 cells for the reflectors, 50 radial and 330 axial cells for the cavity.

The parameters for the  $S_N$  solver have also been fixed and they will be used with these values in the calculations of the successive sections. They are fixed to:

- $10^{-6}$  for the precision on the punctual fluxes in internal iterations;
- $10^{-4}$  for the precision on the punctual fluxes in thermal iterations;

- $10^{-3}$  for the precision on the punctual fluxes in external iterations;
- $10^{-5}$  for the precision on the core eigenvalue;
- A maximum of 20 internal iterations and 10 thermal iterations per external iteration.

By comparing between themselves the AP2 results obtained with the two different meshes, it appeared that the coarse mesh is sufficient to discretize the geometry, since the computed  $k_{eff}$  are the same and the  $\Delta_{sf>1}^{\%} \tau_{PROD}$  and the  $\Delta_{sf>1}^{\%} \tau_{ABSO}$  are smaller than 0.1%. Moreover, the computing time is reduced by a factor 2.3 with the broad mesh.

Finally, it was observed that a large number of external iterations were needed to the  $S_N$  convergence. This was mostly associated to a slow convergence of the highest energy-group fluxes in the graphite reflectors. The fission neutrons, produced at high energy only in the core cavity, are slowed down in graphite, so that the fast flux is very small in the external parts of the reflectors. As convergence is determined by comparing the absolute differences on the flux values between two external iterations to the requested precision, the oscillations on very low flux values can generate convergence problems. Still, the influence of the fast flux in these external regions has negligibly impact on the flux distribution in the core cavity. Thus, the convergence verification on the punctual fluxes was limited to a restrained zone of the reactor. Using the broad spatial mesh, only the 18 cells, of external, top and bottom reflectors, closer to the cavity were considered for the convergence verification. This allowed a gain of a factor 1.8 in computing time without significant differences on the core shape factors.

Coming to the comparison between the T4 and the AP2 results, the core  $k_{eff}$  obtained with the T4 simulation is 1.11874, with an uncertainty of 9 pcm.

The last calculation described in AP2 differed from the T4 simulation by a  $\Delta\rho$  of 12.3 pcm, a  $\Delta_{sf>1}^{\%} \tau_{PROD}$  of 0.28%, a  $\Delta_{sf>1}^{\%} \tau_{ABS}$  of 0.31% and a  $\Delta_{HotSp.}^{\%} \tau_{PROD}$  of -0.10%.

These results demonstrate the reliability of the AP2  $S_N$  RZ solver to compute large size geometries with a core structure and cross-sections characteristics close to the annular PBMR.

#### 4.2.3.2 Heterogeneous Core with Homogeneous Spectrum Zones

For the successive comparisons, the spectrum zones are associated to a homogeneous material, both in the T4 and in the AP2 model, but with different cross sections for each zone. The cross sections are obtained by computing with infinite boundary conditions the multi-pebble geometries associated to the relative zones, as it is done to initialize the iterative core calculation scheme in AP2. From the  $P_{ij}$  flux calculation of a multi-pebble

geometry, the P1 cross sections, homogenized over the whole multi-pebble geometry, are produced using a 281-group structure for the T4 model and the different group structures described in section 4.2.2 for the AP2 model. Furthermore, diffusion calculations were carried out using the CRONOS2 code.<sup>117</sup> The homogenized reflectors cross sections for the AP2 and CRONOS2 models are obtained performing the three radial plus one axial 1D  $S_N$  calculations described in section 4.2.2

The multi-pebble geometry is composed by a single pebble type of 50000 MWd/t and the temperature of pebbles and helium is 27 °C. It differs from the geometry of a simple pebble surrounded by a helium layer as it includes the surface-to-surface geometric probabilities, which will be successively used in the calculations performed in section 4.2.3.3 and 4.2.3.4, and it is so computed by using the CP matrices described in section 3.2.3.

Compared to the previous simulation made with the homogeneous core, all the multi-pebble geometries are constructed with the proper packing fraction reported in table Table 4.III. It has to be noticed that the value of the packing fraction used in the previous simulation (packing fraction equal to 0.61) is not the average value of the ROOT computed packing fractions, but it is the typical value considered in pebble bed modeling.<sup>116</sup>

The comparison with the Monte Carlo reference allows determining the precision of the RZ solvers ( $S_N$  and diffusion) for a heterogeneous core, where the level of heterogeneity is at the spectrum zones size. Moreover, the effect of the group structure on the  $k_{eff}$  and on the production distribution in the core will be estimated, together with an evaluation of the computing time.

The computed core  $k_{eff}$  with T4 was of 1.10591, with a relative standard deviation of 7 pcm, since the production shape factors, with the associated standard deviations, are given in Table 4.V

From the production distribution, it is possible to observe a higher production at the bottom of the core, compared to the one at the top. This distribution is a consequence of the distribution of the packing fractions, which are higher in the core bottom, as observed in section 4.2.1. As expected, the higher production rates are located in the central zones of channel A, which is the most internal one and close to the central graphite reflector. Less expected are the higher shape factors at the central core height of channel E compared to the more radially central channels C and D. One can notice that in a homogeneous cylinder the neutron flux has a cosine distribution in the axial direction and a Bessel function distribution in the radial one. But in this core, due to the presence of the thick internal and external graphite reflectors, the contribution to thermal flux in channel A and E zones of the neutrons slowed down and scattered back from the reflectors is very important.

One can notice that this is not the typical power distribution of an operating pebble bed reactor<sup>21</sup> since a uniform cold temperature is adopted here. At hot operational conditions, considering the thermal-hydraulic feedback, the hot spot will shift toward the top of the core, where the downward-flow of cold helium enters the bed.

**Table 4.V: Production shape factors and standard deviations of T4 heterogeneous core – homogeneous SZs model**

CHAN A	CHAN B	CHAN C	CHAN D	CHAN E
0.62 0.36%	0.53	0.46	0.48	0.44 0.34%
0.85 0.31%	0.34%	0.34%	0.33%	0.62 0.31%
1.11 0.26%	0.78	0.66	0.70	0.79 0.27%
1.33 0.23%	0.29%	0.29%	0.29%	0.95 0.22%
1.51 0.19%	1.02	0.89	0.92	1.08 0.18%
1.64 0.16%	1.22	1.05	1.10	1.17 0.16%
1.76 0.14%	0.17%	0.17%	0.17%	1.25 0.13%
1.78 0.12%	1.35	1.16	1.21	1.30 0.11%
1.80 0.14%	1.40	1.21	1.26	1.30 0.11%
1.74 0.16%	0.12%	0.12%	0.11%	1.26 0.14%
1.62 0.19%	1.38	1.20	1.24	1.17 0.18%
1.46 0.22%	1.28	1.11	1.15	1.04 0.22%
1.23 0.25%	0.17%	0.17%	0.17%	0.91 0.24%
0.97 0.28%	1.11	0.96	1.00	0.73 0.27%
0.71 0.31%	0.87	0.75	0.78	0.52 0.30%
	0.27%	0.27%	0.26%	
	0.60	0.53	0.54	
	0.30%	0.30%	0.30%	

The results of the calculations carried out with the RZ  $S_N$  AP2 model and with the RZ diffusion CRONOS2 model are presented in Table 4.VI.

From the results, it appears that the core transport calculations performed using the 26-group energy structure is the most appropriate and its discrepancies are similar to the ones observed with the 281-group. The 8-group structure is very performing in terms of computing time, but the discrepancies, especially those observed on the production distribution, are quite large (3 to 4%) if considering that a piece-wise homogeneous problem is computed.



**Table 4.VI: Discrepancies of AP2 and CRONOS2 calculations of the heterogeneous core – homogeneous SZs from the T4 reference and computing times**

	$k_{eff}$	$\sigma$ [pcm]		
T4	1.10591	7		
	$\Delta\rho$ [pcm]	$\Delta_{sf>1}^{\%} \tau_{PROD}$	$\Delta_{Hot Sp.}^{\%} \tau_{PROD}$	Calc. time [s]
AP2				
8 gr.	-194.6	4.23%	-3.56%	512
13 gr.	235.7	2.18%	-1.68%	1380
26 gr.	27.8	0.89%	-0.34%	3160
281 gr.	-23.2	0.83%	-0.16%	41419
	$\Delta\rho$ [pcm]	$\Delta_{sf>1}^{\%} \tau_{PROD}$	$\Delta_{Hot Sp.}^{\%} \tau_{PROD}$	Calc. time [s]
CRONOS2				
4 gr.	-39.2	5.60%	-5.10%	82
6 gr.	10.7	3.59%	-3.00%	160
8 gr.	-169.5	3.94%	-3.24%	211
13 gr.	256.1	1.89%	-1.31%	875
26 gr.	55.7	1.21%	0.07%	2356

Diffusion calculations have been performed in order to evaluate the discrepancies and the possible saving of computing time compared to the  $S_N$  transport calculations. Moreover, using also 4-group and 6-group<sup>118</sup> collapsed structures. The 4-group one does not come from any particular reference, but it is based on the laboratory experience in HTR modeling.

When core calculation is performed using diffusion theory, the gain in computing time is evident. The 6-group structure gives results in a very good agreement on the  $k_{eff}$ , but the discrepancies on the production distribution are slightly too large, especially when considering that this comparison is made for homogeneous spectrum zones. Nevertheless, if computing  $k_{eff}$  is the main interest of the calculation, it appears that the 6-group could be used properly, having a gain in time of a factor 8 or 9 compared to the 26-group  $S_N$  calculation. Obviously, this is just a preliminary trend that should be verified with further calculations. To reach an acceptable discrepancy on both  $k_{eff}$  and production shape factors, the number of groups has to be increase. The 26-group structure gives good results, but the associated computing time is long, especially due to the long time needed to construct the diffusion matrices, and the gain compared to the  $S_N$  is no more so interesting.

From these first calculations, it appears that the flux in the cavity zones is highly influenced by the graphite reflectors; especially, due to the thin and high cavity shape, by the internal and external ones. Usually, the neutron migration length, which is the root-mean-square distance travelled by a neutron between his birth with a fission and his absorption in the thermal range,<sup>99</sup> in a typical pebble bed is on the order of 80 cm,<sup>100</sup> which is comparable to the radial cavity size of 87 cm. Thus, a proper treatment of the reflectors is a critical aspect in pebble bed reactors modeling.

To conclude, for this heterogeneous core simulation with homogeneous spectrum zones, the comparison of the AP2 results with the reference T4 ones showed a very good agreement ( $k_{eff}$  in 30 pcm and differences on production shape factors < 1%) on the two codes results. This is observed when using the 26-group structure for the RZ core cross sections.

When using 6-group diffusion as the low-order operator to perform the full-core calculation, a very good agreement with the T4 reference is obtained on the core  $k_{eff}$  (in 10 pcm of difference) with a short computing time. Nevertheless, the comparison on the reaction rates is degraded (rel. diff. of about 3% to 4%).

#### 4.2.3.3 Single Type Individually Positioned Pebbles

In these simulations each pebble has been positioned individually in the T4 model and all of them with the same burnup of 50000 MWd/t.

Two reactor models are simulated, one at low temperature (*LT*), with all the materials at 27 °C, and one at high temperature (*HT*), with the micro-particles (kernel plus coatings) at 900 °C, the graphite of the fuel region matrix, outer pebble shell and reflectors and the helium coolant at 700 °C.

Remember that in both AP2 and T4 models the inner fuel region is described by the homogenized P1 cross sections obtained with the AP2 calculation of the single reflected pebble, as explained in section 4.2.

The T4 simulations have been performed assigning to the graphite materials (reflectors and outer pebbles' shells) too multigroup (281-group) P1 cross sections, from the JEFF-3.1.1 library. This is done to have a higher coherency in between the T4 and the AP2 models and to isolate the possible discrepancies in the results to the treatment of the bed of pebbles.

The validity of using 281-group P1 cross sections for graphite has been verified in section 4.2.3.3.2.

The volume integrated production and absorption rates have been evaluated in each spectrum zone. To do that, the reaction rates in all the pebbles belonging to a given zone were scored and summed up. For the pebbles overlapping between multiple zones, the reaction rates have been accounted separately over the different parts of the volume belonging to the different zones.

Furthermore, the total production and the total absorption over all the pebbles contained in the cavity have been tallied. Thus, the ratio of the total production over the total

absorption in the core, noted as  $P/A$  ratio, can be computed, giving an evaluation of the cavity  $k_{\infty}$ .

The core  $k_{eff}$  and the  $P/A$  ratio, with the associated uncertainties, obtained with the T4 simulations of both  $LT$  and  $HT$  models are shown in Table 4.VII. The corresponding core leakage is also shown.

The production rate distributions, with the associated uncertainties, are presented in Table 4.VIII for the  $LT$  model and in Table 4.IX for the  $HT$  model.

**Table 4.VII:  $k_{eff}$ , core production over absorption ratio and core leakage of the  $LT$  and  $HT$  T4 simulations using 281-group P1 XS for graphite (single pebble type)**

	$k_{eff}$	$\sigma$ [pcm]	$P/A$ ratio	$\sigma$ [pcm]	Core Leakage [pcm]
$LT_{(MG-P1)}$	1.10761	9	1.30111	93	13426
$HT_{(MG-P1)}$	1.07556	10	1.23802	100	12200

**Table 4.VIII: Prod. shape factors and  $\sigma$  of T4  $LT$  simulation (single pebble type)**

CHAN A	CHAN B	CHAN C	CHAN D	CHAN E
0.65 0.42%	0.56	0.50	0.52	0.48 0.41%
0.86 0.39%	0.41%	0.41%	0.41%	0.64 0.38%
1.11 0.37%	0.80	0.69	0.74	0.80 0.32%
1.31 0.29%	0.37%	0.36%	0.35%	0.97 0.27%
1.47 0.23%	1.03	0.91	0.95	1.09 0.21%
1.59 0.18%	0.20%	0.21%	0.20%	1.16 0.17%
1.70 0.16%	1.32	1.16	1.22	1.24 0.15%
1.72 0.14%	0.15%	0.16%	0.15%	1.28 0.14%
1.73 0.16%	1.37	1.21	1.26	1.28 0.17%
1.68 0.20%	0.14%	0.14%	0.14%	1.23 0.19%
1.56 0.24%	1.35	1.19	1.24	1.15 0.23%
1.41 0.27%	0.17%	0.17%	0.17%	1.03 0.28%
1.19 0.33%	1.25	1.10	1.15	0.90 0.34%
0.96 0.41%	0.21%	0.21%	0.21%	0.73 0.39%
0.71 0.45%	1.09	0.95	1.00	0.54 0.44%
	0.28%	0.28%	0.28%	
	0.86	0.75	0.79	
	0.36%	0.35%	0.35%	
	0.61	0.54	0.56	
	0.45%	0.43%	0.42%	

**Table 4.IX: Prod. shape factors and  $\sigma$  of T4  $HT$  simulation (single pebble type)**

CHAN A	CHAN B	CHAN C	CHAN D	CHAN E
0.69 0.46%	0.61	0.54	0.56	0.50 0.45%
0.89 0.42%	0.45%	0.45%	0.43%	0.65 0.40%
1.12 0.35%	0.83	0.72	0.76	0.79 0.35%
1.30 0.28%	0.38%	0.37%	0.38%	0.94 0.30%
1.44 0.21%	1.05	0.93	0.96	1.04 0.24%
1.55 0.20%	1.21	1.07	1.11	1.11 0.19%
1.65 0.16%	0.21%	0.21%	0.21%	1.17 0.17%
1.65 0.17%	1.32	1.16	1.20	1.17 0.17%
1.66 0.18%	0.15%	0.16%	0.17%	1.21 0.18%
1.61 0.19%	1.36	1.20	1.24	1.21 0.19%
1.50 0.23%	1.33	1.18	1.21	1.17 0.19%
1.37 0.31%	0.19%	0.20%	0.19%	1.17 0.19%
1.18 0.33%	1.24	1.10	1.13	1.09 0.24%
0.96 0.38%	0.21%	0.22%	0.22%	0.98 0.27%
0.74 0.45%	1.09	0.96	0.99	0.88 0.31%
	0.29%	0.29%	0.28%	
	0.88	0.77	0.80	
	0.35%	0.35%	0.32%	
	0.96	0.65	0.59	
	0.38%	0.35%	0.32%	
	0.74	0.58	0.59	
	0.45%	0.43%	0.41%	

One can notice that the reactivity difference between the  $P/A$  ratio and the  $k_{eff}$  provides an evaluation of the reactivity loss due to neutron leakage from the cavity. This value is about 3000 pcm for a typical light water reactor core, since it is much higher here, showing that in this type of reactors the leakage is a very important phenomenon and so that a proper treatment of the graphite reflectors is crucial.

In the corresponding AP2 model, all the multi-pebble geometries contain a single pebble type with the burnup of 50000 MWd/t, as in T4. The packing fractions assigned to each spectrum zone are the ones shown in Table 4.III.

The RZ  $S_N$  core calculation is initiated with the same set of cross sections as the one used in the previous section and obtained from the reflected multi-pebble geometries. Successively, after the convergence of the first RZ  $S_N$  core calculation, the entering currents per contact of each spectrum zones are recovered, expanded in 281 groups using the  $\chi_k^{gG}$  and used as the source terms in the next  $P_{ij}$  calculations of the multi-pebble geometries, together with the core  $k_{eff}$ .

The spectrum zones – core iterations (*SZ – core it.*) are repeated until convergence is reached. The following convergence precisions, as they are defined in section 3.2.1, have been imposed: 2 pcm for the core  $k_{eff}$ ,  $10^{-4}$  for the entering currents and the fission integrals and  $10^{-5}$  for the homogenized total cross sections.

In the previous sections, the external iterations of the RZ  $S_N$  core calculations were accelerated using the Tchebycheff method.<sup>119</sup> For the actual comparisons, the multigroup diffusion synthetic acceleration (DSA)<sup>120</sup> has also been tested and the computing times compared. The application of the DSA resulted in a faster calculation for all group structures with no relevant differences in the results compared to the Tchebycheff acceleration. The time gain factor was of the order of 1.2 – 1.3 for both low-temperature and high-temperature calculations. Consequently, only the results obtained with the DSA acceleration will be presented.

The comparison with the reference T4 calculation for the different group structures in AP2 are presented in Table 4.X for the low-temperature cases and in Table 4.XI for the high-temperature ones. The calculations indicated as "*rel. conv.*" were performed with relaxed convergence parameters for the *SZ-core it.* of: 5 pcm for the core  $k_{eff}$ ,  $10^{-3}$  for the entering currents and the fission integrals and  $10^{-4}$  for the homogenized total cross sections. The 281-group calculation was carried out without the restricted control zone around the cavity for the convergence checking. This was done to have a reference AP2 calculation for which the computing time was not a limiting factor.

These observed discrepancies on  $k_{eff}$  and production shape factors are sufficiently small to perform PBR safety studies and they fit the level requested for PWR calculations.

**Table 4.X: AP2 calculations of the *LT* model with diverse group structures and discrepancies from T4 *LT* simulation with *MG-P1 XS* (single pebble type)**

<i>LT</i>	8 gr.	13 gr.	26 gr.	26 gr. rel. conv.	281 gr. No_Zone
$\Delta\rho [pcm]$	194	125	-86	-86	-173
$\Delta\rho [pcm]$ <i>P/A</i> ratio	232	18	103	104	50
$\Delta_{sf>1}^{\%} \tau_{PROD}^{HET}$	2.24%	2.37%	2.63%	2.63%	2.59%
$\Delta_{sf>1}^{\%} \tau_{PROD}^{HOM}$	3.12%	3.19%	3.60%	3.59%	3.40%
$\Delta_{Hot\ Sp.}^{\%} \tau_{PROD}^{HET}$	2.11%	2.25%	2.63%	2.62%	2.46%
$\Delta_{Hot\ Sp.}^{\%} \tau_{PROD}^{HOM}$	2.97%	3.19%	3.60%	3.59%	3.40%
<i>SZ – core it.</i>	15	13	12	8	14
<i>Calc. time [s]</i>	732	1435	3305	2793	71348

**Table 4.XI: AP2 calculations of the *HT* model with diverse group structures and discrepancies from T4 *HT* simulation with *MG-P1 XS* (single pebble type)**

<i>HT</i>	8 gr.	13 gr.	13 gr. rel. conv.	26 gr.	281 gr. No_Zone
$\Delta\rho [pcm]$	264	32	10	-104	-248
$\Delta\rho [pcm]$ <i>P/A</i> ratio	346	-15	-15	104	32
$\Delta_{sf>1}^{\%} \tau_{PROD}^{HET}$	2.22%	2.19%	2.19%	2.49%	2.52%
$\Delta_{sf>1}^{\%} \tau_{PROD}^{HOM}$	3.03%	2.88%	2.88%	3.32%	3.36%
$\Delta_{Hot\ Sp.}^{\%} \tau_{PROD}^{HET}$	2.22%	2.05%	2.05%	2.49%	2.52%
$\Delta_{Hot\ Sp.}^{\%} \tau_{PROD}^{HOM}$	3.03%	2.88%	2.88%	3.32%	3.36%
<i>SZ – core it.</i>	27	120	49	66	29
<i>Calc. time [s]</i>	2438	5969	3465	9563	219566

From these comparisons it appears that the 26-group structure is slightly preferable for computing the *LT* model, since for the *HT* one the 13-group is preferred, also for its lower computing time. As a consequence, the relaxed *SZ* – core convergence parameters were tested using these group-structures for the respective models. The corresponding calculations allow a time gain of a factor ~1.2 for the *LT* model and ~1.7 for the *HT* one, without degrading the results.

It can also be observed that an increase of the number of broad-group induces a decrease of the core  $k_{eff}$ . On the other hand, changing the groups structure (increase of the number of groups) does not impact significantly on the production rate distribution, showing that the residual discrepancies are connected to some other modeling aspects. The calculation carried on with the 281-group structure revealed that the discrepancies on the reaction rate distribution are not connected to the reflector treatment, performed with the calculation of 1D reactor transverses.

The relative differences on the production rate distribution from the reference T4 results are shown for the low-temperature 26-group calculation in Table 4.XII and for the high-temperature 13-groups calculation in Table 4.XIII.

**Table 4.XII: Rel. diff. on prod. shape factors of 26-group AP2 calculation from T4.**  
*LT* model, single pebble type core

CHAN A	CHAN B	CHAN C	CHAN D	CHAN E
-3.91%	-2.73%	-5.02%	-4.29%	-6.58%
-1.53%				-3.95%
-0.25%	-1.76%	-3.87%	-3.06%	-2.11%
1.11%	0.12%	-2.27%	-1.26%	-1.41%
1.66%	1.30%	-1.12%	-0.17%	-0.48%
2.26%				0.24%
2.51%	1.85%	-0.47%	0.47%	0.51%
2.63%	2.16%	-0.30%	0.73%	0.50%
2.63%				0.48%
2.23%	2.40%	-0.08%	0.92%	0.70%
2.59%	2.07%	-0.24%	0.84%	0.54%
1.62%	1.61%	-0.66%	0.28%	0.10%
1.21%				-0.70%
-0.26%	0.33%	-1.88%	-0.77%	-2.14%
-1.94%	0.42%	-1.94%	-1.11%	-4.39%

**Table 4.XIII: Rel. diff. on prod. shape factors of 13-group AP2 calculation from T4.**  
*HT* model, single pebble type core

CHAN A	CHAN B	CHAN C	CHAN D	CHAN E
-1.55%	-0.34%	-2.73%	-2.40%	-4.62%
-0.14%				-2.81%
0.40%	-0.41%	-2.50%	-1.91%	-1.52%
1.26%	0.83%	-1.44%	-0.60%	-1.11%
1.62%	1.74%	-0.73%	0.04%	-0.52%
1.91%				-0.07%
1.91%	1.68%	-0.53%	0.34%	0.03%
1.92%	1.91%	-0.40%	0.46%	-0.13%
2.05%				-0.18%
1.51%	2.19%	-0.36%	0.40%	-0.23%
1.88%	1.78%	-0.59%	0.26%	-0.37%
1.09%	1.38%	-0.94%	-0.15%	-0.69%
0.72%				-1.46%
-0.58%	0.29%	-2.02%	-1.16%	-2.71%
-2.13%	0.36%	-1.98%	-1.24%	-4.50%

The discrepancies on the absorption rates were also computed; the relative differences from the reference presented the same trend and amplitude that for the production distribution and so they are not shown in this analysis.

As it is possible to observe from the relative differences on production rate distribution, the AP2 models systematically over-estimate the reaction rates in the central height zones and under-estimate the ones in the top and bottom zones. Moreover, the relative differences are very small (<1%) in the central zones of the central channel, since they are higher close to the reflectors. This trend is independent to the number of broad groups adopted for the core calculation.

To investigate the causes of this trend several variations were applied to the previous calculations.

The requested precisions on the RZ  $S_N$  core calculations were increased, but without obtaining significant differences in the results.

A refined spatial mesh was implemented, increasing the number of radial and axial computational cells in the zones close to the reflectors and using a non-homogeneous mesh size in the graphite reflectors, with finer mesh close to the cavity. However, it still does not lead to significant improvements in the results.

Nevertheless, the computed results with APOLLO2 are within 100 pcm of reactivity difference from the TRIPOLI4 ones and under 3% of relative difference on the production rate distribution. The rates computed over the heterogeneous multi-pebble geometry are systematically closer to the T4 reference than the ones computed with the RZ flux of the full-core calculations. Thus, in section 4.2.3.4 only the heterogeneous reaction rates will be computed.

#### **4.2.3.3.1 Analysis of the Entering Currents from Reflectors**

The entering currents from the reflectors to the spectrum zones adjacent to them were tallied in 281 groups in T4 for the *LT* simulation and compared to the corresponding currents computed with the 281-group AP2 calculation.

The spectra of the normalized entering currents obtained from T4 are shown, with the error bars indicating the standard deviation, in Figure 4.3 for the top reflector and in Figure 4.4 for the internal one.

It has to be noted that the currents entering the cavity from the top reflector had, in the limit of the standard deviations, the same spectra on the contacts with SZ 1 and 49, and SZ 16 and 38, respectively. The currents from the internal reflector had the same spectra while entering SZ 2 to 14, and SZ 1 and 15, respectively. The entering current from the bottom reflector has the same trend than the one entering from the top one; similarly, the current entering from the external reflector behaves like the one entering from the internal.

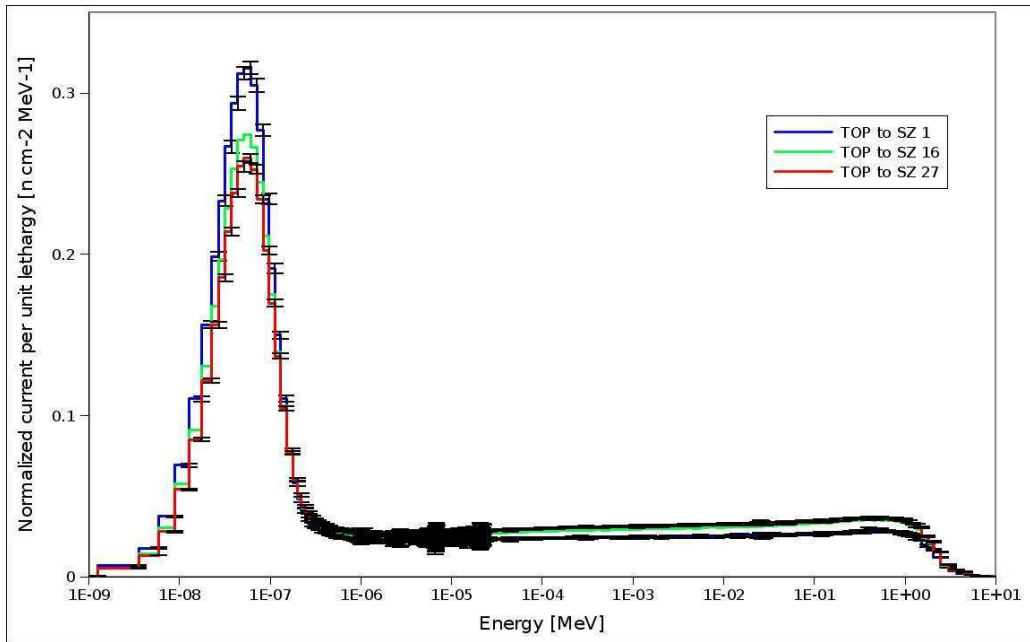


Figure 4.3: T4 normalized entering currents from top reflector to spectrum zones in *LT* model

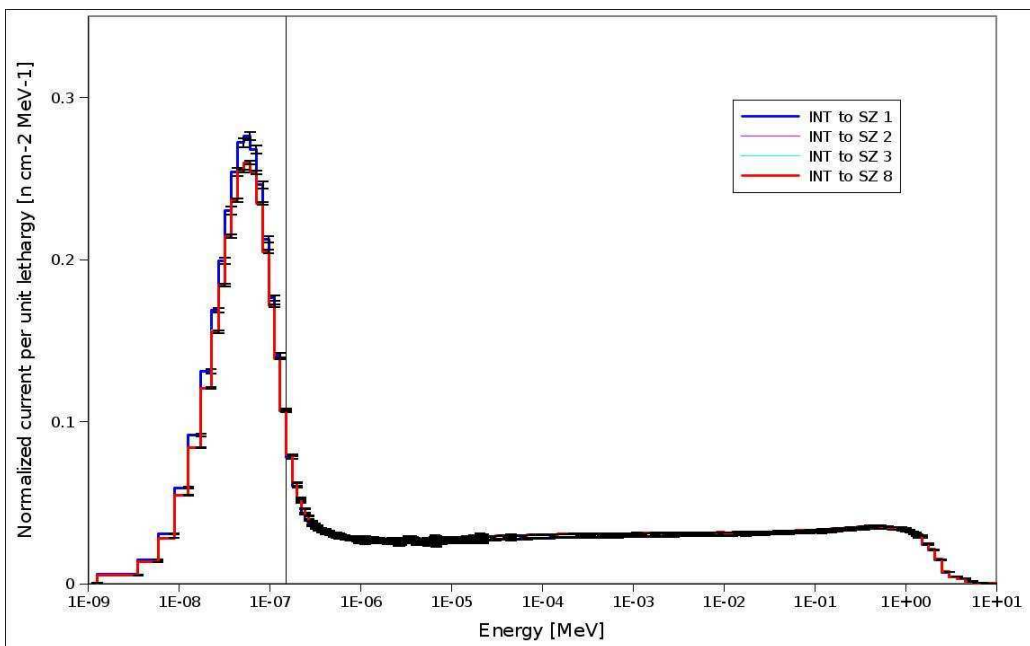


Figure 4.4: T4 normalized entering currents from internal reflector to spectrum zones in *LT* model (currents entering SZ 2, 3 and 8 are coincident)

From these results it is possible to see that the current spectra are influenced by the presence of the reflector corners. The thermal contribution in the spectra increases while approaching the corner regions, with a variation over the entered spectrum zones much stronger for the top and bottom reflector than for the internal and external ones, where only a spectral difference for the highest and lowest zones of channels A and E is



observable. This is due to the size of the zone contact surfaces with the reflectors, since the entering currents are considered piece-wise constant over a zone contact boundary surface. For the top and bottom reflectors, the radial lengths of the contacts with the 5 different spectrum zones of channels A to E are, respectively, 10, 25, 17, 25 and 10 cm. For the internal and external reflectors, the axial heights of the contacts with the spectrum zones are all of 60 cm. This height appears to be too large to correctly capture the spectral variations of the entering current from the reflectors over top and bottom zones of the internal and external channels.

Following this observation, an AP2 reactor model with a higher number of spectrum zones was constructed, obtained axially subdividing the top and bottom SZs. Thus, the top and bottom 80 cm were divided in 4 axial zones of the same height for all the channels. For example, SZ 1 was subdivided in 3 zones of 20 cm height: SZ 1a, 1b and 1c. SZ 2 in two zones of different height: SZ 2a of 21.82 cm height and SZ 2b of 38.2 cm. The same was done for the remaining zones in the other channels. Finally, the total number of spectrum zones was increased to 93.

The calculation of the *LT* model at 281 groups allows recovering the entering current from the reflectors, and particularly the currents entering the top zones and SZ 8 are illustrated in Figure 4.5.

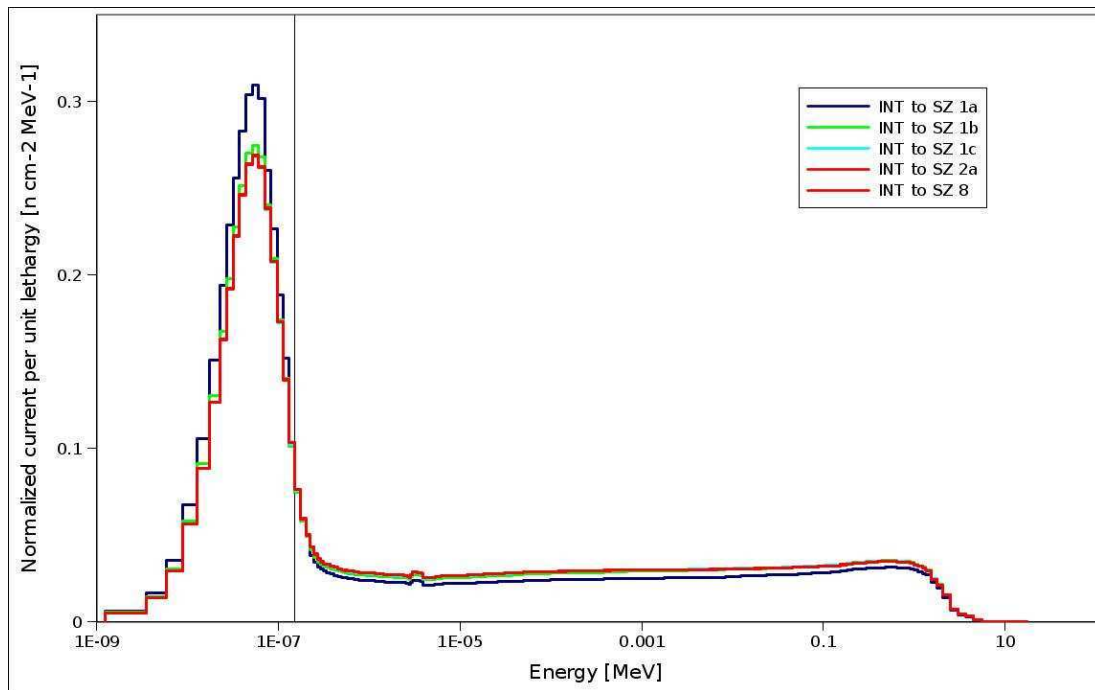


**Figure 4.5: AP2 normalized entering currents from internal reflector to the spectrum zones in the *LT* model with top and bottom zones axially subdivided (currents entering SZ 1c, 2a and 8 are coincident)**

As it can be seen, the current spectral variations over the height of SZ 1 are captured with more details. Nevertheless, after the first 40 cm height from the top, the spectra of the entering currents from the internal reflector remain the same for all the inferior spectrum zones.

In spite of this better entering current representation and the higher number of spectrum zones used to discretize the cavity, the comparison with the reference T4 is not improved.

Finally, comparing the T4 currents with the ones obtained from the AP2 281-groups 63 spectrum zones calculation, it resulted that the spectral differences are within the 2 sigma for the top and bottom reflectors, while some differences are observed for the currents entering from the internal and external reflectors. In the energy groups under 0.162 eV (indicated with a vertical line in Figure 4.6), corresponding to the largest part of the thermal Gaussian distribution, the AP2 spectra are higher than the T4 ones. Particularly, the relative difference is larger, almost the double, for the currents entering SZ 2 to 14 compared to the ones entering SZ 1 and 15.

The relative differences of the AP2 normalized entering currents from the T4 ones are illustrated in Figure 4.6 for the currents entering SZ 8 (the central of channel A) and SZ 1 from the internal reflector. The spectrum of the current entering SZ 8 is also shown. The 2 sigma standard deviations on the relative differences are indicated by the error bars.

The currents entering the SZs of channel E from the external reflector have a similar trend, but the relative differences are smaller. For example, on the energy bin corresponding to the Gaussian peak, the current entering SZ 8 from the internal reflector is 2.5% higher in AP2 than in T4. Correspondingly, the current entering SZ 56 from the external reflector is 1.8% higher in AP2.

The fact that the entering currents from the internal reflector to the central spectrum zones of channel A are more thermal in AP2 than in T4 could explain, partially, the overestimation of the production rates in the corresponding zones of AP2 compared to T4. The lower rates at top and bottom SZs could be an effect of the renormalization. In the same way, the lower discrepancies in the reaction rates of the central zones of channel E, compared to channel A, could be associated to the lower spectral differences of the corresponding entering currents from the external reflector.

However, this hypothesis should be demonstrated by further analysis, which could not be carried out during this thesis for a question of time.

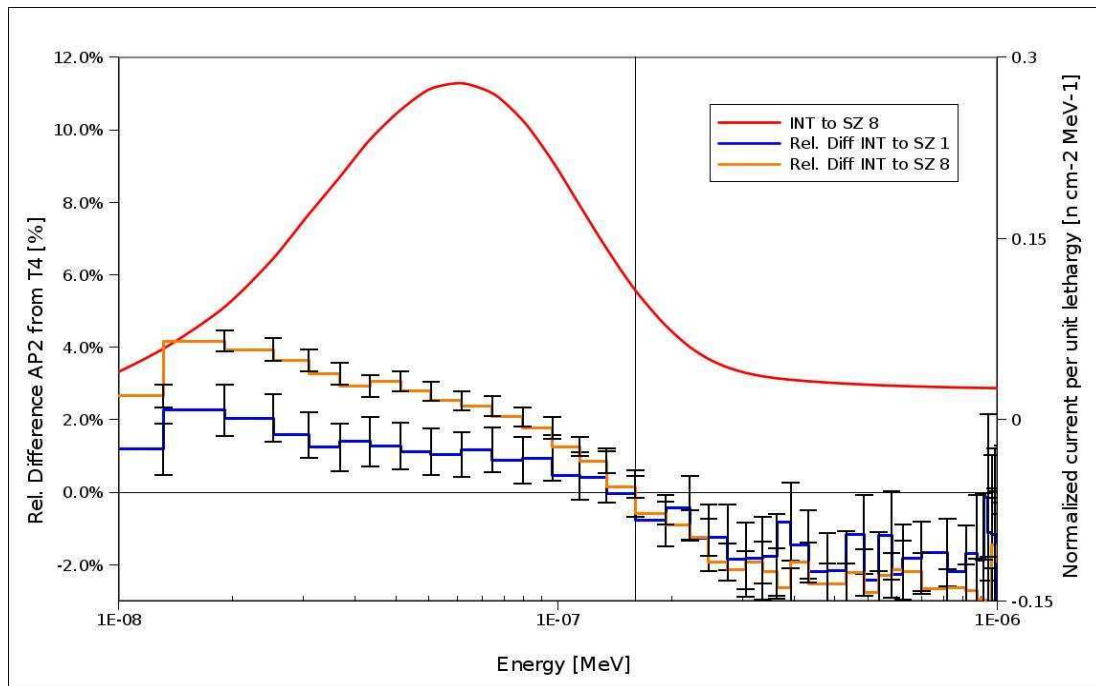


**Figure 4.6: Rel. diff. of AP2 281-group entering currents, from internal reflector to SZ1 and SZ8, from T4 ones in the *LT* model (spectra of current entering SZ8 shown)**

#### 4.2.3.3.2 Evaluation of 281-group P1 XS in T4

In this evaluation, three T4 simulations have been performed assigning to the graphite materials (reflectors and outer pebbles' shells) both 281-group (*MG*), P1 or P0 transport corrected (P0\*), both continuous energy (*CE*) cross sections from the JEFF-3.1.1 library. The positivity of the 281-group transport corrected cross sections has been checked.

The results of the *MG*-P1 simulation are the ones used as reference for the comparison with the AP2 results in section 4.2.3.3.

The comparison between the *MG*-P1 and the *CE* simulations allows quantifying the effects of the group structure and to evaluate the reliability of the P1 approximation (a higher order of anisotropy may be considered). The comparison between the *CE* and the *MG*-P0\* simulations allows assessing the effect of considering isotropic the scattering in graphite. This could allow saving computing time in the deterministic full-core calculation.

The  $k_{eff}$  and the  $P/A$  ratio, with the respective uncertainties, and the corresponding core leakage obtained for the *CE* simulations are presented in

Table 4.XIV. The reactivity differences of the *MG* simulations from the *CE* ones are also shown.

**Table 4.XIV: T4 calculations realized with continuous energy (reference) or with P1 and P0\* 281-group cross sections for graphite (single pebble type)**

	$k_{eff}$	$\sigma$ [pcm]	P/A ratio	$\sigma$ [pcm]	Core Leakage [pcm]
$LT_{(CE)}$	1.10645	10	1.30105	104	13517
$\Delta\rho_{MG-P1\div CE}$ [pcm]	95	9	3	93	-91
$\Delta\rho_{MG-P0*\div CE}$ [pcm]	113	9	-4	87	-117
$HT_{(CE)}$	1.07559	10	1.23809	101	12202
$\Delta\rho_{MG-P1\div CE}$ [pcm]	-3	10	-4	100	-1
$\Delta\rho_{MG-P0*\div CE}$ [pcm]	29	10	-6	93	-35

The discrepancies in the production rate distribution between the *MG-P1* simulations and the *CE* ones are presented respectively in Table 4.XV and Table 4.XVI. These discrepancies results in a  $\Delta_{sf>1}^{\%} \tau_{PROD}$  of 1.62% and a  $\Delta_{HotSp.}^{\%} \tau_{PROD}$  of 0.32% for the *LT* and a  $\Delta_{sf>1}^{\%} \tau_{PROD}$  of 0.68% and a  $\Delta_{HotSp.}^{\%} \tau_{PROD}$  of 0.10% for the *HT* simulations.

One can notice that the discrepancies for the *LT* model are higher than for the *HT* one. Nevertheless, both are quite low and show that the *MG-P1* cross sections can be assigned to the graphite in the T4 reactor model, as it is done for the comparisons with the AP2 calculations, without deviate significantly from the results of a continuous energy simulation.

**Table 4.XV: Rel diff. on prod. shape factors of T4 LT simulation with MG-P1 XS from CE one**

CHAN A	CHAN B	CHAN C	CHAN D	CHAN E
-0.76%	-0.35%	-0.20%	-0.09%	-0.09%
-0.97%				-0.56%
-1.39%	-0.75%	-0.53%	-0.50%	-0.73%
-1.45%	-0.92%	-0.70%	-0.71%	-0.90%
-1.62%	-1.12%	-0.85%	-0.82%	-0.96%
-1.56%				-1.02%
-1.17%	-0.91%	-0.72%	-0.66%	-0.64%
-0.91%	-0.35%	-0.04%	0.07%	-0.14%
-0.32%	0.24%	0.45%	0.46%	0.27%
-0.08%				0.40%
0.04%	0.47%	0.68%	0.70%	0.62%
0.39%	0.85%	1.07%	1.13%	0.81%
0.74%				1.04%
0.86%	1.43%	1.55%	1.55%	1.35%
0.94%	1.44%	1.48%	1.75%	1.79%

**Table 4.XVI: Rel diff. on prod. shape factors of T4 HT simulation with MG-P1 XS from CE**

CHAN A	CHAN B	CHAN C	CHAN D	CHAN E
-1.28%	-0.90%	-0.73%	-0.63%	-0.80%
-0.72%				-0.48%
-0.25%	-0.33%	-0.19%	-0.29%	-0.36%
-0.03%	0.02%	0.02%	-0.08%	-0.08%
-0.30%	-0.27%	-0.12%	-0.13%	-0.20%
-0.51%				-0.17%
-0.13%	0.00%	0.11%	0.09%	-0.09%
-0.02%	0.13%	0.13%	0.19%	0.16%
-0.12%	-0.05%	0.12%	0.15%	-0.05%
-0.14%				0.05%
-0.20%	-0.03%	0.15%	0.20%	0.16%
-0.13%	0.13%	0.26%	0.15%	0.06%
0.07%				0.28%
0.08%	0.21%	0.43%	0.46%	0.50%
0.30%	0.34%	0.51%	0.42%	0.47%

The discrepancies in the production rate distribution between the *MG-P0\** simulations and the *CE* ones resulted in a  $\Delta_{sf>1}^{\%} \tau_{PROD}$  of 1.82% and a  $\Delta_{Hot Sp.}^{\%} \tau_{PROD}$  of 0.28% for the *LT* and a  $\Delta_{sf>1}^{\%} \tau_{PROD}$  of 0.75% and a  $\Delta_{Hot Sp.}^{\%} \tau_{PROD}$  of 0.12% for the *HT* simulations. These relative differences are similar to the ones observed between the *MG-P1* and the *CE* simulations. Thus, it appears that the larger contribution to these discrepancies is due to the multigroup structure of the cross sections rather than to the isotropic scattering approximation.

The low discrepancies observed between the *MG-P0\** simulations and the *CE* ones, both on the core  $k_{eff}$ , on the total core leakage and on the production rate distribution, show that considering isotropic scattering in graphite is an appropriate approximation in this case.

#### 4.2.3.4 Multiple Types Individually Positioned Pebbles

Keeping the same pebble positions used for the T4 models described in the previous section, six different burnup levels of 0, 15000, 30000, 50000, 75000 and 95000 MWd/t were randomly assigned, with uniform probability, to the fuel region of each pebble. The compositions associated to each burnup were obtained, as usual, depleting the reflected single pebble plus helium layer. The homogenized 281-group P1 cross sections were used in the T4 models.

Both low-temperature and high-temperature models were simulated, with the same temperature distribution as the one described in the previous section.

The reaction rates in each spectrum zone were scored over each pebble type separately and then summed up to obtain the total rate in the spectrum zone. To evaluate the associated standard deviation of this sum, the square root of the sum of the quadratic absolute differences was computed. This is not properly right since the reaction rates in the different types are not independent, but it was the only possible evaluation since the correlations between data are not known.

Three different random distributions of pebble burnup values have been simulated, which will be called D1, D2 and D3. The deviation from the average value of the total number of pebbles contained in the  $\frac{1}{4}$  reactor cavity divided by 6 (15931 pebbles) for each pebble type in the 3 distributions is shown in Table 4.XVII.

**Table 4.XVII: Deviation from the expected number of pebbles per type for the 3 burnup distributions**

Deviation from 15931 pebbles	D1	D2	D3
0 MWd/t	0.66%	0.40%	0.93%
15000 MWd/t	0.35%	-0.30%	0.11%
30000 MWd/t	0.89%	0.20%	-0.55%
50000 MWd/t	-0.53%	-0.78%	-0.55%
75000 MWd/t	-0.77%	-0.18%	0.26%
95000 MWd/t	-0.61%	0.65%	-0.20%

The fractions of each pebble type, contained in each spectrum zone, were computed during the ROOT geometry building, as explained in section 4.2.1, and provided as input data to the AP2 models. These were the only data that were changed between D1, D2 and D3.

In accordance with the results obtained in the previous section for a single pebble type, the AP2 calculations were performed using the 26-group and the 13-group structures, both with the relaxed convergence parameters.

The data gathering the comparison between the T4 reference results and the AP2 ones are resumed in Table 4.XVIII.

The production rate distributions obtained with T4, with the associated standard deviations, are presented in APPENDIX F from tables F.I to F.XII, together with the relative differences of the corresponding AP2 results. On the basis of  $k_{eff}$  precision and computing time, the 26-group appears slightly more adapted for the *LT* calculations and the 13-group for the *HT* ones. Thus, the AP2 results considered in APPENDIX F are the one obtained using the 26-group structure for the *LT* calculations and the 13-group structure for the *HT* ones.

**Table 4.XVIII: T4  $k_{eff}$  of *LT* and *HT* simulations ( $\sigma \sim 10$  pcm). Discrepancies of AP2 13- and 26-group calculations (P1-S<sub>8</sub> RZ) from T4 references and computing times (multiple types pebbles)**

	<i>LT</i> - D1	<i>LT</i> - D2	<i>LT</i> - D3	<i>HT</i> - D1	<i>HT</i> - D2	<i>HT</i> - D3
$k_{eff}$ - T4	1.15802	1.15724	1.15802	1.11156	1.11065	1.11145
P1-S <sub>8</sub> and 13-group structure						
$\Delta\rho$ [pcm]	165	123	146	63	43	57
$\Delta_{sf>1}^{\%} \tau_{PROD}^{HET}$	3.07%	2.64%	3.56%	2.66%	1.98%	3.19%
$\Delta_{Hot\ Sp.}^{\%} \tau_{PROD}^{HET}$	2.07%	0.14%	2.70%	1.17%	0.39%	2.28%
<i>SZ</i> - core it.	8	8	8	25	10	9
<i>Calc. time</i> [s]	2636	2256	2170	6516	5773	5410
P1-S <sub>8</sub> and 26-group structure						
$\Delta\rho$ [pcm]	-39	-83	-59	-72	-94	-83
$\Delta_{sf>1}^{\%} \tau_{PROD}^{HET}$	3.41%	2.88%	3.75%	2.51%	2.35%	3.01%
$\Delta_{Hot\ Sp.}^{\%} \tau_{PROD}^{HET}$	2.35%	0.35%	2.89%	1.46%	0.45%	2.09%
<i>SZ</i> - core it.	8	8	8	37	13	20
<i>Calc. time</i> [s]	4008	3480	3415	11580	8155	8984

From the results, it appears that the differences between the AP2 calculations and the reference T4 ones are always in an acceptable range, with the discrepancies on the production rate distribution < 3% at the hot spot and < 4% over the zones with a production density higher than the core average.

It must be observed, from the tables in APPENDIX F, that D3 has the hot spot located in SZ 8, differently than D1 and D2 which have it on SZ 9. The AP2 calculations rightly compute the position of the hot spot for all the distributions, thus taking properly into account the differences between them.

The agreement on the  $k_{eff}$  is very good; the reactivity discrepancy is lower than 100 pcm for all the cases, except for the *LT* 13-group calculations.

The *HT* results, which are the interesting ones for operational conditions, appear to be closer to the references than the *LT* ones.

#### 4.2.3.4.1 Reaction Rates per Pebble Type

As a final comparison between the T4 simulations and the AP2 calculations, a more detailed investigation can be done by analyzing the reaction rates of each pebble type individually in a spectrum zone. One possible observable quantity could be the distribution of the production rate over the six different types. Nevertheless, this quantity is influenced by the relative abundance of each pebble type in the zone. As it has been explained in section 4.2.1, these data contain an un-quantified uncertainty linked to manner in which the pebbles were positioned in the ROOT geometry. Thus, the relative differences of the AP2 results from the T4 ones would not be truly representative of the physical model precision. It is necessary to compare a value which does not depend on the fractions of the different pebble types contained in a zone. Thus, in each spectrum zone the ratio of the production rate over the absorption rate for each pebble type, noted as  $(P/A)_p$  ratio, was computed.

The results on the comparison made for the D1 *HT* model are shown for some spectrum zones in Table 4.XIX. The  $(P/A)_p$  ratios obtained in the T4 simulation are shown together with the respective uncertainties. The relative differences of the AP2 calculation results (P1-S<sub>8</sub> and 13-group structure) from the T4 ones are also presented.

**Table 4.XIX: production over absorption ratio per pebble type in T4 D1 *HT* simulations and rel. diff. of the computed values with AP2 13-group calculation (P1-S<sub>8</sub> RZ)**

	0 MWd/t	15000 MWd/t	30000 MWd/t	50000 MWd/t	75000 MWd/t	95000 MWd/t
<b>SZ 1</b>						
$(P/A)_p$ ratio	1.66	1.53	1.47	1.38	1.26	1.14
$\sigma$ [%]	0.55%	0.62%	0.60%	0.55%	0.58%	0.58%
$\Delta\%$ <sub>AP2-T4</sub>	-0.01%	0.29%	0.17%	0.57%	0.35%	-0.01%
<b>SZ 8</b>						
$(P/A)_p$ ratio	1.62	1.51	1.44	1.35	1.22	1.11
$\sigma$ [%]	0.26%	0.28%	0.25%	0.25%	0.27%	0.28%
$\Delta\%$ <sub>AP2-T4</sub>	0.48%	0.26%	0.48%	0.42%	0.61%	0.48%



	0 MWd/t	15000 MWd/t	30000 MWd/t	50000 MWd/t	75000 MWd/t	95000 MWd/t
<b>SZ 15</b>						
$\left(P/A\right)_p$ ratio	1.66	1.54	1.47	1.38	1.27	1.14
$\sigma$ [%]	0.65%	0.68%	0.68%	0.67%	0.64%	0.65%
$\Delta\%_{AP2-T4}$	0.55%	0.34%	0.22%	0.67%	0.24%	0.55%
<b>SZ 32</b>						
$\left(P/A\right)_p$ ratio	1.44	1.35	1.28	1.19	1.06	0.94
$\sigma$ [%]	0.23%	0.24%	0.22%	0.24%	0.23%	0.22%
$\Delta\%_{AP2-T4}$	-0.61%	-0.53%	-0.64%	-0.64%	-0.78%	-0.61%
<b>SZ 56</b>						
$\left(P/A\right)_p$ ratio	1.63	1.51	1.45	1.36	1.23	1.11
$\sigma$ [%]	0.23%	0.23%	0.22%	0.23%	0.23%	0.23%
$\Delta\%_{AP2-T4}$	0.17%	0.25%	0.16%	0.35%	0.14%	0.17%

Analyzing the results, in channel A the  $\left(P/A\right)_p$  ratios are higher for all the pebble types contained in SZ 1 and SZ 15, which are at the corner of the core cavity, compared to the ones contained in the central SZ 8. On the same way, at the core middle height, the ratio values are similar in SZ 15 and SZ 56, which are close to the lateral graphite reflectors, and both are higher than in SZ 32 of the central channel C.

One can notice that the most burnt pebbles with 95000 MWd/t, except in the top and bottom zones, have a  $\left(P/A\right)_p$  ratio lower than the core  $k_{eff}$ , meaning that this pebble type in these core positions act as a neutron sink rather than a neutron source, while still having fissions which deplete the fuel and produce power. In the central part of the core also the pebbles of 75000 MWd/t show the same trend.

To conclude, even when comparing the reaction rates at a more detailed scale that is, at the level of the different pebble types comprised in a zone, the developed model computes the production over absorption ratio per type within the  $3\sigma$  from the TRIPOLI4 results. This shows that the neutron exchanges between the pebbles of different type are properly modeled with the APOLLO2 "macro-stochastic" method.

#### 4.2.3.4.2 Analysis of the Computing time

The weak point of the calculations performed in the verification process is the computing time, which is clearly too high for industrial reactor design.

The calculations at high-temperature generally requested more SZ – core iterations to converge, and so a longer computing time. This is probably due to the increased importance of scattering in graphite reflectors, which could lead to an increase of the iterations needed to converge the coupling between the multi-pebble geometries (which account for the reflectors only by the entering currents through the contact surfaces) and the core RZ calculation.

In order to evaluate the capability to accelerate the calculation, the 13-group D2 *HT* calculation (which has the middle computing time between D1,D2 and D3) was analyzed in more detail and the total time shares associated to each main computational block are shown in Table 4.XX.

**Table 4.XX: Computing time shares of each main computational block in AP2 13-group D2 *HT* calculation (multiple type pebbles)**

Geometry and materials creation	0.08%
1D $S_N$ for reflectors homog.	7.71%
Multi-pebble geom. critical buckling homog.	2.20%
RZ – core iterations	
SN RZ core calculation	69.32%
Entering currents to SZs reconstruction	2.28%
Multi-pebble geom. homog. with currents and $k_{eff}$	18.41%

It is clear that the most time consuming part is represented by the core RZ computation that is performed with the  $S_N$  method. Usually, diffusion theory using a low number of energy groups (2 or 4) is applied for a 2D or 3D core calculation. To better understand how the RZ core calculation weights on the total time, the associated times of each RZ – core iterations are illustrated in Table 4.XXI, where the indication "SZs calculation" includes both the reconstruction of the fine groups entering currents in the zones and the  $P_{ij}$  calculations of the multi-pebble geometries.

**Table 4.XXI: Computing time of each SZ – core iteration in AP2 13-group D2 *HT* calculation**

Iteration n <sup>o</sup>	1	2	3	4	5	6	7	8	9	10
SZs calc. [s]	114	263	124	106	99	94	97	97	99	96
RZ $S_N$ [s]	898	1207	1123	44	49	56	55	54	55	54

For the SZs calculations, in iteration n° 1 the reflected multi-pebble geometries are computed with the critical buckling search assumption. In the second iteration, the surface currents are recovered from the core calculation for the first time. Thus, the necessary informatic structures associated to all the multi-pebble geometry objects have to be built, leading to a computing time higher than for the successive iterations. For all the successive iterations the data of the previous iteration are updated in the already existing structures and the flux computations are initiated with the converged flux of the previous SZ – core iteration. Consequently, starting from iteration n° 3 the computing time settles on a reduced stable value.

For the RZ  $S_N$  core calculation, in the first SZ – core iteration a maximum number of 100 external iterations is fixed for the flux computation which takes 898 s. In the others SZ – core iterations, the maximum number of external iterations for the  $S_N$  solver is fixed to 500 and this limit is never reached as the calculation converges before. Also, every core  $S_N$  calculation is initiated with the converged flux of the previous iteration. This explains the observed trend.

Computing time can be reduced by substituting the RZ  $S_N$  full-core calculation with diffusion. i.e., performing the initial calculation with a 6-group diffusion (which appeared to have a good agreement with the T4 reference on the  $k_{eff}$  and on the production rate distribution, as shown in Table 4.VI), only 160 s are required to converge. Furthermore, surely a shorter time would be associated to the further iterations initiated with the previous converged flux.

A simple and effective solution to reduce computing time of the core RZ  $S_N$  calculation, is to reduce the angular quadrature order. In a previous study concerning the RZ  $S_N$  calculation of the PBMR-400 core it was observed that the core eigenvalue, the axial power and flux distribution changed very little of the results of varying angular quadrature after  $S_4$  and scattering order after P1.<sup>88</sup> Thus, the *LT* and the *HT* models have been recomputed, using respectively the 26-group and the 13-group structure, with a P1- $S_4$  approximation in the RZ core calculation. The results are presented in Table 4.XXII.

As it can be seen from the results, the adoption of the  $S_4$  angular quadrature, instead of the  $S_8$ , has practically no effects on the  $k_{eff}$  and degrades very little (<0.5%) the relative differences for the reference production rates. Nevertheless, it allows reducing consistently the computing time, with an average gain factor of 1.7 for the *LT* models and of 1.6 for the *HT* ones. Moreover, for the *HT* models it allows stabilizing the number of SZ – core iterations required for convergence (to about 8 or 9) for all the 3 random distributions.

Consequently, in Chapter 5, where the research of the equilibrium core composition is performed for the reactor operating at high temperature, the P1- $S_4$  approximation and the 13-group structure will be used in the RZ core calculations

**Table 4.XXII: Discrepancies of AP2 26-group *LT* and 13-group *HT* calculations (P1-S<sub>4</sub> RZ) from T4 references and computing times (multiple types pebbles)**

	<i>LT</i> – D1	<i>LT</i> – D2	<i>LT</i> – D3	<i>HT</i> – D1	<i>HT</i> – D2	<i>HT</i> – D3
$k_{eff}$ - T4	1.15802	1.15724	1.15802	1.11156	1.11065	1.11145
	P1-S <sub>4</sub> and 26-group structure			P1-S <sub>4</sub> and 13-group structure		
$\Delta\rho$ [pcm]	-40	-83	-59	61	42	50
$\Delta_{sf>1}^{\%} \tau_{PROD}^{HET}$	3.40%	2.92%	3.85%	3.00%	2.13%	3.08%
$\Delta_{Hot Sp.}^{\%} \tau_{PROD}^{HET}$	2.44%	0.46%	2.98%	1.68%	0.84%	2.29%
<i>SZ</i> – core it.	8	8	8	8	9	9
<i>Calc. time</i> [s]	2400	2081	2066	3741	3238	2962

Finally, an effective way to accelerate the calculation scheme would be to parallelize the  $P_{ij}$  calculations of the multi-pebble geometries associated to each spectrum zone. As Table 4.XXI shows, after the initial iterations the core calculation takes less time than the corresponding SZs calculations. Thus, parallel computing of the multi-pebble geometries would be interesting, and also straightforward. Once the currents entering the spectrum zones are recovered from the core calculation, the source term for each  $P_{ij}$  calculation, together with the core  $k_{eff}$ , can be assigned to an individual processor. The flux computations in the multi-pebble geometries could then be solved in parallel and, afterward, the homogenized cross sections from each spectrum zone could be recovered and assigned to the next core calculation. This will lead to a time gain, for the SZs calculation part, of the order of the number of the core spectrum zones.

#### 4.2.3.4.3 Sensitivity Analysis to $pkf$ and $p_{k'/k}^{b,b}$ Variations

To conclude the verification process, the sensitivity of the core  $k_{eff}$  and of the production rate distribution was tested with respect to the variation of the packing fraction ( $pkf$ ) and  $p_{k'/k}^{b,b}$  boundary-to-boundary probabilities. The AP2 D1 *HT* calculation (P1-S<sub>8</sub> and 13 groups) was taken as reference. Zones' packing fractions and  $p_{k'/k}^{b,b}$  were varied, and the corresponding results compared to the reference.

As depicted in Table 4.IV, the packing fractions computed with T4 for each spectrum zone differ from the ones computed with ROOT, which were used in the verification calculations. The T4 ones were used here. The resulting model does not present a significant variation in  $k_{eff}$  ( $\Delta\rho < 4$  pcm) and the production rate distribution differs from the reference (with ROOT computed  $pkf$ ) as shown in Table 4.XXIII.

**Table 4.XXIII: Rel. diff. of AP2 13-group D1  $HT$  calculation (P1-S<sub>8</sub> RZ), using T4 computed packing fractions, with the reference, where ROOT computed  $pkf$  are used**

CHAN A	CHAN B	CHAN C	CHAN D	CHAN E
0.53%	0.26%	0.16%	0.11%	-0.23%
0.54%	0.21%	0.10%	0.09%	-0.21%
0.49%				-0.39%
0.46%	0.19%	0.05%	0.01%	-0.40%
0.42%	0.11%	-0.05%	-0.12%	-0.45%
0.29%				-0.49%
0.31%	0.11%	-0.11%	-0.12%	-0.48%
0.37%	0.03%	-0.10%	-0.14%	-0.49%
0.37%	0.03%	-0.12%	-0.16%	-0.50%
0.30%				-0.46%
0.38%	0.05%	-0.06%	-0.10%	-0.49%
0.40%	0.13%	-0.01%	-0.06%	-0.44%
0.41%	0.17%	0.06%	0.05%	-0.36%
0.61%				-0.29%
0.58%	0.23%	0.16%	0.17%	-0.33%

It is evident that the variations of the production shape factors closely follow those of the packing fraction. On the average, the difference between the  $pkf$  values for T4 and those computed with ROOT were of +0.4% in channel A and -0.5% in channel E, with lower values in the central channels. The same trend is observed here with similar amplitudes on the production distribution.

This means that the packing fraction affects significantly the production rate distribution, but it has less impact on the  $k_{eff}$  value, for which the major contribution is the total number of pebbles contained in the cavity and the fraction of each type

Nevertheless, this does not mean that a large variation of the packing fraction distribution would not affect the  $k_{eff}$ . As shown by other authors in Ref. 121, considering an average packing fraction, instead of higher ones in the central channels and lower ones in the channels close to the reflectors, decreases the  $k_{eff}$ . This is connected to the compaction of the bed in the central channels, which leads to a positive reactivity effect.

In order to evaluate the sensitivity with respect to the variation of the  $p_{k'k}^{b,b}$ , the values which were used for the reference model were all divided or multiplied by a factor 10. The model with lower  $p_{k'k}^{b,b}$ , which simulates a bed with less leakage in between the pebbles, resulted in no observed  $k_{eff}$  variation and the one with higher  $p_{k'k}^{b,b}$  had a  $\Delta\rho$  of -4 pcm from the reference. This variation is negligible, but it shows that an increase in  $p_{k'k}^{b,b}$  correspond effectively to a negative reactivity effect. The variations on the production rate distribution are shown in Table 4.XXIV for the lower  $p_{k'k}^{b,b}$  values and in Table 4.XXV for the higher ones.

**Table 4.XXIV: Rel. diff. of AP2 13-group D1 HT calculation (P1-S<sub>8</sub> RZ) with  $p_{k'k}^{b,b}/10$  from ref.**

CHAN A	CHAN B	CHAN C	CHAN D	CHAN E
0.14%	-0.07%	-0.03%	-0.08%	0.14%
0.11%	-0.09%	-0.04%	-0.09%	0.14%
0.19%	-0.07%	-0.03%	-0.05%	0.14%
0.16%	-0.05%	0.00%	-0.05%	0.11%
0.13%	-0.04%	-0.02%	-0.02%	0.09%
0.08%	-0.04%	0.00%	-0.03%	0.13%
0.02%	-0.02%	0.01%	-0.02%	0.11%
0.08%	-0.03%	-0.03%	-0.06%	0.15%
0.16%	-0.06%	-0.02%	-0.05%	0.15%
0.23%	-0.02%	-0.03%	-0.05%	0.17%
0.05%	-0.03%	-0.03%	-0.06%	0.10%
0.18%	-0.06%	-0.02%	-0.05%	0.11%
0.24%	-0.07%	-0.03%	-0.04%	0.15%
0.15%	-0.03%	-0.03%	-0.06%	0.09%
0.00%	-0.07%	-0.03%	-0.04%	0.09%

**Table 4.XXV: Rel. diff. of AP2 13-group D1 HT calculation (P1-S<sub>8</sub> RZ) with  $p_{k'k}^{b,b} \cdot 10$  from ref.**

CHAN A	CHAN B	CHAN C	CHAN D	CHAN E
-0.44%	0.33%	0.21%	0.18%	-1.55%
0.08%	0.37%	0.38%	0.29%	-0.96%
0.06%	0.41%	0.33%	0.27%	-0.95%
0.02%	0.30%	0.30%	0.21%	-1.01%
0.00%	0.25%	0.24%	0.21%	-1.15%
-0.15%	0.29%	0.22%	0.17%	-1.12%
-0.25%	0.24%	0.23%	0.17%	-1.16%
-0.20%	0.25%	0.19%	0.14%	-1.10%
-0.11%	0.29%	0.25%	0.19%	-1.16%
-0.05%	0.25%	0.25%	0.19%	-1.15%
-0.23%	0.14%	0.04%	-0.04%	-1.23%
-0.08%	0.33%	0.21%	0.15%	-1.16%
-0.16%	0.25%	0.25%	0.19%	-1.12%
-0.27%	0.25%	0.25%	0.19%	-1.23%
-2.10%	0.14%	0.04%	-0.04%	-1.84%

As it can be seen from the distribution of the relative differences, the lower  $p_{k'k}^{b,b}$  values gave a higher production in the reflector-adjacent channels A and E and a lower one in the central channels. The opposite trend is associated to the higher  $p_{k'k}^{b,b}$  values. This

means that the influence of the  $p_{k'k}^{b,b}$  is stronger on the side channels than in the central ones. In fact, a higher  $p_{k'k}^{b,b}$  corresponds to a higher probability for neutrons entering a spectrum zone of travelling through the bed of pebbles without entering any pebble. Close to the reflectors this means that a higher fraction of neutrons leak out of the cavity without contributing to the production in the zone. The variation on the shape factors in the central zones could be mainly due to a renormalization effect.

It is interesting to observe that for higher  $p_{k'k}^{b,b}$  values the shape factors in the external channel E decreases much more than the ones in channel A. This could be due to the fact that neutrons leaking out of the cavity in E enter the external reflector; since the one leaking out in A enter the internal one and so have a higher probability of reentering the cavity after several collisions.

Nevertheless, except for the effects on channel E zones, the variations of one order of magnitude of the  $p_{k'k}^{b,b}$  values did not lead to large variations in the reaction rate distribution.

Hence, the sensitivity of the results toward the boundary-to-boundary geometrical probabilities values appears to be quite low, with sensible effects observable only on the production rates of the external channel zones.

### 4.3 Validation on the HTR-10 First Criticality

The HTR-10 is a 10 MW<sub>th</sub> pebble bed high temperature reactor built in the site of the Institute of Nuclear Energy Technology (INET) of Tsinghua University, near Beijing in China.<sup>122</sup> Its first criticality was attained on December 1, 2000. It is a cylindrical type reactor, where the cavity has a diameter of 180 cm, a height of 197 cm and a cone-shaped bottom. The external graphite reflector has an effective thickness of 100 cm and the top reflector of 130 cm. In the bottom reflector there is a defueling tube of 50 cm diameter to carry out the pebbles for a continuous reload operation, using the typical multi-pass refueling scheme of pebble bed reactors. Several holes are drilled in the external reflector: 10 control rod channels and 3 experimental channels, each of 13 cm diameter, 7 ellipsoid shape boron absorber ball channels with a 16x6 cm diameter, 20 helium flow channels with of 8 cm diameter for the cold helium inlet.

The HTR-10 vertical-cut schematic is shown in Figure 4.7, since a horizontal core view in Figure 4.8.

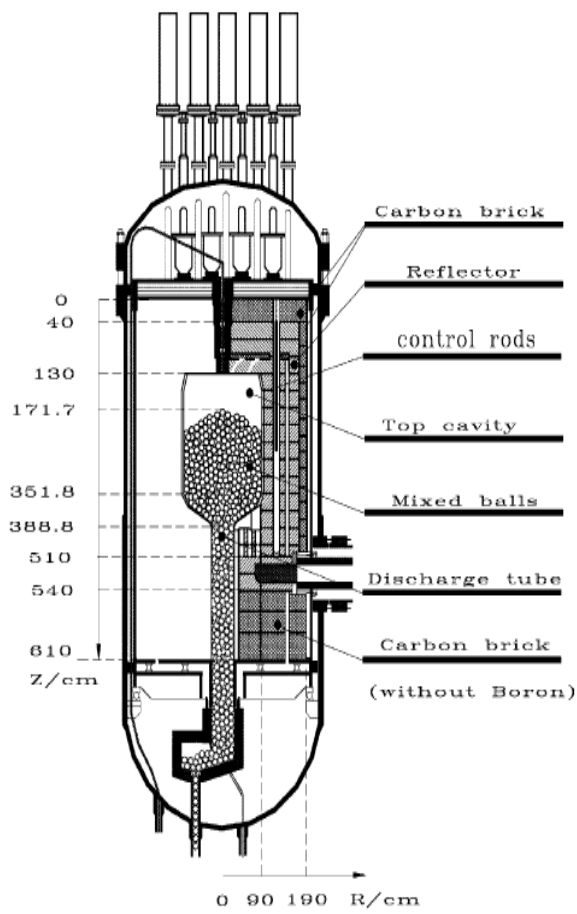


Figure 4.7: HTR-10 vertical-cut schematic<sup>122</sup>

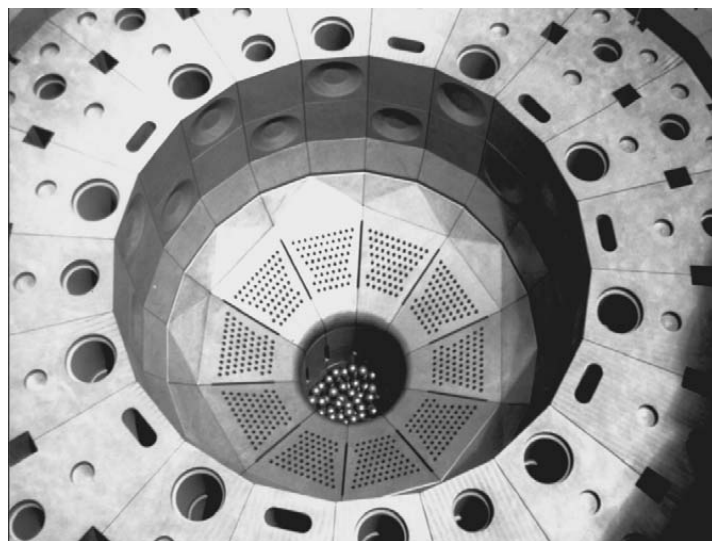


Figure 4.8: HTR-10 horizontal core view<sup>122</sup>



Together with the fuel pebbles containing the  $UO_2$  TRISO microparticles, the HTR-10 was charged also with graphite-only moderator pebbles (called "dummy balls"). The characteristics of the pebbles, fabricated in China and used in the HTR-10, are summarized in Table 4.XXVI.

**Table 4.XXVI: Characteristics of HTR-10 graphite and fuel pebbles**

<i>Pebbles packing fraction in the core</i>	0.61
<b><i>Fuel pebbles</i></b>	
<i>Pebble diameter [cm]</i>	6.0
<i>Fuel zone diameter [cm]</i>	5.0
<i>Density of graphite in matrix and outer shell [g/cm<sup>3</sup>]</i>	1.73
<i>Heavy metal (uranium) loading (weight) per pebble [g]</i>	5.0
<i><sup>235</sup>U enrichment (weight)</i>	17%
<i>Equivalent natural boron impurities in uranium [ppm]</i>	4.0
<i>Equivalent natural boron impurities in graphite [ppm]</i>	1.3
<i>Radius of <math>UO_2</math> kernel [mm]</i>	0.25
<i><math>UO_2</math> density [g/cm<sup>3</sup>]</i>	10.4
<i>Coating layers materials (starting from kernel)</i>	PyC/PyC/SiC/PyC
<i>Coating layers thickness [mm]</i>	0.09/0.04/0.035/0.04
<i>Coating layers density [g/cm<sup>3</sup>]</i>	1.1/1.9/3.18/1.9
<b><i>Moderator pebbles</i></b>	
<i>Pebble diameter [cm]</i>	6.0
<i>Graphite density [g/cm<sup>3</sup>]</i>	1.84
<i>Equivalent natural boron impurities in graphite [ppm]</i>	0.125

To enhance confidence in predictions of neutron physics behavior, the International Atomic Energy Agency (IAEA) set up a Coordinated Research Project (CRP) on validity of safety related physics calculations for HTGRs.<sup>123</sup> Countries participating in this CRP include China, France Japan, Switzerland, Germany, Indonesia, the Netherlands, the USA and the Russian Federation. The benchmark analyses regarded the HTR-10 start-up core physics experiments and included the calculation of the critical bed height of initial criticality (benchmark problem B1), the temperature coefficient of the fully loaded core (benchmark problem B2) and the control rod worth for initial and full core (benchmark problem B3).

To evaluate the control rod worth, a proper modeling of the graphite reflector should be implemented and this goes forward the scope of this thesis. Regarding the temperature coefficient calculation of the fully loaded core, no physical measurements have been done on it, meaning that its calculation can not be used for validation purposes. As a consequence, only the benchmark problem B1 has been tackled.

The RZ model of the reactor, together with the equivalent graphite densities, computed averaging the void spaces, and natural boron impurities of each region, was furnished by the benchmark organizers. A schematic of the RZ model is shown in Figure 4.9.

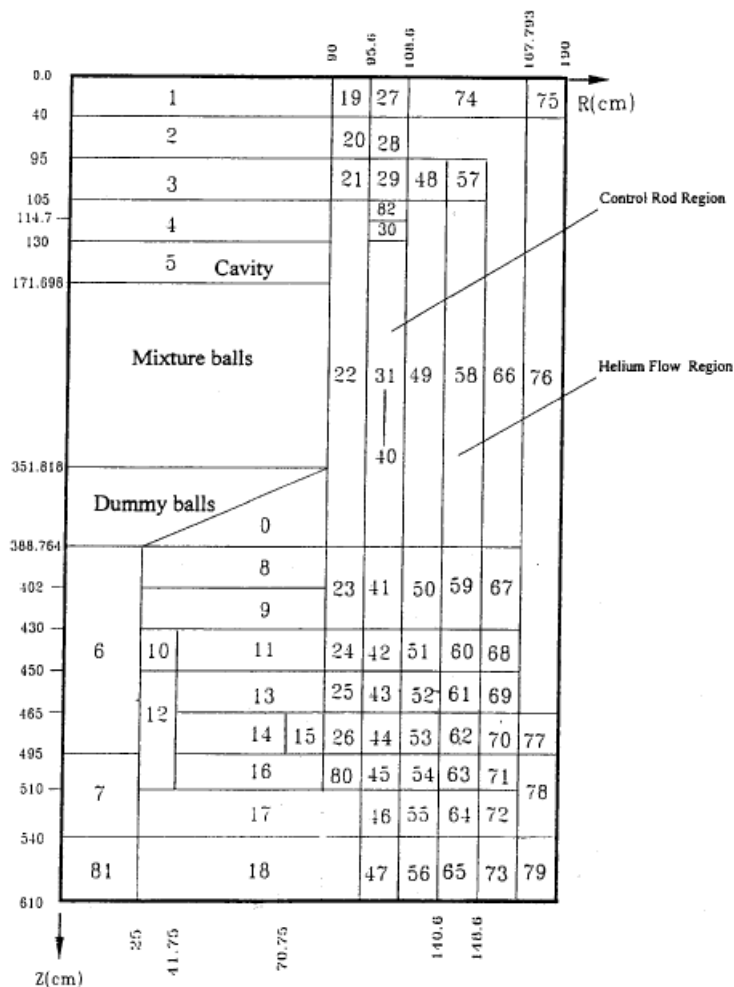


Figure 4.9: RZ model of HTR-10 (different materials depicted)<sup>123</sup>

The first criticality experiment of the HTR-10 was carried out in moist air atmosphere at 15 °C, at a pressure of 0.1013 MPa. For the calculation, the relative moisture of the air has been assumed as 100%. The moist air has been considered in the upper cavity and in the space between the pebbles in the core. Under the condition of saturation humidity, the density of vapor in the moist air is equal to  $2.57 \cdot 10^{-5} \text{ g/cm}^3$ , so the density of the moist air is about  $1.175 \cdot 10^{-3} \text{ g/cm}^3$  and the density of air is about  $1.149 \cdot 10^{-3} \text{ g/cm}^3$ .

Finally, the weight proportion in air of nitrogen and oxygen were 75.53% and 23.14% respectively.

In the experiment, the first criticality was reached when a total number of 16890 pebbles were loaded into the reactor core, of which 9627 were fuel pebbles and 7263 were graphite moderator pebbles, for a ratio of 57:43. This loading corresponds to a loading height of 123.06 cm.

### 4.3.1 APOLLO2 Reactor Model and Results

The RZ geometry of the APOLLO2 model has the same boundaries as the schematic shown in Figure 4.9, except for the conical shape of the lower dummy balls and the bottom reflector indicated with material 0. To describe this region a unique material has been used mixing the dummy balls, the inter-pebble helium and the graphite reflector.

The part of the cavity filled with the mix of fuel and moderator pebbles has been divided in 5 radial channels. The boundaries of the channels are showed in Table 4.XXVII. The external channel is radially thinner than the others in order to capture the streaming effect through the rearranged bed close to the reflector wall.

**Table 4.XXVII: Radial positions of channels boundary in AP2 model of HTR-10**

	<i>Chan. A</i>	<i>Chan. B</i>	<i>Chan. C</i>	<i>Chan. D</i>	<i>Chan. E</i>
<i>Ext. radius [cm]</i>	21.15	41.75	60.91	80.38	90.0

The channels have then been subdivided axially in 4 or 6 or 8 equivalent-height spectrum zones, giving 3 different number of total spectrum zones in the core of 20, 30, 40. This has been done in order to investigate the influence of the spectrum zone core subdivision on the  $k_{eff}$ . It has to be noticed that a spectrum zone should comprise a group of pebbles with similar spectral characteristics and that the optimal boundaries of the zone should lie where some spectral index varies.<sup>111</sup> Thus, differently from the case of the spatial meshing for a discretized problem, a larger number of zones does not necessarily correspond to a better physical representation.

Every spectrum zone is associated to a multi-pebble geometry composed by 2 pebble types, corresponding to the HTR-10 fuel pebbles and moderator pebbles in proportion 57:43. A constant packing fraction of 0.61 has been used. The  $p_{k'/k}^{b,b}$  computed in section 3.4 have been used, also if they have been computed on a distribution of pebbles corresponding to the annular type PBMR-400 core. Nevertheless, the data corresponding to the internal channels and to the external one can be used because, as it was shown in section 4.2.3.4.3, the sensitivity of the  $k_{eff}$  to the  $p_{k'/k}^{b,b}$  values is very small.

Both the  $P_{ij}$  and the RZ  $S_N$  calculations were performed using the 281-group SHEM structure issued from the JEFF-3.1.1 library. This leads to high computing times, but for the validation benchmark problem this is not a main worry. On the other side, avoiding

the energy homogenization in the RZ  $S_N$  simplified the reflector treatment as no 1D  $S_N$  calculations are needed.

All the other parameters (spatial mesh size, convergence precisions, P1 cross sections) have the optimized values obtained in the previous verification part.

The first calculations were carried out with a fixed core height of 123.06 cm, corresponding to the experimental critical height. Humid air atmosphere has been considered and a uniform 15 °C core temperature distribution.

The  $k_{eff}$  computed with the APOLLO2 model and different numbers of spectrum zones are shown in Table 4.XXVIII. The total number of pebbles contained in the core varies with the total number of spectrum zones. The reason for this is that each multi-pebble geometry comprises a whole number of pebbles. This number is computed with the corresponding zone packing fraction and volume, so that it is affected by a round off error.

**Table 4.XXVIII: Computed HTR-10  $k_{eff}$  for 123.06 cm height core with diverse SZ number in the AP2 model**

	$k_{eff}$	$\Delta\rho [pcm]$	$N^\circ Pebbles$
20 SZ	1.01542		16888
30 SZ	1.01596	52	16896
40 SZ	1.01609	65	16896

From these results, it appears that the variation of the spectrum zones number does not impact significantly the  $k_{eff}$  and that the greater values for 30 and 40 SZ are mainly due to the 8 more mixed pebbles contained in the core. As a consequence, the subdivision in 20 SZ that has been chosen as the corresponding core contains the closer number of total pebbles to the reference of 16890.

From these first results it appears that the computed  $k_{eff}$  value for the critical core height is largely supercritical. This is expectable and it is due to the fact that in the RZ modeling of the reactor the streaming effect of control rod holes, coolant channels and boron absorber ball channels is not considered. A three-dimensional core calculation is necessary to evaluate the effect on reactivity of neutron streaming through these void channels drilled in the external reflector. The Chinese team performed the benchmark calculations both using the VSOP code both the Monte Carlo code MCNP<sup>124</sup> and reported a correction factor of -1.2%  $\Delta k/k$  to be applied to the RZ calculation in order to account for this streaming effect.

In a more recent study,<sup>79</sup> the first criticality of the HTR-10 has been computed by two different models with the Monte Carlo module KENO IV of the SCALE 6 code system: a Simplified and a High-Fidelity model. Both models describe the bed of pebbles using the same lattice disposition. They differ in the way the void channels in the reflector are represented. In the Simplified model the holes are homogenized with the reflector materials and the benchmark-furnished densities for the RZ model are used. In the High Fidelity model all the void channels drilled in the reflectors are explicitly described in

the geometry. The physical conditions in which these two models are computed being the same, and corresponding to the HTR-10 first criticality experimental conditions, the difference in the resulting core  $k_{eff}$  measures the reactivity lost associated to the streaming effect in the reflector holes. The computed  $k_{eff}$  of the Simplified model was 1.02804 with  $\sigma = 27$  pcm, since for the High-Fidelity model it was 1.01399 with  $\sigma = 27$  pcm, thus resulting in a streaming effect reactivity lost of 1.35%  $\Delta k/k$ . This value is slightly higher than the one reported by the Chinese team and it will be used for the APOLLO2 model validation.

The calculations with the 20 SZ APOLLO2 model have been performed for different core heights. The results on the  $k_{eff}$  relative difference  $(k_{eff} - 1)/k_{eff}$ , both as obtained from the APOLLO2 calculations and corrected by the streaming coefficient, are represented in Figure 4.10.

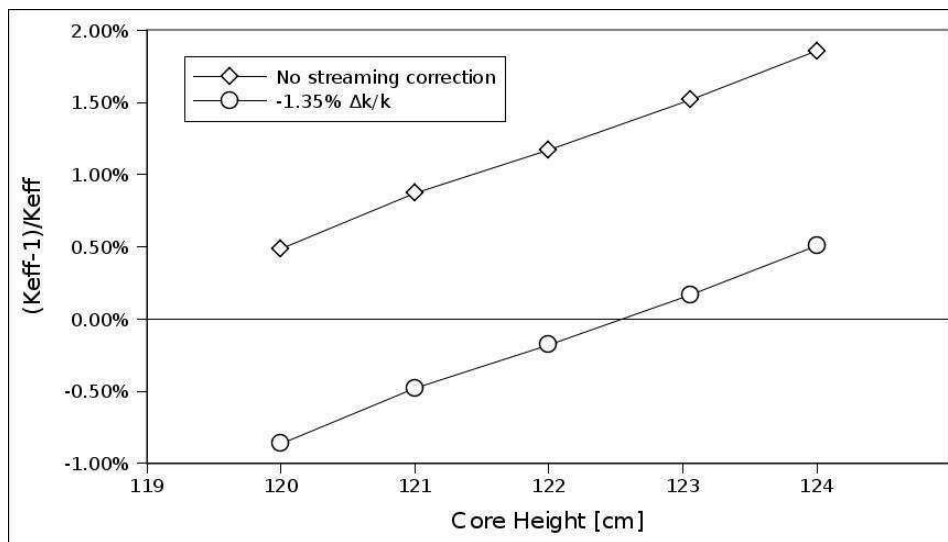


**Figure 4.10: HTR-10  $k_{eff}$  varying with core height. -1.35%  $\Delta k/k$  streaming correction applied to AP2 results**

Interpolating the streaming corrected results, the computed core critical height is of 122.55 cm, corresponding to 16819 mixed pebbles, which is 77 mixed pebbles fewer than the experimental result. The computed number of critical mixed pebbles and the experimental number are in good agreement, with a relative difference of -0.42%.

The VSOP calculation performed by the Chinese predicted the critical core with 16759 pebbles, which is 60 pebbles farther from the experimental value (-137 pebbles) than the result obtained with APOLLO2.

Finally, as the initial benchmark specifications were formulated with a homogeneous core temperature of 27 °C, the APOLLO2 calculations have also been performed with moist air at this temperature. The computed reactivity lost at the critical height when the core temperature increases from 15 °C to 27 °C is of -153 pcm. The interpolated critical height resulted of 123.02 cm, corresponding to 16885 pebbles, increasing by 66 mixed

pebbles the required number at 15 °C. Moreover this result is very close to the Chinese one, who evaluated the corresponding reactivity lost to 62 mixed pebbles.

In conclusion, the validation calculations on the HTR-10 first criticality confirmed the very good capability of the developed APOLLO2 model to compute the  $k_{eff}$  of a pebble bed reactor charged with different pebble types. Nevertheless, due to the limitations of a 2D core model, the streaming effect associated to the void channels in the reflector have to be determined in a separate study. However, since the reflector configuration is known, this study can be simply performed once by two Monte Carlo simulations, one considering a graphite reflector where the voids are homogenized and one describing explicitly the void channels. In this study the whole bed of pebble can be described by a homogeneous equivalent material or by a lattice disposition.

#### 4.4 Conclusions to the Chapter

In this Chapter the method developed in APOLLO2 for the neutronic calculation of PBRs has been verified with several Monte Carlo reference simulations of a simplified PBMR-400 model and validated with the first criticality experiment of the HTR-10.

##### Conclusions on verification

Firstly, simulations with the spectrum zones described with a homogeneous material were carried on. They allow determining the proper RZ spatial mesh, the number of broad groups, the scattering order and the convergence parameter to be used.

Diffusion calculations of the core were tested too with the CRONOS2 code. This showed the potential gain in computing time which could be achieved using diffusion as the low-order operator for the full-core calculation instead of the discrete ordinates diamond differencing method.

Successively, pebbles were individually positioned in the Monte Carlo geometry.

The use of multigroup P1 cross sections for describing the graphite reflector in Monte Carlo geometry has been verified. The relative differences on the Monte Carlo simulations, using rather continuous or 281-group P1 cross sections, showed that assuming isotropic scattering results on a core reactivity difference of 95 pcm at low temperature and -4 pcm at high temperature. The maximum difference on the production densities, over the spectrum zones with a value higher than core average, is of 1.62% at low temperature and 0.68% at high temperature.

A comparison between different ways of computing the spectrum zones reaction rates shows that, while computed with the fine-group heterogeneous fluxes over the multi-pebble geometries, the rates better match the Monte Carlo reference.

Investigations on the entering currents from the graphite reflectors were performed in order to understand the trend of the relative difference between the APOLLO2 and the T4 results. A higher thermalized current entering the core cavity from the lateral reflectors have been observed in APOLLO2. More studies are needed to explain this discrepancy.

A sensitivity analysis on the core eigenvalue and reaction rates to the variations of the zones' packing fraction and the  $p_{k'k}^{b,b}$  boundary-to-boundary probabilities was performed.

It showed that varying the packing fraction of an half of percent created a variation of the same order on the production shape factors, with practically no effects on the  $k_{eff}$ . The variation of the  $p_{k'k}^{b,b}$  of an order of magnitude did not influence the core eigenvalue and only in a small manner (~1%) the production shape factors of the external channel zones while increasing.

Both a low temperature (*LT*) and a high temperature (*HT*) models were analyzed. It has been determined that the best results are obtained using 26 broad groups for the *LT* and 13 broad groups for the *HT*, with a P1-S<sub>4</sub> approximation, in the core RZ flux computation. This allowed computing the simplified PBMR-400 model containing a random mix of 6 different burnup level pebbles in a reasonable computing time (<1h), both for the *LT* (faster) and the *HT* model. The reactivity discrepancy from the T4 references resulted smaller than 100 pcm and the relative differences on the production rate distribution were smaller than < 3 to 4% in the zones with a shape factor larger than 1, and < 3% on the hot spot.

These observed discrepancies on  $k_{eff}$  and production shape factors are sufficiently small to perform PBR safety studies and they fit the level requested for PWR calculations.

Nevertheless, the computing time remains high. This is mostly due to the high computing time spent in the RZ S<sub>N</sub> flux solver. A solution could be envisaged using diffusion as the low-order core flux solver operator. A small decrease in precision, especially on the reaction rate distribution, was observed with diffusion, but this was not evaluated while computing the heterogeneous reaction rates. Another practical and effective solution is the parallelization of the multi-pebble geometries P<sub>ij</sub> calculations. This would be mostly useful after the first spectrum zones – core iterations, when the core flux solver initiated with the previous iteration flux values speed up greatly the convergence.

Even when comparing the reaction rates at a more detailed scale that is, at the level of the different pebble types comprised in a zone, the developed model computes the production over absorption ratio per type within the 3σ from the TRIPOLI4 results. This shows that the neutron exchanges between the pebbles of different type are properly modeled with the APOLLO2 "macro-stochastic" method.

### Conclusions on Validation

The developed APOLLO2 model was then validated with the first criticality experiment of the HTR-10. The critical number of pebbles to be introduced in the core was evaluated. Compared to the experimental value of 16890 mixed (graphite and fuel) pebbles, the APOLLO2 model evaluates the critical number only to 77 pebbles less. This is a very good agreement, better than the one obtained with a lot of other codes. Nevertheless, the streaming effect associated to the void channels in the reflectors have to be determined in a separate Monte Carlo study, focused on detailed reflector geometry and simply representing the pebble bed core by a homogeneous material.

<b>5</b>	<b>Search of the Equilibrium Core .....</b>	<b>129</b>
5.1	Survey of Existing Codes Methodologies .....	132
5.2	Developed Method in APOLLO2.....	137
5.2.1	Depletion Algorithm.....	138
5.2.2	Mixing Algorithm.....	142
5.3	HTGRs Fuel Cycles.....	144
5.4	Equilibrium Core Calculations for Different Fuel Cycles.....	146
5.4.1	Low Enriched Uranium Fuel Cycle.....	149
5.4.1.1	Average Composition Pebble Approximation.....	153
5.4.1.2	Limitations of the Implemented Mixing Algorithm.....	158
5.4.2	Plutonium Based Fuel Cycle .....	161
5.4.2.1	Average Composition Pebble Approximation.....	166
5.4.3	Mixed Plutonium – Minor Actinides Based Fuel Cycle .....	171
5.4.3.1	Average Composition Pebble Approximation.....	175
5.5	Conclusions to the Chapter.....	179

## 5 Search of the Equilibrium Core

The continuous fuel reloading and the downward flow of the pebbles through the core lead to specific features for the fuel cycle in pebble bed reactors that do not exist in the most common reactor cores (PWR, BWR, ...). Usually, for these reactors, the fuel is loaded periodically (intervals varying from 12 to 18 months depending on the reactor design and the fuel loading strategy). During the fuel reloading, a fraction of the fuel assemblies is discharged and replaced with fresh fuel assemblies. After the reloading phase, the reactor operates until the core becomes under-critical. For such operation, it is necessary to have an excess reactivity at the beginning of the cycle, this reactivity being compensated by burnable poisons, boron diluted in water and control rods. The loss of reactivity during core operation is correlated to the fuel depletion (loss of fissile isotopes), while the average burnup of the core increases.

As it has been explained in section 1.3, in systems such as PBRs, where a continuous reloading strategy is adopted, the initial excess reactivity of the cold state core with all rod extracted does not need to be as large as for a BOL (Beginning Of Life) PWR core. Due to the continuous reloading, at hot core full power conditions no reactivity excess is needed to compensate the loss of reactivity during operation. Only a small reactivity excess is maintained to ensure the fine reactivity regulation. Since the fresh fuel is continuously inserted in the core and the depleted one extracted, after a start-up period



called running-in phase, an equilibrium condition is reached where the average burnup of the core does not change with time. This equilibrium core burnup is targeted during the reactor design in order to ideally ensure a critical core with no control rods inserted. In reality, a slightly over-critical core is designed in order to ensure the reactivity control in nominal operation. The analysis of the non-equilibrium core is important during the running-in phase corresponding to the transition from the fresh core to the equilibrium one. However, this phase is relatively short compared to the period in which the reactor will be operated at full power with an equilibrium core (for the HTR-10 the running-in phase is estimated to last about 1100 Equivalent Full Power Days (EFPD), to be compared with the average irradiation time of a fuel pebble in the equilibrium core of 1080 EFPD).<sup>125</sup> As a consequence, the major part of the works conducted for PBRs reactor design concern the equilibrium core conditions for which are performed the neutronic and thermal-hydraulic calculations, the safety analysis and the fuel cost estimation. Most of the performance and licensing calculations assume the equilibrium core configuration.

The configuration of the equilibrium core depends also on the refueling strategy adopted for a specific Pebble Bed Reactor design. Three possible fuel management schemes have been studied for PBRs: the "OTTO" (Once-through-then-out), the "peu-à-peu" and the "multipass" (also called MEDUL in reference to the first build AVR reactor).

- In the OTTO scheme the fresh fuel pebble is inserted on the top of the pebble bed filling the reactor cavity (except for the upper void space) and it flows once through the core, then it is discharged and sent to the spent fuel tank.
- In the peu-à-peu scheme, the initially loaded pebbles fill up only a partial height of the reactor cavity, which is generally higher than the one designed for the other fuel management schemes. The pebbles do not flow through the reactor, but fresh pebbles are periodically dropped on the top of the bed in order to compensate for the reactivity lost due to fuel depletion, since the cavity is not completely filled. The core is then discharged and a new cycle begins.
- In the multipass scheme, a pebble which has already flown through the reactor is extracted from the bottom of the core and then its burnup is estimated by an indirect measure. If the measured burnup does not exceed the target limit fixed for recycling, the pebble is pneumatically re-transported on the upper part of the reactor and dropped on the top of the bed, both randomly or in a specific radial position, to pass again through the core. If the measured burnup exceed the target limit, the pebble is discarded and sent to the spent fuel tank, and a fresh pebble is dropped on the top of the core instead.

The OTTO and the peu-à-peu schemes have been studied but not really envisaged for a realistic reactor application. The disadvantage of the peu-à-peu scheme is the refueling period that implies a reactor shutdown, lowering the availability factor. Compared to the OTTO cycle, where the burnup of the pebbles vary axially from zero to the maximum value, the multipass has the advantage of flattening the axial flux profile, because the

average burnup of the mixture of pebbles with different number of passes through the reactor cavity has a smaller variation from the top to the bottom of the core. As a consequence, the power peaking factors are reduced so as the maximum pebble center temperature at operational condition for a given total core power and coolant temperature. Moreover, in the case of a Depressurized Loss of Coolant (DLOFC) accident, which can be considered as the worst case scenario for an HTR, a lower power density in a pebble at operational conditions implies a lower decay heat, hence a reduced maximum fuel temperature during the transient. This allows keeping the TRISO particles temperature under the 1600 °C limit, ensuring the effectiveness of the SiC barrier in retaining the fission products and so the inherent safety feature of the reactor, as explained in section 1.1. Moreover, in the multipass scheme the DLOFC power peak can be further reduced of about 200 °C adopting a radially-dependent repositioning strategy of the recycled pebbles, called radial fuel zoning.<sup>126</sup> The capability of managing the fuel zoning depends upon the design of the mechanical device which inserts the fresh or recycled pebbles on the top of the core. For example, in the PBMR-400 design, this mechanism drops the pebbles by some fixed pipes positioned over the bed. Then, under these positions a hill of pebbles is formed on the top of the bed. An inserted pebble will roll over the hill until reaching a stable radial position, from where it will start to flow downward in an almost purely axial direction, surrounded by the other pebbles in a plug type flow, whose characteristics are depicted in section 1.4. In this reactor design no radial zoning is possible and a random distribution of the re-circulated pebbles at the entry plane of the core cavity has to be simulated.

To better understand how the multipass scheme should be simulated, let in detail analyze how a discharged pebble is recycled or discarded. Generally, when a pebble is extracted from a defueling cone at the bottom of the reactor, its burnup is estimated by a gamma detector measuring the concentration of Cs<sup>137</sup> in the fuel. This isotope is chosen because it has a strong  $\gamma$ -emission at 0.661642 MeV and it is a fission product with a long half-life (30.2 years), which avoids the effects of the short period flux fluctuations on the cumulated atomic density. A target burnup limit for recirculation is fixed; beyond this limit a discharged pebble is discarded rather than re-circulated. The limit for recirculation is determined in order to avoid the discharged pebble to exceed the maximum allowed burnup for the TRISO particles integrity with a further passage through the reactor. This TRISO burnup limit is fixed by the regulators and it depends on the physical properties of the fuel under irradiation. As it has been described in Chapter 1, in the German AVR reactor some pebbles were irradiated up to 160 MWd/t without significant damage.

The burnup cumulated by a pebble during a pass through the core depends both on its burnup value at insertion and on the radial position in which it flows through the cavity. For example, in the case of an annular core, pebbles flowing close to the reflectors have the lowest flow velocity, and so the highest residence time in the core. Moreover, while flowing close to the internal reflector they also pass through the zones with the highest

core thermal flux and, thus, power density. Thus, for the same entering burnup at the top of the core, their discharge burnup will be higher than the one of the pebbles flowing in other radial positions. As a consequence, the target burnup limit for recirculation has to be determined considering that the discharged pebble will make his further pass in the most penalizing radial position. This position corresponds to the most internal flow channel in an annular reactor. For example, in the HTR-10 (which is cylindrical) fuel management scheme the target burnup limit for recirculation is fixed to 72000 MWd/t, which gives an average burnup of the spent fuel for the equilibrium core of 80000 MWd/t and a peak value of about 96000 MWd/t.<sup>125</sup>

The selection method described, which allows a discharged pebble to be recycled or not, entails that not all the pebbles will do the same number of passes through the core before being discarded. This trend was partially analyzed for the PBMR-400<sup>115</sup> and it should be addressed in a proper modeling of the multipass scheme.

This Chapter will focus on the research of the equilibrium core with a multipass fuel management scheme. In section 5.1, an overview of the methods implemented in the codes presently used for pebble bed reactors simulation precedes the description of the method developed in APOLLO2, presented in section 5.2. Then, the developed method is applied for several fuel cycles proposed in PBRs, described in section 5.3. The characteristics of the corresponding equilibrium cores are evaluated for the simplified PBMR-400 geometry, already used in Chapter 4, in section 5.4.

In this last section, the potential of the method developed in APOLLO2 is exploited to quantify the bias committed by using the average composition pebble approximation. This bias concerns both the homogenized cross section generation and the fuel depletion calculations.

Finally, the conclusion on the equilibrium core simulations will be given in section 5.5.

## 5.1 Survey of Existing Codes Methodologies

Before describing the various methods specific to each code, let introduce the common features and techniques implemented in all methodologies.

First of all, since the pebble flow through the cavity is practically vertical, the core is subdivided in parallel flow channels and the pebbles entering the top of the bed in a given channel are supposed to flow till the bottom in the same channel. The only exception to this trend appears at the bottom of the core, where the defueling cones are present and the flow lines curve approaching ones each other.

Several codes represent the cone bottom by a flat profile, which does not introduce a great error as the flux at the bottom end is very small, due to the higher pebble burnup, the increased coolant temperature and the cosine shape characteristic of a homogeneous core.

The radial width of the flow channels is chosen to capture two common features of the pebbles comprised in the corresponding spectrum zones: the flow velocity and the neutron flux shape. As a consequence, the channels close to the reflectors are radially

thinner, both to assign to the pebbles a slower flow velocity and to capture the spectral effects connected to the reflectors neighborhood, which result in a higher thermalized flux. Some codes assign a constant velocity through the width of the flow channel, while others assign a different velocity to each computational cell in the radial direction of the RZ core model. Moreover, some codes allow assigning a different flow speed to each channel, while others subdivide the different channels in a different number of axial spectrum zones with a constant residence time in all of them, so that the relative numbers of zones in the channels determine the relative flowing speeds.

To find the pebble burnup values corresponding to the equilibrium core, all the codes compute a steady-state reactor model with a given distribution of burnup and then use the calculated fluxes to deplete the fuel pebbles and to find the next core burnup profile. Two main approaches are used. In the first one, the core equilibrium search is treated explicitly, from the fresh core to the final asymptotic loading, simulating the whole running-in phase. In this case the successive burnup profiles computed correspond to consecutive steps of the running-in phase. In the second approach, the equilibrium state is directly calculated iteratively, converging to the equilibrium burnup distribution without modeling the succession of running-in states. A third approach based on statistical considerations on pebble distribution has also been developed, but it has not been particularly used.<sup>36,127</sup>

In the simulation of the multipass fuel management scheme, it is necessary to develop both a depletion algorithm, used to follow the burnup evolution of the pebbles flowing through the core, and a mixing algorithm, which simulates the reintroduction of the recycled pebbles on the top of the bed and the substitution of the discarded pebbles with fresh ones. In the following, the methodologies adopted by some existing codes are described in a deeper detail.

#### - VSOP

The VSOP code system solves the problem in a time-dependent manner, employing a sequential fuel shuffling and burnup algorithms to follow the evolution of the pebbles burnup through the running-in phase till the equilibrium core.<sup>128</sup> It assigns a fixed residence time to all spectrum zones, dividing the channels in a different number of spectrum zones. The pebbles with the same number of passes in each zone are lumped into batches. The volumes of each batch in a zone are the same and equal to the total batch volume divided by the average number of passes in the core. Batches that are co-located in a zone define pebbles that move together, simulating the mixing of the pebbles with different burnup levels within the region. A single average batch is computed for each spectrum zone, volume-weighting the different batches nuclide densities, to define a single material. All the numerical mesh cells belonging to a spectrum zone in the RZ model are associated to the same set of microscopic cross sections and average nuclide densities, so that the macroscopic cross sections are constant in the zone. The nuclide densities in the zone should represent the average composition for that volume over the time interval in which the pebbles flow through

the zone. It is therefore typically defined to be the composition half-way through the time interval (or burnup step). Given a burnup distribution of the core at a given time step during the running-in phase, the RZ core is computed with the finite difference diffusion code CITATION in 4 energy groups. With the diffusion broad-group flux averaged over the zone volume, the different batches belonging to a zone are depleted for the duration of the time step and then shuffled downwards to the next spectrum zone. In reality a more complex subdivision in 2 substeps is employed, where the flux distribution and the microscopic cross sections are recalculated at the midpoint and the flux is renormalized to preserve the core total power. More details can be found in Ref. 128, where an analysis is also performed comparing the use of these two different flux vectors per substep with a unique constant average flux during the whole step. The obtained results did not show any observable differences on the computed concentrations of the main nuclides.

The batches belonging to the bottom spectrum zone of each channel are mixed together to obtain the composition of the batches to be reinserted at the top of the core. The mixing algorithm is the simplest and most commonly used one, consisting in computing a flow-weighted average over the channels per each pass (which in this case corresponds to a volume-weighted average over the corresponding last batches per channel) and then assigning this average composition to the next pass at the top of the core. The last pass is completely discarded and the first pass at the top of the core is composed by fresh pebbles. As the number of pebbles (or the batch volume) per each pass is the same in all spectrum zones, the number of last pass pebbles discarded at the bottom is equal to the number of fresh pebbles inserted at the top, maintaining constant the pebbles inventory in the core.

This implemented mixing algorithm can not automatically treat the case of a radial fuel zoning strategy, and a case to case reloading pattern has to be implemented to describe the radial distribution of the pebbles according to their burnup level. Moreover, this simple scheme does not account for the dispersion around the average burnup values used to represent the set of pebbles of the same family contained in a zone. Thus, the physical mechanism of imposing a target burnup limit for recirculation can not be properly simulated and all the pebbles perform the same number of passes through the core. As explained in the previous section, this is not the realistic situation.

#### - BATAN-MPASS

BATAN-MPASS<sup>129</sup> was the first code which allows computing directly the asymptotic burnup distribution of the equilibrium core by an iterative coupling of the core flux calculation and the depletion calculation, each calculation being performed separately. This differs to an earlier developed code, the PREC code,<sup>130</sup> where the coupled discretized depletion and diffusion equations are treated as a system of algebraic equations and solved simultaneously with the SOR-Newton method. The PREC code could consider only a single burnup value flowing through the core and so it was applied only to OTTO cycle simulations. In BATAN-MPASS the burnup and core flux calculations are solved separately, mostly to ensure the convergence of each calculation.

Differently from VSOP, the axial flow of the pebbles is not considered at the level of the flow channels but over the spatial mesh used to discretize the RZ geometry, with radially varying flow velocities. Thus, the flux obtained from the diffusion solver is used to compute the axial variation of the nuclide densities over each cell of the mesh. A different flow velocity can be assigned to each axial mesh, so that a fine velocity profile can be simulated. Nevertheless, assuming a varying flow velocity over a mesh size smaller than a pebble diameter is certainly not physical.

The diffusion code computes a single flux value per energy group in each mesh cell and this flux is used in the Bateman equation for depleting the different nuclide densities corresponding to the different pass pebbles. The nuclide densities vary in the group of mesh cells corresponding to a spectrum zone, implying that the microscopic cross sections are constant in a spectrum zone, but not the macroscopic cross sections.

The mixing algorithm appears to be the simple one used in VSOP too and the core flux calculation iterates with the depletion solver calculation until reaching convergence on the core  $k_{eff}$ , the group flux values and the nuclide densities of each pass in each spatial mesh cell.

Finally, an external iteration loop adjusts the pebble flow velocity, by linear interpolation, until the corresponding computed equilibrium core matches a predetermined  $k_{eff}$ . Given that the reactor dimensions are fixed, together with the total power, the number of passes and the pebble characteristics, varying the flow velocity indeed results in a variation of the equilibrium core  $k_{eff}$ . For example, increasing the pebble flow velocity, a larger number of fresh pebbles is introduced in a given period given an increase of the reactor multiplication factor, together with a decrease of the average burnup value of the discarded pebbles.

#### - PEBBED

The recently developed PEBBED code uses the PREC methodology of coupling the core diffusion equation and the fuel depletion equation. The diffusion equation is solved over the RZ core geometry with a different average pebble composition per computational cell. The fuel depletion equation is written with a term which accounts for the axial flowing of pebbles. This term varies at the size of the cells width. This depletion equation is solved iteratively with the flux computed by diffusion over the spatial mesh of the core. Moreover, it introduces an analytical formulation which allows deriving the burnup of the different pass pebbles comprised in a spectrum zone from the average fuel composition.<sup>59</sup> An interesting feature implemented in PEBBED concerns the mixing algorithm, which is based on a sophisticated recirculation matrix which allows defining recirculation and transfer coefficients.<sup>131</sup> Through these coefficients the fractions of each pass to be loaded in the different radial positions are determined. It is so possible to parameterize the specifications of any fuel reloading strategy and to automatically explore different strategies by simply varying the matrix coefficients, allowing efficient optimization researches based on genetic algorithms.<sup>132</sup> Recently,<sup>133</sup> PEBBED has also been applied to analyze the burnup distribution of the discarded pebbles around the average values per pass obtained from the equilibrium

core calculation. This has been done using the converged flux values of the equilibrium core, computed with the average composition pebble approximation and an equal fraction of pebble type per pass. The flux values are used to perform the depletion calculations associated to all the realizable exposure histories. An exposure history is a given combination of the flowed channels by the pebble during its life in the reactor. Thus, if the core is divided in  $N_{chan}$  channels and the average number of passes for the pebbles is  $N_{pass}$ , the total possible combinations, representing the different exposure histories, are  $(N_{chan})^{N_{pass}}$ . The simulation of all these histories individually is very time consuming. In the example given in the referenced article a core with 4 channels and 10 passes was simulated and the computation of all the  $(N_{chan})^{N_{pass}}$  combinations required about 2 weeks on a single processor. Furthermore, does not simulate the recirculation strategy based on the measurement of the burnup value of discharged pebbles. As it has been explained in the previous section, in reality the number of passes used in the existing codes to compute the equilibrium core is only an average value, but some pebbles could make less passes and other more than the average. To properly evaluate this dispersion around the average value some strategies should be implemented in-line with the iterations between the core flux solver and the depletion solver, in order to properly estimate the fraction of pebbles with different passes in the equilibrium core.

#### - DALTON – THERMIX

The methodology recently developed at the Delft University of Technology,<sup>126</sup> in The Netherlands, is the closest one to the methodology developed in APOLLO2. An iterative scheme is employed to find the asymptotic nuclide distribution directly by a loosely coupling of the core diffusion solver DALTON and the depletion solver ORIGEN of the SCALE-5 code system. The iterative principle is the same as in BATAN-MPASS. An outer loop allows adjusting the core residence time  $T_{SZ}$  of the pebbles to obtain an equilibrium reactor with a prescribed  $k_{eff}$ . The depletion and flowing algorithm are mostly similar to the VSOP ones. The RZ core model is divided in spectrum zones with constant homogenized microscopic cross sections and nuclide densities in all the computational mesh cells of the zone. This differs from the BATAN-MPASS method where the nuclide densities vary over each mesh cell. After a burnup iteration which modifies the nuclide densities in the spectrum zones the self-shielding step is repeated and the microscopic cross sections are computed by 1D transport calculations for the TRISO coated particle surrounded by the moderator graphite matrix. A 172-group XMAS energy structure, based on the JEFF3.1 library, is used. Radial and axial 1D transport calculations are used to calculate zone weighted cross sections for the entire reactor and obtain the macroscopic cross sections for each zone. The diffusion solver computes the RZ multi-group flux profile and an average flux value is computed for each spectrum zone and scaled to the desired reactor power. The average flux value is then used to deplete the nuclide densities associated to each spectrum zones during

the time period in which a pebble would flow through the zone. This also differs from the BATAN-MPASS approach where the flux values in each computational cell belonging to the zone are used to deplete the corresponding nuclide densities, considering the axial and radial variation of the flux in the zone. The axial downward movement is taken into account by assigning the exiting densities from a zone to the entering ones of the following zone. The convergence of the core flux – depletion calculations is checked on the absolute difference of the RZ flux values between two successive iterations. The mixing algorithm is the VSOP one used in almost all codes.

- The PANTHERMIX scheme uses a somewhat more sophisticated model for shifting batches of pebbles that accounts for the numerical diffusion in the shift calculation arising from the variation in pebble speed in different flow zones.
- The HELIOS/CAPP code system<sup>134</sup> recently developed by the Korea Atomic Energy Research Institute adopts as flowing and mixing schemes practically the same as VSOP, using the flux computed over each spectrum zone by the diffusion solver to perform the micro-depletion calculation for each pebble-type.

Finally, other developed methodologies use the already mentioned flowing and mixing algorithms, but adopt Monte Carlo codes to compute the flux values to be passed to the depletion solver.<sup>135-137</sup> While these methods could be useful for reactors with particular complex geometries, they are still not competitive with deterministic methods due to the long computing times of Monte Carlo and to the relatively basic, or null, existing methodologies to propagate the flux uncertainties on the nuclide densities obtained by the depletion solver. Moreover, for pebble bed reactors where the pebbles are stochastically distributed in the reactor cavity, the flux computed in the Monte Carlo geometry using a given pebble disposition, often in a lattice arrangement, is not representative of the stochastic variations physically present in the flowing bed.

## 5.2 Developed Method in APOLLO2

The methodology implemented in APOLLO2 is similar to the BATAN-MPASS one, but, as for the method developed at Delft University, it uses the VSOP concept of considering an average flux value over the spectrum zone to deplete the pebbles during their passage through the zone. In reality, as it has been explained in the previous section, VSOP uses a flux vector subdividing the passage in the spectrum zone in various substeps, but in the comparative study made with PEBBED it appeared that there were only small differences if an average spectrum over the zone is used.

The research of the flow velocity, giving a burnup profile distribution in the equilibrium reactor corresponding to a prescribed  $k_{eff}$  value, is performed outline and it is not done in an external loop as in other codes. This allows launching several calculations with different velocities in parallel on a cluster of processors. Then, interpolating linearly the



couples of corresponding  $k_{eff}$  and velocities, the velocity giving the desired  $k_{eff}$  is found with a few iterations.

The developed methodology aims to compute directly the asymptotic equilibrium core. The calculation of the running-in phase, nevertheless, is easily achievable as it is only a succession of static reactor configurations, with a successive downward shuffling of the fuel kernels nuclide densities associated to the pebbles contained in the spectrum zones. The depletion and the mixing algorithm are explained in more details in the next sections.

### 5.2.1 Depletion Algorithm

The RZ core model is subdivided in channels and spectrum zones, as usually done in PBRs modeling. The pebbles are expected to flow downward inside the channel in which they enter the core cavity. The bottom cone region could be described using a stepwise approximation on the geometrical RZ mesh. As the RZ model is Cartesian it is not possible to describe curved lines, but if the core flux solver would allow it, it would be straightforward to implement this method coupled with such a model, provided that the entering currents through the spectrum zones boundary surfaces are recoverable from the core flux solver.

The iterative core calculation method developed in APOLLO2, based on iterations between the  $P_{ij}$  calculations of the multi-pebble geometries associated to the spectrum zones and the RZ  $S_N$  core calculation, is used to compute a given steady-state of the reactor. For steady-state, we mean a core with a given nuclide atomic densities distribution assigned to the fuel kernels of all the pebbles in all the multi-pebble geometries associated to the core spectrum zones. The number of pebble types contained in the core equals the maximum number of passes through the reactor which a pebble can perform before being discarded. The volumetric fractions of each pebble type in the spectrum zones are determined by a mixing algorithm; it is equal to  $1/N_{pass}$  for all types with the implemented mixing algorithm, similar to the VSOP one and described in the next section. These values (number and fractions of types) are constant in the zones belonging to the same channel but they can differ between the different channels. This allows simulating radial zoning strategies.

In a steady-state calculation, the nuclide densities assigned to the different pebble types in a zone represent the average values of each pass at the half height of the zone. The burnup of a pebble type is an average value, whereas in reality the burnup values of the pebbles with the same number of passes differ depending on their exposure histories. Considering this average value per pass, a spectrum zone contains pebbles of a given type with the burnup increasing from the entering value at the top boundary surface to the exiting value at the bottom boundary surface. Since the multi-pebble geometry accounts for a single burnup value per pebble type, the value at the half-height of the zone is retained as the average one. The flow velocity in a zone being constant, the value at the half-height corresponds to the value at the half of the time period

$T_{SZ}$  employed by a pebble to flow through the zone. It must be noticed that  $T_{SZ}$  can vary in the different spectrum zones belonging to a channel and that the zones do not need to be equi-volumetric. The time in which a pebble flow through the full height of a channel,  $T_{ch}$ , is the sum of the  $T_{SZ}$  of the zones belonging to the channel.

When the iterative core-calculation scheme has converged to a steady-state, the entering currents per boundary surface in all the spectrum zones are known. If the core is at equilibrium, these entering currents are constant over the time. The fine-group fluxes in each pebble, computed by the  $P_{ij}$  calculation of the multi-pebble geometry with the converged entering currents and core  $k_{eff}$ , are used to deplete the corresponding pebble type. This is done over the time step  $T_{SZ}$ , depleting the nuclide densities from the entering values in the spectrum zone to the exiting ones. The densities of each pebble type at time  $T_{SZ}/2$  are stored and they will be assigned to the multi-pebble geometry for the next iteration flux. The macroscopic cross sections are updated at interval  $T_{SZ}$  substeps, but the fluxes in the pebbles remain constant over all  $T$ .

A schematic illustrating how is performed the depletion calculation for the pebbles flowing through a zone is given in Figure 5.1.

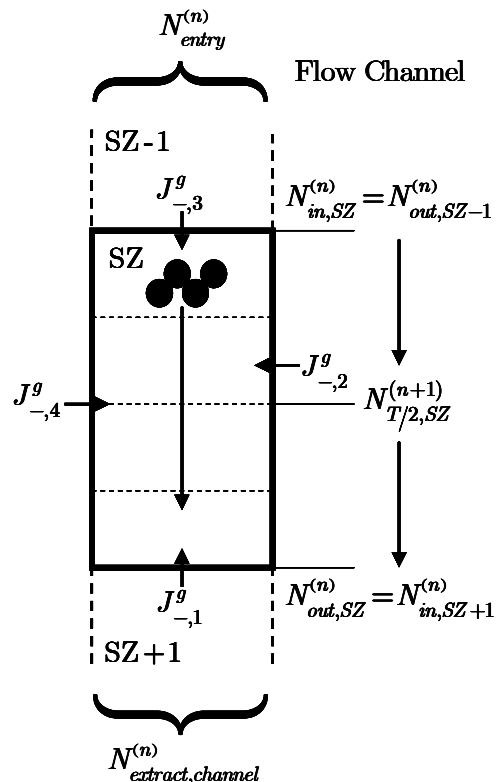


Figure 5.1: Depletion calculation of the pebbles flowing through a zone

The entering nuclide densities  $N_{in,SZ}$  of the different pebble types in the zone SZ are the exiting densities from the upper zone,  $N_{out,SZ-1}$ .

If the spectrum zone is the top one of the channel, the entering nuclide densities are determined by the mixing algorithm, which will be described in the next section. For the bottom zones, the exiting nuclide densities are the discharged ones from the channel.

The depletion solver performs the micro-depletion of the fuel kernels of each pebble type using their own heterogeneous fine-group fluxes. As a consequence, the flux used for depleting the kernels differs between the different types comprised in a zone.

This can not be accounted for by other codes that use the single flux value computed in the average composition pebble. Moreover, the previous implemented methodologies use the broad-group flux obtained from the core diffusion solver to condense the broad-group cross sections to the one-group value used in the depletion equations.

Furthermore, in the developed method the flux in the multi-pebble geometries are renormalized to match the total core power using the fine-group heterogeneous rates computed for the different pebble types, as described in section 4.2.3. These rates were closer to the Monte Carlo reference values compared to the rates computed with the broad-group flux over the homogeneous spectrum zones. Nevertheless, this last approach is the one used by all existing codes.

Once the atomic densities of the different pebble types have been successively depleted through the spectrum zones of a channel, the atomic densities at  $T_{SZ}/2$  in each spectrum zone are used to define the steady-state at the iteration  $n+1$ .

It has to be noted that the depletion through a channel is independent from the other channels. Thus it is possible to parallel compute the depletion sequences in the different channels, with a consequent gain in computing time in the order of  $N_{chan}$ .

Then, the collision probabilities matrices are recomputed for all the multi-pebble geometries and the fine-group cross sections are self-shielded with new isotopic compositions (note that also this process can be parallelized for the  $N_{SZ}$  spectrum zones), to perform a next spectrum zones – core iterative calculation.

The iterations between the depletion calculations and the spectrum zones – core flux calculations are repeated until convergence to the equilibrium core is reached.

The core is defined in equilibrium when a pebble entering the same channel with the same burnup between two successive iterations, reaches the same burnup levels at all the exiting surfaces of the SZs belonging to the channel. Of course, the same burnup level means that the relative difference between the burnups at two successive iterations is smaller than a prescribed convergence precision.

Convergence is checked on the following quantities:

- the equilibrium core  $k_{eff}$ ,

- the burnup values of the different pebble types at the exit surfaces of the spectrum zones,
- the concentrations of some user specified nuclide densities (for example  $U^{235}$ ,  $Pu^{239}$ ,  $Pu^{240}$ ) in the different pebble types at the zones' exit surfaces,
- the zone-averaged core power distribution.

The flow scheme of the iterative calculation procedure for computing the equilibrium core is shown in Figure 5.2.

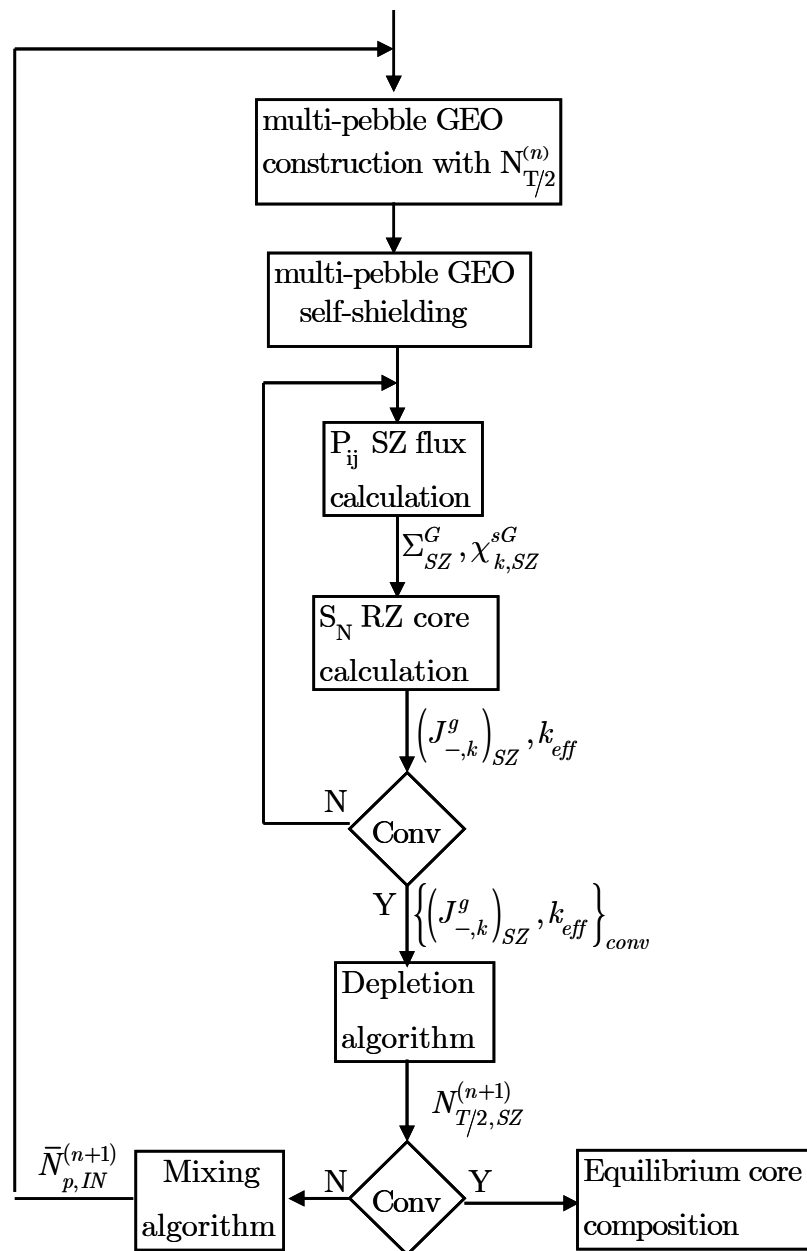


Figure 5.2: Flow scheme of the iterative calculation procedure for computing the equilibrium core.

In this Figure,  $\bar{N}_{p,IN}^{(n+1)}$  indicates the average (over the core channels) atomic density of the pass  $p - 1$  discharged pebbles at iteration  $n$ , which become the average reloaded pass  $p$  at iteration  $n + 1$ . As it is explained in next section, the implemented mixing algorithm discards all the pebbles which have performed the last pass.

In conclusion, the new APOLLO2 algorithm differs from the previously developed ones mainly for two features:

- the heterogeneous fine-group fluxes of the multi-pebble geometries are used to compute the power distribution in the core,
- the depletion of the different pebble types comprised in a zone is computed with the different fluxes for each type and not with an unique flux computed in an average composition pebble.

### 5.2.2 Mixing Algorithm

The mixing algorithm combines the exiting nuclide densities at the bottom surfaces of the last spectrum zones per channel at the iteration  $n$  to build the entering nuclide densities at the top of the channels at iteration  $n + 1$ .

In the projected pebble bed reactors, the South African PBMR-400 and the Chinese HTR-PM, the pebbles inserted in the reactor cavity are dropped over the bed from fix charging pipes, so the radial positions in which the pebbles flow through the core may be assumed randomly distributed. At the entering plane the atomic densities assigned to each pass are the same for all channels and the pebbles of the first pass are always fresh pebbles. As the radial zoning is not accounted for in actual designed reactor, the random distribution will be adopted in the studies performed in section 5.3. Nevertheless, with the developed method in APOLLO2 any fuel management strategy can be simulated simply modifying the mixing algorithm in the calculation scheme.

In the case of a random radial distribution, all the existing codes use the mixing algorithm of VSOP. In this algorithm, if the number of passes through the core is equal to  $N_{pass}$ , each spectrum zone in each channel contains the different pebble types, corresponding to the different passes, in the fixed fraction  $1/N_{pass}$ .

To initialize the first steady-state core, the fresh pebble composition can be assigned to the pebbles of all passes or the user can assign some physically burnup values close to the possible equilibrium ones. The latter can be obtained depleting a single pebble with a reflected boundary condition. This could reduce the number of required iterations to reach the equilibrium state, but it will not influence the convergence of the scheme.

After the depletion calculation at iteration  $n$  is done, the nuclide densities at the bottom surfaces of the last spectrum zones per channels are obtained.

Then the average atomic density  $\bar{N}_{p,OUT}^{(n)}$  of the discharged pebbles at pass  $p$  is obtained flow-weighting the corresponding densities  $N_{p,c}^{(n)}$  in each channel as

$$\bar{N}_{i,p,OUT}^{(n)} = \omega_c^p N_{i,p,c}^{(n)}, \quad (5.1)$$

with

$$\omega_c^p = \frac{f_{p,c} V_c / T_c}{\sum_c f_{p,c} V_c / T_c}, \quad (5.2)$$

and

- $i$  indicates an isotope in the fuel kernels of the pebbles,
- $c$  denotes a channel,
- $f_{p,c}$  the relative abundance of pass  $p$  pebbles in the channel,
- $V_c$  the volume of the channel,
- $T_c$  the flowing time period associated to the channel.

Note that, if the pebbles are randomly inserted in the core,  $f_{p,c} \rightarrow f_p$  has to be independent of the channel.

Once the average atomic densities of the discharged pebbles from the core,  $\bar{N}_{p,OUT}^{(n)}$ , have been determined, the entering densities assigned to the pass  $p$  pebbles,  $\bar{N}_{p,IN}^{(n+1)}$ , starting from  $p = 2$ , for the successive iteration, are defined as

$$\bar{N}_{i,p,IN}^{(n+1)} = \bar{N}_{i,p-1,OUT}^{(n)}. \quad (5.3)$$

At the core entry plane the  $p = 1$  pebbles are always fresh ones.

The discharged pebbles from the core for  $p = N_{pass}$  are totally discarded and their channel-averaged burnup exit value is defined as the average discard burnup level of the pebbles.

We have to point out here that the mixing algorithm implemented in APOLLO2, during this thesis, is similar to the one firstly used in VSOP, and then in all the other codes. The limitations of this model are illustrated in section 5.4.1.2 for the equilibrium core calculation of a simplified PBMR-400 model with Low Enriched Uranium. The main weak point of the model is that the rejection policy for the discharged pebbles is based

on the number of passes, whereas in reality it is based on the discharge burnup value. Nevertheless, it would be necessary to account for all the depletion histories, during the calculation of the equilibrium core, to properly compute the distribution of the atomic densities of the discharged pebbles at each pass. As explained in section 5.1, PEBBED computed this distribution for the discarded pebbles simulating individually all the possible histories, but using for depletion the equilibrium flux computed with a model based on the average composition pebble approximation. This required 2 weeks of computing time.

In our analysis, we show how, in a channel, the accumulated burnup per pass is linearly proportional to the entering burnup value. This allows a fast calculation of all the possible histories by interpolating the values computed for the pebble types of the multi-pebble geometries. An "improved mixing algorithm", based on this technique, is under development.

### 5.3 HTGRs Fuel Cycles

High Temperature Gas-cooled Reactors, both the block-type and the pebble bed design, are able to accommodate a wide variety of mixtures of fissile and fertile materials without any significant modification of the core design.<sup>138</sup> They have several fundamental features which distinguish them from other types of reactors, and provide significant operational advantages. It is possible to modify the moderation ratio without modifying the cooling geometry, by simply changing the diameter of the TRISO particles fuel kernels and the number of them contained in each fuel element. Using a gaseous coolant instead of a liquid one, such as in PWRs, avoids having a positive void coefficient, which for example limits the MOX content in PWR MOX fuels. Moreover, an HTR core has a better neutron economy than a LWR one because there are much less parasitic captures in the moderator (capture cross section of graphite is 100 times less than the one of water) and in internal structures. Finally, HTR fuels are able to reach very high burnups, far beyond the possibilities offered by other thermal reactors. The burnup limitations come from two main constraints: the criticality of the core and the resistance under irradiation of the TRISO fuel particles. In previous experiment performed in the DRAGON reactor,<sup>139</sup> burnups as high as 750 MWd/t have been achieved without degradation of the fuel particles. In the case of plutonium fuel cycles, this deep burn capability allows burning efficiently the plutonium without reprocessing the fuel elements, minimizing proliferation risks.<sup>140</sup>

The main investigated fuel cycles for HTRs are listed below.

- 1) The LEU (Low Enriched Uranium) cycles, which are actually the prospected ones for the commercial designs of the PBMR-400 and the HTR-PM. They use  $\text{UO}_2$  kernels with uranium enrichment of about 9% which in a multipass scheme, generally based on an average of six passes, allows reaching an average discharged pebbles burnup of about 90000 MWd/t. The enrichment is higher than the one

commonly used in current light water reactors. This is due to a rather diluted and homogeneous uranium distribution, on the form of the micro-particles dispersed in the graphite matrix, which favors  $U^{238}$  resonance captures (self-shielding effect is reduced). On the other hand, this apparent enrichment penalty is compensated by a higher conversion ratio (typically 0.7 to 0.8 or even more) leading to a greater "in situ" formation of fissile isotopes (plutonium).

- 2) The plutonium cycles exploits the unique flexible features of the HTRs to fully load the core with Pu fuel. The idea to use plutonium as the only fissile material (but together with thorium, in the same core, as fertile material) was considered very early in the 60's within the framework of the DRAGON project. Recently, the PUMA project, which is a Specific Targeted Research Project of the European Union EURATOM 6<sup>th</sup> Framework Program, aimed at providing key elements for the utilization and transmutation of plutonium and minor actinides (MA) in HTR designs.<sup>141</sup> Three different types of plutonium fuels are envisaged to be used: weapons grade plutonium and civil plutonium reprocessed from spent LWR uranium fuel (first generation Pu) or LWR MOX fuel (second generation Pu). Numerous studies have been done with the different codes described in section 5.1 to compute the equilibrium core of both the HTR-PM<sup>142,143</sup> and the PBMR-400<sup>144-146</sup> loaded with plutonium.
- 3) The thorium cycles, which are not specific to HTRs, even though HTRs are better adapted than other reactors to take advantage of thorium neutronic properties. Thorium is the fertile material utilized in this cycle and generates  $U^{233}$  which is an optimum fissile isotope for thermal spectrum reactors. Furthermore, there are probably more thorium resources than uranium ones, and its utilization as a fertile isotope in reactors has been extensively studied, particularly for HTRs. For these reasons, the cycle using High Enriched Uranium (HEU) as a driver for thorium fuel was considered as the reference cycle at the very beginning of HTR development in both the USA and Germany. As a result, four prototype power reactors that operated in the past (AVR, THTR, Peach Bottom and Fort Saint Vrain) were initially operated with fuel containing thorium in various forms, such as carbides and oxides in single thorium particles or mixtures with uranium. In pebble bed reactors, thanks to the continuous reloading of the pebbles, it is possible to envisage fuel cycles using simultaneously pebbles with two different fuel types, one as driver and the other as fertile. More complex cycles have also been studied, for example a PBMR-400 based on a 5 passes scheme, where half of the loaded pebbles contain Pu kernels and half a mixture of 93% enriched uranium and thorium (8.4% + 91.6%).<sup>147</sup>

In addition to the different fuel types which may be used in the fuel kernels, burnable poisons could be dispersed as micro-particles in the graphite matrix or directly inserted in the fuel composition to shape the flux profile. This option has been studied particularly for block-type reactors, but also in PBRs and the use of boron, gadolinium and erbium isotopes has also been considered.<sup>148,62</sup>



## 5.4 Equilibrium Core Calculations for Different Fuel Cycles

The method developed in APOLLO2 to search the equilibrium core has been applied to the reactor model used for the verification process, described in Chapter 4, with pebbles containing different fuel types. This model, which is based on the PBMR-400 but with a core height restricted to 9 m, is represented in the RZ  $S_N$  core model, illustrated in Figure 4.2 with 5 flow channels subdivided in 15 equivalent-height spectrum zones for channel A and E (the ones close to the reflectors) and 11 zones in channels B, C and D. This has been adopted in Chapter 4 to represent the VSOP zone partitioning of the PBMR reactor. Hence, by using different numbers of spectrum zones per channel it is possible to assign the same transit time  $T_{SZ}$  to all the zones, even though the flow velocities are different per channel. It has to be noted that, with the developed model, it would have been possible also to subdivide all the channels with the same number of zones and to assign a different  $T_{SZ}$  to the zones of each channel. This would permit a better tailoring of the flow velocity profile.

Because the PBMR-400 has a core of 11 m height, to maintain the same power density in this lesser height core, a total power of 330 MW has been imposed. Since the pebbles flow without exiting the channels, the same packing fraction has been assigned to all the multi-pebble geometries of the spectrum zones belonging to a given channel. The packing fractions have been derived averaging over the channels the values assigned to each SZ in the simplified PBMR-400 model simulated in the verification process. The packing fractions per SZ are given in Table 4.III. The resulting packing fraction per channel, the number of pebbles contained in the channels' zones and the fraction of pebbles discharged from each channel over the total are shown in Table 5.I. The full core contains 369887 pebbles.

**Table 5.I:  $pkf$ , pebbles per zone and channels flow-weighted fractions in the PBMR-400 model used for equilibrium core calculations**

	Chan A	Chan B	Chan C	Chan D	Chan E
Pebbles packing fraction (pkf)	0.53	0.60	0.61	0.60	0.48
n° of pebbles in a SZ	1886	8550	6984	11518	2935
Fraction of discharged pebbles	5.92%	26.83%	21.91%	36.14%	9.21%

In average six passes of the pebbles through the core have been assumed. As a consequence in all multi-pebble geometries  $1/6^{\text{th}}$  of the pebbles belong to the different pass types.

The temperature distribution is not the one of a realistic core, as no thermal-hydraulic feedback has been taken into account in the calculation (no coupling between neutronic and thermal calculation). The temperatures of 900 °C for the fuel kernels and 700 °C for the other materials used in the High Temperature models described in section 4.2 have been adopted.

In the depletion algorithm, the time step over a spectrum zone has been subdivided in 8 substeps. The precisions requested for the convergence of the iterations on the core flux – depletion calculations have been set at 10 pcm for the absolute difference in the core  $k_{eff}$  and at  $10^{-3}$  for the maximum relative difference for the zone-averaged powers, the burnup values and the concentrations of U<sup>235</sup> (only for the LEU cycle), Pu<sup>239</sup> and Pu<sup>240</sup> at the exit planes of the zones.

The time period  $T_{SZ}$  has been adjusted in order to converge to a critical core (no reactivity margin taken into account in the target core  $k_{eff}$ ).

To evaluate the bias introduced by the use of a single flux value, as explained in section 5.1, the calculations were also performed using this approximation.

Keeping the same time period  $T_{SZ}$  computed for the critical equilibrium core, after having determined the compositions at  $T_{SZ}/2$  during the depletion calculations, a volume-weighted average composition over the different types is computed for the fuel kernels and assigned at the kernels of all passes. Thus, that all the six pebble types in the multi-pebble geometry associated to a spectrum zone have the same average composition. In the next iteration, the self-shielding of the multi-pebble geometries, the core flux calculation and the normalization through the heterogeneous reaction rates are performed with these average composition pebbles per zone. The resulting fine-group flux is used to deplete all the different pebble types, as it is done in the existing codes.

Thus, two methodologies are used to calculate the equilibrium core with the same  $T_{SZ}$  :

- the APOLLO2 one employing the different fluxes per pebble type, and
- the other codes' one using the single flux computed in the corresponding average composition pebble.

The analysis of the results obtained with these two methodologies is performed by comparing the following quantities:

- the  $k_{eff}$  of the equilibrium core,
- the power shape factors over the spectrum zones,
- the average burnup of the re-circulated pebbles at the core entry plane,
- the channel flow-weighted burnup of the discharged pebbles,
- the channel flow-weighted isotopic densities of the discharged pebbles.

As a second type of comparison, once the equilibrium isotopic composition distribution is determined with the APOLLO2 method, the steady-state of the equilibrium core is re-

computed averaging the composition of the pebbles in all the multi-pebble geometries. So the bias introduced by the average composition pebble approximation is evaluated also for a steady-state core.

The spectrum zones – core flux calculations were performed with the parameters optimized in Chapter 4. The core  $S_N$  RZ calculations were performed with the 13-group energy structure, a P1 scattering order of the cross sections and both the  $S_8$  and  $S_4$  angular quadratures. A complete presentation of the results obtained with the  $S_8$  is given, whereas only a comparison on computing time, core  $k_{eff}$  and power distribution is given for the  $S_4$ . The  $P_{ij}$  multi-pebble geometries calculations have been performed with the 281-group SHEM structure.

A first calculation was performed with the  $UO_2$  fuel, subdividing the pebbles fuel region into three computational equal-volumetric shells and the kernels in a single region. Moreover, the self-shielding of the multi-pebble geometries was performed at the beginning of all the depletion iterations, as indicated in the flow scheme in Figure 5.2.

Successively, the same calculation was performed but with a single fuel region in the pebble. Moreover, the self-shielding of the multi-pebble geometries was performed only for the first  $2 * N_{pass}$  flux calculation – depletion iterations. This was done because the entering burnup per pass depends on the exiting burnups of the previous pass, so after  $(N_{pass} - 1)$  iterations all the entering burnups have been determined once with the levels of the exiting burnups of previous pass. After  $(2 * N_{pass} - 1)$  iterations they all have been determined at almost their converged value. The burnup values of the pebbles at  $T_{SZ}/2$  being approximately constant, the self-shielded microscopic cross sections of each pebble do not vary anymore. This is also assured by the high number of energy groups used for the  $P_{ij}$  calculation of the multi-pebble geometries. As a consequence, after  $2 * N_{pass}$  iterations only the nuclide atomic densities at  $T_{SZ}/2$  are updated in between the iterations.

The results of this second calculation do not present any observable differences compared to the first one, but a reduction in the computing time by a factor 1.7 was obtained. So these calculation parameters were adopted for the analysis of all fuel types.

### 5.4.1 Low Enriched Uranium Fuel Cycle

The standard 9.6% enriched  $\text{UO}_2$  pebbles of the PMBR-400 design used throughout the precedent studies, with the characteristics summarized in table 1.II, were used as fresh pebbles. To initiate the iterations, in the first steady-state, the same burnup levels of 0,15000,30000,50000, 75000 and 95000 MWd/t were assigned to the different passes pebbles in all the spectrum zones. The corresponding isotopic compositions were computed with a reflected boundary condition on a single pebble surrounded by an equivalent helium layer. The core could have been initiated also assigning the fresh composition to all passes, but the iterations needed to reach the equilibrium core were expected to be somewhat higher.

In the PBMR-400 design the average total residence time (over the six passes) of the pebbles in the core is 923 days, corresponding to a time period  $T_{SZ}$  of 13.266 days. The average burnup of the discarded pebbles is 90800 MWd/t.

In the 9 m height 330 MW power simulated reactor model, the time period  $T_{SZ}$  of 13.235 days gives an equilibrium core with  $k_{eff}$  equal 1.00015.

The corresponding pebbles discharged per day are about 2408 and, due to the implemented mixing algorithm, 2408/6 ~ 401 fresh pebbles are loaded daily. The average burnup of the discarded pebbles is 94045 MWd/t.

The equilibrium core search converged in 22 iterations, taking 12h43m on a AMD/Opteron 64 bit 2,8 GHz CPU.

While computing the RZ core  $S_N$  calculation with a  $S_4$  angular quadrature, the equilibrium core search converged always in 22 iterations, taking 11h57m. This is a small time gain. Compared to the  $S_8$  as reference, the  $k_{eff}$  of the core obtained with this simulation differed by a  $\Delta\rho=24$  pcm and a  $\Delta_{sf>1}^{\%} \tau_{PROD}^{HET} = 0.07\%$ . The saved computing time is minimal, but the equilibrium cores computed using the  $S_8$  or the  $S_4$  angular quadratures are practically the same.

The burnup distribution of the different pass pebbles flowing through the different channels is illustrated in Figure 5.3. Note that the entering burnup value for a given pass is the same for all channels, due to the radially random distribution of the inserted pebbles.

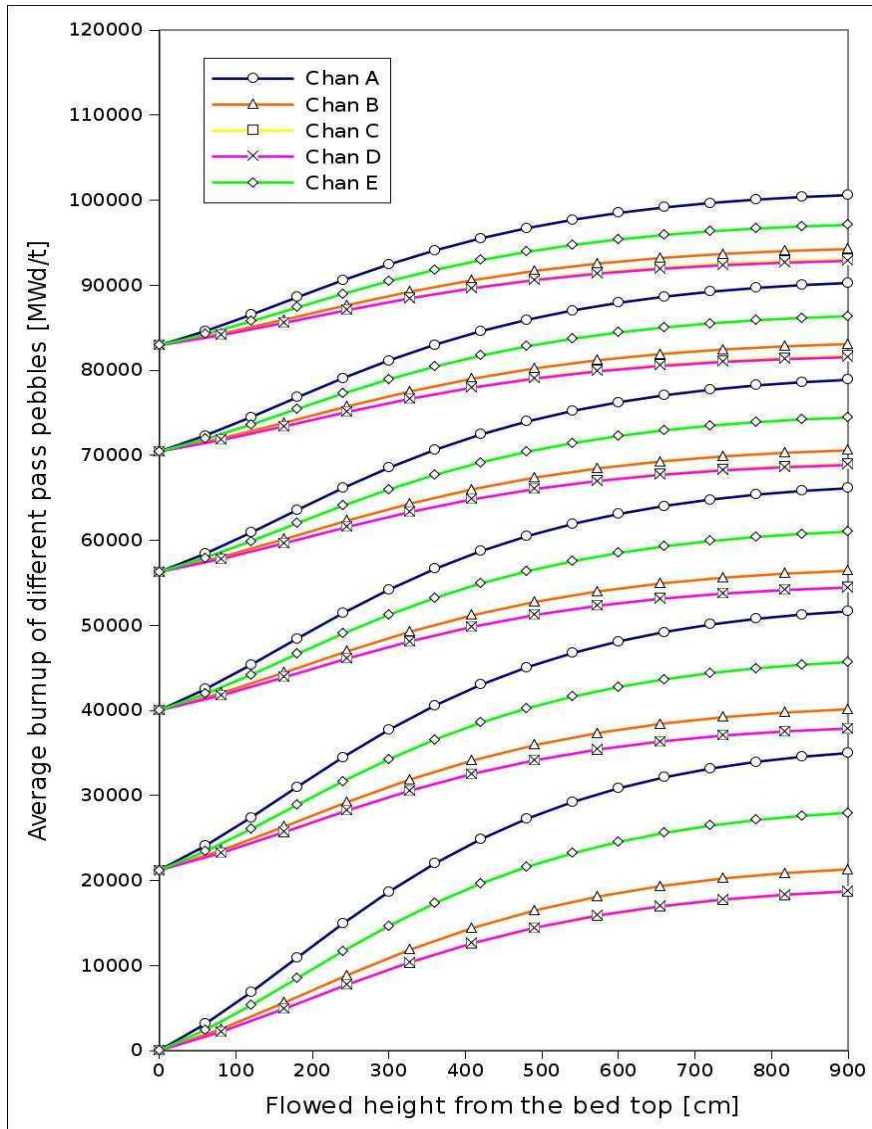


**Figure 5.3: Burnup distribution of the different pass pebbles flowing through the different channels (LEU cycle equilibrium core)**

The average flow-weighted discharge burnups and the corresponding accumulated burnups per pass are shown in Table 5.II.

**Table 5.II: Channel flow-weighted discharge burnup and accumulated burnup values per pass (LEU cycle equilibrium core)**

	Pass 1	Pass 2	Pass 3	Pass 4	Pass 5	Pass 6
Av. disch. BU [MWd/t]	21192	39980	56243	70398	82876	94045
Av. ΔBU per pass [MWd/t]	21192	18789	16262	14155	12479	11168

As it can be noticed, the accumulated burnup per pass decreases with the increase of the entering pebbles burnup, as the  $U^{235}$  depletes.

The power distribution (average power per spectrum zones), computed with the heterogeneous reaction rates,  $\tau^{HET}$ , is shown in Table 5.III. It is to be noticed the upward peak in the power profile, due to the fuel reloaded from the top. The power peaking factor will increase when taking into account the thermal-hydraulic feedback, as the coolant flows downward through the pebble bed, so that the upper part is colder than the bottom one.

**Table 5.III: Power shape factors of LEU cycle equilibrium core**

CHAN A	CHAN B	CHAN C	CHAN D	CHAN E
1.61	1.50	1.34	1.32	1.11
1.86	1.75	1.56	1.55	1.31
2.00				1.42
1.96	1.82	1.63	1.61	1.40
1.82	1.68	1.52	1.49	1.31
1.61	1.44	1.30	1.27	1.17
1.38				1.01
1.16	1.17	1.06	1.03	0.85
0.96	0.91	0.83	0.81	0.70
0.78				0.58
0.63	0.69	0.63	0.61	0.46
0.50	0.51	0.47	0.45	0.37
0.39	0.36	0.33	0.32	0.29
0.29				0.21
0.21	0.25	0.23	0.22	0.16

The channel flow-weighted concentrations of the major heavy nuclides and fission products in the discharged pebbles per pass are summarized in Table 5.IV.

**Table 5.IV: LEU cycle flow-weighted nuclide concentrations in the discharged pebbles per pass**

	Pass 1	Pass 2	Pass 3	Pass 4	Pass 5	Pass 6
BU	21192	39980	56243	70398	82876	94045
Atomic densities [atoms barn <sup>-1</sup> cm <sup>-1</sup> ]						
U <sup>238</sup>	2.07E-02	2.06E-02	2.04E-02	2.02E-02	2.00E-02	1.98E-02
U <sup>235</sup>	1.68E-03	1.25E-03	9.33E-04	6.93E-04	5.15E-04	3.83E-04
U <sup>236</sup>	9.72E-05	1.67E-04	2.18E-04	2.53E-04	2.77E-04	2.93E-04
Pu <sup>239</sup>	9.97E-05	1.25E-04	1.30E-04	1.31E-04	1.31E-04	1.31E-04
Pu <sup>240</sup>	2.39E-05	5.45E-05	7.53E-05	8.78E-05	9.48E-05	9.86E-05
Pu <sup>241</sup>	4.98E-06	1.95E-05	3.42E-05	4.49E-05	5.18E-05	5.59E-05
Pu <sup>242</sup>	4.62E-07	3.96E-06	1.15E-05	2.22E-05	3.46E-05	4.76E-05
Am <sup>241</sup>	4.24E-08	2.45E-07	5.49E-07	8.46E-07	1.07E-06	1.24E-06
Cm <sup>244</sup>	2.74E-10	9.74E-09	6.95E-08	2.57E-07	6.65E-07	1.38E-06
Tc <sup>99</sup>	3.17E-05	5.88E-05	8.11E-05	9.95E-05	1.14E-04	1.27E-04
Ag <sup>110m</sup>	3.64E-08	1.91E-07	4.66E-07	8.34E-07	1.26E-06	1.73E-06
Xe <sup>135</sup>	1.44E-08	1.25E-08	1.08E-08	9.47E-09	8.40E-09	7.57E-09
Cs <sup>132</sup>	3.37E-05	6.26E-05	8.62E-05	1.05E-04	1.21E-04	1.34E-04
Cs <sup>137</sup>	3.21E-05	6.03E-05	8.43E-05	1.04E-04	1.22E-04	1.38E-04
Pr <sup>141</sup>	2.50E-05	5.15E-05	7.40E-05	9.30E-05	1.09E-04	1.23E-04
Nd <sup>144</sup>	7.91E-06	2.53E-05	4.80E-05	7.32E-05	9.91E-05	1.24E-04
Sm <sup>149</sup>	1.70E-07	1.65E-07	1.56E-07	1.46E-07	1.36E-07	1.28E-07

The Am<sup>241</sup> and Cm<sup>244</sup> have been included as the most representative minor actinides, the Ag<sup>110m</sup> due to its particular trend to migrate through the SiC barrier of the coated particles, the Xe<sup>135</sup> and the Sm<sup>149</sup> due to their strong absorption resonance in the thermal region, the Cs<sup>137</sup> as it has been proposed for measuring the discharged pebbles burnup by  $\gamma$ -detection. The other fission products have been chosen among the ones with the highest density in the last pass pebble.

### 5.4.1.1 Average Composition Pebble Approximation

Keeping the same  $T_{SZ}$  of 13.266 days, the equilibrium core was computed using the spectrum of the average composition pebble per zone to deplete all the corresponding pebble types. Moreover, also the steady-state core is computed with the average composition pebble (both for the self-shielding of the multi-pebble geometries than for the SZ – core iterations).

The  $\Delta\rho$  of the resulting core from the previous reference one is of -17 pcm.

The relative differences between the equilibrium cores obtained with the two methodologies (the one with the average composition pebble flux from the one with the proper fluxes per pass) described in section 5.4, are shown in Table 5.V for the average discharge burnups and for the average burnup values cumulated per pass.

**Table 5.V: LEU cycle rel. diff. between the two depletion methodologies on discharge burnup and accumulated burnup values per pass**

	Pass 1	Pass 2	Pass 3	Pass 4	Pass 5	Pass 6
Rel. diff. on average discharge BU	0.59%	0.39%	0.24%	0.13%	0.06%	0.00%
Rel. diff. on average $\Delta$ BU per pass	0.59%	0.17%	-0.15%	-0.28%	-0.35%	-0.47%

The relative differences on the nuclide densities of the discharged pebbles are presented in Table 5.VI.

**Table 5.VI: LEU cycle rel. diff. between the two depletion methodologies on flow-weighted nuclide concentrations in the discharged pebbles per pass**

	Pass 1	Pass 2	Pass 3	Pass 4	Pass 5	Pass 6
U <sup>238</sup>	-0.01%	-0.01%	-0.01%	-0.01%	0.00%	0.00%
U <sup>235</sup>	-0.19%	-0.26%	-0.21%	-0.05%	0.21%	0.53%
U <sup>236</sup>	0.51%	0.32%	0.15%	0.00%	-0.10%	-0.17%
Pu <sup>239</sup>	1.00%	0.62%	0.37%	0.14%	-0.07%	-0.29%
Pu <sup>240</sup>	2.66%	2.36%	1.02%	-0.54%	-1.94%	-3.09%
Pu <sup>241</sup>	-4.55%	-0.89%	1.21%	2.06%	2.12%	1.78%
Pu <sup>242</sup>	-4.68%	-1.96%	-0.24%	0.67%	1.04%	1.05%
Am <sup>241</sup>	-5.36%	-1.91%	0.31%	1.59%	2.16%	2.25%
Cm <sup>244</sup>	-6.09%	-4.22%	-2.56%	-1.26%	-0.28%	0.47%
Tc <sup>99</sup>	0.59%	0.40%	0.23%	0.12%	0.03%	-0.05%



	Pass 1	Pass 2	Pass 3	Pass 4	Pass 5	Pass 6
Ag <sup>110m</sup>	0.57%	0.54%	0.51%	0.54%	0.57%	0.56%
Xe <sup>135</sup>	0.94%	0.79%	0.80%	0.90%	0.95%	0.91%
Cs <sup>132</sup>	0.57%	0.39%	0.23%	0.12%	0.04%	-0.03%
Cs <sup>137</sup>	0.59%	0.39%	0.24%	0.13%	0.05%	-0.01%
Pr <sup>141</sup>	0.45%	0.34%	0.21%	0.11%	0.04%	-0.02%
Nd <sup>144</sup>	0.57%	0.47%	0.30%	0.14%	0.01%	-0.10%
Sm <sup>149</sup>	-0.33%	-0.15%	0.18%	0.51%	0.71%	0.79%

Finally, the relative differences on the power distribution are shown in Table 5.VII.

**Table 5.VII: LEU cycle rel. diff. between the two depletion methodologies on power shape factors**

CHAN A	CHAN B	CHAN C	CHAN D	CHAN E
-0.83%	-0.92%	-0.96%	-0.92%	-0.85%
-0.75%				-0.77%
-0.57%	-0.78%	-0.84%	-0.79%	-0.60%
-0.35%	-0.51%	-0.57%	-0.51%	-0.37%
-0.10%	-0.17%	-0.23%	-0.18%	-0.13%
0.14%				0.12%
0.38%	0.18%	0.12%	0.17%	0.37%
0.61%	0.51%	0.46%	0.51%	0.60%
0.81%	0.81%	0.77%	0.81%	0.81%
0.99%				1.00%
1.16%	1.07%	1.03%	1.07%	1.17%
1.29%	1.28%	1.24%	1.28%	1.31%
1.41%	1.45%	1.41%	1.45%	1.43%
1.51%				1.53%
1.59%	1.59%	1.57%	1.59%	1.62%

It appears that computing the equilibrium core with the average composition pebble in each spectrum zone results in relatively small differences, compared with the reference calculation of section 5.4.1. It mostly influences the isotopic densities of the plutonium

and of the minor actinides, and the difference reduces from the discharged pebbles at the first pass to the one discarded at the last pass. The difference is higher for Am<sup>241</sup> and on Pu<sup>240</sup>, where a noticeable difference is present also in the discarded pebbles composition. Nevertheless, these differences are quite small.

To analyze the flux differences in between the different pebble types and with the flux computed in the related average composition pebble, the steady-state of the reference equilibrium core, with the nuclide distribution presented in Table 5.IV, was re-computed with the average pebbles in each spectrum zone.

Thus, in this case, the equilibrium core with the same nuclide distribution is computed both with the proper fluxes per pebble type both with the average flux methodology.

The resulting  $k_{eff}$  has a  $\Delta\rho$  of -74 pcm and  $\Delta_{sf>1}^{\%} \tau_{POWER}^{HET}$  of 0.33% from the calculation with proper fluxes per pass. Comparing the homogenized broad-group cross sections per spectrum zone, the larger relative difference is of 0.06% on the total cross sections and 1.37% on the fission cross sections.

The fluxes computed in the multi-pebble geometry associated to SZ 32, which is the central one in the core and less influenced by the reflectors, have also been compared.

Renormalizing the fluxes to the total power produced in the spectrum zone, the flux in the fuel kernels of the different pebble types have been compared with the one of the average composition pebble. The differences calculated on the total fluxes are shown in Table 5.VIII, since the differences in the 281-groups fluxes of pass 1 and 6 from the one in the average composition kernels, together with the flux spectrum in these average composition kernels, are illustrated in Figure 5.4.

The same process is applied to the fluxes in the multi-pebble geometries of SZ 3, where the hot spot is located. The results are gathered in Table 5.IX and Figure 5.5. The differences calculated on the multi-group fluxes for pebbles of the pass 2 to 5 are comprised in between the differences of pass 1 and 6 for the intermediary passes.

**Table 5.VIII: Rel. diff. of the proper total fluxes per type in the pebble kernels, comprised in SZ 32, from the average composition pebble flux (LEU cycle equilibrium core)**

	Pass 1	Pass 2	Pass 3	Pass 4	Pass 5	Pass 6
Total flux rel. diff.	0.57%	0.24%	0.00%	-0.17%	-0.29%	-0.38%

**Table 5.IX: Rel. diff. of the proper total fluxes per type in the pebble kernels, comprised in SZ 3, from the average composition pebble flux (LEU cycle equilibrium core)**

	Pass 1	Pass 2	Pass 3	Pass 4	Pass 5	Pass 6
Total flux rel. diff.	0.84%	0.43%	0.10%	-0.14%	-0.31%	-0.43%

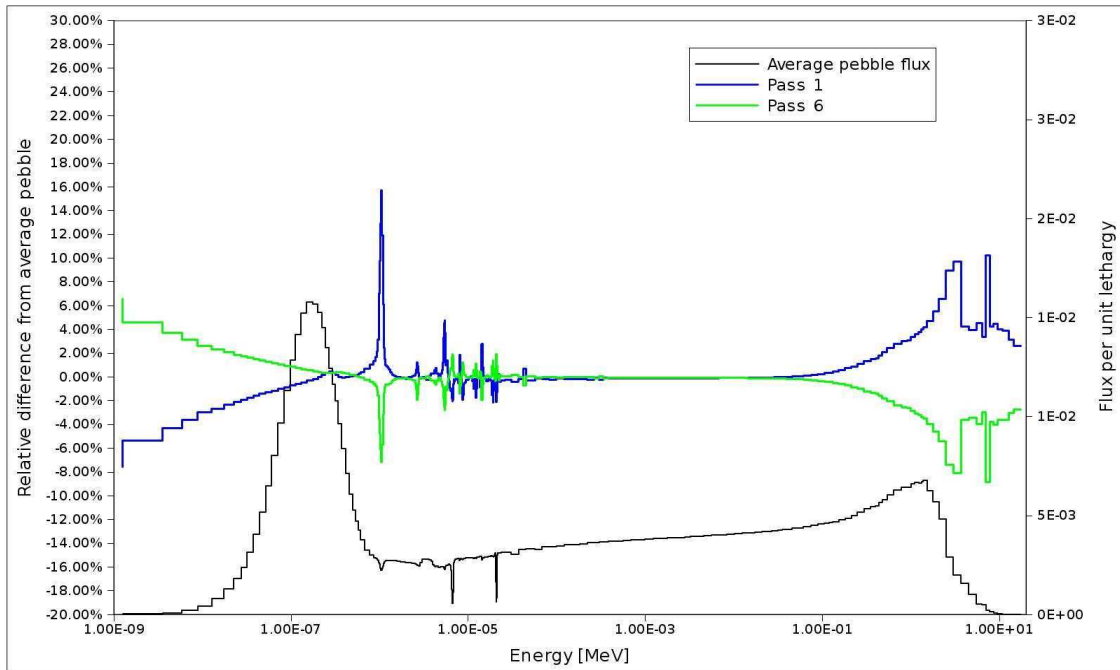


**Figure 5.4: Rel. diff. of the proper 281-group fluxes per type in the pebble kernels, comprised in SZ 32, from the average composition pebble flux (LEU cycle equilibrium core)**

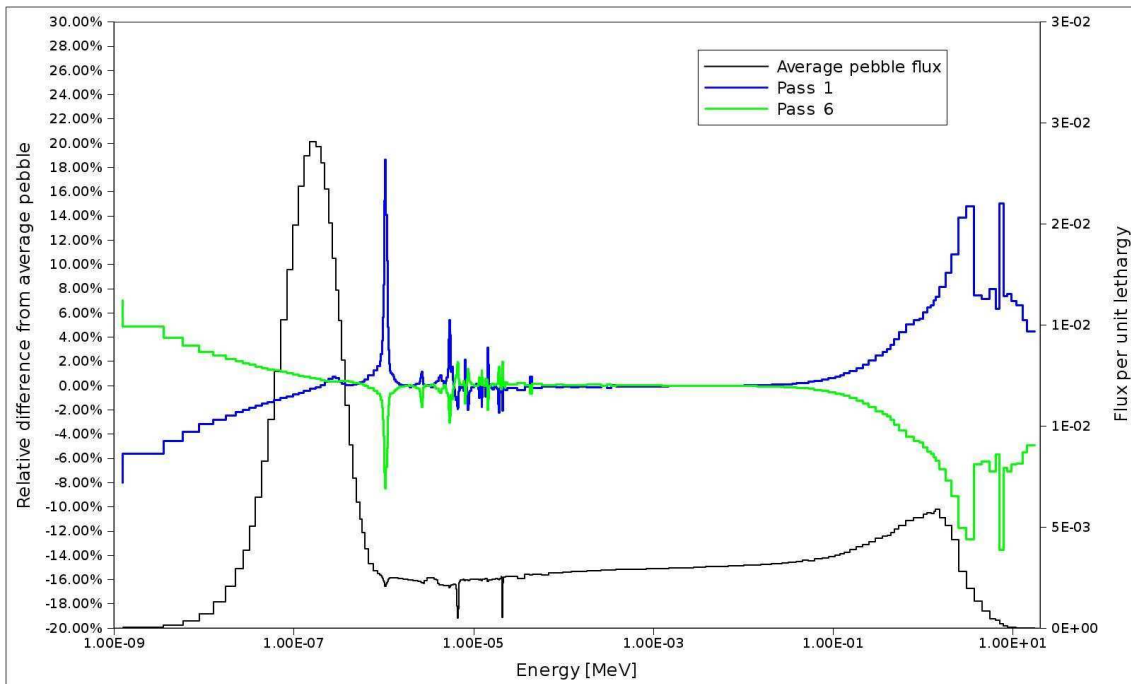


**Figure 5.5: Rel. diff. of the proper 281-group fluxes per type in the pebble kernels, comprised in SZ 3, from the average composition pebble flux (LEU cycle equilibrium core)**

From these results it appears that in the regions located both in the central channel or close to the reflectors the total flux value in pass 1 pebbles, compared to average composition pebbles, is higher whereas in pass 6 the total flux is lower. The differences are symmetrically distributed around pass 3 and 4, which are at half-way of the pebble exposure history. In spite of the lower total flux in the average pebble, the average discharge burnup of pass 1 pebble in the equilibrium core computed with the average compositions at  $T_{SZ}/2$ , is higher than the respective burnup value computed with the proper fluxes per pass, as shown in Table 5.V. This means that the spectral effects drive the burnup differences over the total flux value. The flux computed in the average pebble is higher than the flux in pass 1 pebble in the thermal energy range, where the flux thermal Gaussian is situated. As the fissions occurs mostly in the thermal energy range, this explains why the burnup, which is the fission power cumulated over the time, of the discharged pass 1 pebbles is higher when depletion is computed with the average spectrum.

These spectral differences in the thermal range are, however, symmetrically distributed around the average flux from pass 1 to pass 6. This directly influences the relative difference in the accumulated burnup per pass, shown in Table 5.V, but finally results in a "*cancellation of errors*" for the final burnup value of the discarded pass 6 pebbles.

The same trend is observed for the nuclide densities of most of the fission products, as shown in Table 5.VI. Nevertheless, the cancellation of errors does not occur for the plutonium isotopes, other than the  $\text{Pu}^{239}$ , and the minor actinides. This is due to the large differences which can be identified in the resonance region, in particular around 1 eV.

These energies correspond to the capture cross-section resonance of  $\text{Pu}^{240}$  (large resonance at 1.06 eV),  $\text{Pu}^{239}$  and  $\text{Pu}^{241}$ , with a first resonance at 0.43 eV. The capture cross section resonances of these Pu isotopes are illustrated Figure 5.6 (the JEFF-3.1 library data was taken from KAERI<sup>149</sup>).

The effect is large for pass 1 pebbles in particular, where the flux in the fuel kernels is about 15% higher than the average pebble flux in energy groups corresponding to the  $\text{Pu}^{240}$  resonance, since in the first pass the plutonium build up has just began.

The fluxes relative differences are observable also in energy groups corresponding to higher energy resonances, which belong both to the plutonium and the other minor actinides.

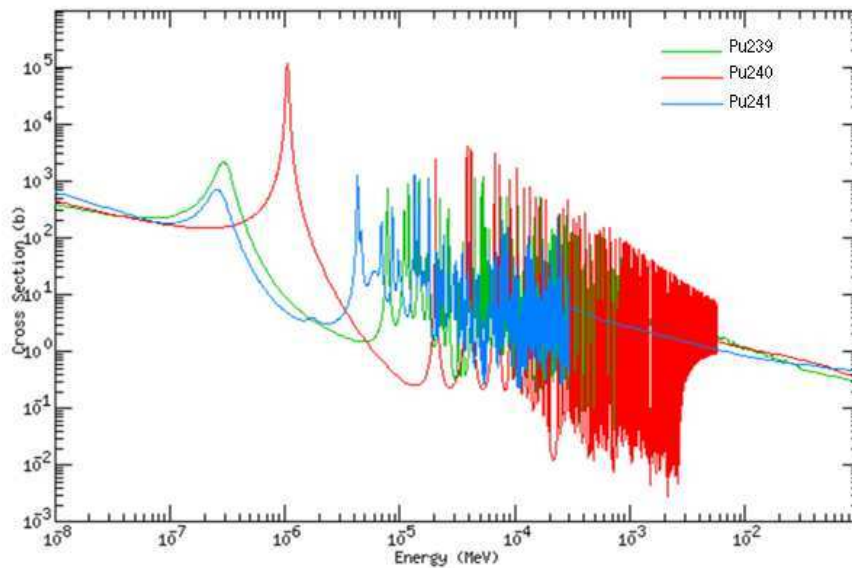


**Figure 5.6: Resonance region Pu cross sections from JEFF-3.1 at 293 K**

Finally, it appears that the average composition pebble approximation induces limited discrepancies, for both static core calculations and equilibrium conditions search, in the case of a  $\text{UO}_2$  fuel cycles. This is mainly due to the spectral properties of the uranium based fuel. Nevertheless, the influence of the observed spectral differences should be evaluated also on the calculation of the dynamic core parameters, as the temperature reactivity feedback coefficients.

#### **5.4.1.2 Limitations of the Implemented Mixing Algorithm**

The mixing algorithm implemented in APOLLO2 during this thesis considers that all the pebbles perform the same number of passes through the core before being discarded. In order to illustrate the limitation of such an assumption, the accumulated burnup per pass per each channel, in function of the entering burnup, are plotted in Figure 5.7. From this Figure it is possible to observe a nearly linear trend. Moreover, it can be observed that considering a limit for the maximum allowable burnup, the target burnup limit for recirculation have to be determined on the channel having the higher  $\Delta\text{BU}$  per pass. In this annular reactor model, this channel is the internal channel A.

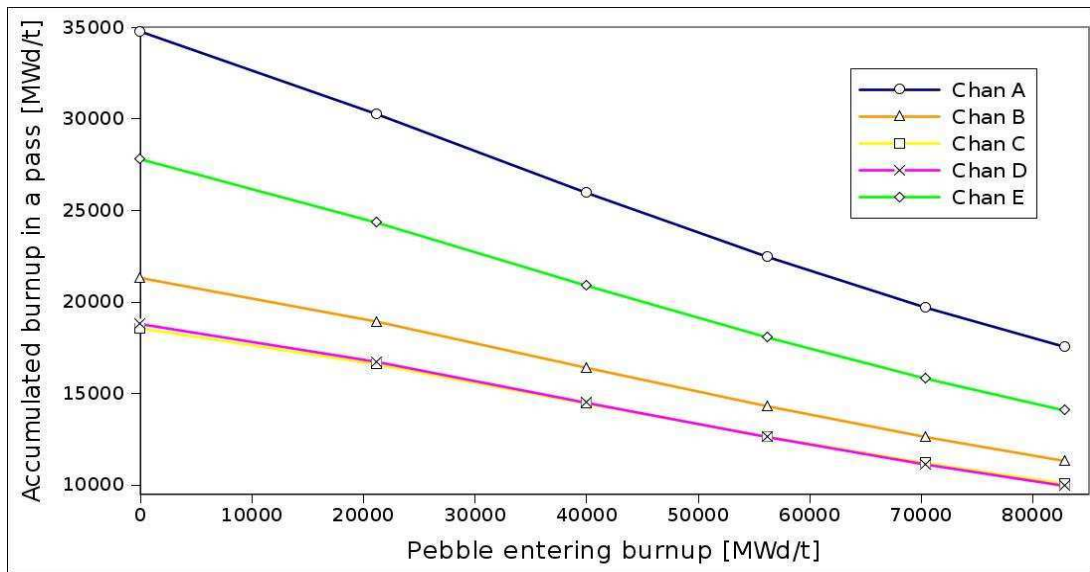


**Figure 5.7: Burnup accumulated in a pass through a core channel varying with the entering burnup (LEU cycle equilibrium core)**

For example, in this equilibrium core, fixing the maximum allowable burnup to 105000 MWd/t and interpolating linearly the accumulated burnups of pass 5 and pass 6 in channel A, we obtain that a pebble entering channel A with a burnup value of about 88400 MWd/t will reach the maximum allowable burnup at the discharge of the core. This is graphically shown in Figure 5.8.

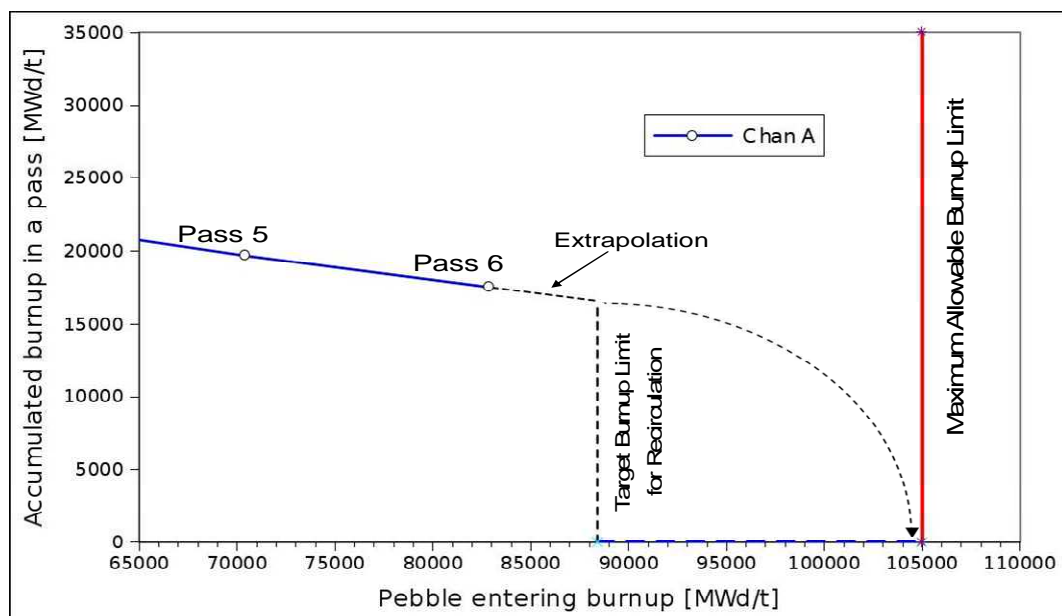


**Figure 5.8: Extrapolation of the 88400 MWd/t target burnup limit for recirculation**

From the data obtained in this equilibrium core calculation, shown in Table 5.II, one could deduce that all the pebbles would complete 6 passes through the core before being

discarded, since the flow-weighted average burnup value of the discharged fifth pass (corresponding with the reloaded sixth pass) is lower than 88400 MWd/t.

Nevertheless, the pebble history giving the smallest number of passes in the core is the one associated to a pebble always re-circulated in channel A. Thus, the depletion history of this pebble has to be determined, and this can be done using the graph in Figure 5.7. From this graph, it is actually possible to deduce the discharge burnup of a pebble loaded in a given channel with a certain entering burnup value. The discharge burnup value ( $BU_{OUT}$ ) is found summing the entering burnup value ( $BU_{IN}$ ) and the corresponding accumulated burnup in a pass ( $\Delta BU$ ), for the given channel, recovered from the graph.

This is shown graphically in Figure 5.9 and it is resumed in Table 5.X for a pebble always re-circulated in channel A.

This pebble reaches the target burnup limit for recirculation in only 4 passes.

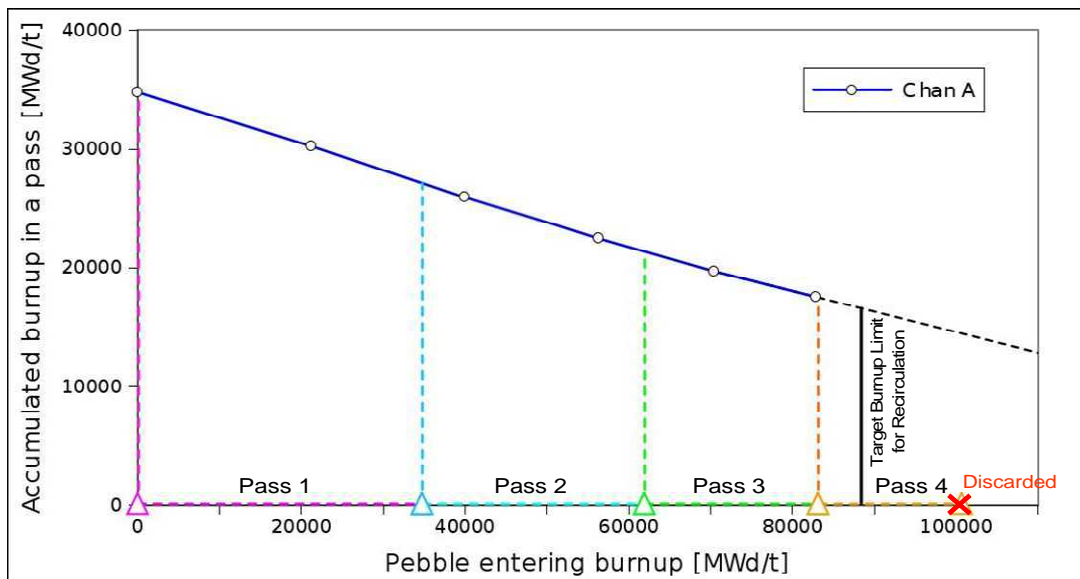


Figure 5.9: Exposure history of a pebble always re-circulated in channel A

Table 5.X: Exposure history of a pebble always re-circulated in channel A (tab.)

Channel A	Interpolation between	$BU_{IN}$	$\Delta BU$	$BU_{OUT}$
pass 1	$P1 \ \& \ P2$	0	34773	34773
pass 2	$P2 \ \& \ P3$	34773	27156	61928
pass 3	$P4 \ \& \ P5$	61928	21230	83158
pass 4	$(P5 \ \& \ P6)^+$	83158	17496	100654

In the same way, we deduced that a pebble re-circulated always in the channels C or D would be discharged at the end of the sixth pass with a burnup value of about 86000

MWd/t, so performing an additional seventh pass through the core before being discarded.

It is so possible to conclude that for the rightly modeling of such a configuration, the multi-pebble geometries should contain seven types of pebbles, with a constant relative abundance per type until pass 4 and then with progressively decreasing ones. This trend can not be simulated with the implemented mixing algorithm, but an improved mixing algorithm should be applied

#### 5.4.2 Plutonium Based Fuel Cycle

In the simulated plutonium based fuel cycle, the TRISO fuel kernels contain  $\text{PuO}_{1.7}$  first generation plutonium (i.e. issued from recycled LWR  $\text{UO}_2$  fuel). The isotopic composition vector is given in Table 5.XI.<sup>150</sup>

**Table 5.XI: First generation Pu isotopic vector**

$\text{Pu}^{238}$	$\text{Pu}^{239}$	$\text{Pu}^{240}$	$\text{Pu}^{241}$	$\text{Pu}^{242}$
2.59%	53.84%	23.66%	13.13%	6.78%

Each fresh fuel pebble contains 2 g of first generation Pu loaded in coated fuel particles with a kernel diameter of 200  $\mu\text{m}$ , resulting in a total of 48728 micro-particles dispersed in the graphite matrix or the fuel region. The thickness of the coating buffer, internal PyC, Sic and outer PyC are respectively 90/40/35/40  $\mu\text{m}$ , since the densities of the fuel and coatings, and all the other pebbles characteristics, are the same as for the  $\text{UO}_2$  pebbles.

In the simulated 9 m height 330 MW power reactor model, the time period  $T_{SZ}$  of 19.60 days gives an equilibrium core with  $k_{eff}$  equal 1.00016.

The corresponding pebbles discharged per day are about 1626, with 271 fresh pebbles loaded daily. The average burnup of the discarded pebbles is 627482 MWd/t.

The equilibrium core search converged in 30 iterations, taking 30h16m on a AMD/Opteron 64 bit 2,8 GHz CPU.

While computing the RZ core  $S_N$  calculation with a  $S_4$  angular quadrature, the equilibrium core search converged always in 30 iterations, taking 18h08m. This is a huge time gain of about a 1.7 factor. Compared to the  $S_8$  as reference, the  $k_{eff}$  of the core obtained with this simulation differed by a  $\Delta\rho=5$  pcm and a  $\Delta_{sf>1}^{\%} \tau_{PROD}^{HET} = 0.13\%$ .

Also in this case, the equilibrium cores computed using the  $S_8$  or the  $S_4$  angular quadratures are practically the same.

The average flow-weighted discharge burnups and the corresponding accumulated burnups per pass are presented in Table 5.XII.



**Table 5.XII: Channel flow-weighted discharge burnup and accumulated burnup values per pass (Pu cycle equilibrium core)**

	Pass 1	Pass 2	Pass 3	Pass 4	Pass 5	Pass 6
Av. disch. BU [MWd/t]	196443	338066	441287	519027	579550	627482
Av. $\Delta$ BU per pass [MWd/t]	196443	141623	103221	77739	60523	47933

The burnup evolution of the different passes pebbles flowing through the different channels is illustrated in Figure 5.10.

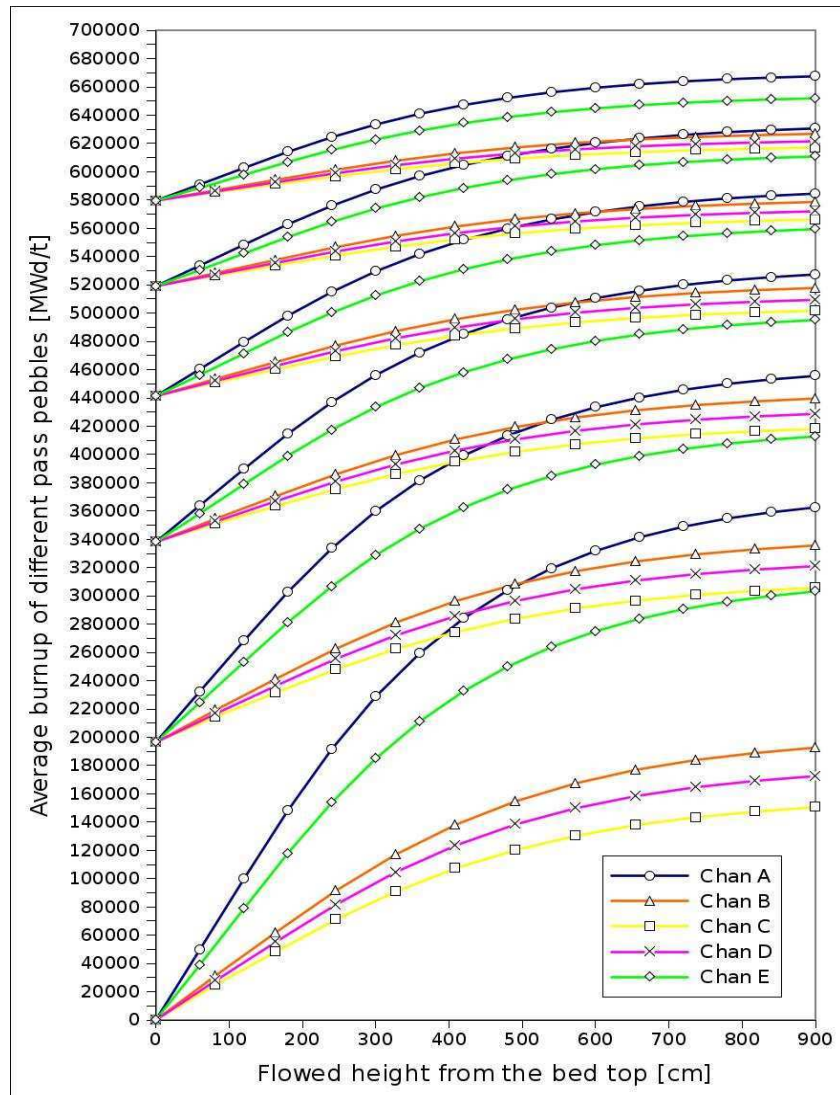


**Figure 5.10: Burnup distribution of the different pass pebbles flowing through the different channels (Pu cycle equilibrium core)**

As it can be noticed, particularly for the first pass, the distribution of the discharged burnups per channel is much more dispersed around the average discharge value than in the  $\text{UO}_2$  cycle. In this case, the APOLLO2 iterative core calculation model, which properly account for the currents entering the core from the reflectors, is well suited to treat the depletion of the pebbles flowing in the channels close to the walls. The entering currents from the reflectors, in fact, highly contribute to the thermal flux in the neighboring spectrum zones, as it can be seen from Figure 5.13. This leads to a much higher accumulated burnup per pass while pebbles flow through channels A and E. Due to this spread distribution of burnup values per pass in the different channels, an improved mixing algorithm could significantly improve the mixing modeling, approaching the physical reactor fuel management.

As previously described in section 5.4.1.2 for the LEU cycle, the variation of the accumulated burnup in a pass per channel depends almost linearly on the entry burnup value, as shown in Figure 5.11. Even if the variation is not properly linear over the whole entering burnup range, the linear approximation in between of two entering values still appears to be satisfactory. The same considerations on the target burnup limit for recirculation made for the  $\text{UO}_2$  fuel are valid here too.

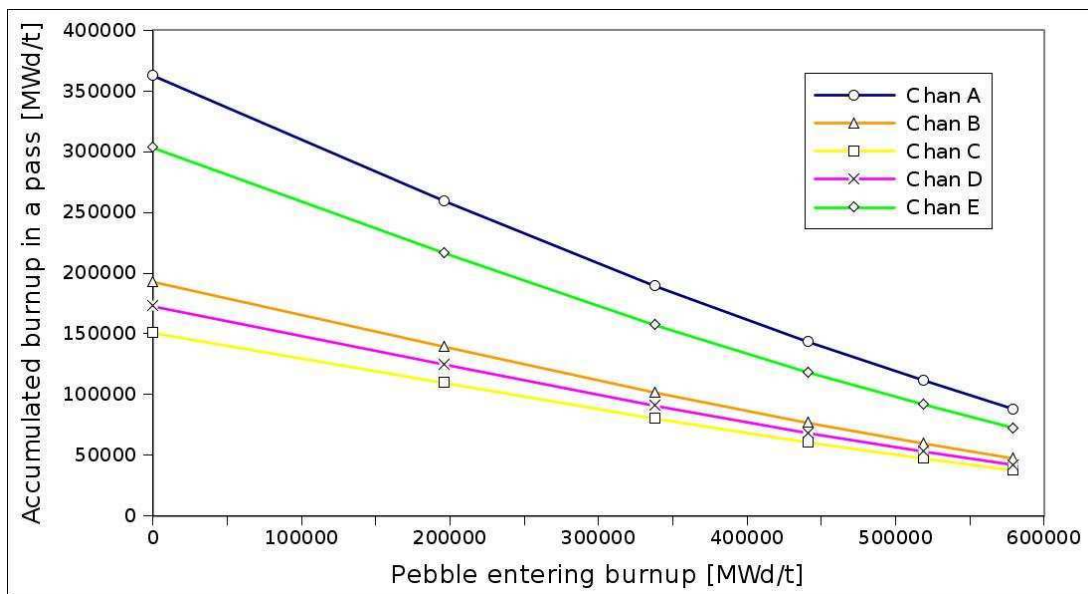


**Figure 5.11: Burnup accumulated in a pass through a core channel varying with the entering burnup (Pu cycle equilibrium core)**

The power distribution over the spectrum zones of the equilibrium core is shown in Table 4.III

**Table 5.XIII: Power shape factors of Pu cycle equilibrium core**

CHAN A	CHAN B	CHAN C	CHAN D	CHAN E
2.67	1.91	1.55	1.69	1.87
2.67				1.91
2.60	1.85	1.46	1.66	1.89
2.34	1.79	1.42	1.61	1.73
2.01	1.57	1.26	1.41	1.50
1.67				1.27
1.35	1.29	1.04	1.16	1.04
1.09	1.02	0.83	0.92	0.85
0.87				0.68
0.69	0.78	0.64	0.70	0.54
0.54	0.59	0.48	0.53	0.43
0.42	0.43	0.36	0.39	0.34
0.33				0.26
0.25	0.31	0.25	0.28	0.20
0.19	0.24	0.20	0.21	0.16

In this equilibrium core, one can observe that the power peaking occurs in the top spectrum zones and this is probably connected to the high fission rate occurring in fresh plutonium pebbles. Moreover, compared to the LEU cycle, the power shape factor at the hot spot is 0.34% higher. Again, these values are not the one observable in a operating reactor, as no thermal feedback is considered in this neutronic calculations.

The flow-weighted concentrations of the main actinides and fission products in the discharged pebbles per pass are shown in Table 5.XIV.

**Table 5.XIV: Pu cycle flow-weighted nuclide concentrations in the discharged pebbles per pass**

	Pass 1	Pass 2	Pass 3	Pass 4	Pass 5	Pass 6
BU	196443	338066	441287	519027	579550	627482
Atomic densities [atoms barn <sup>-1</sup> cm <sup>-1</sup> ]						
Pu <sup>238</sup>	5.57E-04	5.20E-04	5.01E-04	4.95E-04	4.93E-04	4.92E-04
Pu <sup>239</sup>	6.98E-03	3.63E-03	1.82E-03	8.96E-04	4.50E-04	2.39E-04
Pu <sup>240</sup>	5.85E-03	5.30E-03	4.33E-03	3.24E-03	2.24E-03	1.42E-03
Pu <sup>241</sup>	3.17E-03	3.13E-03	2.94E-03	2.63E-03	2.25E-03	1.84E-03
Pu <sup>242</sup>	1.84E-03	2.12E-03	2.39E-03	2.61E-03	2.77E-03	2.86E-03
Am <sup>241</sup>	7.99E-05	1.26E-04	1.46E-04	1.48E-04	1.38E-04	1.23E-04
Cm <sup>244</sup>	1.71E-05	6.41E-05	1.37E-04	2.31E-04	3.43E-04	4.68E-04
Tc <sup>99</sup>	2.83E-04	4.73E-04	5.97E-04	6.79E-04	7.33E-04	7.67E-04
Ag <sup>110m</sup>	2.61E-07	7.54E-07	1.24E-06	1.64E-06	1.93E-06	2.12E-06
Xe <sup>135</sup>	1.29E-07	9.05E-08	6.53E-08	4.90E-08	3.79E-08	2.96E-08
Cs <sup>137</sup>	3.09E-04	5.24E-04	6.74E-04	7.81E-04	8.59E-04	9.17E-04
Pr <sup>141</sup>	2.24E-04	4.02E-04	5.27E-04	6.19E-04	6.88E-04	7.41E-04
Nd <sup>144</sup>	6.64E-05	1.84E-04	3.16E-04	4.45E-04	5.64E-04	6.72E-04
Sm <sup>149</sup>	3.47E-06	2.66E-06	2.09E-06	1.68E-06	1.37E-06	1.13E-06

Even if this calculation is performed for a simplified isothermal reactor model, it is possible to observe the outstanding capability of pebble bed reactors, common to all HGTRs, to incinerate reactor grade plutonium, which is considered a waste in PWRs, while still producing energy.

For example, the atomic densities of the Pu<sup>239</sup> and Pu<sup>240</sup> in the fresh fuel are respectively of 1.27E-02 and 5.54E-02 atoms barn<sup>-1</sup> cm<sup>-1</sup>. Thus, in the average discarded pebbles their content is reduced by a factor 53 and 39 respectively.

One can observe that while incinerating the 239, 240 and 241 Pu isotopes, the 238 reach an asymptotic atomic density after 3 or 4 passes through the core, since the 242 is built up during the pebble depletion.

Moreover, adopting this fuel cycle does not imply significant reactor design changes. The same simplified PBMR-400 core cavity which could reach an equilibrium core configuration accommodating LEU pebbles, as it has been shown in section 5.4.1, can properly achieve the equilibrium conditions also with this pure plutonium fuel.

The inherent safety characteristics of the pebble bed reactors are conserved also with the pure plutonium fuel cycle.<sup>62</sup>

#### 5.4.2.1 Average Composition Pebble Approximation

In the following, we do the same comparisons as the one performed in section 5.4.1.1 for the LEU cycle. It consists in considering the average composition pebble in all the spectrum zones, both for the SZ – core calculations both for the depletion ones, when computing the equilibrium core of the plutonium based fuel cycle.

The  $\Delta\rho$  of the resulting core compared to the reference one is of -109 pcm.

The relative differences on the average discharge burnups and on the average burnup values cumulated per pass are shown in Table 5.XV.

**Table 5.XV: Pu cycle rel. diff. between the two depletion methodologies on discharge burnup and accumulated burnup values per pass**

	Pass 1	Pass 2	Pass 3	Pass 4	Pass 5	Pass 6
Rel. diff. on average discharge BU	11.67%	6.68%	4.07%	2.41%	1.11%	0.01%
Rel. diff. on average $\Delta$ BU per pass	11.67%	-0.23%	-4.49%	-7.02%	-10.07%	-13.29%

The relative differences on the nuclide densities of the discharged pebbles obtained with the average composition pebble approximation, compared to the ones exposed in Table 5.XIV, are shown in Table 5.XVI.

**Table 5.XVI: Pu cycle rel. diff. between the two depletion methodologies on flow-weighted nuclide concentrations in the discharged pebbles per pass**

	Pass 1	Pass 2	Pass 3	Pass 4	Pass 5	Pass 6
Pu <sup>238</sup>	-0.63%	-0.60%	-0.24%	0.16%	0.47%	0.67%
Pu <sup>239</sup>	-9.26%	-12.24%	-10.99%	-6.81%	-0.69%	6.18%
Pu <sup>240</sup>	-1.70%	-7.09%	-10.34%	-9.86%	-4.14%	9.59%
Pu <sup>241</sup>	3.91%	5.28%	3.08%	-1.09%	-5.61%	-9.06%
Pu <sup>242</sup>	4.15%	5.67%	5.25%	3.62%	1.41%	-0.88%
Am <sup>241</sup>	1.83%	3.11%	4.42%	4.95%	4.66%	4.09%
Cm <sup>244</sup>	-5.66%	-3.39%	-1.48%	-0.04%	0.90%	1.35%
Tc <sup>99</sup>	11.58%	6.34%	3.62%	1.94%	0.65%	-0.45%

	Pass 1	Pass 2	Pass 3	Pass 4	Pass 5	Pass 6
Ag <sup>110m</sup>	10.97%	7.76%	5.26%	3.18%	1.24%	-0.67%
Xe <sup>135</sup>	-6.89%	-12.40%	-14.29%	-16.25%	-19.05%	-21.67%
Cs <sup>137</sup>	11.52%	6.42%	3.79%	2.15%	0.87%	-0.22%
Pr <sup>141</sup>	12.65%	7.00%	4.15%	2.44%	1.16%	0.09%
Nd <sup>144</sup>	15.60%	10.35%	6.99%	4.63%	2.81%	1.31%
Sm <sup>149</sup>	1.22%	-1.20%	-1.27%	-2.10%	-3.98%	-5.83%

The relative differences on the power distribution between the reference case and the equilibrium core computed with the average pebble fluxes are shown in Table 5.XVII.

**Table 5.XVII: Pu cycle rel. diff. between the two depletion methodologies on power shape factors**

CHAN A	CHAN B	CHAN C	CHAN D	CHAN E
10.88%	10.25%	10.13%	10.33%	11.19%
7.65%	7.14%	6.99%	7.26%	8.27%
4.18%	3.78%	3.73%	3.91%	5.06%
0.73%	0.25%	0.32%	0.40%	1.80%
-2.44%	0.25%	0.32%	0.40%	-1.28%
-5.25%	-3.15%	-2.97%	-2.97%	-4.10%
-7.68%	-6.22%	-5.96%	-6.03%	-6.59%
-9.78%	-8.91%	-8.61%	-8.71%	-8.78%
-11.59%	-11.20%	-10.89%	-11.00%	-10.70%
-13.17%	-13.10%	-12.78%	-12.90%	-12.37%
-14.53%	-14.55%	-14.24%	-14.35%	-13.83%
-15.69%	-15.42%	-15.05%	-15.21%	-15.07%
-16.65%	-15.42%	-15.05%	-15.21%	-16.10%
-17.35%	-15.42%	-15.05%	-15.21%	-16.85%
-17.74%	-15.42%	-15.05%	-15.21%	-17.28%

One can observe that with the plutonium fuel cycle the average composition pebble approximation gives very high discrepancies with the reference calculation of the equilibrium core, both on the main nuclides discharge atomic densities both on the power distribution.

The relative differences on the atomic densities are in the order of 10% for the plutonium isotopes. On the other nuclides, the differences can be also higher, resulting, for example, in an underestimation of about 22% on the  $Xe^{135}$  atomic density in the average discarded pebble.

The biases on the power shape factors are also high, with, for example, an overestimation of the power peaking factor of about 11%.

To analyze in detail the flux differences in between the different pebble types and with the flux computed in the related average composition pebble, the reference equilibrium core, with the nuclide distribution presented in Table 5.XIV, was re-computed with the average pebbles in each spectrum zone.

Thus, in this case, the equilibrium core with the same nuclide distribution is computed both with the proper fluxes per pebble type both with the average flux methodology.

The resulting  $k_{eff}$  has a  $\Delta\rho$  of -147 pcm and  $\Delta_{sf>1}^{\%} \tau_{POWER}^{HET}$  of 9.39% from the reference calculation with the proper pebble compositions per pass. Comparing the homogenized broad-group cross sections per spectrum zone, the larger relative difference is 0.51% on the total cross sections and 11.94% on the fission cross sections.

One can observe that with plutonium fuel the discrepancies between the proper spectra and the average pebble spectrum calculations of the steady-state reactor are much larger.

Renormalizing the fluxes to the total power produced in the spectrum zone, the flux in the fuel kernels of the different pebble types have been compared with the one of the average composition pebble. One can notice from Table 5.XVIII and Table 5.XIX that in this case, differently for what it was observed for the LEU cycle in section 5.4.1.1, also with this renormalization the total flux values of the different pass pebbles are all higher than the one in the average pebble.

The fluxes computed in the multi-pebble geometry associated to SZ 32, which is the central one in the core and less influenced by the reflectors, have been compared.

The differences calculated on the total fluxes are shown in Table 5.XVIII, since the differences in the 281-groups fluxes of pass 1 and 6 from the one in the average composition kernels, together with the flux spectrum in these average composition kernels, are illustrated in Figure 5.12.

The same process is applied to the fluxes in the multi-pebble geometries of SZ 2, where the hot spot is located. The results are gathered in Table 5.XIX and Figure 5.13. The differences calculated on the multi-group fluxes for pebbles of the pass 2 to 5 are comprised in between the differences of pass 1 and 6.

The relative differences in correspondence of the Pu240 resonance spike is pass 1 pebbles are up to about 105%.

**Table 5.XVIII: Rel. diff. of the proper total fluxes per type in the pebble kernels, comprised in SZ 32, from the average composition pebble flux (Pu cycle equilibrium core)**

	Pass 1	Pass 2	Pass 3	Pass 4	Pass 5	Pass 6
Total flux rel. diff.	3.16%	2.68%	2.54%	2.64%	2.90%	3.28%

**Table 5.XIX: Rel. diff. of the proper total fluxes per type in the pebble kernels, comprised in SZ 2, from the average composition pebble flux (Pu cycle equilibrium core)**

	Pass 1	Pass 2	Pass 3	Pass 4	Pass 5	Pass 6
Total flux rel. diff.	6.33%	5.27%	4.76%	4.61%	4.71%	4.96%

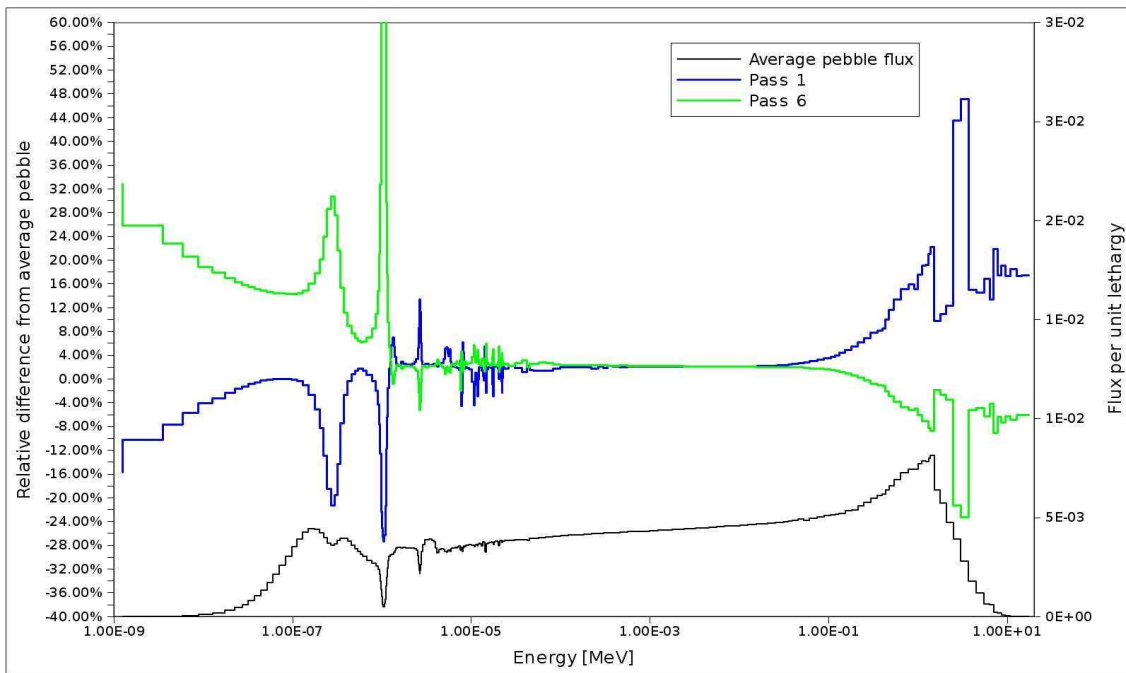


**Figure 5.12: Rel. diff. of the proper 281-group fluxes per type in the pebble kernels, comprised in SZ 32, from the average composition pebble flux (Pu cycle equilibrium core)**



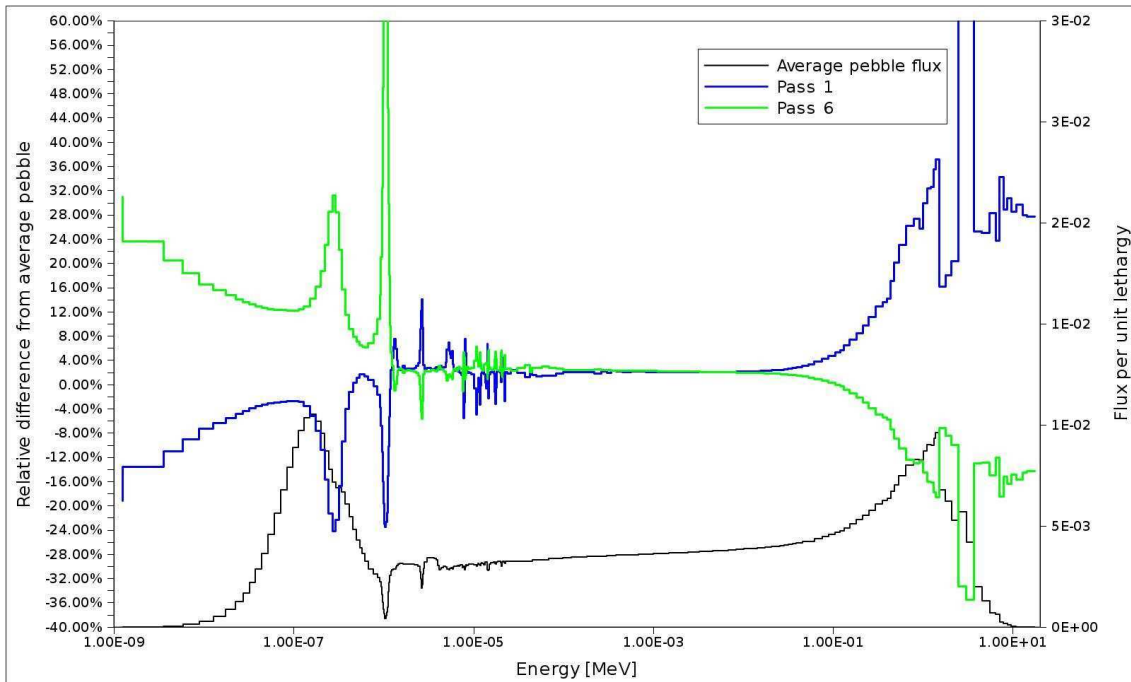


**Figure 5.13: Rel. diff. of the proper 281-group fluxes per type in the pebble kernels, comprised in SZ 2, from the average composition pebble flux (Pu cycle equilibrium core)**

As to conclude, the biases introduced by using in all the zones the spectrum of the average composition pebbles are much higher for plutonium cycles than for the LEU ones. This is mainly due to the large spectral differences from the different passes pebbles in the energy range of the plutonium resonances. The final burnup value of the discarded pebbles does not differ greatly from the value computed when the proper fluxes per type are used, but this is due to the fact that the same fresh pebbles are loaded in the core, and are irradiated for the same total period in the same total power core.

On the other hand, the irradiation histories influence greatly the depleted fuel composition, and this can not be considered properly by the existing codes which use the average composition pebble approximation.

The low discrepancy on the core eigenvalue evidences the effect of "errors cancellation".

However, the differences in the power distribution are quite large, with an overestimation of the power peaking factor of about 12%. Moreover, the differences on the average nuclide concentrations of the discharged pebbles per pass are large, both for the minor actinides and for some important fission products.

As it has been evidenced in a recent work conducted on the use of first generation  $\text{PuO}_{1.7}$  fuel for a deep burn PBMR-400 fuel cycle,<sup>62</sup> the role played by the absorptions in the  $\text{Pu}^{239}$ ,  $\text{Pu}^{240}$  and  $\text{Pu}^{241}$  resonances is crucial to determine the fuel depletion, but also to determine fuel and moderator temperature reactivity feedback coefficients. Thus, it would be crucial to use the proper spectrum in each pebble to determine these coefficients due to the large spectral differences rightly on these resonance energy regions.

### 5.4.3 Mixed Plutonium – Minor Actinides Based Fuel Cycle

In this last case, the TRISO fuel kernels contain a mixture of plutonium and minor actinides (MA), namely  $\text{Am}^{241}$ ,  $\text{Am}^{242\text{m}}$ ,  $\text{Am}^{243}$  and  $\text{Np}^{237}$ , hypothetically coming from the reprocessing of a spent LWR fuel after five years of cooling. The isotopic composition vector is given in Table 5.XX.<sup>150</sup>

**Table 5.XX: First generation Pu + Minor Actinides isotopic vector**

$\text{Pu}^{238}$	$\text{Pu}^{239}$	$\text{Pu}^{240}$	$\text{Pu}^{241}$	$\text{Pu}^{242}$	$\text{Am}^{241}$	$\text{Am}^{242\text{m}}$	$\text{Am}^{243}$	$\text{Np}^{237}$
2.9%	49.38%	23.0%	8.8%	4.9%	2.8%	0.02%	1.4%	6.8%

The reference plutonium oxide kernel with a diameter of 200  $\mu\text{m}$  was used in this analysis, with the same characteristic of the  $\text{PuO}_{1.7}$  fresh pebbles used in the previous section.

In the 9 m height 330 MW power simulated reactor model, the time period  $T_{SZ}$  of 12.56 days provides an equilibrium core with  $k_{eff}$  equal to 1.00007. The corresponding pebbles discharged per day are about 2538, with 423 fresh pebbles loaded daily. The average burnup of the discarded pebbles is of 402579 MWd/t. The equilibrium core search converged in 26 iterations, taking 19h14m on a AMD/Opteron 64 bit 2,8 GHz CPU.

While computing the RZ core  $S_N$  calculation with a  $S_4$  angular quadrature, the equilibrium core search converged always in 30 iterations, taking 16h49m. This is a decent time gain of about a 1.15 factor, not as large as in the plutonium based fuel cycle analyzed in the previous section. Compared to the  $S_8$  as reference, the  $k_{eff}$  of the core obtained with this simulation is exactly the same and a  $\Delta_{sf>1}^{\%} \tau_{PROD}^{HET} = 0.18\%$ . Thus, also in this last case, the equilibrium cores computed using the  $S_8$  or the  $S_4$  angular quadratures are practically the same.

The average flow-weighted discharge burnups and the corresponding accumulated burnups per pass are shown in Table 5.XXI.

**Table 5.XXI: Channel flow-weighted discharge burnup and accumulated burnup values per pass (Pu+MA cycle equilibrium core)**

	Pass 1	Pass 2	Pass 3	Pass 4	Pass 5	Pass 6
Av. disch. BU [MWd/t]	92315	172535	242182	302806	355853	402579
Av. $\Delta\text{BU}$ per pass [MWd/t]	92315	80220	69647	60624	53047	46725

The burnup evolution of the different pass pebbles flowing through the different channels is illustrated in Figure 5.14.

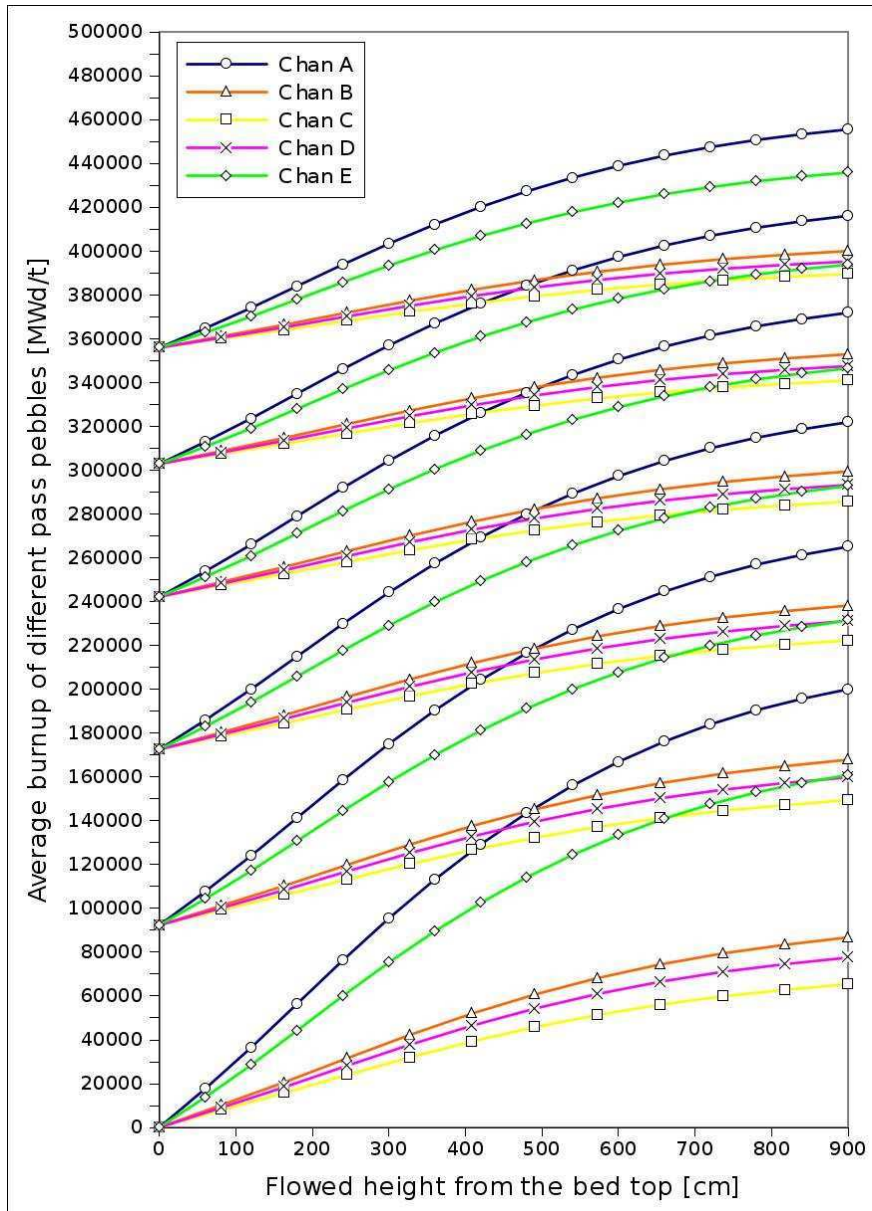


Figure 5.14: Burnup distribution of the different pass pebbles flowing through the different channels (Pu+MA cycle equilibrium core)

The power distribution over the spectrum zones of the equilibrium core is shown in Table 5.XXII.

**Table 5.XXII: Power shape factors of Pu+MA cycle equilibrium core**

CHAN A	CHAN B	CHAN C	CHAN D	CHAN E
2.04	1.34	1.08	1.19	1.43
2.17	1.35	1.04	1.21	1.53
2.30				1.63
2.29	1.42	1.10	1.28	1.63
2.19	1.39	1.07	1.24	1.57
2.03				1.47
1.84	1.28	0.99	1.14	1.34
1.64	1.13	0.87	1.01	1.20
1.44	0.97	0.75	0.87	1.06
1.25				0.92
1.07	0.81	0.63	0.73	0.79
0.90	0.66	0.51	0.59	0.67
0.74	0.51	0.40	0.46	0.56
0.60				0.45
0.50	0.44	0.35	0.39	0.37

One can notice that in this Pu+MA fuel cycle the position of the power peaking is again in SZ 3, like it is shown for the LEU cycle in Table 5.III, and not in the top SZ 1 and 2 as shown for the pure plutonium cycle in Table 5.XIII. Moreover the peaking factor is 14% lower than in the plutonium cycle.

The flow-weighted concentrations of the main actinides and fission products in the discharged pebbles per pass are summarized in Table 5.XXIII.

**Table 5.XXIII: Pu+MA cycle flow-weighted nuclide concentrations in the discharged pebbles per pass**

	Pass 1	Pass 2	Pass 3	Pass 4	Pass 5	Pass 6
BU	92315	172535	242182	302806	355853	402579
Atomic densities [atoms barn <sup>-1</sup> cm <sup>-1</sup> ]						
Pu <sup>238</sup>	7.85E-04	9.13E-04	1.04E-03	1.15E-03	1.24E-03	1.32E-03
Pu <sup>239</sup>	8.61E-03	6.41E-03	4.72E-03	3.45E-03	2.51E-03	1.83E-03
Pu <sup>240</sup>	5.35E-03	5.19E-03	4.86E-03	4.42E-03	3.91E-03	3.37E-03
Pu <sup>241</sup>	2.42E-03	2.71E-03	2.89E-03	2.98E-03	2.98E-03	2.92E-03
Pu <sup>242</sup>	1.21E-03	1.32E-03	1.44E-03	1.57E-03	1.70E-03	1.82E-03
Am <sup>241</sup>	5.39E-04	4.61E-04	4.01E-04	3.54E-04	3.17E-04	2.88E-04
Am <sup>243</sup>	3.58E-04	3.98E-04	4.41E-04	4.85E-04	5.30E-04	5.76E-04
Am <sup>242m</sup>	1.29E-05	1.46E-05	1.40E-05	1.27E-05	1.15E-05	1.03E-05
Np <sup>237</sup>	1.47E-03	1.36E-03	1.25E-03	1.16E-03	1.07E-03	9.82E-04
Cm <sup>244</sup>	4.18E-05	8.61E-05	1.33E-04	1.83E-04	2.36E-04	2.91E-04
Tc <sup>99</sup>	1.31E-04	2.41E-04	3.33E-04	4.09E-04	4.71E-04	5.23E-04
Ag <sup>110m</sup>	8.23E-08	2.69E-07	5.02E-07	7.45E-07	9.78E-07	1.19E-06
Xe <sup>135</sup>	1.71E-07	1.46E-07	1.25E-07	1.08E-07	9.32E-08	8.14E-08
Cs <sup>137</sup>	1.43E-04	2.65E-04	3.68E-04	4.56E-04	5.32E-04	5.96E-04
Pr <sup>141</sup>	8.89E-05	1.88E-04	2.74E-04	3.48E-04	4.11E-04	4.66E-04
Nd <sup>144</sup>	1.84E-05	5.82E-05	1.10E-04	1.69E-04	2.31E-04	2.93E-04
Sm <sup>149</sup>	3.85E-06	3.53E-06	3.21E-06	2.91E-06	2.64E-06	2.40E-06

One can observe that the PBR incineration capabilities for the minor actinides are not so effective than for the Pu isotopes.

The Am<sup>241</sup> and the Np<sup>237</sup>, whose atomic density in the fresh fuel is of 6.42E-04 and 1.58E-03 atoms barn<sup>-1</sup> cm<sup>-1</sup> respectively, are reduced in the average discarded pebble by a factor 2.2 and 1.6 respectively. Nevertheless, the Am<sup>243</sup> and the Am<sup>242m</sup>, whose atomic density in the fresh fuel is of 3.18E-04 and 4.57E-06 atoms barn<sup>-1</sup> cm<sup>-1</sup> respectively, are built up during the pebble depletion.

### 5.4.3.1 Average Composition Pebble Approximation

In the following, we do the same comparisons as the ones performed in section 5.4.1.1 for the LEU cycle and in section 5.4.2.1 for the plutonium cycle. It consists in considering the average composition pebble in all the spectrum zones, both for the SZ – core calculations both for the depletion ones, when computing the equilibrium core of the Pu+MA based fuel cycle.

The  $\Delta\rho$  of the resulting core when comparing to the reference one is -77 pcm.

The relative differences on the average discharge burnups and on the average burnup values cumulated per pass are shown in Table 5.XXIV.

**Table 5.XXIV: Pu+MA cycle rel. diff. between the two depletion methodologies on discharge burnup and accumulated burnup values per pass**

	Pass 1	Pass 2	Pass 3	Pass 4	Pass 5	Pass 6
Rel. diff. on average discharge BU	8.49%	5.62%	3.56%	2.06%	0.92%	0.02%
Rel. diff. on average $\Delta$ BU per pass	8.49%	2.33%	-1.54%	-3.95%	-5.57%	-6.85%

The relative differences on the nuclide densities of the discharged pebbles obtained with the average composition pebble approximation, compared to the ones exposed in Table 5.XIV, are shown in Table 5.XXV.

**Table 5.XXV: Pu+MA cycle rel. diff. between the two depletion methodologies on flow-weighted nuclide concentrations in the discharged pebbles per pass**

	Pass 1	Pass 2	Pass 3	Pass 4	Pass 5	Pass 6
Pu <sup>238</sup>	0.52%	0.78%	0.75%	0.59%	0.37%	0.18%
Pu <sup>239</sup>	-2.95%	-4.40%	-4.56%	-3.62%	-1.73%	0.92%
Pu <sup>240</sup>	0.38%	-0.57%	-1.61%	-2.07%	-1.56%	0.27%
Pu <sup>241</sup>	1.46%	2.25%	2.18%	1.44%	0.23%	-1.23%
Pu <sup>242</sup>	1.39%	2.13%	2.24%	1.81%	0.94%	-0.20%
Am <sup>241</sup>	-1.92%	-2.53%	-2.08%	-0.93%	0.58%	2.16%
Am <sup>242m</sup>	-0.51%	-0.49%	-0.17%	0.31%	0.82%	1.30%
Am <sup>243</sup>	2.95%	0.26%	-1.27%	-1.68%	-1.28%	-0.41%
Np <sup>237</sup>	-0.20%	-0.30%	-0.32%	-0.26%	-0.15%	0.03%
Cm <sup>244</sup>	-0.06%	-0.20%	-0.20%	-0.11%	0.01%	0.15%

	Pass 1	Pass 2	Pass 3	Pass 4	Pass 5	Pass 6
Tc <sup>99</sup>	8.57%	5.59%	3.44%	1.88%	0.71%	-0.21%
Ag <sup>110m</sup>	7.95%	6.39%	4.95%	3.67%	2.52%	1.45%
Xe <sup>135</sup>	3.43%	-0.98%	-3.60%	-5.16%	-6.20%	-7.11%
Cs <sup>137</sup>	8.50%	5.58%	3.48%	1.96%	0.81%	-0.08%
Pr <sup>141</sup>	9.10%	6.12%	3.92%	2.31%	1.11%	0.19%
Nd <sup>144</sup>	10.07%	7.63%	5.64%	4.00%	2.64%	1.49%
Sm <sup>149</sup>	2.92%	0.28%	-0.81%	-1.20%	-1.37%	-1.57%

The relative differences on the power distribution between the reference case and the equilibrium core computed with the average pebble fluxes are shown in Table 5.XXVI.

**Table 5.XXVI: Pu+MA cycle rel. diff. between the two depletion methodologies on power s.f.**

CHAN A	CHAN B	CHAN C	CHAN D	CHAN E
2.53%	2.33%	2.31%	2.34%	2.57%
2.09%	1.80%	1.76%	1.82%	2.16%
1.58%	1.24%	1.20%	1.26%	1.68%
1.02%	0.62%	0.57%	0.63%	1.15%
0.44%	-0.04%	-0.09%	-0.02%	0.60%
-0.15%	-0.68%	-0.73%	-0.67%	0.04%
-0.72%	-1.29%	-1.34%	-1.28%	-0.51%
-1.25%	-1.84%	-1.89%	-1.82%	-1.04%
-1.75%	-2.30%	-2.35%	-2.28%	-1.53%
-2.21%	-2.65%	-2.69%	-2.63%	-1.97%
-2.61%	-2.84%	-2.85%	-2.82%	-2.37%
-2.95%				-2.72%
-3.23%				-3.00%
-3.43%				-3.20%
-3.54%				-3.31%

One can observe that in the Pu+MA cycle the discrepancies, on the power distribution and on the nuclide concentrations, with the reference equilibrium cycle, are on the same

entity that for the LEU cycle described in section 5.4.1.1 and no so high as it is observed for the plutonium cycle in section 5.4.2.1.

Thus to understand this trend, as for the previous analyzed fuel cycles, the reference equilibrium core, with the nuclide distribution presented in Table 5.XXV, was re-computed with the average pebbles in each spectrum zone.

As a result the equilibrium core with the same nuclide distribution is computed both with the proper fluxes per pebble type both with the average flux methodology.

The resulting  $k_{eff}$  has a  $\Delta\rho$  of 104 pcm and  $\Delta_{sf>1}^{\%} \tau_{POWER}^{HET}$  of 0.95% from the reference calculation with the proper pebble compositions per pass. Comparing the homogenized broad-group cross sections per spectrum zone, the larger relative difference is 0.24% on the total cross sections and 3.96% on the fission cross sections.

The relative differences of the total fluxes computed in the multi-pebble geometry associated to SZ 32, renormalized to match the power computed with the different spectra calculation, are presented in Table 5.XXVII. The differences in the 281-group fluxes of pass 1 and 6 from the one in the average composition kernels, together with the flux spectrum in these last, are illustrated in Figure 5.15.

The same is done for the fluxes in the multi-pebble geometries of SZ 3, where the hot spot is situated, in Table 5.XXVIII and Figure 5.16.

**Table 5.XXVII: Rel. diff. of the proper total fluxes per type in the pebble kernels, comprised in SZ 32, from the average composition pebble flux (Pu+MA cycle equilibrium core)**

	Pass 1	Pass 2	Pass 3	Pass 4	Pass 5	Pass 6
Total flux rel. diff.	1.22%	1.06%	0.97%	0.95%	0.99%	1.07%

**Table 5.XXVIII: Rel. diff. of the proper total fluxes per type in the pebble kernels, comprised in SZ 3, from the average composition pebble flux (Pu+MA cycle equilibrium core)**

	Pass 1	Pass 2	Pass 3	Pass 4	Pass 5	Pass 6
Total flux rel. diff.	2.19%	1.85%	1.61%	1.47%	1.41%	1.41%



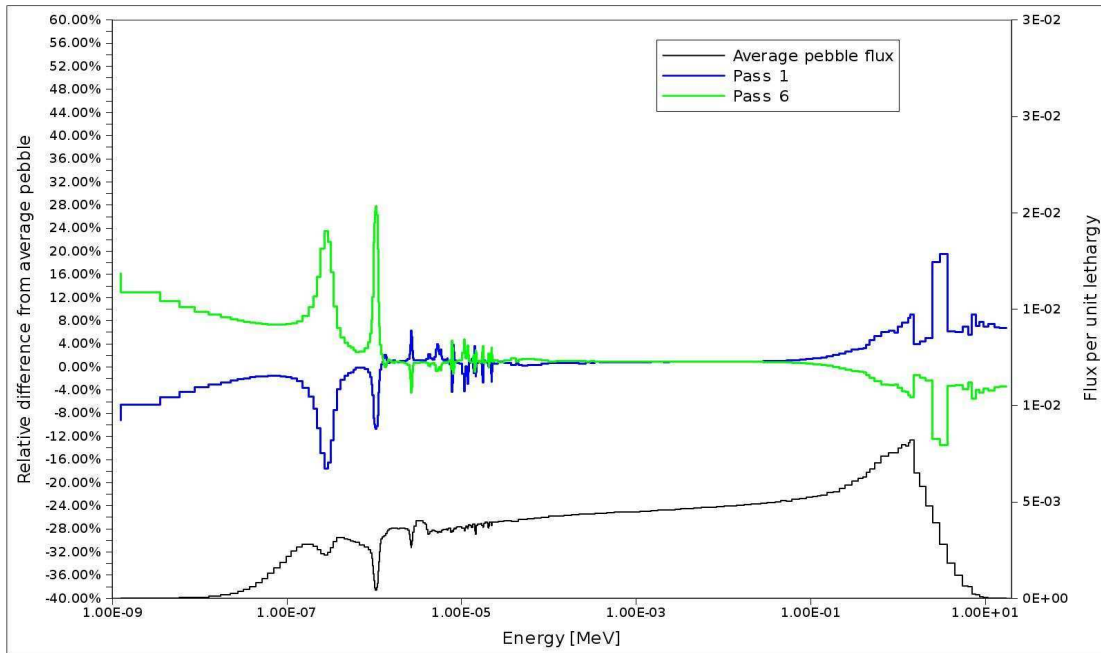


**Figure 5.15: Rel. diff. of the proper 281-group fluxes per type in the pebble kernels, comprised in SZ 32, from the average composition pebble flux (Pu+MA cycle equilibrium core)**

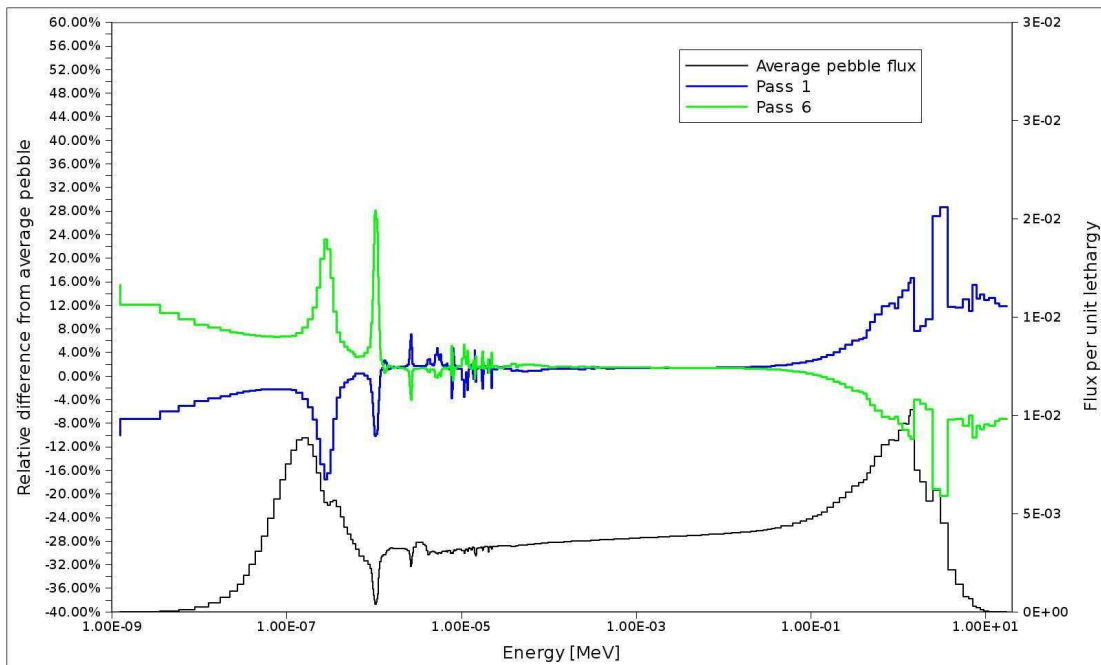


**Figure 5.16: Rel. diff. of the proper 281-group fluxes per type in the pebble kernels, comprised in SZ 3, from the average composition pebble flux (Pu+MA cycle equilibrium core)**

As to conclude, in this case the differences due to the use of an average composition pebble spectrum are much smaller than in the previous case with first generation plutonium fuel and mostly in the order of the UO<sub>2</sub> fuel.

Though the isotopic vectors of the Pu+MA fuel is not so different from the Pu fuel, especially for the different plutonium isotopes content (except a lower weight percentage of Pu<sup>241</sup> and Pu<sup>242</sup>), the spectral differences between the different pebbles comprised in a SZ and the average one are smaller than with the pure plutonium pebbles, especially in the resonance region of the Pu<sup>240</sup>.

To understand this trend, let analyze the Pu<sup>240</sup> densities for the different pass pebbles at the exit plane of SZ 32 of the equilibrium cores loaded with both PuO<sub>1.7</sub> and (Pu+MA)O<sub>1.7</sub> fuels. They are exposed in Table 5.XXIX together with the relative differences from the respective average composition pebble density.

**Table 5.XXIX: Pu<sup>240</sup> atomic densities in the pebbles exiting SZ 32 for Pu and Pu+MA fuel cycles and rel. diff. with the average composition pebble**

	Pass 1	Pass 2	Pass 3	Pass 4	Pass 5	Pass 6
Pu <sup>240</sup> atomic densities [atoms barn <sup>-1</sup> cm <sup>-1</sup> ] in Pu fuel cycle						
Density	5.56E-03	5.32E-03	4.50E-03	3.46E-03	2.44E-03	1.58E-03
Rel. diff. Vs average	46.00%	39.71%	18.11%	-9.23%	-35.97%	-58.62%
Pu <sup>240</sup> atomic densities [atoms barn <sup>-1</sup> cm <sup>-1</sup> ] in Pu+MA fuel cycle						
Density	5.18E-03	5.13E-03	4.88E-03	4.50E-03	4.03E-03	3.51E-03
Rel. diff. Vs average	14.20%	12.99%	7.57%	-0.86%	-11.24%	-22.66%

It appears that the Pu<sup>240</sup> consumption is significantly smaller in the Pu+MA fuel cycle. Thus, in the Pu+MA cycle the atomic densities of the different pass pebbles are closer to the average composition pebble density compared to the Pu fuel cycle.

That's why the spectral differences are smaller in the region of the Pu<sup>240</sup> resonance absorption in the Pu+MA fuelled core.

This seems to be the main reason of the larger bias committed while computing the equilibrium core of the plutonium fuel cycle with the average composition pebble approximation.

## 5.5 Conclusions to the Chapter

A new methodology to compute the asymptotic equilibrium PBR core has been implemented in APOLLO2. The method is inspired on the previous developed methodologies included in the present codes used for PBRs analysis which treat the physical quantities (core fluxes and nuclide densities) over the spectrum zones size rather than over the computational mesh cells size. The different zones belonging to a

flow channel do not need to be equal-volumetric nor rectangular in the RZ model of the core, allowing the potential proper modeling of the defueling cone and the associated flow velocity variations.

For the stochastic nature of the pebbles positions inside the core during their downward flow, it was considered more correct to evaluate all the quantities averaged over sufficiently large core sub-regions (the spectrum zones) in order to have an acceptable statistical description of the problem.

Nevertheless, the developed methodology exploits the possibility of computing the heterogeneous flux over the multi-pebble geometries associated to the core spectrum zones. This leads to calculate the power distribution in the core, used to normalize the multi-pebble geometries fluxes, by the heterogeneous reaction rates. Moreover, the proper fluxes per pebble type are used to deplete the different types over the time period  $T_{SZ}$  associated to the zone.

Simulations were conducted to compute the equilibrium core composition in a simplified PBMR-400 model for different types of fuel cycles: uranium, plutonium and plutonium + minor actinides. The code flexibility allowed computing in a coherent manner all the fuel cycles and the associated  $T_{SZ}$  to obtain a critical core.

The biases associated with the approximation used by all existing codes, of calculating a single flux in an average composition pebble per spectrum zone, were evaluated.

It appeared that the differences are mostly connected to the spectral differences between the different pass pebbles in the resonance regions, especially in the major capture resonance of  $\text{Pu}^{240}$ . In the  $\text{UO}_2$  and  $\text{Pu}$  + minor actinides fuel cycles the biases are limited and mostly compensated by a "cancellation of errors". Nevertheless, in the pure plutonium cycle the biases are quite large i.e., in the average discarded pebbles, in the order of 10% for the atomic densities of plutonium isotopes and of 22% for  $\text{Xe}^{135}$  ones. The biases on the power shape factors are also high, with, for example, an overestimation of the power peaking factor of about 11%.

For the advanced fuel cycles, using for example two fuel types simultaneously or burnable poison particles dispersed in the pebble matrix, it is expected that the spectral differences between the different pebble types contained in a zone would be larger. It will be necessary to consider the proper flux in each pebble type to correctly compute the core power distribution and to perform the depletion calculations needed to find the equilibrium core composition. Further investigations regarding these advanced fuel cycles are needed.

By implementing in APOLLO2 an improved mixing algorithm it will be possible to in-line consider the burnup values distribution around the average values per pass used in the core calculation. This would allow accounting for the different depletion histories and better simulating the physical rejection mechanism based on a target burnup limit for recirculation.

## 6 Conclusions and Perspectives

In this thesis an innovative neutronic model has been developed to compute Pebble Bed Reactors. As it is universally done, the RZ model of the core is divided into a finite number of (vertical) channels, each one of which is axially subdivided in spectrum zones. The spectrum zones play the role of "assemblies", allowing for the traditional two-step reactor calculation where the core calculation is carried out with few macrogroups and "assembly"-homogenized cross sections.

The main difference with the traditional two-step reactor calculation is that spectrum zone homogenization has to account for surface leakage and this naturally leads to an iterative homogenization and core calculation technique. At each iteration, every spectrum zone is independently homogenized by solving a fixed  $k_{eff}$  source problem, where the  $k_{eff}$  and the entering currents are obtained from the previous core calculation. This technique is akin to the iterative advanced techniques investigated for LWRs.<sup>49</sup>

The main innovative aspects of the APOLLO2 modeling are:

- the association of a multi-pebble geometry to each spectrum zone to perform the fine-flux heterogeneous calculations for cross section homogenization;
- the "macro-stochastic" collision probability treatment of the multi-pebble geometries, based on surface-to-surface geometrical probabilities, which

accounts for multiple pebble types in interaction among themselves and with the zone boundary surfaces;

- the representation of entering currents of the multi-pebble geometry with fine-group reconstructed currents per boundary surface;
- the calculation of the one-dimensional pebbles with the APOLLO2 double-heterogeneity treatment for the microparticles;
- the application of the APOLLO2 self-shielding technique which evaluates the "exact" reaction rates on the reflected multi-pebble geometry;
- the use of boundary-to boundary probabilities, computed by a Monte Carlo simulation, to account for the increased neutron streaming through the bed of pebbles close to the reflector walls;
- the use of the fine-group fluxes computed in each different pebble type to perform the depletion calculations;
- the representation of a cluster of pebbles of the same type in a spectrum zone by increasing, as compared to the uniform mix, the self pebble-to-pebble probability;
- the calculation of the RZ core model with the  $S_N$  method and cross sections iteratively generated.

The verification of the new APOLLO2 PBR modeling was performed with reference TRIPOLI4 Monte Carlo simulations of a simplified PBMR-400 model. Different core models were simulated to perform a verification by successive steps, starting from the capability of the RZ  $S_N$  solver to compute large size PBR cores.

The effects on the core  $k_{eff}$ , production shape factors, core production over absorption ratio and computing time were analyzed varying the following computing parameters: broad-group structure, spatial mesh,  $S_N$  angular quadrature, converge precisions in flux solvers and number of spectrum zones.

The sensitivity of the observed quantities to the variation of boundary-to-boundary probabilities and zone packing fractions was also analyzed and it was found small.

A comparison between different ways of computing spectrum zone reaction rates showed that, the rates computed with the fine-group heterogeneous fluxes over the multi-pebble geometries matches better the Monte Carlo reference.

The most important results issued from the verification phase were obtained for a TRIPOLI4 model where pebbles, of six randomly assigned burnup levels, are individually positioned in the core with a realistic distribution.

Both, a low temperature (*LT*) and a high temperature (*HT*) models, were analyzed with the computing parameters optimized in the previous verification steps. The RZ APOLLO2 core model was computed with 13 or 26 broad groups and  $S_4$  angular quadrature. This allowed calculating the flux in the simplified PBMR-400 model in a reasonable computing time (<1h), both for the *LT* and the *HT* model.

The discrepancies with the T4 reference results were

- smaller than 100 pcm on the core  $k_{eff}$ ,
- within  $\pm 4\%$  on the production rate distribution for the zones with a shape factor larger than 1,
- smaller than 3% on the production shape factor at the hot spot.

Even when comparing the reaction rates at a more detailed scale, that is, at the level of the different pebble types comprised in a zone, the developed model computes the production over absorption ratio per type within the  $3\sigma$  from the TRIPOLI4 results. This shows that the neutron exchanges between the pebbles of different type are properly modeled with the APOLLO2 "macro-stochastic" method.

The observed discrepancies on  $k_{eff}$  and production shape factors are in good agreement with the common requested level of accuracy of a neutronic modeling.

The developed APOLLO2 model was also validated with the first criticality experiment of the HTR-10. The critical number of pebbles to be introduced in the core was evaluated. Compared to the experimental value of 16890 mixed (graphite and fuel) pebbles, the APOLLO2 model evaluates the critical number only to 77 pebbles less. This is a very good agreement, better than the one obtained with several other codes. This preliminary result shows the accuracy of the model developed in APOLLO2. Further analysis is needed in order to consider fine parameters calculation (reaction rate distribution, control rod worth, flux distribution).

A new methodology to compute the asymptotic equilibrium PBR core has been implemented in APOLLO2. The developed methodology exploits the possibility of computing the heterogeneous fluxes of the multi-pebble geometries and uses these fine-group fluxes for depletion calculations.

Simulations were conducted to compute the equilibrium core composition in a simplified PBMR-400 model for different types of fuel cycles: uranium, plutonium and plutonium + minor actinides.

The biases associated with the average composition pebble approximation, used by all existing codes, were evaluated. In the  $\text{UO}_2$  and Pu + minor actinides fuel cycles the biases are limited and mostly compensated by a "cancellation of errors". Nevertheless, in the pure plutonium cycle the biases are quite large i.e., in the average discarded pebbles, up to 10% for the atomic densities of plutonium isotopes and of 22% for  $\text{Xe}^{135}$  ones. The biases on the power shape factors are also high, with, for example, an overestimation of the power peaking factor of about 11%.

## Perspectives

- The RZ  $S_N$  full-core calculation should be replaced by a diffusion calculation in order to save computing time.
- Based on the experience accumulated at CEA, a coupled neutronic-thermal hydraulic calculation of a PBR could be easily implemented. This is necessary to perform design and safety studies. For the modeling of prismatic block-type HTRs the NEPHTIS scheme has been developed,<sup>151</sup> where a coupling between the diffusion code CRONOS2 and the thermal-hydraulic code CAST3M has been realized.<sup>152</sup> Thermal-hydraulic analyzes of the HTR-10 in operational and accidental conditions have also been performed with CAST3M.<sup>153</sup> Thus, all the bricks are there for building coupled PBR calculation schemes.
- The iterative homogenization method developed in APOLLO2 is transposable to all full-core solvers via data exchange between codes. Using a 3D diffusion solver, like the one available in the CEA diffusion code CRONOS2, a three-dimensional core can be computed with the developed method by simply recovering the entering currents from the spectrum zone surfaces and passing them to the associated multi-pebble geometry in APOLLO2, together with the core  $k_{eff}$ .
- In coupled neutronic-thermal hydraulic calculations the iterative homogenization scheme should be efficiently accelerated. An effective way is the parallel computing of the multi-pebble geometries: the zone entering currents, together with the core  $k_{eff}$ , are recovered from the full-core calculation and then the homogenized cross sections per SZ are re-computed over multiple processors.
- In the calculation of the equilibrium core, the depletion calculations for the different channels can also be executed in parallel.
- An improved mixing algorithm is under development. The algorithm will properly account for all the possible depletion histories of the pebbles. The nuclide composition distributions, around the average values assigned to the pebble types, are considered while computing the equilibrium core. This allows simulating the rejection strategy actually used in a PBR operation, which is based on a comparison of the burnup measured, for a discharged pebble, with a target limit burnup value.
- A more extensive validation should be performed with the critical experiments for which data are available (HTR-10, ASTRA,<sup>154</sup> PROTEUS<sup>155</sup>).

## REFERENCES

1. <http://www.gen-4.org>
2. R. A. H. Huddle, "*H.T.G.C. fuel material*", Patent N° C. 10950/59, United Kingdom Atomic Energy Authority, 25<sup>th</sup> March 1960.
3. G. P. Greyvenstein, "*HTGR Thermal-Fluid Analysis*", North-West University, Potchefstroom, South Africa, (2006).
4. U. Colak, "*HTR Concepts*", Article of the HTR Fuel Factbook 1.3 (2006).
5. R. F. Turner, D. L. Hanson, D. W. McEachern, A. Shenoy, "*Design Basis for Hexagonal Block Fuel Element*", Article of the HTR Fuel Factbook 1.3 (2006).
6. J. Engelhard, "*Final report on the construction, start-up and first period of operation of the AVR experimental power plant*", BMBW-FB K 72-23 (1972).
7. K. Kugeler et. al., "*Reactor Safety*", Manuscript Textbook, Reactorsicherheit und-technik an der RWTH Aachen, Germany (2005).
8. G. H. Lohnert, "*Technical design features and essential safety-related properties of the HTR-module*", Nucl. Eng. and Design, 121 (1990).
9. E. J. Mulder, "*General Overview of the Pebble Bed Modular Reactor*", Lecture Notes of the course "Pebble Bed Reactor Design", North-West University, Potchefstroom, South Africa (2006).
10. F. Grisotto, *Personal communication* (2010).
11. J. Wang, R.G. Ballinger, "*Fracture Mechanics Based Coated Particle Fuel Failure Models*", Proc. of HTR 2004, Beijing (2004).
12. L. Van Der Merwe, W. Theron, J. Slabber, "*Technical Description of the PBMR Power Plant*", PBMR internal report 016956 Rev 3A, South Africa (2005).
13. D. Petti, "*Fuel Failure Mechanisms*", Article of the HTR Fuel Factbook 1.3 (2006).
14. J. Slabber, "*Pebble Fuel Advantages*", Proc. of HTR 2004, Beijing (2004).
15. H. J. MacLean and R.G. Ballinger, "*Silver Ion Implantation and Annealing in CVD Silicon Carbide: the Effect of Temperature on Silver Migration*", Proc. of HTR 2004, Beijing (2004).
16. J. M. Kendall, R.E. Bullock, "*Advanced Coated Particle Fuel Options*", Proc. of HTR 2004, Beijing (2004).
17. D. Matzner, "*PBMR Project Status and the Way Ahead*", Proc. of HTR 2004, Beijing (2004).
18. P.J. Venter, M. N. Mitchell, "*Integrated design approach of the pebble BeD modular reactor using models*", Nucl. Eng. and Design, 237 (2007).
19. Z. Zhang, Z. Wu, D. Wang, Y. Xu, Y. Sun, F. Li, Y. Dong, , "*Current status and technical description of Chinese 2 x 250 MW<sub>th</sub> HTR-PM demonstration plant*", Nucl. Eng. and Design, 239 (2009).
20. J. Slabber, "*PBMR Nuclear Material Safeguards*", Proc. of HTR 2004, Beijing (2004).
21. F. Reitsma, "*The Pebble Bed Modular Reactor Layout and Neutronics Design of the Equilibrium Cycle*", Proc. of PHYSOR 2004, Chicago, USA (2004).
22. C. Stoker, "*PBMR Nuclear Design and Safety Analysis: An Overview*", Proc. of PHYSOR 2006, Vancouver (2006).
23. G. Strydom, "*Xenon-induced axial power oscillations in the 400 MW pebble bed modular reactor*", M.Sc. Dissertation, North-West University, South Africa (2008).
24. A. Ooms, "*Pebble flow in a High Temperature Reactor*", M.Sc. Dissertation, Delft University of Technology, The Netherlands (2008).
25. C. H. Rycroft, G. S. Grest, J. W. Landry, M. Z. Bazant, "*Analysis of granular flow in a pebble-bed nuclear reactor*", Physical Review, 74 (2006).
26. P.A. Cundall, Paper n°II-8, Proc. of the Symposium of the International society of Rock Mechanics, Vol.1 (1971).
27. R. Sanchez, I Zmijarevic, M. Coste-Delclaux, E. Masiello, S. Santandrea, E. Martinolli, L. Villatte, N. Schwartz, N. Guler, "*APOLLO2 year 2010*", to be published in Nuclear Technology
28. S. Loubière, R. Sanchez, M. Coste, A.Hebert, Z. Stankovski, "*APOLLO2 Twelve Years Later*", Proc. of M&C'99, Madrid (1999).
29. R. Sanchez, J. Mondot, Z. Stankovski, A. Cossic and I. Zmijarevic, "*APOLLO II: A User-Oriented, Portable, Modular Code for Multigroup Transport Assembly Calculation*", Nucl. Sci. Eng., 100 (1988).



30. H. Golfier, R. Lenain, C. Calvin, J-J. Lautard, A-M. Baudron, P. Fougeras, P. Magat, E. Martinolli, Y. Dutheillet, "APOLLO3: A Common Project of CEA, AREVA and EDF for the Development of a New Deterministic Multi-purpose Code for Core Physics Analysis", Proc. of M&C 2009, Saratoga Springs (2009).
31. P. Bellier, M. Coste, A. Hébert, R. Sanchez, Z. Stankovski, I. Zmijarevic, "APOLLO2.5: Notice théorique", SERMA/LENR/RT/99-2719/A (2002).
32. A. Hébert, "Applied Reactor Physics", Presses Internationales Polytechnique, Canada (2009).
33. R. Sanchez, A. Chetaine, "A Synthetic Acceleration for a Two-Dimensional Characteristic Method in Unstructured Meshes", Nucl. Sci. Eng., 136 (2000).
34. A. Kavenoky, R. Sanchez, "The APOLLO assembly spectrum code", Proc. of M&C '87, Paris (1987).
35. C. J. Dean, R. J. Perry, "Weighting spectra for the Xmas group scheme", Winfrith Technology Center (1990).
36. A. Santamarina, N. Hfaiedh, "Determination of the Optimized SHEM Mesh For Neutron Transport Calculations" - International Conference on Mathematics and Computation, M&C 2005, France (2005).
37. R. Sanchez, J. Mondot, "A model for calculating multigroup self-shielded cross sections for a mixture of resonant absorbers in heterogeneous media", Proc. of Mtg. on Advances in Reactor Physics and Radiation Protection and Shielding, Chicago (1984).
38. R. Sanchez, M. Coste, Z. Stankovski, C. Van der Gucht, "Model for multi-group self-shielded cross-sections calculations in the code APOLLO2", Proc. Int Conf. on the Physics of Reactors: Operation, Design and Computation, Marseille (1990).
39. M. Livolant, F. Jeanpierre, "Autoprotection des resonances dans les réacteurs nucléaires. Application aux isotopes lourds", CEA-R-4533, Commissariat à l'Energie Atomique, France (1974).
40. M. Coste-Delclaux, S. Mengelle, "New resonant mixture self-shielding treatment in the code APOLLO2", Proc. of PHYSOR 2004, Chicago (2004).
41. R. E. MacFarlane, D. W. Muir, R. M. Boiscourt, "NJOY99 nuclear data processing system", Report 12740-M, LANL (1994).
42. M. Coste-Delclaux, "Modélisation du phénomène d'autoprotection dans le code de transport multigroupe APOLLO2", PhD Thesis, Conservatoire National des Arts et Métiers, France (2006).
43. A. Hébert, G. Mathonnière, "Development of a third-generation superhomogenization method for the homogenization of a pressurized water reactor assembly", Nucl. Sci. Eng., 115 (1993).
44. E. E. Lewis, W. F. Miller, "Computational methods of neutron transport", American Nuclear Society edition (1993).
45. R. Sanchez, G. C. Pomraning, "A statistical analysis of the double-heterogeneity problem", Ann. of Nucl. Energy, 18 (1991).
46. A. Hébert, "A collision probability analysis of the double-heterogeneity problem", Nucl. Sci. Eng., 115 (1993).
47. H. Bateman, "Solution of a System of Differential Equations Occurring in the Theory of Radioactive Transformations", Proc. of Cambridge Philos. Soc. 15 (1910).
48. L. Massimo, "Physics of High-Temperature Reactors," A. Wheaton and Co., Exeter, Great Britain (1976).
49. P. Mondot, R. Sanchez, "An iterative homogenization technique that preserves assembly core exchanges", Proc. of SNA Conference, Paris (2003).
50. E. Teuchert, U. Hansen, K. Haas, "VSOP – Computer Code System for Reactor Physics and Fuel Cycle Simulations", JUL – 1649, Kernforschungsanlage Jülich, (1980).
51. F. Reitsma, H. J. Rütten, W. Sherer, "An Overview of the FZJ Tools for HTR Core Design and Reactor Dynamics, the Past, Present and Future", Proc. of M&C 2005, Avignon (2005).
52. J. Oppe, J. B. M. De Haas and J. C. Kuijper, "PANTHERMIX (PANTER-THERMIX) User Manual", ECN-I-98-019, ECN Petten (1998).
53. "The ANSWER Software Package – WIMS – A Modular Scheme for Neutronics Calculations", in "User Guide for Version 8", ANSWER/WIMS(99), AEA Technology (1999).
54. P. K. Hutt et al., "The UK Core Performance Package", Nucl. Energy, 30 (1991).
55. S. Struth, "Thermix – Direkt: Ein rechenprogramm zur instationären zweidimensionalen simulation thermohydraulischer transienten", FZ Jülich, Germany.
56. B. Boer, D. Lathouwers, M. Ding, J. L. Kloosterman, "Coupled neutronics / thermal hydraulics calculations for High Temperature Reactors with the DALTON – THERMIX code system", Proc. of PHYSOR 2008, Interlaken (2008).

57. "SCALE-5. Modular Code System for Performing Standardized Computer Analysis for Licensing Evaluations", Oak Ridge National Laboratory, Tennessee, USA (2005).
58. P. E. MacDonald, J. W. Sterbentz, R. L. Sant, P. D. Bayless, R. R. Shultz, H. D. Gougar, R. L. Moore, A. M. Ougouag, W. K. Terry, "NGNP Preliminary Point Design, - Results of the Initial Neutronics and Thermal-Hydraulic Assessment", INEEL/EXT-03-00870, Rev. 1, Idaho National Engineering and Environmental Laboratory (2003).
59. W. K. Terry, H. D. Gougar, A. M. Ougouag, "Direct deterministic method for neutronic analysis and computation of asymptotic burnup distribution in a recirculating pebble-bed reactor", Ann. of Nucl. Energy, 29 (2002).
60. D. Mathews, "An improved version of the MICROX-2 code", Technical report PSI Bericht Nr. 97-11, Paul Scherrer Institute (1997).
61. R. A. Grimesey, D. W. Nigg, R. L. Curtis, "COMBINE/PC – A Portable ENDF/B Version 5 Neutron Spectrum and Cross Section Generation Program", Technical Report EGG-2589 (1990).
62. B. Boer, A. M. Ougouag, "Core analysis, design and optimization of a deep-burn pebble bed reactor", Proc. of PHYSOR 2010, Pittsburgh, USA (2010).
63. H. C. Lee, C. K. Jo, J. M. Noh, "Development of the HELIOS/CAPP code system for the analysis of pebble type VHTR cores", Proc. of PHYSOR 2010, Pittsburgh (2010).
64. R. M. Westfall, M. A. Bjerke, "An interface-current integral transport model for treating doubly-heterogeneous, multisystem geometries", Oak Ridge National Laboratory report n° 790406-17.
65. R. M. Westfall, "Resolved Resonance Processing in the AMPX Modular Code System", Oak Ridge National Laboratory report ORNL/RSIC-41 (1978).
66. Nuclear Reactor Analysis course at NECSA, Module 1 Section 4.2, PBMR Neutronics: VSOP Modeling (2006).
67. L. W. Nordheim and G. F. Kuncir, "A program of research and calculations of resonance absorption", General Atomics – 2527, TID-4500 (1961).
68. L. W. Nordheim, G. Birkhoff, E. P. Wigner, "The Theory of Resonance Absorption", Am. Math. Soc. (1961).
69. S.M. Dancoff, M. Gisburg, "Surface resonance absorption in a close-packed lattice", CP-2157 (1944).
70. J. B. M. de Haas, J. C. Kuijper, "Feasibility of burning first- and second-generation plutonium in pebble bed high temperature reactors", Nuclear Technology, 151 (2005).
71. E. E. Bende, "Plutonium Burning in a Pebble-Bed Type High Temperature Nuclear Reactor", PhD Thesis, Delft University of Technology, The Netherlands (2000).
72. E. E. Bende, A. H. Hogenbirk, J. L. Kloosterman, H. Van Dam, "Analytical Calculation of the Average Dancoff Factor for a Fuel Kernel in a Pebble-Bed High Temperature Reactor", Nucl. Sci. Eng., 133 (1999).
73. R. Rühle, "RSYST, ein integriertes Modulsystem mit Datenbasis zur automatisierten Berechnung von Kernreaktoren", IKE-4-12, Universität Stuttgart (1973).
74. V. Drüke, D. Filges, R. D. Neef, N. Paul, H. Schall, "Experiments on Inhomogeneous Fuel Loading at the Critical HTGR Test Facility KAHTER: A Study for the Future Loading Concept of Pebble-Bed Reactors", Nucl. Sci. Eng., 97 (1987).
75. M. Ding, B. Boer, J. L. Kloosterman, D. Lathouwers, "Evaluation of experiments in the AVR with the DALTON – THERMIX coupled code system", Nucl. Eng. and Design, 239 (2009).
76. I. I. Bondarenko, "Group Constants for Nuclear Reactor Calculations", Authorised Translation from the Russian, Consultants Bureau, New York (1964).
77. B. Boer, D. Lathouwers, J. L. Kloosterman, T.H.J.J. Van Der Hagen, G. Strydom, "Validation of the DALTON-THERMIX code system with transient analyses of the HTR-10 and application to the PBMR", Nucl. Technology, 170 (2010).
78. S. Goluoglu, "Analysis of a Computational Benchmark for a High-Temperature Reactor Using SCALE", Proc. of PHYSOR 2006, Vancouver (2006).
79. E. E. Sunny, G. Ilas, "SCALE 6 analyses of HTR-10 pebble-bed reactor for initial critical configuration", Proc. of PHYSOR 2010, Pittsburgh (2010).
80. M. L. Williams, M. Asgari, "Computation of Continuous-Energy Neutron Spectra with Discrete Ordinates Transport Theory", Nucl. Sci. Eng., 121 (1995).
81. G. Ilas, N. H. Hudson, F. Rahnama, A. M. Ougouag, H. G. Gougar, "On the few-group cross-section generation methodology for PBR analysis", Ann. of Nucl. Energy, 33 (2006).

82. N. H. Hudson, A. M. Ougouag, F. Rahnema, H. G. Gougar, "A Pebble Bed Reactor cross section methodology", Ann. of Nucl. Energy, 36 (2009).
83. H. D. Gougar, "Results of a Neutronic Simulation of the HTR-Poteus Core 4.2 Using PEBBED and Other INL Reactor Physics Tools", INL Report FY-09 (2009).
84. H. D. Gougar, A. M. Ougouag, W. Yoon, "Multiscale Cross Section Generation for Pebble Bed Reactors – a Review/Preview", presentation at PBMR Workshop, PHYSOR 2010, Pittsburg (2010).
85. J. L. Kloosterman, A. M. Ougouag, "Comparison and Extension of Dancoff Factors for Pebble-Bed Reactors", Nucl. Sci. Eng., 157 (2007).
86. H. Gerwin, W. Sherer, "Treatment of the Upper Cavity in a Pebble-Bed High-Temperature Gas-Cooled Reactor by Diffusion Theory", Nucl. Sci. Eng., 97 (1987).
87. J. Lieberoth, A. Stojadinovic, "Neutron Streaming in Pebble Beds", Nucl. Sci. Eng., 76 (1980).
88. B. Tyobeka, K. Ivanov, A. Pautz, "Utilization of two-dimensional deterministic transport methods for analysis of pebble-bed reactors", Ann. of Nucl. Energy, 34 (2007).
89. J. O. Johnson, "A users manual for Mash 1.0, a Monte Carlo adjoint shielding code system" (contains the documentation for DORT), Oak Ridge National Laboratory Report ORNL/TM-11778 (1992).
90. B. Tyobeka, K. Ivanov, "Analysis of the PBMR-268 benchmark transient cases with the NEM-THERMIX coupled code", Transactions of the ANS Winter Meeting, Washington DC (2004).
91. V. Kulik, R. Sanchez, "Core Homogenization Method for Pebble Bed Reactors," Proc. of M&C 2005, Avignon (2005).
92. Tripoli Project Team, "TRIPOLI-4 version 4 user guide", CEA-R-6169 (2008).
93. <http://www.itascacg.com/pfc>
94. F. Reitsma and W. R. Joubert, *personal communication* (2008).
95. P.J. Venter, M. N. Mitchell, "Integrated design approach of the pebble BeD modular reactor using models", Nucl. Eng. and Desing, 237 (2007).
96. F. Reitsma and W. R. Joubert, "Investigation of the Power Peaking in the PBMR Pebble Bed Reactor," Proc. of M&C 2005, Avignon (2005).
97. M. Grimod, Z. Karriem, W. R. Joubert, F. Reitsma, "Analysis of the Neutron Flux Spectral Differences and Effects on the Depletion in the Fuel Kernels of the PBMR Fuel Spheres," Proc. of ICAPP 2007, Nice (2007).
98. A. M. Ougouag, H. D. Gougar, W. K. Terry, F. Reitsma, W. R. Joubert, "PEBBED analysis of hot spots in pebble-bed reactor", Proc. of M&C 2005, Avignon (2005).
99. J. J. Duderstadt, J. Hamilton, "Nuclear Reactor Analysis", John Wiley & Sons, New York (1976).
100. X. Raepsaet, "Physics of the High Temperature Gas-Cooled Reactor Core", Presentation at 1<sup>st</sup> Eurocourse on V/HTR, Stuttgart, Germany (2007).
101. N. Fujimoto, N. Nojiri, K. Yamashita, "Validation of the nuclear design code system for the HTR using the criticality assembly VHTRC", Nuclear Eng. and Design, 233, (2004).
102. A. Santamarina, D. Bernard, "The recommended JEFF3.1.1 file and CEA2005V4 library for accurate neutronic Calculations", Note Technique DER/SPRC/LEPh 08-002.
103. G. Iilas, F. Rahnema, A. M. Ougouag, "Effect of Fuel Particles Distribution Model on PBR Cell Parameters", Trans. of the ANS, vol. 92, p 654-656 (2005).
104. F. Damian, "Analyses des capacités des réacteurs à haute température sous l'aspect de l'utilisation des matières fissiles", PhD Thesis, Institut National Polytechnique de Grenoble, France (2002).
105. H. Chang, X. Raepsaet, F. Damian, "Analysis of HTR-10 First Criticality with Monte Carlo Code Tripoli-4.3", Proc. of HTR2004 Conf., Beijing (2004).
106. <http://root.cern.ch>
107. F. C. Difilippo, "Monte Carlo Calculations of Pebble Bed Benchmarks Configurations of the PROTEUS Facility", Nucl. Sci. Eng., 143 (2003).
108. U Colak, V. Seker, "Monte Carlo Criticality Calculations for a Pebble Bed Reactor with MCNP", Nucl. Sci. Eng., 149 (2005).
109. S. Sen, F. Albornoz, F. Reitsma, "Comparison of VSOP and MCNP Results of PBMR Equilibrium Core Model", Proc. of HTR2006, Johannesburg (2006).
110. H. Jeong, S. H. Chang, "Development of a Method of Evaluating an Inventory of Fission Products for a Pebble Bed Reactor", Ann. Nucl. Energy, 35 (2008)
111. R. Mphahlele, A. M. Ougouag, K. N. Ivanov, H. D. Gougar, "Spectral Zones Selection Methodology for Pebble Bed Reactors", Proc. of PHYSOR2008, Interlaken (2008).

112. E. Richebois, "*Calcul de coeur REP en transport 3D*", Université Aix-Marseille, France (1999).
113. "*Gas Turbine Modular Helium Reactor conceptual design report*", GENERAL ATOMICS, July 1996.
114. "Verification du schéma de référence optimisé REL2005 pour le calcul des assemblages REP UOX en evolution", CEA technical report, September 2006.
115. C.C. Stoker, F. Reitsma, "*PBMR Fuel Spheres Source Terms*", Proc. of HTR2004, Beijing (2004).
116. A. M. Ougouag, J. J. Cogliati, J.L. Kloosterman, "*Methods for modeling the packing of fuel elements in pebble bed reactors*", Intern. Conf. M&C2005, France (2005).
117. J.J. Lautard, S. Loubière, C. Magnaud, "*CRONOS, A Modular Computational System for Neutronic Core Calculations*", IAEA Specialists Meeting, France (1990).
118. "*Gas Turbine Modular Helium Reactor conceptual design report*", GENERAL ATOMICS, July 1996.
119. R. S. Varga, "*Matrix iterative Analysis*", Prentice-Hall, Englewood Cliffs, N. J. (1962).
120. M.L. Adams, E. W. Larsen, "*Fast iterative methods for discrete-ordinates particle transport calculations*", Nuclear Energy, Vol. 40, 1 (2002).
121. G.J. Auwerda, J. L. Kloosterman, D. Lathouwers, T.H.J.J. Van der Hagen, "*Effects of random pebble distribution on the multiplication factor in HTR pebble bed reactors*", Annals of Nuclear Energy, Vol. 37, (2010).
122. X. Jing, X. Xu, Y. Yang, R. Qu, "*Prediction calculations and experiments for the first criticality of the 10 MW High Temperature Gas-cooled Reactor-Test Module*", Nuc. Eng and Design, 218 (2002).
123. IAEA-TECDOC-1382, "*Evaluation of high temperature gas cooled reactor performance: benchmark analyses related to initial testing of the HTTR and HTR-10*", IAEA, Vienna (2003).
124. Briesmeister, "*MCNP – A General Monte Carlo N-Particle Transport Code. Version 4C.*", LA-13709-M.
125. Y. Yang, Z. Luo, X. Jing, Z. Wu, "*Fuel management of the HTR-10 including the equilibrium state and the running-in phase*", Nucl. Eng. and Design, 218 (2002).
126. B. Boer, J.L. Kloosterman, D. Lathouwers, T.H.J.J. van der Hagen, "*In-core fuel management optimization of pebble-bed reactors*", Annals of Nuclear Energy, 36 (2009).
127. M.G. Izenson, "*Effects of Fuel Particle and Reactor Core Design on Modular HTGR Source Terms*", Doctoral dissertation, Massachusetts Institute of technology, US (1986).
128. H. D. Gougar, F. Reitsma, W. Joubert, "*A Comparison of Pebble Mixing and Depletion Algorithms Used in Pebble-Bed Reactor Equilibrium Cycle Simulation*", M&C2009 Conference, Saratoga Springs, USA (2009).
129. P.H. Liem, "*BATAN-MPASS: a general fuel management code for pebble-bed high temperature reactors*", Annals of Nuclear Energy, 21 (1994).
130. H. Sekimoto, T. Obara, S. Yukinori, E. Suetomi, "*New method to analyze equilibrium cycle of pebble-bed reactors*", Journal of Nuclear Science and Technology, 24 (1987).
131. H. D. Gougar, W. K. Terry, A. M. Ougouag, "*Matrix formulation of pebble circulation in the PEBBED code*", Proc. of the HTR-2002 meeting, Petten (2002).
132. H. D. Gougar, A. M. Ougouag, W. K. Terry, K. N. Ivanov, "*Design of Pebble-Bed reactors using genetic algorithms*", Proc. of HTR 2004 Conference, Beijing (2004).
133. H. D. Gougar, A. M. Ougouag, W. K. Terry, "*Automated Design and Optimization of Pebble-Bed Reactor Cores*", Nucl. Sci. Eng., 165 (2010).
134. H. C. Lee, C. K. Jo, J. M. Noh, "*Development of the HELIOS/CAPP code system for the analysis of pebble type VHTR cores*", Proc. of PHYSOR 2010, Pittsburgh (2010).
135. M. Fratoni, E. Greenspan, "*Determination of the equilibrium compositions of cores with continuous fuel feed and removal using MOCUP*", Proc. of M&C + SNA 2007, Monterey (2007).
136. H. Jeong, S. H. Chang, "*Development of a method of evaluating an inventory of fission products for a pebble bed reactor*", Ann. of Nucl. Energy, 35 (2008).
137. E. Bomboni, N. Cerullo, E. Fridman, G. Lomonaco, E. Shwageraus, "*Comparison among MCNP-based depletion codes applied to burnup calculations of pebble-bed HTR lattices*", Nucl. Eng. and Design, 240 (2010).
138. B. Bonin, D. Greneche, "*Prospective studies of HTR fuel cycles involving plutonium*", Proc. of HTR2002 Conference, Petten (2002).
139. H. Hansen, "*Plutonium in high temperature reactors*", DRAGON project report 899 (1974).
140. A. Talamo, W. Gudowski, J. Cetnar, F. Venneri, "*Key physical parameters and temperature reactivity coefficients of the deep burn helium modular reactor fueled with LWRs waste*", Ann. of Nucl. Energy, 31 (2004).

141. J. C. Kuijper, X. Raepsaet, J. B. M. de Haas, W. von Lensa, U. Ohlig, H.-J. Ruetten, H. Brockmann, F. Damian, F. Dolci, W. Bernnat, J. Oppe, J.-L. Kloosterman, N. Cerullo, G. Lomonaco, A. Negrini, J. Magill, R. Seiler, "*HTGR reactor physics and fuel cycles studies*", Nucl. Eng. and Desing, 236 (2006).
142. C. Hong, Y. Yongwei, J. Xingqing, X. Yunlin, "*Thorium-Based Fuel Cycles in the Modular High Temperature Reactor*", Tsinghua Science and Technology, 11 (2006).
143. A. Meier, W. Bernnat, K. Hossain, G. Lohnert, "*Analysis of High Temperature Pebble Bed Reactors with Plutonium Fuel*", Proc. of M&C 2009, Saratoga Springs, USA (2009).
144. E. Mulder, E. Teuchert, "*Plutonium disposition in the PBMR-400 High-Temperature Gas-Cooled Reactor*", Proc. of PHYSOR 2004, Chicago, USA (2004).
145. J. B. M. de Haas, J. C. Kuijper, J. Oppe, "*Burnup and transient analysis of a HTR-400 design loaded with PuO<sub>2</sub>*", Proc. of HTR2006 Conference, Johannesburg (2006).
146. B. Boer, A. M. Ougouag, "*Core analysis, design and optimization of a deep-burn pebble bed reactor*", Proc. of PHYSOR 2010, Pittsburgh, USA (2010).
147. E. Mulder, E. Teuchert, "*Characteristics of different fuel cycle in a PBMR-400 for burning reactor grade plutonium*", Nucl. Eng. and Design, 238 (2008).
148. J. L. Kloosterman, "*Application of boron and gadolinium burnable poison particles in UO<sub>2</sub> and PUO<sub>2</sub> fuels in HTRs*", Ann. of Nucl. Energy, 30 (2003).
149. <http://atom.kaeri.re.kr/ton/nuc8.html>
150. J. Jonnet, J. L. Kloosterman, B. Boer, "*Performance of TRISO particles fueled with plutonium and minor actinides in a PBMR-400 core design*", Nucl. Eng. and Design, 240 (2010).
151. F. Damian, "*VHTR core preliminary analysis using NEPHTIS3 / CAST3M coupled modeling*", Proc. of HTR-2008, Washington (2008).
152. I. Limaiem, F. Damian, X. Raepsaet, E. Studer, "*VHTR core modeling: coupling between neutronics and thermal hydraulics*", Proc. of M&C 2005, Avignon (2005).
153. E. Studer et al., "*CAST3M/ARCTURUS: A coupled heat transfer CFD code for thermal-hydraulic analyzes of gas cooled reactors*", Nucl. Eng. and Design, 237 (2007).
154. N.N. Ponomarev-Stepnoi, N.E. Kukharkin, A.A. Bobrov, E.I. Chunaiev, V.P. Garin, E.S. Glushkov, G.V. Kompaniets, A.M. Krutov, V.A. Lobintsev, D.N. Polyakov, O..N. Smirnov, A.A. Zimin, "*Experiments on HTR criticality parameters at the ASTRA facility of the Kurchatov Institute*", Proc. of HTR-2002, Petten (2002)
155. <http://proteus.web.psi.ch>

## Acknowledgments

I would like to thank, firstly, all the researchers at SERMA, who helped me with their nice attitude to appreciate plenty the three years spent there for my thesis. A lot of them helped me directly, with suggestions or patient discussions, to the realization of this work. A lot of others contributed on keeping high my mood with happy conversations and good croissants at the coffee machine.

In particular, I would like to thank my supervisor, Frédéric Damian, who is always nice and patient and who helped me all the time I needed. I thank also Pierre Bellier, for his precious helps on the APOLLO2 code, Eric Dumonteil and Alexey Lokhov for their helps with TRIPOLI4 and ROOT geometry, Igor Zmijarevic for all the APOLLO2 insights, Emiliano Masiello and Simone Santandrea for the huge moral and technical supporting, Céline Guénaut for the suggestions during the redaction phase, François-Xavier Hugot and Alain Mazzolo for the ideas on Monte Carlo problems. I thank Christine Poinot-Salanon for the very effective contribution to the final version of the manuscript.

I thank Richard Lenain, the director of SERMA, for his support.

A special thank goes to all my gym-friends for have saved, at least for what it was possible, my physical tonus during these years.

I thank Frederik Reitsma and Wessel Joubert, from what it was the South African PBMR company, for their friendship and collaboration.

Finally, I really thank my thesis director, Richard Sanchez, for all what I learnt from him.



## APPENDIX A: Notation

General notation:

### dimensions

- $N_p$  = number of different pebble types ,
- $N_i$  = number of pebbles of type  $i$  ,
- $N_b$  = number of boundary surfaces of a spectrum zone .

### surfaces

- $A_i = 4\pi R_i^2$  is the area of pebble of type  $i$  ,
- $a_i^p = N_i A_i / \sum_i N_i A_i$  = relative area of pebbles of type  $i$  ,
- $A_k^b$  = area of boundary surface  $k$  ,
- $a_k^b = A_k^b / \sum_k A_k^b$  = relative area of boundary surface  $k$  ,
- $A_{He} = \sum_k A_k^b + \sum_i N_i A_i$  = total area of interaction ,
- $f_p = \sum_i N_i A_i / A_{He}$  = fraction of pebbles area ,
- $f_b = \sum_k A_k^b / A_{He}$  = fraction of surface area .

### surface-to-surface geometric probabilities

- $p_{ij}^{p,p}$  = probability for neutrons leaving a pebble of type  $j$  to enter a pebble of type  $i$  without crossing any other pebble,
- $p_{ki}^{b,p}$  = probability for neutrons leaving a pebble of type  $i$  to leave the spectrum zone via boundary surface  $k$  without crossing any other pebble,
- $p_{ik}^{p,b}$  = probability for neutrons entering boundary surface  $k$  to enter a pebble of type  $i$  without crossing any other pebble,



- $p_{k',k}^{b,b}$  = probability for neutrons entering boundary surface  $k$  to leave the spectrum zone via boundary surface  $k'$  without crossing any pebble.

### currents

- $J_{\pm,i}$  = total current exiting (+) or entering (-) the pebbles of type  $i$ ,
- $J_{\pm,k}^{bd}$  = total current exiting (+) or entering (-) the spectrum zone via boundary surface  $k$

### helium coolant

- $V_{He}$  = total helium volume in the spectrum zone,
- $\lambda_{He} = 4V_{He}/A_{He}$  = mean chord length in helium evaluated by Cauchy's formula,
- $\Phi_{He}$  = flux in helium region,
- $\Sigma_{He}$  = helium total cross section,
- $F_{He}$  = region-averaged, angle-integrated emission density in helium.

Vector and matrix notation:

#### surfaces

- $\vec{a}^p = \{a_i^p, i = 1, N_p\}$ ,
- $\vec{a}^b = \{a_k^b, k = 1, N_b\}$ .

#### surface-to-surface geometric probabilities

- $p^{p,p} = \{p_{ij}, i, j = 1, N_p\}$ ,
- $p^{b,p} = \{p_{ki}^{b,p}, k = 1, N_b, i = 1, N_p\}$ ,
- $p^{p,b} = \{p_{ik}^{p,b}, i = 1, N_p, k = 1, N_b\}$ ,
- $p^{b,b} = \{p_{k',k}^{b,b}, k', k = 1, N_b\}$ .

#### currents

- $\vec{J}_{\pm} = \{J_{\pm,i}, i = 1, N_p\}$ ,

- $\vec{J}_{\pm}^{bd} = \{J_{\pm,k}^{bd}, k = 1, N_b\}$ .

### unit vectors

- $\vec{1}^p = \{1, i = 1, N_p\}$ ,
- $\vec{1}^b = \{1, k = 1, N_b\}$ .

CP notation:

### pebble

- $N_{\Phi,i}$  = number of fluxes regions in pebble of type  $i$ ,
- $\vec{\Phi}_i = \{N_i \Phi_{i,n}, n = 1, N_{\Phi,i}\}$  = region-averaged fluxes ,
- $\vec{Q}_i = \{N_i Q_{i,n}, n = 1, N_{\Phi,i}\}$  = region-averaged, angle-integrated sources ,
- $\vec{F}_i = \sum_{si} \vec{\Phi}_i + \vec{Q}_i$  = region-averaged, angle-integrated emission density ,
- $V_i = \text{diag} \{V_{i,n}, n = 1, N_{\Phi,i}\}$  = region volumes ,
- $\vec{\Sigma}_i = \text{diag} \{\Sigma_{si,n}, n = 1, N_{\Phi,i}\}$  = region total cross section ,
- $\Sigma_{si}$  = region scattering cross section ,
- $C_i = \{C_{i,nm}, n, m = 1, N_{\Phi,i}\}$  = collision matrix ,
- $\vec{I}_i = \{I_{i,n}, n = 1, N_{\Phi,i}\}$  = incoming probabilities ,
- $\vec{E}_i = \{E_{i,n}, n = 1, N_{\Phi,i}\}$  = escape probabilities ,
- $T_i$  = transmission probability .

### multi-pebble geometry

- $N_{\Phi,SZ} = \sum_i N_{\Phi,i} + 1$  = number of flux regions in the geometry, including helium

as last one,

- $N = \text{diag} \{N_i, i = 1, N_p\}$ ,
- $A = \text{diag} \{A_i, i = 1, N_p\}$ ,
- $A^b = \text{diag} \{A_k^b, k = 1, N_b\}$ ,

- $\vec{\Phi} = \{\vec{\Phi}_i, i = 1, N_p\}$  = region-averaged fluxes in pebbles regions ,
- $\vec{\Phi}' = \{\vec{\Phi} \quad \Phi_{He}\}$  = region-averaged fluxes in geometry, including helium ,
- $\vec{F}' = \{\vec{F}_r, r = 1, N_{\Phi, SZ}\}$  = angle-integrated emission densities in geometry regions ,
- $V' = \text{diag}\{V_r, r = 1, N_{\Phi, SZ}\}$  = region volumes ,
- $C = \text{diag}\{C_i, i = 1, N_p\}$  = collision matrix without considering helium ,
- $I = \{\vec{I}_i, i = 1, N_p\}$  = incoming matrix without considering helium ,
- $E = \{\vec{E}_i, i = 1, N_p\}$  = escape matrix without considering helium ,
- $T = \text{diag}\{T_i, i = 1, N_p\}$  = trasmission matrix without considering helium .

## APPENDIX B: Model for Macro Stochasticity

Let begin considering a spectrum zone and neglecting the scattering and the absorption in the interpebble helium coolant.

The currents entering the different pebble types  $\vec{J}_-(E)$  originate from the currents exiting the pebbles  $\vec{J}_+(E)$  and from the currents entering the zone surfaces  $\vec{J}_-^{bd}(E)$ :

$$\vec{J}_-(E) = p^{p,b}\vec{J}_-^{bd}(E) + p^{p,p}\vec{J}_+(E), \quad (\text{B.1})$$

where  $\vec{J}_\pm = \{J_{\pm,i}\}$  and  $J_{\pm,i}$  is the total current exiting (+) or entering (-) the overall surface of the pebbles of type  $i$ ,  $\vec{J}_\pm^{bd} = \{J_{\pm,k}^{bd}\}$  and  $J_{\pm,k}^{bd}$  is the total current exchanged through the zone surface  $k$ .

The total current leaving the domain via its surfaces is:

$$\vec{J}_+^{bd}(E) = p^{b,b}\vec{J}_-^{bd}(E) + p^{b,p}\vec{J}_+(E), \quad (\text{B.2})$$

In these equations  $p^{p,p}$ ,  $p^{p,b}$ ,  $p^{b,p}$  and  $p^{b,b}$  are pebble-to-pebble, surface-to-pebble, pebble-to-surface and surface-to-surface geometrical probabilities and their values depend upon the modeling, described in Appendix D. The geometrical probabilities obey the conservation and reciprocity relations; a consequence is the conservation identity

$$J_-^{bd}(E) + J_+(E) = J_+^{bd}(E) + J_-(E), \quad (\text{B.3})$$

where  $J_\pm = \vec{1}_p \cdot \vec{J}_\pm$  is the total current exiting or entering all the pebbles,  $J_\pm^{bd} = \vec{1}_b \cdot \vec{J}_\pm^{bd}$  is the total current exiting or entering the total surface of the spectrum zone,  $\vec{1}_p$  and  $\vec{1}_b$  are the unit vectors with the dimension respectively of the number of different pebble types  $N_p$  and of the number of zone surfaces  $N_b$ .

This equation specifies that neutrons entering the domain via its surfaces or leaving the pebbles have to either leave the domain via its surfaces or enter the pebbles.

Let include now the contribution of the coolant. The effects of the presence of helium are small and, to first order, can be incorporated in the previous formulation by introducing simple approximations.

Consider, for instance, the pebble-to-pebble contribution to  $J_{-,i}(E)$  in Eq. (B.1). The total current of neutrons exiting the pebbles and entering the external surfaces to enter pebbles of type  $i$  can be written as

$$J_{-,i}(E) = \int_{S_i} dS \int_{(2\pi)_-} d\Omega |\Omega \cdot \mathbf{n}| \psi_{-,i}(\mathbf{r}, E, \Omega), \quad (\text{B.4})$$

where the integration on  $S_i$  is over the surface  $N_i A_i$  of all the pebbles of type  $i$ , being  $N_i$  the number of pebbles of that type contained in the spectrum zone and  $A_i$  the area of the pebble, and

$$\psi_{-,i}(\mathbf{r}, E, \Omega) = e^{-\Sigma_{He} l} \psi_+(\mathbf{r} - l\Omega, E, \Omega) + \int_0^l dl' e^{-\Sigma_{He}(l-l')} q_{He}(\mathbf{r} - l'\Omega, E, \Omega), \quad (\text{B.5})$$

Here  $l = l(\mathbf{r}, \Omega)$  is the length of the chord from the exiting sphere to the entering point  $(\mathbf{r}, \Omega)$  and  $\psi_+(\mathbf{r} - l\Omega, E, \Omega)$  is the flux leaving another pebble or entering via an external surface. Let now replace the source in the helium by its volume-averaged value and assume further that it is isotropic,  $q_{He}(\mathbf{r}, E, \Omega) \sim F_{He}(E)/(4\pi)$ , where  $F_{He}(E) = \Sigma_{s,He}(E)\Phi_{He} + Q_{He}(E)$  is the emission density for the helium.

Next, it is assumed that the flux exiting the pebbles and entering the surfaces is piecewise uniform and isotropic,

$$\psi_+(E) \sim \frac{1}{\pi} \frac{\sum_k p_{i,k}^{p,b} J_{-,k}^{bd}(E) + \sum_j p_{i,j}^{p,p} J_{+,j}(E)}{N_i A_i}. \quad (\text{B.6})$$

With these assumptions the incoming flux becomes a function of only the chord length  $l$ :

$$\psi_{-,i}(\mathbf{r}, E, \Omega) = e^{-\Sigma_{He} l} \psi_+(E) + \frac{F_{He}(E)}{4\pi \Sigma_{He}} (1 - e^{-\Sigma_{He} l}), \quad (\text{B.7})$$

and Eq. (B.4) can be written as

$$J_{-,i}(E) = \langle e^{-\Sigma_{He} l} \rangle J_{-,i}^0(E) + \left(1 - \langle e^{-\Sigma_{He} l} \rangle\right) \frac{N_i A_i F_{He}(E)}{4\Sigma_{He}}. \quad (\text{B.8})$$

In this equation  $J_{-,i}^0(E)$  is the current given in Eq. (B.1) in the absence of helium and

$$\langle e^{-\Sigma_{He} l} \rangle = \int_0^{\infty} dl p(l) e^{-\Sigma_{He} l}, \quad (\text{B.9})$$

where

$$p(l) = \frac{\int_S dS \int_{(2\pi)_+} d\Omega |\mathbf{\Omega} \cdot \mathbf{n}| \delta |l - l(\mathbf{r}, \mathbf{\Omega})|}{\int_S dS \int_{(2\pi)_+} d\Omega |\mathbf{\Omega} \cdot \mathbf{n}|}, \quad (\text{B.10})$$

is the density of probability for a chord length  $l$  between pebbles.

It has been shown<sup>B.1</sup> that a very good approximation for  $p(l)$  is the Markovian distribution

$$p(l) = \frac{e^{-l/\lambda_{He}}}{\lambda_{He}}, \quad (\text{B.11})$$

where  $\lambda_{He}$  is the mean chord length between pebbles. It can be computed through the Cauchy's formula  $\lambda_{He} = 4V_{He}/A_{He}$  where  $V_{He}$  is the total helium volume in the spectrum zone and  $A_{He}$  is the total area of interaction  $A_{He} = \sum_k A_k^{bd} + \sum_i N_i A_i$ . Use of this result gives

$$t_{He} = \langle e^{-\Sigma_{He} l} \rangle = \frac{1}{1 + \lambda_{He} \Sigma_{He}} \quad (\text{B.12})$$

And the expression for  $J_{-,i}(E)$  of Eq. (B.8) becomes

$$\vec{J}_{-}(E) = t_{He} \left[ \vec{J}_{-}^0(E) + \vec{a}^p f_p V_{He} F_{He}(E) \right], \quad (\text{B.13})$$

A similar treatment can be applied to  $J_{+,k}^{bd}(E)$ , leading to the expression

$$\vec{J}_{+}^{bd}(E) = t_{He} \left[ \vec{J}_{+}^{bd,0}(E) + \vec{a}^b f_b V_{He} F_{He}(E) \right], \quad (\text{B.14})$$

where  $J_{+,k}^{bd,0}(E)$  is the current in Eq. (B.2),  $\vec{a}^p$  and  $\vec{a}^b$  are the relative areas of each pebble type and surface, respectively, and  $f_p$  and  $f_b$  are the fraction of the overall pebbles area and of the zone surfaces over the total area of interaction  $A_{He}$ .

The conservation equation for the spectrum zone domain reads now

$$V_{He} \Sigma_{He}(E) \Phi_{He}(E) = J_-^{bd}(E) + J_+(E) - [J_+^{bd}(E) + J_-(E)] + V_{He} F_{He}(E). \quad (\text{B.15})$$

On the other hand, proceeding as in the derivation of Eq. (B.3) we obtain

$$J_+^{bd}(E) + J_-(E) = t_{He} [J_-^{bd}(E) + J_+(E) + V_{He} F_{He}(E)]. \quad (\text{B.16})$$

By combining both equations we obtain

$$\frac{\Phi_{He}(E)}{4} = \frac{J_{-,He}(E)}{A_{He}}, \quad (\text{B.17})$$

where  $J_{-,He}(E) = J_+^{bd}(E) + J_-(E)$  is the total current entering the helium volume.

This expression shows that, as a consequence of the adopted assumptions, the flux in the helium assumes an infinite-medium equilibrium.

Finally, with the help of Eq. (B.16), we recast Eq. (B.17) as

$$V_{He} \Phi_{He} = \lambda_{He} t_{He} \left( \vec{1}^b \cdot \vec{J}_-^{bd} + \vec{1}^p \cdot \vec{J}_+ + V_{He} F_{He} \right). \quad (\text{B.18})$$

As a final comment, it has to be noted that the average  $\langle e^{-\Sigma_{He} l} \rangle$  for chords between a surface of the spectrum zone and the pebbles, or a close surface, has been approximated by the interpebble chord length distribution.

## REFERENCES

- B.1. A. Mazzolo, B. Roesslinger, "Monte Carlo Simulation of the Chord Length Distribution Function Across Convex Bodies, Non-Convex Bodies and Random Media", IV IMACS Seminar on Monte Carlo Method, Berlin (2003).

## APPENDIX C: CP Treatment of the Multi-Pebble Geometries

To formulate a numerical approximation for Eq. 3.1 presented in Chapter 3, let consider each pebble type as a 1D spherical geometry and cast the corresponding transport equations into a collision probability formulation:

$$\begin{aligned} V_i \vec{\Phi}_i &= C_i \vec{F}_i + \vec{I}_i J_{-,i}, \\ J_{+,i} &= \vec{E}_i \vec{F}_i + T_i J_{-,i}, \end{aligned} \quad (\text{C.1})$$

where the group index is omitted,  $i$  denotes the pebble type,  $C_i$ ,  $\vec{I}_i$ ,  $\vec{E}_i$  and  $T_i$  are the CP coefficients,  $V_i$  contains the pebble region volumes,  $\vec{\Phi}_i$  is the vector of region-averaged fluxes,  $\vec{F}_i = \sum_{si} \vec{\Phi}_i + \vec{Q}_i$  and  $\vec{Q}_i$  accounts for fission and external transfers. To take into account the multiplicity of the pebbles of type  $i$  in the spectrum zone, a factor  $N_i$ , which is the number of pebbles of type  $i$  contained in the spectrum zone, has been included in the volumes, in the matrix  $C_i$  and in the vector  $\vec{E}_i$ . Finally,  $J_{\pm,i}$  is the total current exiting (+) or entering (-) the overall surface of the pebbles of type  $i$ . We point out that the stochastic distribution of the TRISO particles in the pebble is treated with the double-heterogeneity method of APOLLO2, based on the Askew's approximation and on the conservation of the first collision rate in a homogenized matrix – particles material, and it is thus incorporated in the CP coefficients. The CP coefficients obey the reciprocity and conservation relations:

$$\begin{aligned} C_i &= C_i^t, \quad \vec{I}_i = \frac{4}{N_i A_i} \vec{E}_i \\ \vec{I}_i \cdot V_i &= \vec{E}_i + \vec{\Sigma}_i \cdot \vec{C}_i, \\ 1 &= T_i + \vec{\Sigma}_i \cdot \vec{I}_i. \end{aligned}$$

The first equation in (C.1) allows the region fluxes to be computed within any pebble type in terms of the total current entering the pebbles of that type. This current is derived from the currents exiting the pebbles and those entering the surfaces of the spectrum zone accounting for the absorption and diffusion of the helium.

In the following a global vector will be introduced that contains all the region fluxes for all pebble types  $\vec{\Phi} = \{\vec{\Phi}_i\}$  and, with the obvious notation the CP equations are rewritten as



$$\begin{aligned}
V\vec{\Phi} &= C\vec{F} + I\vec{J}_- \\
\vec{J}_+ &= E\vec{F} + T\vec{J}_-
\end{aligned} \tag{C.2}$$

With the reciprocity and conservation relations

$$\begin{aligned}
C &= C^t, \quad INA = 4E^t, \quad T = T^t, \\
\vec{1}_\Phi \cdot V &= \vec{1}_p \cdot E + \vec{\Sigma} \cdot C, \quad \vec{1}_p = \vec{1}_p \cdot T + \vec{\Sigma} \cdot I.
\end{aligned}$$

Let now proceed by eliminating the currents. Eq. (B.13) is written as  $\vec{J}_- = \vec{J}_0 + \beta\vec{J}_+$ , where  $\vec{J}_0 = t_{He} \left( p^{p,b} \vec{J}_-^{bd} + \vec{a}^p f_p V_{He} F_{He} \right)$  and  $\beta = t_{He} p^{p,p}$  is the albedo operator. Then, with the help of the second equation in (C.2) it follows

$$\vec{J}_- = (1 - \beta T)^{-1} \left( \vec{J}_0 + \beta E \vec{F} \right)$$

and the CP equations are written as

$$\begin{aligned}
V\vec{\Phi} &= C'\vec{F} + I'\vec{J}_0 \\
\vec{J}_+ &= E'\vec{F} + T'\vec{J}_0
\end{aligned} \tag{C.3}$$

with the modified CP matrices  $C' = C + I\beta(1 - T\beta)^{-1}$ ,  $I' = I(1 - \beta T)^{-1}$ ,  $E' = (1 - T\beta)^{-1} E$  and  $T' = (1 - T\beta)^{-1} T$ . These matrices obey the reciprocity and conservation equations

$$\begin{aligned}
C' &= C'^t, \quad I'NA = 4(E')^t, \quad T'NA = (T'NA)^t, \\
\vec{1}_\Phi \cdot V &= \vec{1}_p \cdot (1 - \beta) E' + \vec{\Sigma} \cdot C', \quad \vec{1}_p = \vec{1}_p \cdot (1 - \beta) T' + \vec{\Sigma} \cdot I'.
\end{aligned}$$

In order to introduce the coolant region inside the equations let redefine  $\vec{\Phi}' = \left[ \vec{\Phi}, \vec{\Phi}_{He} \right]$ . Then let add  $V_{He}$  and  $F_{He}$  to the volumes diagonal matrix to obtain  $V'$  and to the volumetric productions vector to obtain  $\vec{F}'$ .

Substituting  $\vec{J}_+$  in Eq. (B.18) with the expression given by the second equation in (C.3), an expression for  $V_{He} \Phi_{He}$  is found which depends on the entering currents

through the spectrum zone surface. Combining it with the first equation in (C.3) the system of equations for  $V'\vec{\Phi}'$  is determined. Finally, substituting  $\vec{J}_+$  in Eq. (B.14) with the expression given by the second equation in (C.3), an equation is found for the exiting currents through the spectrum zone surfaces, depending only on the fluxes in the pebble regions and in the helium and on the entering currents through the surfaces. The CP equations for all the regions in the spectrum zone are so obtained, connected by the currents exchanged through the zone boundaries:

$$\begin{aligned} V'\vec{\Phi}' &= \tilde{C}\vec{F}' + \tilde{I}\vec{J}_-^{bd} \\ \vec{J}_+^{bd} &= \tilde{E}\vec{F}' + \tilde{T}\vec{J}_-^{bd} \end{aligned} \quad (\text{C.4})$$

where (indicating within square-bracket the dimensions of vector and matrices, with the first element being the number of rows and the second of columns;  $N_{\Phi,p}$  is the total number of pebble flux regions)

$$\tilde{C} = \begin{bmatrix} C' & C'' \\ C''' & c \end{bmatrix}$$

with  $C''[N_{\Phi,p},1] = t_{He} V_{He} f_p I' \cdot \vec{a}^p$ ,  $C'''[1,N_{\Phi,p}] = \lambda_{He} t_{He} \vec{1}^p \cdot E'$  and  $c = \lambda_{He} t_{He} V_{He} (1 + t_{He} f_p \vec{1}^p \cdot T' \cdot \vec{a}^p)$

$$\tilde{I} = \begin{bmatrix} t_{He} I' \cdot p^{p,b} [N_{\Phi,p}, N_b] \\ \lambda_{He} t_{He} (\vec{1}^b + t_{He} \vec{1}^p \cdot T' \cdot p^{p,b}) [1, N_b] \end{bmatrix}$$

$$\tilde{E} = \begin{bmatrix} t_{He} p^{b,p} \cdot E' [N_b, N_{\Phi,p}] & t_{He} V_{He} (f_b \vec{a}^b + t_{He} f_p p^{b,p} \cdot T' \cdot \vec{a}^p) [N_b, 1] \end{bmatrix}$$

$$\tilde{T}[N_b, N_b] = t_{He} (p^{b,b} + t_{He} p^{b,p} \cdot T' \cdot p^{p,b})$$

The matrices  $\tilde{C}$ ,  $\tilde{I}$ ,  $\tilde{E}$  and  $\tilde{T}$  satisfy the reciprocity and conservation equations (this is demonstrated by using the reciprocity and conservation relations of the surface-to-surface geometrical probabilities):

$$\begin{aligned} \tilde{C} &= \tilde{C}^t, \quad \tilde{I} N A = 4 (\tilde{E})^t, \quad \tilde{T} A^b = (\tilde{T} A^b)^t, \\ \vec{1}_{\Phi'} \cdot V' &= \vec{1}_b \cdot \tilde{E} + \vec{\Sigma}' \cdot \tilde{C}, \quad \vec{1}_b = \vec{1}_b \cdot \tilde{T} + \vec{\Sigma}' \cdot \tilde{I}. \end{aligned}$$

If reflected boundary conditions are imposed for the spectrum zone one obtains ( $\vec{J}_{-}^{bd} = \vec{J}_{+}^{bd}$ ). This is used for example when initializing the iterative core homogenization scheme by a critical-buckling infinite-lattice calculation, or if the matrices are computed for the self-shielding procedure, Eq. (C.4) becomes

$$\begin{aligned} V' \vec{\Phi}' &= \tilde{C}_{ref} \vec{F}' \\ \vec{J}_{+}^{bd} &= \tilde{E}_{ref} \vec{F}' \end{aligned} \tag{C.5}$$

with  $\tilde{C}_{ref} = \tilde{C} + \tilde{I}(1 - \tilde{T})^{-1} \tilde{E}$  and  $\tilde{E}_{ref} = (1 - \tilde{T})^{-1} \tilde{E}$ , being the computed matrices.

Thus, all the pebble flux regions, plus the helium region, are spatially coupled while computing the reflected multi-pebble geometry. This is important especially for the self-shielding of microscopic cross sections using the APOLLO2 method described in section 2.4.

## APPENDIX D: Surface-to-Surface Geometrical Probabilities

A neutron entering a surface  $k$  or leaving a pebble either leaves the domain through its boundary or enters a pebble. Obviously the surface-to-surface geometrical probabilities depend on the packing fraction and on the shape of the domain, but, because of purely geometrical reasons, they have to obey the reciprocity and conservation relations:

$$\begin{aligned}
 p_{ji}^{p,p} N_i A_i &= p_{ij}^{p,p} N_j A_j, \\
 p_{ki}^{b,p} N_i A_i &= p_{ik}^{p,b} A_k^b, \\
 p_{k'k}^{b,b} A_k^b &= p_{kk'}^{b,b} A_{k'}^b, \\
 1 &= \sum_{k'} p_{k'k}^{b,b} + \sum_i p_{ik}^{p,b} \\
 1 &= \sum_k p_{ki}^{b,p} + \sum_j p_{ji}^{p,p}
 \end{aligned} \tag{D.1}$$

These relations are based on the fact that the probability for a neutron leaving uniformly and isotropically surface  $a$  to attain surface  $b$  is:

$$p_{ba} = \frac{1}{\pi A_a} \iint_{a \leftrightarrow b} dS dS' \frac{|\boldsymbol{\Omega} \cdot \mathbf{n}| |\boldsymbol{\Omega} \cdot \mathbf{n}'|}{R^2} \tag{D.2}$$

Where the integral is carried out over every part of points  $\mathbf{r}$  and  $\mathbf{r}'$  on surfaces  $a$  and  $b$  separated by a direct straight path of length  $R$ ,  $\boldsymbol{\Omega}$  is the angular direction from  $\mathbf{r}$  and  $\mathbf{r}'$  and  $\mathbf{n}$  and  $\mathbf{n}'$  the unit vectors normal to surface  $a$  and  $b$ , respectively.

Several possible models could be used to express the surface-to-surface geometrical probabilities. Two different ones are introduced here, a *uniform* model and a *renormalized* one. They are both based on having the values of the  $p_{k'k}^{b,b}$  furnished externally. These lasts can be obtained from Monte Carlo simulations (as we describe in section 3.3) or from geometrical approximations. Then, from the first conservation equation in Eq. (D.1)

$$p_k^b = \sum_i p_{ik}^{p,b} = 1 - \sum_{k'} p_{k'k}^{b,b}, \tag{D.3}$$

is obtained, and it is possible to write

$$p_{ik}^{p,b} = a_i^b p_k^b, \quad p_{ki}^{b,p} = a_i^b p_k^b \frac{A_k^b}{N_i A_i}, \quad (\text{D.4})$$

where  $p_k^b$  is the probability for a neutron entering via surface  $k$  to enter a pebble in the spectrum zone and  $a_i^b$  is the probability that the pebble in which the neutron enters is of type  $i$ . Notice that the expression for  $p_{ki}^{b,p}$  has been obtained from reciprocity. This gives

$$p_i = \sum_k p_{k,i}^{b,p} = a_i^b \frac{\sum_k p_k^b A_k^b}{N_i A_i}, \quad (\text{D.5})$$

where  $p_i$  is the probability for neutrons leaving a pebble of type  $i$  to exit the spectrum zone via its surfaces without crossing any other pebbles.

Let define the average value of  $p_i$  as

$$\bar{p} = \sum_i a_i p_i = \frac{\sum_k p_k^b A_k^b}{\sum_i N_i A_i} \quad (\text{D.6})$$

so that

$$a_i^b = \frac{p_i}{\bar{p}} a_i. \quad (\text{D.7})$$

This relation shows that the condition  $p_i \leq 1$  entails  $a_i^b/a_i \leq 1/\bar{p}$ . Because of the form for  $\bar{p}$ , this condition must be imposed independently of the condition  $a_i^b \leq 1$ .

The *uniform* model is defined by taking  $a_i^b$  equal to the surface proportion in the entire domain:

$$a_i^b = a_i = \frac{N_i A_i}{\sum_i N_i A_i}. \quad (\text{D.8})$$

This gives  $p_i = \bar{p}$  and

$$p_{ik}^{p,b} = a_i^b p_k^b, \quad p_{ki}^{b,p} = \frac{p_k^b A_k^b}{\sum_i N_i A_i}. \quad (\text{D.9})$$

Thus the probability  $p_{ki}^{b,p}$  is the same for all pebbles types. Next, from the second conservation equation in (D.1) it is obtained

$$\sum_j p_{ji}^{p,p} = 1 - \bar{p}.$$

It remains to determine the  $p_{ji}^{p,p}$ . A simple model, consistent with the adopted stochastic approach, is to take  $p_{ji}^{p,p} \propto N_j A_j$  and obtain the proportionality constant from the above conservation relation. This gives

$$p_{ji}^{p,p} = a_j (1 - \bar{p}). \quad (\text{D.10})$$

These equations define all the surface-to-surface geometrical probabilities in terms of the single parameter  $0 < p_k^b < 1$ . Note that the constraint  $p_{ki}^{b,p} \leq 1$  entails the extra-condition  $p_k^b A_k^b \leq \sum_i N_i A_i$ , but this condition is surely satisfied.

The basic problem with the above formulation is that the value of  $p_{ii}^{p,p}$  for  $N_i = 1$  is unphysical:  $p_{ii}^{p,p} (N_i = 1) = a_i (1 - \bar{p})$  when the true value should be 0.

From Eq. (D.2) it can be written

$$p_{ji}^{p,p} N_i A_i = \left(1/\pi\right) \iint_{S_j \leftrightarrow S_i} dS dS' \frac{|\boldsymbol{\Omega} \cdot \mathbf{n}| |\boldsymbol{\Omega} \cdot \mathbf{n}'|}{R^2} \quad (\text{D.11})$$

where  $S_i = N_i A_i$  is the emission area for pebbles of type  $i$  and  $S_j$  is the available entering surface for pebbles of type  $j$ . The *uniform* model is based on the assumption that the integral is proportional to the product of area of emission times that of reception, where the latter is taken as  $S_j = N_j A_j$ . Clearly, this assumption is not correct when  $j = i$ . To have the correct physics it is proposed to take the integral proportional to  $N_i A_i \times (N_j - \delta_{ij}) A_j$ . This yields the following expression

$$p_{ji}^{p,p} = a_j (1 - p_i) \frac{1 - \delta_{ij}/N_i}{1 - a_i/N_i} \quad (\text{D.12})$$

However this formula does not account for boundary effects that effectively diminish the emission areas and the receiving ones and, as a consequence, does not respect

symmetry. A *renormalized uniform model* is then defined where symmetry is enforced by the relation

$$\frac{1 - p_i}{1 - a_i/N_i} = \bar{\alpha}, \quad (\text{D.13})$$

where the constant  $\bar{\alpha}$  can be calculated from Eq. (D.7) and the normalization  $\sum_i p_i^b = 1$ :

$$\bar{\alpha} = \frac{1 - \bar{p}}{1 - \sum_i a_i^2/N_i}. \quad (\text{D.14})$$

The final expression for the pebble-to-pebble probabilities is

$$p_{ji}^{p,p} = a_j (1 - \bar{p}) \frac{1 - \delta_{ij}/N_i}{1 - \sum_i a_i^2/N_i} = \bar{\alpha} a_j (1 - \delta_{ij}/N_i). \quad (\text{D.15})$$

Because it is expected  $\bar{p} \geq \sum a_i^2/N_i$ , it follows  $\bar{\alpha} \leq 1$  and, therefore,  $p_{ji}^{p,p} \leq 1$ . Note that this model carries over to the *uniform* model at the limit  $N_i \rightarrow \infty$ :  $\lim_{N_i \rightarrow \infty} p_{ji}^{p,p} = a_j (1 - \bar{p})(1 + r_{ji})$ . However as opposed to the *uniform* model, here the  $p_i$  and therefore the  $a_i^b$  depend on  $i$ .

Finally, from the asymptotic behavior it is derivable

$$p_{ji}^{p,p} = a_j (1 - \bar{p})(1 + r_{ji}), \quad (\text{D.16})$$

where

$$r_{ji} = \frac{\sum_i a_i^2/N_i - \delta_{ij}/N_i}{1 - \sum_i a_i^2/N_i}$$

is symmetric,  $r_{ji} = r_{ij}$ ,  $\lim_{N_i \rightarrow \infty} r_{ji} = 0$  and satisfies the normalization

$$\sum_j a_j r_{ji} = (\bar{p} - p_i)/(1 - \bar{p}).$$

## APPENDIX E: Clustering

The *uniform* model can be easily modified to represent clustering. Assume pebbles of type  $m$  cluster. This ought to result in an increase of  $p_{mm}$  and a variation of  $p_m$ , or equivalently of  $a_m^b$ , with respect to the values predicted by the *uniform* model. Let pose  $p_{mm} = \alpha(p_{mm})$ , where the  $(\ )$  denotes values from the *uniform* model, and, for  $i \neq m$ ,  $p_{im} = \beta(p_{im})$  with  $\alpha$  user given. Reciprocity yields  $p_{mi} = \beta(p_{mi})$  for  $i \neq m$ , while conservation gives

$$\sum_i p_{im} = 1 - p_m \rightarrow \beta = \frac{(1 - p_m)/(1 - \bar{p}) - \alpha a_m}{1 - a_m}. \quad (\text{E.1})$$

Next, for  $j, i \neq m$ , we pose  $p_{ji} = \gamma(p_{ji})$  and from conservation it is obtained

$$\sum_j p_{ji} = 1 - p \rightarrow \gamma = \frac{(1 - p)/(1 - \bar{p}) - \beta a_m}{1 - a_m}. \quad (\text{E.2})$$

It remains to define  $p_m$  and  $p$ , or alternatively  $a_m^b$  and  $a_i^b$  for  $i \neq m$ . It shall be written

$$p_m = \alpha^b(p_m), \quad p_i = \beta^b(p_i), \quad i \neq m, \quad (\text{E.3})$$

which gives

$$a_m^b = \alpha^b a_m \frac{(p_m)}{\bar{p}}, \quad a_i^b = \beta^b a_i \frac{(p_i)}{\bar{p}}. \quad (\text{E.4})$$

From the normalization condition

$$\beta^b = \frac{\bar{p} - \alpha^b a_m (p_m)}{\bar{p} - a_m (p_m)}. \quad (\text{E.5})$$

For the uniform model  $(p_m) = (p_i) = \bar{p}$  and it derives



$$\begin{aligned}
p_m &= \alpha^b \bar{p}, \quad p_i = p = \beta^b \bar{p}, \quad i \neq m, \\
a_m^b &= \alpha^b a_m, \quad a_i^b = \beta^b a_i,
\end{aligned} \tag{E.6}$$

Eq. (E.5) becomes

$$\beta^b = \frac{1 - \alpha^b a_m}{1 - a_m}. \tag{E.7}$$

Then, from Eq. (D.4) it is obtained

$$\begin{aligned}
p_{mk}^{p,b} &= \alpha^b (p_{mk}^{p,b}), \quad p_{km}^{b,p} = \alpha^b (p_{km}^{b,p}), \\
p_{ik}^{p,b} &= \beta^b (p_{ik}^{p,b}), \quad p_{ki}^{b,p} = \beta^b (p_{ki}^{b,p}).
\end{aligned} \tag{E.8}$$

Hence, the clustering model is completely defined by the positive parameters  $\alpha^b$  and  $\alpha$ , with the constraints  $0 \leq a_m^b, a_i^b, p_m, p_i \leq 1$  and  $0 \leq p_{mm}, p_{im}, p_{mi}, p_{ji} \leq 1$ . The first condition gives  $0 \leq \alpha^b \leq \min(1/a_m, 1/\bar{p})$ ,  $0 \leq \beta^b \leq \min(1/a_{max}, 1/\bar{p})$ , with  $a_{max} = \max_{i \neq m} a_i$ . This constraints the value of  $\alpha^b$  to

$$\frac{1}{a_m} \max \left[ 0, 1 - (1 - a_m) \min \left( \frac{1}{a_{max}}, \frac{1}{\bar{p}} \right) \right] \leq \alpha^b \leq \min \left( \frac{1}{a_m}, \frac{1}{\bar{p}} \right). \tag{E.9}$$

The second condition gives  $0 \leq \alpha \leq (1/p_{mm})$ ,  $0 \leq \beta \leq \beta_{max}$  and  $0 \leq \gamma \leq \gamma_{max}$ , with

$$\begin{aligned}
\beta_{max} &= 1 / \max_{i \neq m} [(p_{im}), (p_{mi})], \\
\gamma_{max} &= 1 / \max_{i, j \neq m} (p_{ji}),
\end{aligned}$$

resulting in a limited domain for the value of  $\alpha$ :

$$\alpha_{min} \leq \alpha \leq \alpha_{max} \tag{E.10}$$

with

$$\alpha_{min} = \frac{1}{a_m} \max \left[ 0, \frac{1-p_m}{1-\bar{p}} - (1-a_m) \min \left( \beta_{max}, \frac{1-p}{a_m(1-\bar{p})} \right) \right],$$

$$\alpha_{max} = \frac{1}{a_m} \min \left\{ \frac{1}{1-\bar{p}}, \frac{1-p_m}{1-\bar{p}} - \frac{1-a_m}{a_m} \max \left[ 0, \frac{1-p}{1-\bar{p}} - (1-a_m)\gamma_{max} \right] \right\}.$$

Clearly, a solution is  $\alpha^b = \alpha = 1$ . In practice, Eq. (E.9) is used to adjust the user given value of  $\alpha^b$ , then  $p$  and  $p_m$  are computed and Eq. (E.10) is used to adjust the user's value for  $\alpha$ .

For the *renormalized* model, as for the clustering with the uniform model, user's parameter  $\alpha^b$  shall be used in equations (E.3) to (E.7). From  $0 \leq a_m^b, a_i^b, p_m, p_i \leq 1$  it derives  $0 \leq \alpha^b \leq \alpha_{max}^b$  and  $0 \leq \beta^b \leq \beta_{max}^b$ , with  $\alpha_{max}^b = 1/(p_m) \min(1, \bar{p}/a_m)$  and  $\beta_{max}^b = \min \left\{ 1/\max_{i \neq m} (p_i), \max_{i \neq m} 1/[a_i(p_i)] \right\}$ . This gives the bounds:

$$\max \left[ 0, \beta_{max} + (1 - \beta_{max}) \frac{\bar{p}}{a_m(p_m)} \right] \leq \alpha^b \leq \alpha_{max}^b \quad (\text{E.11})$$

The technique to modify the  $p_{ji}$  is similar to the one used for the *homogeneous* model, with the exception that, for the renormalized model, symmetry requires to define  $p_{ji} = \alpha_{ji}(p_{ji})$ , with  $\alpha_{ji}$  symmetric ( $\alpha_{ji} = \alpha_{ij}$ ). The following tensor shall be used:  $\alpha_{mm} = \alpha$ ,  $\alpha_{im} = \alpha_{mi} = \beta_i$  for  $i \neq m$  and  $\alpha_{ji} = \alpha_{ij} = \gamma$  for  $i, j \neq m$ . The normalization conditions for the  $p_{ji}$  yield:

$$1 - p_m = \alpha(p_{mm}) + \sum_{i \neq m} \beta_i(p_{im}),$$

$$1 - p_i = \beta_i(p_{mi}) + \gamma \sum_{j \neq m} (p_{ji}).$$
(E.12)

Because  $\gamma$  must be independent of  $i$ , the last equation determines the value of

$$\beta_i = \frac{1 - p_i - \gamma \sum_{j \neq m} (p_{ji})}{(p_{mi})} \quad (\text{E.13})$$

in terms of  $p_i$  and  $\gamma$ . Next, replacing this expression into the first equation in (E.12) gives the value of

$$\gamma = \frac{1 - \bar{p} + a_m [\alpha (p_{mm}) - 2(1 - p_m)]}{\sum_{i \neq m} a_i \sum_{j \neq m} (p_{ji})} \quad (\text{E.14})$$

In terms of  $p_m$  and  $\alpha$ .

Next, the constraints  $0 \leq p_{mm}, p_{im}, p_{mi}, p_{ji} \leq 1$  yield  $0 \leq \alpha \leq 1/(p_{mm})$ ,  $0 \leq \beta_i(p_{mi}) \leq \min(1, a_m/a_i)$  and  $0 \leq \gamma \leq \gamma_{max}$ . From the constraints on the  $\beta_i$  and on  $\gamma$  it is obtained that  $\gamma_- \leq \gamma \leq \gamma_+$ , with

$$\gamma_- = \max \left[ 0, \max_{i \neq m} \frac{1 - p_i - \min(1, a_m/a_i)}{\sum_{j \neq m} (p_{ji})} \right], \gamma_+ = \min \left[ \gamma_{max}, \min_{i \neq m} \frac{1 - p_i}{\sum_{j \neq m} (p_{ji})} \right]. \quad (\text{E.15})$$

And finally, the constraints for  $\alpha$  as in Eq. (E.10) with

$$\alpha_{min} = \frac{1}{a_m (p_{mm})} \max(0, \gamma_- D - B),$$

$$\alpha_{max} = \frac{1}{a_m (p_{mm})} \min(a_m, \gamma_+ D - B),$$

where  $D = \sum_{i \neq m} a_i \sum_{j \neq m} (p_{ji})$  and  $B = 1 - \bar{p} - 2a_m(1 - p_m)$ .

## APPENDIX F: Mixed Type Individual Pebbles Simulation Results

**Table F.I: Prod. shape factors and  $\sigma$  of T4 LT D1 simulation with MG-P1 XS (mixed pebble types)**

CHAN A	CHAN B	CHAN C	CHAN D	CHAN E
0.66 0.21%	0.57	0.50	0.53	0.48 0.18%
0.85 0.19%	0.20%	0.19%	0.18%	0.62 0.17%
1.10 0.17%	0.77	0.68	0.72	0.79 0.15%
1.26 0.13%	0.16%	0.16%	0.15%	0.94 0.12%
1.41 0.11%	1.00	0.88	0.92	1.06 0.10%
1.58 0.09%	0.13%	0.13%	0.13%	1.16 0.09%
1.64 0.08%	1.16	1.03	1.08	1.21 0.07%
1.74 0.07%	0.10%	0.09%	0.09%	1.26 0.07%
1.77 0.07%	1.29	1.14	1.19	1.28 0.07%
1.71 0.08%	0.08%	0.08%	0.07%	1.26 0.08%
1.62 0.10%	1.37	1.19	1.24	1.17 0.11%
1.45 0.12%	0.07%	0.07%	0.06%	1.11 0.12%
1.22 0.14%	1.37	1.20	1.25	0.93 0.14%
1.00 0.15%	0.07%	0.07%	0.07%	0.76 0.15%
0.80 0.16%	1.27	1.12	1.17	0.57 0.16%
	0.09%	0.09%	0.09%	
	1.10	0.97	1.02	
	0.12%	0.12%	0.12%	
	0.88	0.77	0.81	
	0.15%	0.14%	0.14%	
	0.64	0.57	0.59	
	0.15%	0.15%	0.15%	

**Table F.II: Rel. diff. on prod. shape factors of 26-group P1-S<sub>8</sub> AP2 calculation from T4 LT D1**

CHAN A	CHAN B	CHAN C	CHAN D	CHAN E
-6.51%	-4.00%	-6.23%	-5.81%	-7.78%
-3.17%				-4.26%
-2.98%	-2.96%	-5.70%	-4.58%	-4.13%
-0.96%	-1.47%	-3.57%	-2.53%	-2.43%
-0.45%	0.13%	-2.43%	-1.39%	-0.94%
0.82%				-0.59%
1.92%	1.58%	-1.49%	-0.47%	0.42%
3.41%	2.53%	0.18%	1.07%	1.27%
2.35%	2.89%	0.27%	1.63%	2.42%
2.98%				0.75%
1.99%	2.98%	0.57%	1.60%	1.34%
1.92%	2.38%	0.85%	1.55%	2.00%
1.75%				1.63%
0.70%	1.31%	-0.87%	0.77%	0.56%
-1.43%	1.84%	-0.86%	0.14%	-1.15%

**Table F.III: Prod. shape factors and  $\sigma$  of T4 LT D2 simulation with MG-P1 XS (mixed pebble types)**

CHAN A	CHAN B	CHAN C	CHAN D	CHAN E
0.69 0.21%	0.57	0.51	0.53	0.49 0.20%
0.88 0.18%	0.20%	0.20%	0.19%	0.63 0.19%
1.11 0.17%	0.78	0.70	0.73	0.80 0.17%
1.28 0.14%	0.17%	0.18%	0.18%	0.95 0.14%
1.46 0.11%	1.02	0.90	0.94	1.06 0.11%
1.58 0.09%	0.15%	0.15%	0.14%	1.15 0.09%
1.66 0.08%	1.18	1.04	1.10	1.23 0.08%
1.68 0.08%	0.10%	0.11%	0.10%	1.26 0.07%
1.73 0.08%	1.30	1.15	1.19	1.28 0.08%
1.64 0.11%	0.08%	0.08%	0.08%	1.21 0.10%
1.61 0.12%	1.35	1.19	1.24	1.17 0.12%
1.39 0.14%	0.07%	0.07%	0.07%	1.09 0.13%
1.22 0.16%	1.34	1.17	1.22	0.94 0.15%
0.99 0.17%	0.09%	0.09%	0.09%	0.75 0.17%
0.80 0.20%	1.25	1.10	1.16	0.56 0.19%
	0.11%	0.11%	0.11%	
	1.09	0.97	1.01	
	0.13%	0.13%	0.13%	
	0.88	0.77	0.80	
	0.16%	0.16%	0.15%	
	0.64	0.57	0.59	
	0.19%	0.19%	0.18%	

**Table F.IV: Rel. diff. on prod. shape factors of 26-group P1-S<sub>8</sub> AP2 calculation from T4 LT D2**

CHAN A	CHAN B	CHAN C	CHAN D	CHAN E
-2.25%	0.67%	-1.72%	-1.18%	-3.94%
1.96%				-0.03%
2.80%	1.72%	-1.21%	-0.01%	0.77%
2.88%	2.47%	-0.10%	0.75%	1.17%
2.71%	2.27%	0.23%	0.89%	1.18%
2.72%				1.18%
1.45%	1.77%	-0.40%	0.79%	0.02%
1.91%	1.34%	-1.10%	0.09%	0.04%
0.35%	1.11%	-0.53%	0.25%	-0.59%
1.76%				0.36%
0.61%	1.54%	-0.97%	-0.40%	-0.42%
0.07%	0.24%	-2.08%	-0.72%	-0.47%
-0.76%				-2.03%
-2.55%	-1.50%	-3.82%	-2.27%	-3.50%
-5.31%	-2.13%	-4.77%	-3.42%	-5.47%

**Table F.V: Prod. shape factors and  $\sigma$  of T4 LT D3 simulation with MG-P1 XS (mixed pebble types)**

CHAN A	CHAN B	CHAN C	CHAN D	CHAN E
0.68 0.19%	0.59	0.51	0.54	0.50 0.18%
0.89 0.16%	0.17%	0.17%	0.16%	0.63 0.15%
1.11 0.14%	0.79	0.70	0.73	0.81 0.12%
1.28 0.11%	0.14%	0.14%	0.13%	0.97 0.11%
1.50 0.11%	1.02	0.90	0.94	1.06 0.10%
1.64 0.10%	0.10%	0.09%	0.09%	1.16 0.08%
1.68 0.08%	1.33	1.17	1.22	1.25 0.08%
1.76 0.07%	0.08%	0.08%	0.08%	1.27 0.07%
1.74 0.07%	1.39	1.21	1.26	1.27 0.07%
1.66 0.08%	0.07%	0.07%	0.07%	1.22 0.07%
1.53 0.10%	1.36	1.19	1.23	1.14 0.09%
1.41 0.12%	0.06%	0.07%	0.07%	1.05 0.11%
1.19 0.14%	1.25	1.09	1.14	0.91 0.14%
0.95 0.17%	1.07	0.94	0.98	0.73 0.17%
0.76 0.21%	0.85	0.74	0.78	0.55 0.22%
	0.15%	0.15%	0.15%	
	0.61	0.55	0.56	
	0.20%	0.20%	0.20%	

**Table F.VI: Rel. diff. on prod. shape factors of 26-group P1-S<sub>8</sub> AP2 calculation from T4 LT D3**

CHAN A	CHAN B	CHAN C	CHAN D	CHAN E
-4.91%	-3.49%	-4.94%	-4.74%	-7.27%
-3.11%				-3.19%
-1.59%	-2.12%	-4.99%	-3.31%	-1.93%
-0.36%	-0.78%	-3.18%	-2.37%	-1.51%
0.04%	0.50%	-2.07%	-1.24%	-0.46%
0.87%				0.20%
1.26%	0.66%	-1.03%	0.26%	0.98%
2.89%	2.42%	-0.26%	1.20%	1.27%
1.59%	2.92%	0.94%	2.01%	1.86%
2.65%				2.29%
3.75%	2.33%	1.09%	2.00%	1.42%
1.57%	2.20%	0.13%	0.82%	0.98%
1.37%				-0.51%
-0.22%	0.25%	-1.50%	-0.60%	-2.41%
-3.07%	1.10%	-2.04%	-0.86%	-4.43%

**Table F.VII: Prod. shape factors and  $\sigma$  of T4 HT D1 simulation with MG-P1 XS (mixed pebble types)**

CHAN A	CHAN B	CHAN C	CHAN D	CHAN E
0.70 0.20%	0.63	0.55	0.57	0.50 0.18%
0.88 0.17%	0.19%	0.18%	0.18%	0.62 0.17%
1.09 0.16%	0.82	0.73	0.75	0.78 0.15%
1.25 0.13%	0.16%	0.16%	0.16%	0.91 0.13%
1.38 0.11%	1.04	0.92	0.94	1.01 0.11%
1.53 0.09%	0.10%	0.10%	0.10%	1.09 0.09%
1.58 0.08%	1.31	1.17	1.19	1.15 0.08%
1.66 0.08%	0.08%	0.08%	0.08%	1.18 0.07%
1.68 0.09%	1.37	1.20	1.23	1.19 0.07%
1.61 0.09%	0.07%	0.07%	0.07%	1.17 0.08%
1.52 0.10%	1.36	1.20	1.22	1.08 0.10%
1.36 0.13%	0.08%	0.07%	0.07%	1.02 0.12%
1.17 0.14%	1.26	1.12	1.14	0.88 0.13%
0.97 0.14%	1.10	0.98	1.00	0.72 0.14%
0.79 0.17%	0.89	0.78	0.81	0.56 0.16%
	0.13%	0.13%	0.13%	
	0.67	0.59	0.61	
	0.16%	0.16%	0.16%	

**Table F.VIII: Rel. diff. on prod. shape factors of 13-group P1-S<sub>8</sub> AP2 calculation from T4 HT D1**

CHAN A	CHAN B	CHAN C	CHAN D	CHAN E
-4.74%	-2.21%	-3.99%	-3.75%	-5.60%
-2.16%				-3.23%
-1.90%	-1.62%	-3.88%	-3.08%	-2.96%
-0.62%	-0.68%	-2.58%	-1.81%	-1.87%
-0.33%	0.47%	-1.92%	-1.04%	-1.11%
0.49%				-0.78%
0.86%	1.14%	-1.28%	-0.60%	-0.64%
1.89%	1.92%	-0.28%	0.35%	0.17%
1.17%	2.38%	0.04%	1.07%	0.75%
1.81%				0.01%
1.41%	2.66%	0.28%	1.20%	0.86%
1.62%	2.50%	0.79%	1.32%	1.08%
1.53%				0.93%
0.59%	1.60%	-0.22%	0.91%	0.02%
-0.74%	2.04%	-0.22%	0.51%	-1.19%

**Table F.IX: Prod. shape factors and  $\sigma$  of T4 HT D2 simulation with MG-P1 XS (mixed pebble types)**

CHAN A	CHAN B	CHAN C	CHAN D	CHAN E
0.72 0.21%	0.63	0.57	0.58	0.51 0.20%
0.90 0.19%	0.19%	0.19%	0.19%	0.63 0.18%
1.11 0.16%	0.84	0.75	0.77	0.79 0.16%
1.26 0.14%	0.17%	0.17%	0.17%	0.92 0.14%
1.42 0.13%	1.05	0.94	0.96	1.01 0.12%
1.52 0.10%	0.15%	0.15%	0.14%	1.09 0.10%
1.59 0.09%	1.21	1.07	1.11	1.16 0.09%
1.62 0.09%	0.11%	0.12%	0.11%	1.18 0.08%
1.64 0.08%	1.31	1.17	1.19	1.18 0.08%
1.56 0.09%	0.09%	0.09%	0.09%	1.13 0.09%
1.50 0.12%	1.34	1.20	1.23	1.08 0.11%
1.33 0.14%	0.07%	0.08%	0.08%	1.01 0.14%
1.17 0.17%	1.24	1.10	1.13	0.89 0.18%
0.97 0.21%	1.09	0.98	1.00	0.72 0.21%
0.80 0.25%	0.89	0.79	0.81	0.56 0.24%
	0.19%	0.19%	0.19%	
	0.67	0.60	0.61	
	0.24%	0.24%	0.24%	

**Table F.X: Rel. diff. on prod. shape factors of 13-group P1-S<sub>8</sub> AP2 calculation from T4 HT D2**

CHAN A	CHAN B	CHAN C	CHAN D	CHAN E
-2.89%	-0.15%	-2.35%	-2.01%	-4.46%
0.22%				-1.15%
1.35%	0.81%	-1.58%	-0.89%	-0.28%
1.83%	1.69%	-0.51%	0.04%	-0.05%
1.44%	1.70%	-0.42%	0.19%	0.17%
1.50%				0.14%
0.96%	1.50%	-0.51%	0.33%	-0.50%
1.05%	1.52%	-0.92%	-0.11%	-0.35%
0.39%	1.62%	-0.17%	0.44%	-0.43%
1.67%				0.10%
1.01%	1.98%	-0.16%	0.18%	-0.39%
0.66%	1.30%	-0.95%	0.00%	-0.31%
-0.10%				-1.56%
-1.53%	-0.07%	-2.46%	-1.30%	-2.80%
-3.70%	-0.51%	-2.91%	-2.10%	-4.31%

**Table F.XI: Prod. shape factors and  $\sigma$  of T4 HT D3 simulation with MG-P1 XS (mixed pebble types)**

CHAN A	CHAN B	CHAN C	CHAN D	CHAN E
0.68 0.21%	0.59	0.51	0.54	0.50 0.20%
0.89 0.19%	0.19%	0.19%	0.19%	0.63 0.18%
1.11 0.16%	0.79	0.70	0.73	0.81 0.16%
1.28 0.14%	0.17%	0.17%	0.17%	0.97 0.14%
1.50 0.13%	1.02	0.90	0.94	1.06 0.12%
1.64 0.10%	0.15%	0.15%	0.14%	1.16 0.10%
1.68 0.09%	0.11%	0.12%	0.11%	1.25 0.09%
1.76 0.09%	1.33	1.17	1.22	1.27 0.08%
1.74 0.08%	0.09%	0.09%	0.09%	1.27 0.08%
1.66 0.09%	1.39	1.21	1.26	1.22 0.09%
1.53 0.12%	0.08%	0.08%	0.08%	1.14 0.11%
1.41 0.14%	1.36	1.19	1.23	1.14 0.11%
1.19 0.17%	0.07%	0.08%	0.08%	1.05 0.14%
0.95 0.21%	1.25	1.09	1.14	0.91 0.18%
0.76 0.25%	1.07	0.94	0.98	0.73 0.21%
	0.14%	0.14%	0.15%	0.55 0.24%
	0.85	0.74	0.78	
	0.19%	0.19%	0.19%	
	0.61	0.55	0.56	
	0.24%	0.24%	0.24%	

**Table F.XII: Rel. diff. on prod. shape factors of 13-group P1-S<sub>8</sub> AP2 calculation from T4 HT D3**

CHAN A	CHAN B	CHAN C	CHAN D	CHAN E
-3.57%	-1.78%	-3.54%	-3.13%	-5.34%
-2.01%				-2.68%
-0.69%	-0.80%	-3.22%	-2.12%	-1.57%
-0.06%	0.15%	-1.98%	-1.35%	-1.13%
0.34%	1.13%	-1.30%	-0.57%	-0.37%
1.04%				-0.05%
1.40%	1.35%	-0.47%	0.46%	0.71%
2.28%	2.88%	0.51%	1.47%	1.10%
1.78%	3.19%	1.19%	2.14%	1.56%
2.68%				1.79%
2.90%	2.84%	1.39%	2.06%	1.43%
1.68%	2.57%	0.73%	1.25%	0.97%
1.06%				-0.27%
-0.18%	0.94%	-0.82%	0.02%	-1.96%
-2.11%	1.38%	-1.28%	-0.59%	-3.64%

